Physical properties of strange-modes appearing in pulsations of very luminous stars

(
)

25　12

Department of Astronomy, Graduate School of Science,
The University of Tokyo

Supervisor

Prof. Hiromoto Shibahashi

Jury members

Prof. Masanori Iye, Chair

Prof. Wako Aoki

Prof. Hirohisa Hara

Prof. Toshitaka Kajino

Prof. Umin Lee

Abstract

Stars keep hydrostatic equilibrium during most of their lifetimes. But many of them show some variability of the brightness in short timescales. While the causes for the variability are mass ejecting, rotation, flare, etc., pulsation is also responsible. Stellar pulsations are phenomena that a star repeats to expand and shrink periodically. They are powerful tools to investigate stellar interiors. Simultaneously, they are thought to affect profiles of stellar structure by inducing mass loss, angular momentum transfer, etc. It had been originally known that there had been two types of pulsation modes, p (pressure) and g (gravity) modes. Their physical properties are well-understood with the adiabatic approximation, since their pulsations only slightly deviate from adiabatic processes. In theoretical models of very luminous stars with $L/M \gtrsim 10^4 L_\odot/M_\odot$ such as massive stars, helium stars and Wolf-Rayet (WR) stars, etc., on the other hand, there exist eigenmodes which show different behaviors from p and g modes, and they have been called "strange-modes". Due to the extremely high luminosity, heat capacity of envelopes of such stars is much smaller than thermal energy flux flowing from the stellar center. In this situation, pulsations significantly differ from adiabatic processes. Then, the adiabatic approximation is no longer valid, and properties of strange-modes have not been understood enough. But since amplitude of strange-modes grows much more rapidly than that of ordinary modes, strange-modes may have higher possibility for nonlinear phenomena, such as mass loss, and be influential on stellar evolutions.

So far calculations of strange-modes have been carried out with the frozen-in convection (FC) approximation, under which convective luminosity is assumed to be constant during pulsations. One of reasons for this is that there are still lots of uncertainties on convection theories. In envelopes of hot massive stars, particularly, convection is not so dominant as in those of stars in the redder side of the classical instability strip. In a convection zone at around 200,000K, which is caused by the opacity bump due to ionizations of Fe group elements, of hot massive stars, however, convection contributes a few dozen percent in energy transport. Then, we cannot definitely neglect a process that pulsation changes convective luminosity, and that the change in the convective luminosity in turn gives the pulsation the feedback.

In this study, calculations of strange-modes are carried out by adopting the time-dependent convection (TDC) theory, which deals with convection-pulsation interactions. This study found that convection suppresses pulsational instability of some of the strange-modes. The excitation of such modes takes place at the Fe opacity bump, around which convection certainly contributes to energy transport. But it is confirmed that the strange-mode instability certainly exists even if convective effects are included. Massive stars experience the luminous blue variable (LBV) stage, at which substantial amount of mass is lost. Although the mass-loss mechanism has not yet been established, the instability of strange-modes has been suggested as one of the candidates for the mechanism by calculation with FC. This study supports this suggestion even with the convective effects.

Nonradial pulsations are also analyzed in the main-sequence stage. Nonradial modes have an additional parameter l, which indicates the number of node lines on the stellar surface. In

the low l cases, the mode amplitude is confined to the outer layer including the Fe bump. As the l increases, however, waves become propagate in the radiative zone below the Fe bump convective zone. That is, the amplitude leaks to this zone and the mode comes to suffer from radiative damping. The instability becomes weaker with increasing l, and finally disappears with $l = 4$. That is, the radial pulsation ($l = 0$) is most responsible for the instability.

This study also investigates the physical origin of strange-modes. In fact, there are two types of strange-modes, one with and without adiabatic counterparts. The type having adiabatic counterparts appears in the main-sequence stage, while the other type dominantly does in the post main-sequence stage. The type with adiabatic counterparts has the corresponding solutions in the adiabatic analysis. This type is excited by the classical κ-mechanism like the ordinary modes. But since waves are trapped in a narrow region around the Fe bump, the excitation works very strongly, and leads to the extremely rapid growth of the amplitude.

On the other hand, the second type, the strange-modes without adiabatic counterparts, are not excited by the κ-mechanism. Instead, dominance of radiation pressure is important. This study demonstrates that this type of instability is suppressed and needs higher luminosity in the zero-metallicity case, where radiation pressure is weaker than the Population I case due to lack of the Fe opacity bump. While this type of instability takes place for $\gtrsim 50 M_{\odot}$ in the Population I case, it does for $\gtrsim 100 M_{\odot}$ in the Population III case. With the zero-metallicity, however, we can expect that very massive stars were formed due to lack of cooling process due to heavy element emission lines. Particularly, the pair-instability supernova (PISN) is proposed in the mass range of $130 - 300 M_{\odot}$. Its existence is controversial since it produces peculiar chemical composition, which is inconsistent with observations of extremely metal poor stars. This study finds that the instability of the strange-mode occurs during evolution of stars which could evolve toward PISN, and suggests the possibility for non-existence of PISN in agreement with the observation.

Contents

II Origin and pulsational instability of strange-modes   76

4 Stability analysis of radial pulsations   77

5 Existence and excitation of strange-modes   105

6 Stability analysis of nonradial pulsations   139

List of Figures

List of Tables

1

Introduction

1.1 Pulsations of stars

Stars keep hydrostatic equilibrium in their own structure during most of their lifetimes. That is, they almost keep their constant shapes, or change them very slowly. Thus, their brightness should not change abruptly. But some of them show some variability of the brightness in much shorter timescale than that of their lives. While it can be caused by mass ejecting, rotation, flare, etc., pulsation is also responsible for the variability. Stellar pulsation is a phenomenon that a star repeats to expand and shrink periodically. It was first found in ø Ceti by Fabricius in 1596 (Ledoux and Walraven, 1958). It was observed that the brightness of the star changed by 8 magnitude with period 332 days. Then, the star was named "Mira", and had become the prototype of Mira variables. After that, pulsations were also found in η Aquila and δ Cepheid, for which the brightness changed by 1 magnitude with period 6 days. These stars are now categorized as pulsating stars called "Cepheids". At that time, however, pulsations had not yet been regarded as the cause for the brightness change of these stars.

Pulsations have been thought to be responsible for some stellar variability from Shapley (1914), and was given a firm mathematical foundation by Eddington (1918a,b). On the other hand, Leavitt and Pickering (1912) found the period-luminosity relation among Cepheids in the Small Magellanic Cloud, and then stellar pulsations have been widely used as distance indicators in the universe.

While improvement in precision of the observation has made the roles as the distance indicators broader, it enabled us to observe other types of pulsations around 1970. In pulsations of Miras and Cepheids, stars repeat shrinking and expanding while keeping their spherical symmetry. Such phenomena are called "radial pulsations". But we also became able to observe "nonradial pulsations", phenomena that a star loses the spherical symmetry during pulsations. That is, some parts on a surface of a star shrink, while others expand at the

8
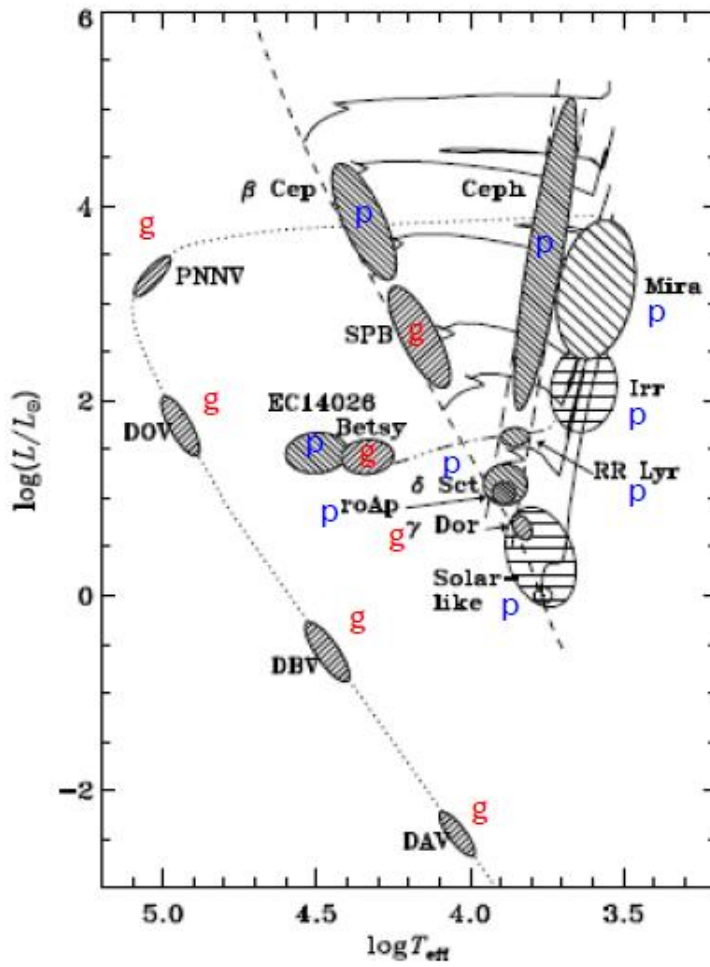
Figure 1.1: Distribution of different types of pulsating stars in the HR diagram. Provided by Jørgen Christensen-Dalsgaard.

same time. In general, stars having nonradial pulsations are likely to show pulsations with plural different periods, or different pulsational modes. Pulsations are caused by propagation of waves in stellar interiors, and properties of the waves reflect those of media in which they

propagate. Then, we can investigate the interiors by use of them. In particular, having a lot of pulsational modes gives us advantages to obtain information in the interiors. A field to study stellar interiors by use of pulsations is called "asteroseismology". In this field, there are a lot of attempts to reveal properties in stellar interiors. As representative examples, asteroseismology in the Sun ("helioseismology") has been finding that the outer convection zone has differential rotation, while the inner core has rigid rotation. Recently, the evidences for large difference in rotational frequency between inner and outer parts of red giants have been found by use of Kepler data. In roAp stars, 3D information of atmosphere can be obtained thanks to pulsations having short wavelength near the surface by use of line profile variations (Nomura *et al.*, 2012).

On the other hand, stellar pulsations itself can affect structure of stars. Asymptotic Giant Branch (AGB) stars pulsate as Mira variables, and the pulsation is thought to play an important role in mass loss and to lead to evolution toward white dwarfs. The pulsationally-driven mass loss has been also considered to give the upper limit mass of main sequence stars (Appenzeller, 1970b,a; Talbot, 1971a,b; Papaloizou, 1973a,b). Pulsations can also cause angular momentum transport and affect the rotation profile (Ando, 1982). This idea has been applied to Be phenomena. As angular momentum is transported toward the stellar surface, surface rotational velocity is raised and episodic mass loss takes place (e.g. Ando, 1986; Lee, 1993; Shibahashi and Ishimatsu, 2013). In the case of the Sun, on the other hand, internal gravity waves excited at the bottom of convective envelope might propagate in the inner radiative core, transport angular momentum and realize the rigid rotation profile of the core as introduced above (e.g. Charbonnel and Talon, 2005).

Fig.1.1 shows distribution of different types of pulsating stars. Stellar pulsations happen as waves propagate and standing waves are formed. In general, there are two types of standing waves in pulsating stars. The first type is "p (pressure) mode", which is a standing wave or an eigenmode of acoustic waves. The second type is "g (gravity) mode", which is that of internal gravity waves. The restoring force of this type of wave is buoyancy. In cases of main sequence stars, p modes propagate in outer envelopes, while g modes in deep interiors. That is, the former and the latter are useful to investigate structure of outer and inner regions, respectively. In cases of white dwarfs, on the other hand, g modes cannot propagate in the deep interiors due to degeneracy of the cores, but instead propagate in the outer envelopes.

1.2 Pulsational instability

When pulsation is generated with tiny amplitude, it may be damped or grow in time. If it is damped, this situation is referred to as being "pulsationally stable". If it grows, as being "pulsationally unstable"(Fig.1.2).

In fact, one star has a number of eigenmodes. Ideally speaking, a star thought to have no pulsations has no unstable modes, and all the eigenmodes are pulsationally stable. In a pulsating star, some of the eigenmodes are unstable, but the others are stable. Unstable modes correspond to phenomena of stellar pulsations. Stars in the hatched regions of Fig.1.1 are thought to have some unstable modes. The most famous region is "classical instability strip", which is between the two dashed straight lines and includes the zones of Cepheid, RR
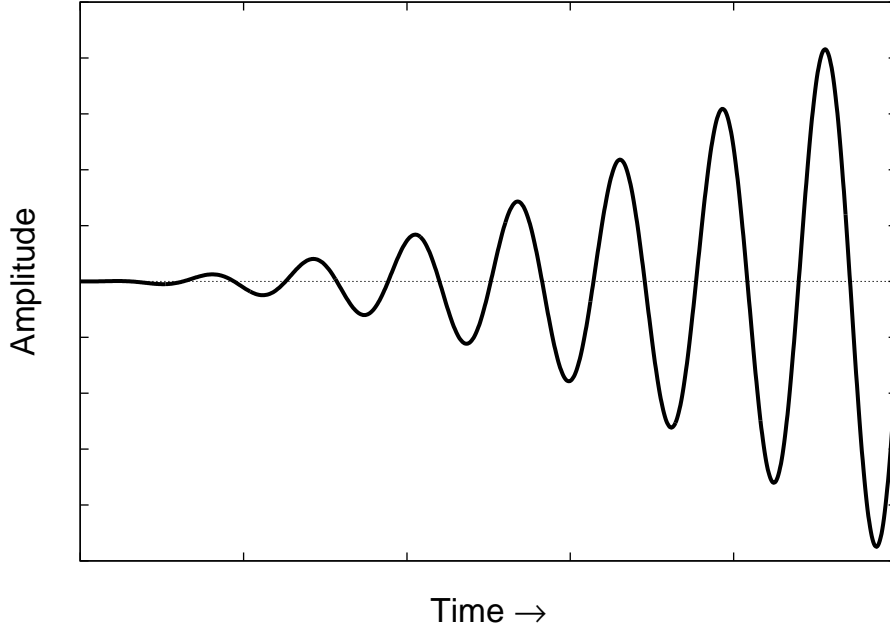
Figure 1.2: Pulsational instability.

Lyrae, and δ Scuti. Many of stars in the strip have some unstable p modes.

What causes pulsational instability? In most cases, heat engine mechanisms are responsible for it. In case of the Cepheid instability strip, the pulsations are excited by the κ-mechanism, which is one type of heat engine mechanisms. In the κ-mechanism, thermal flux is absorbed more in shrinking phase of pulsation, while dissipated more in expanding phase. Through this process, the absorbed thermal energy is converted into work or mechanical pulsational energy, and pulsational amplitude grows, which means pulsational instability.

1.3 Strange-modes

Properties of p and g modes are well-understood, and then reliable for investigating internal structure. In theoretical models of very luminous stars, on the other hand, there exist eigenmodes which show different behaviors from p and g modes, and they have been called "strange-modes". Strange-modes are originally found by the numerical study of Wood (1976), who analyzed radial (spherically symmetric) modes in high luminosity helium stars. As a matter of fact, those modes had not yet called as "strange-modes" at that time, but Cox *et al.* (1980) named them in the study of pulsations in hydrogen deficit carbon stars. Shibahashi and Osaki (1981) found radial and nonradial (non-spherically symmetric) strange-modes while analyzing pulsations in the higher temperature side of the Cepheid instability strip. After that, many authors have been working on analyses of strange modes in helium stars (Saio and Jeffery, 1988; Saio *et al.*, 1984; Gautschy and Glatzel, 1990; Gautschy, 1995; Saio, 1995), Wolf-Rayet stars (Glatzel *et al.*, 1993; Kiriakidis *et al.*, 1996), hot massive stars (Gautschy, 1992; Glatzel

11
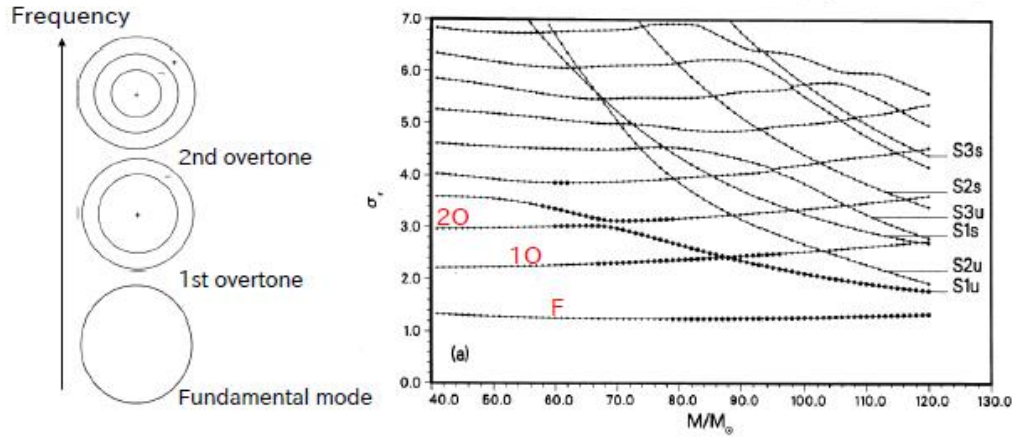
Figure 1.3: The lowest three frequency modes of ordinary radial pulsations (*left*) and modal diagram for radial modes in ZAMS stars, of which the abscissa is stellar mass of ZAMS stars and the vertical axis is nondimensional frequency multiplied by free-fall timescale, from Glatzel and Kiriakidis (1993b, *right*).

and Kiriakidis, 1993b,a; Kiriakidis *et al.*, 1993; Glatzel and Mehren, 1996; Saio *et al.*, 1998; Saio, 2009, 2011; Saio *et al.*, 2013; Godart *et al.*, 2010, 2011), etc.

What is the difference between strange-modes and ordinary p, g modes? Fig.1.3 shows an example of radial modes. Note that radial modes correspond to p modes. The left part of the figure shows ordinary radial modes. As for radial modes, there exists the lowest limit of frequency. An eigenmode with the lowest frequency is called "fundamental mode", for which the phase of the pulsation is homogeneous in a whole star. An eigenmode having the second lowest frequency is "1st overtone". In this case, a star has a node, and the pulsational phases are opposite in both sides of the node. The next one is "2nd overtone", which has two nodes.

The right part of Fig.1.3 shows frequencies of radial modes for Zero Age Main Sequence (ZAMS) stars. Such a diagram in which eigenmodes are plotted with the abscissa indicating some parameter and with the vertical axis indicating frequency is called modal diagram. Here, the abscissa is the mass of the ZAMS stars. The frequencies are normalized by multiplying the free-fall timescale. The sequences labeled "F", "1O" and "2O" correspond to the fundamental mode, the 1st overtone and the 2nd overtone, respectively. The frequencies on these sequences are almost constant along the change of the stellar mass. On the other hand, there are descending sequences with increase in the mass, labeled "S*u" or "S*s". They actually correspond to strange-modes. That is, we can find different behaviors of strange-modes from ordinary modes in modal diagrams.

The previous studies also have found the other characteristics of strange-modes. For

12
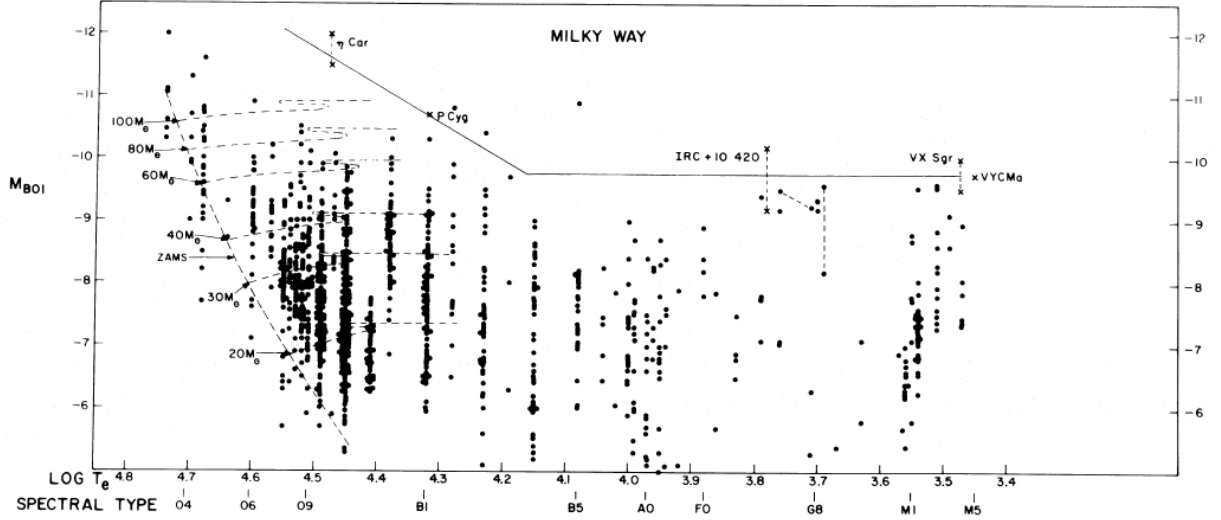
Figure 1.4: Observed Milky Way stars and Humphreys-Davidson (HD) limit, which is expressed as the solid line (Humphreys and Davidson, 1979).

instance, they appear in very luminous star models with $L/M \gtrsim 10^4 L_\odot/M_\odot$. In the outer regions of such stars, heat capacity is relatively small compared with the flowing energy from the stellar center. It causes that timescale of heat transport or thermal timescale becomes so short that heat can leak easily. Then, the short thermal timescale has been thought to be responsible for appearance of strange-modes. Besides, excitation or damping of strange-modes is extremely strong compared with that of ordinary modes. That is, unstable strange-modes have so high growth rate that it could be influential on stellar evolution.

1.4 Evolution of massive stars

While core of a star with $M \lesssim 8M_\odot$ encounters degeneracy and evolves toward white dwarfs, that of a star with $M \gtrsim 8M_\odot$ never does, and instead experiences different burning cycles until the central part becomes an iron core, after which the star explodes as a core-collapse supernova. By this phenomena, it provides its surrounding with different types of elements made by nuclear reactions. Besides, the more massive a star is, the stronger radiation-driven mass loss it suffers from.

Due to the mass loss, their evolution becomes very interesting. Humphreys and Davidson (1979) gave a limit line so-called "Humphreys-Davidson (HD) limit", over which there is a lack of observed stars, on the HR diagram on the basis of observed samples in the Milky Way

13
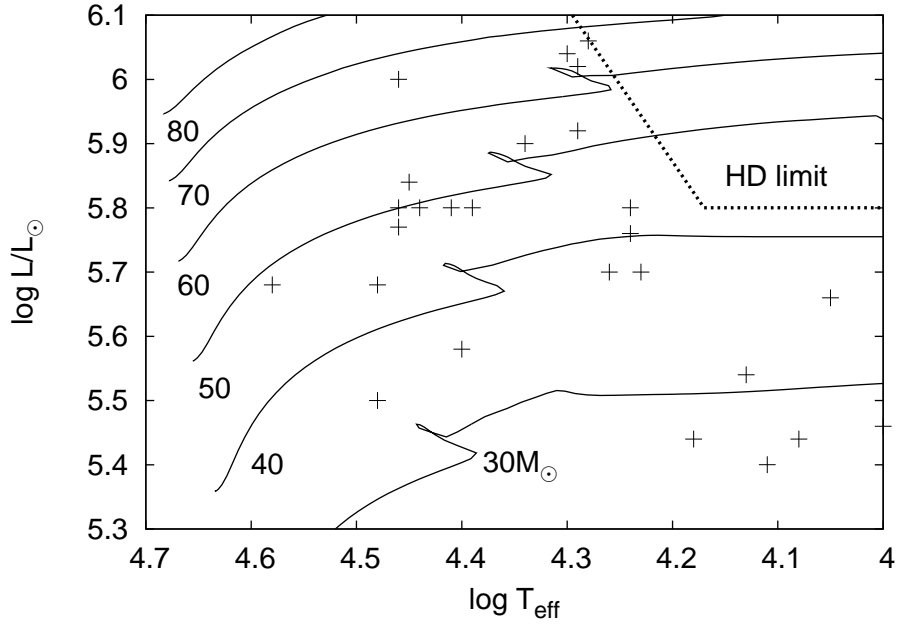
Figure 1.5: Distribution of luminous blue variables (LBVs) on the HR diagram. The crosses are observed LBVs listed in van Genderen (2001). The solid lines are evolutionary tracks with $X = 0.70$, $Z = 0.02$, which are results of computation without taking into account mass loss.

(Fig.1.4) and in the Large Magellanic Clouds. This phenomenon implies that massive stars with $M \gtrsim 50 M_\odot$ never evolve toward red supergiants, and that some instability takes place before evolving beyond the HD limit. As a matter of fact, drastic variability has been observed in the higher temperature side of the limit (Fig.1.5). Stars showing such variability are called "luminous blue variables (LBVs)", or "S Dor variables". P Cyg is the first LBV, which was observed in 1600. In August of that year, it suddenly appeared as a very luminous star. In 1655, it became very luminous again, and had been able to be observed by naked eyes. After that, it has been seen again from around 1700, has been gradually increasing its brightness, and now brightening at $V \simeq 5$. LBVs in the high effective temperature side on the HR diagram are dark in the visible light, and thought to be at quiescence. But LBVs abruptly eject matter comparable to the solar mass, and the ejected matter expands and hides the core. This causes that the pseudo-photosphere is formed in the ejected matter, and that the apparent effective temperature decreases. By this, the LBVs become luminous in the visible light. When the eruption ceases and the core becomes exposed again, the LBVs get back toward the higher effective temperature side.

LBVs are thought to repeat the above phenomena, that is, quiescence $\rightarrow$ eruption $\rightarrow$ quiescence ... After that, they are thought to become Wolf-Rayet (WR) stars. WR stars are located in the high temperature and luminosity side on the HR diagram. Because of the existence of emission lines, WR stars are thought to have stellar wind around themselves. The

14

mass loss rate exceeds $10^{-5} M_\odot$ yr^{-1}. Considering that the lifetime of WR stars is in the order of 10^5 yr, the stellar wind should substantially affect the stellar evolution. While stars with the initial mass of $\gtrsim 25 M_\odot$ are thought to be WR stars, the mass of WR stars are 5 to a few ten times of solar mass. When the initial mass is in the range of $25 - 50 M_\odot$, stars first evolve from main sequence to red supergiants, and then might be WR stars. When the initial mass is over $50 M_\odot$, on the other hand, stars never become red supergiants, instead evolve toward LBVs, and then might be WR stars.

We have not yet obtained an established mechanism for the sporadic eruptions occurring in LBVs, although many authors have proposed different explanations by effects of radiation pressure in the situation near the Eddington limit, close-binary models, rapid rotations, etc (see Humphreys and Davidson, 1994). Pulsational instability is also one of the candidates for the LBVs' eruption trigger. Glatzel and Kiriakidis (1993a) suggested that the instability of strange-modes appears around the HD limit. But their analysis did not take into account effects of convection, although the strange-modes are excited at convection zones.

1.5　Aim of this study

As mentioned above, strange-modes have been analyzed by many studies. Most of them have been working on pulsational stability analyses of strange-modes, and have found unstable strange-modes in very luminous stars. By the way, most of stars have convection zones. Convection should have some effects on pulsations. However, we still have difficulty in theoretical description of convection itself, and also of convection-pulsation couplings. Then all of the previous stability analyses of strange-modes have been carried out by neglecting the effects of convection.

We need to adopt a time-dependent convection (TDC) theory to carry out a pulsational stability analysis with effects of convection. So far several TDC theories have been proposed by Unno (1967), Gough (1965, 1977), Xiong (1989) and others. Particularly, the theory of Unno (1967) was extended to nonradial pulsations by Gabriel *et al.* (1974), and recently adopted to calculation of the pulsational stability analysis by Grigahcène *et al.* (2005) and Dupret *et al.* (2005), who analyzed the stability of δ Scuti stars and has succeeded in explaining suppression of the pulsational instability in the redder side of the classical instability strip, where convection plays a significant role in energy transfer in the stellar envelopes.

This study focuses on strange-modes in hot massive stars. As a matter of fact, convection in envelopes of hot massive stars is not as dominant as in those in the redder side of the classical instability strip. But unstable strange-modes are excited in convection zones and we cannot definitely conclude that convection never affects the stability of the strange-modes. Then, this study carries out a pulsational stability analysis of strange-modes with the TDC theory originally derived by Unno (1967), although the previous studies neglected effects of convection. As mentioned above, the strange-modes seem responsible for the LBV phenomena.

Although strange-modes have been found by many previous studies, it is still puzzling why strange-modes exist as eigenmodes and how unstable strange-modes are excited. Physical properties of ordinary modes can be explained by the WKB approximation based on the

adiabatic approximation. But such a procedure is no longer available for some of the strange-modes. It has been found that the strange-modes appear only in pulsations of very luminous stars with $L/M \gtrsim 10^4 L_\odot/M_\odot$. In envelopes of such stars, the luminosity is too high that matter can save thermal energy flowing from the stellar center. In this very nonadiabatic situation, adiabatic scheme may not be suitable for some of the strange-modes, and then this study carries out local analyses suitable for the situation.

Part I

Equilibrium structure and pulsations of stars

2
Hydrostatic structure of stars

2.1 Introduction

Stars are born from molecular clouds. The dense part in the clouds experiences gravitational collapse and then a protostar, in which the hydrostatic equilibrium is realized, is generated in the central region. In this phase, the surrounding gas accretes into it and the protostar's mass increases. It brights by the release of the gravitational energy through the accretion. Its light, however, is absorbed and re-emitted by the surrounding dust. Hence it can be observed not by the visible light, but by the infrared. Later, the surrounding matter gets blown away by the stellar wind and the accretion stops. Then, the star can become observed by the visible light.

Next, the star experiences the gravitational contraction while keeping the hydrostatic equilibrium. This stage is called "pre–main-sequence stage." The energy flows from the hot center to the cool surface, and is emitted as the stellar light. Since the equilibrium between the income and outgoing of the energy must be realized, the gravitational energy is released by contraction. Some of the energy flows to the surface as described above, the rest is converted into the internal energy, which raises up the central temperature.

When the central temperature reaches 10^7 K, the nuclear burning of hydrogen is set up. It provides the energy required for the energy flow due to the temperature gradient between the center and the surface. That terminates the gravitational contraction, which means reaching "Zero Age Main Sequence" (ZAMS) stage.

This study deals with stars after the ZAMS stage, at which structure realizes the hydrostatic equilibrium as well as the pre–main-sequence stage. In the following, we discuss prescription for hydrostatic structure of stars.
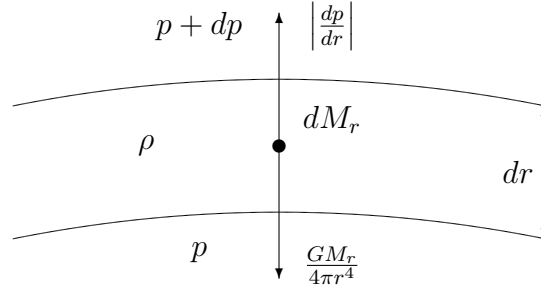
Figure 2.1: Hydrostatic layer

2.2 Differential equations

Structure of stars is described by four differential equations of hydrostatic equilibrium. The first one is the equation of continuity,

$$\frac{\partial r}{\partial M_r} = \frac{1}{4\pi r^2 \rho},\tag{2.1}$$

where r denotes distance from the center, M_r enclosed mass in the sphere with radius r, and ρ local density.

The second equation is the equation of hydrostatic equilibrium,

$$\frac{\partial p}{\partial M_r} = -\frac{GM_r}{4\pi r^4},\tag{2.2}$$

where p denotes pressure. It describes balance between gravity and force due to pressure gradient.

The third one is the equation of the diffusion approximation for radiative transfer,

$$\frac{\partial T}{\partial M_r} = -\frac{3\kappa L_R}{64\pi^2 acr^4 T^3},\tag{2.3}$$

where T denotes temperature, κ opacity, L_R radiative luminosity, a radiative constant, c light speed. It represents the radiative energy transfer in regions where movement of photons can be described as diffusion. In stellar interiors, a mean free path of photons is very short compared with the scale in which the structure changes. Thus the radiative energy transport can be regarded as a diffusive process. The derivation of this approximation is introduced in §A.

The last one is the equation of energy conservation,

$$\frac{\partial L_r}{\partial M_r} = \varepsilon - T\frac{dS}{dt},\tag{2.4}$$

where L_r denotes local, total luminosity, ε nuclear energy production rate, S entropy. The second term in the right hand side (RHS) represents thermal energy transformed from gravitational energy released by gravitational contraction.

2.3 Additional conditions described as algebraic equations

We still need some more conditions to solve the above fourth differential equation system. The first one is of a relation among thermodynamical variables p, ρ and T,

$$p = p(\rho, T, X_i), \tag{2.5}$$

where X_i is abundances of different chemical elements. This study mainly adopts the OPAL EOS table (Rogers and Nayfonov, 2002) to calculate p. The EOS tables are also used to get thermodynamical variables, e.g. $\left(\frac{\partial \ln p}{\partial \ln T}\right)_\rho$, which appears the differential equations for stellar pulsations, shown in §3. They are also required for calculation of stellar structure with the relaxation method, although it does not explicitly appear in the differential equations, Eqs.(2.1)–(2.4).

Like the above, opacity κ, and nuclear energy production rate ε are functions of ρ, T, X_i as

$$\kappa = \kappa(\rho, T, X_i) \tag{2.6}$$

$$\varepsilon = \varepsilon(\rho, T, X_i). \tag{2.7}$$

The opacity is calculated by using the OPAL opacity table (Iglesias and Rogers, 1993, 1996), while the nuclear energy production rate with Caughlan and Fowler (1988) and Angulo *et al.* (1999).

The last condition is that luminosity is composed of radiative and convective luminosities,

$$L_r = L_R + L_C, \tag{2.8}$$

In most cases including this study, the convective luminosity is evaluated with Böhm-Vitense (1958)'s mixing length theory (MLT), which will be discussed in the next section.

2.4 Mixing length theory (MLT)

In most of stars, temperature becomes maximum at the center and decreases toward the surface. Then, thermal energy flows from the center to the surface along the temperature gradient. But temperature gradient is different by location. Thermal energy is transferred by radiation in a place with low temperature gradient. But convection comes to contribute to energy transfer in case radiative temperature gradient exceeds adiabatic temperature gradient, $\nabla_{\rm ad} \equiv \left(\frac{\partial \ln T}{\partial \ln p}\right)_{\rm ad}$. Namely, the temperature gradient can be evaluated as

$$\frac{d\ln T}{d\ln p} \equiv \nabla = \begin{cases} \nabla_{\rm rad} & (\nabla_{\rm rad} < \nabla_{\rm ad}, \text{ radiative}) \\ \text{``?''} & (\nabla_{\rm rad} > \nabla_{\rm ad}, \text{ convective}) \end{cases} \tag{2.9}$$

where $\nabla_{\rm rad}$ is called radiative temperature gradient, of which the definition is described as Eq.(A.12). It is the fictional gradient in case all energy is transported only by radiation. To be
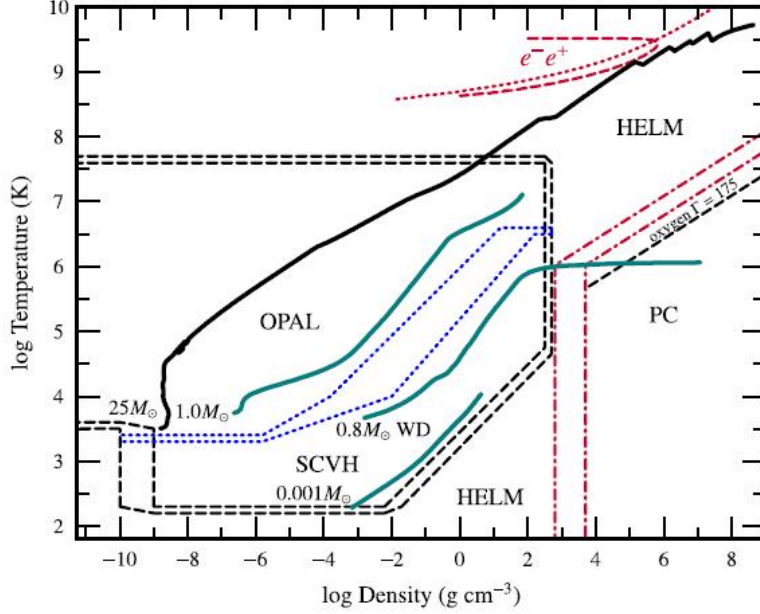
Figure 2.2: Ranges of EOS tables used in MESA code, adopted by this study to calculate stellar evolution and structure, on the $\rho - T$ plane (Paxton *et al.*, 2011).

exact, convection comes to contribute when the radiative temperature gradient $\nabla_{\rm rad}$ exceeds the adiabatic temperature gradient $\nabla_{\rm ad}$. When $\nabla_{\rm rad} < \nabla_{\rm ad}$, temperature gradient and total luminosity are identical to radiative temperature gradient and radiative luminosity, respectively. But when $\nabla_{\rm rad} > \nabla_{\rm ad}$, we have to evaluate convective luminosity and temperature gradient by considering physics of convection.

In most cases including this study, the Böhm-Vitense (1958)'s mixing length theory (MLT) is usually adopted to evaluate the convective luminosity and temperature gradient. In convection of MLT, a gas clump having slightly higher temperature than its surrounding is rising mixing length Λ. Then, it mixes with the surrounding and releases the exceeding energy. On the other hand, the clump cooler than its surrounding goes down Λ.

Let us consider the equation of motion for the clump. We now write density as $\rho = \rho_0 + \Delta\rho$ where the subscript "0" denotes values at the point r in the equilibrium state of the clump. In this state, we have $\rho = \rho_0$, and the equation of motion becomes

$$\ddot{r}_0 = -g_0 - \frac{1}{\rho_0}\left(\frac{\partial p}{\partial r}\right)_0 = 0. \tag{2.10}$$

21
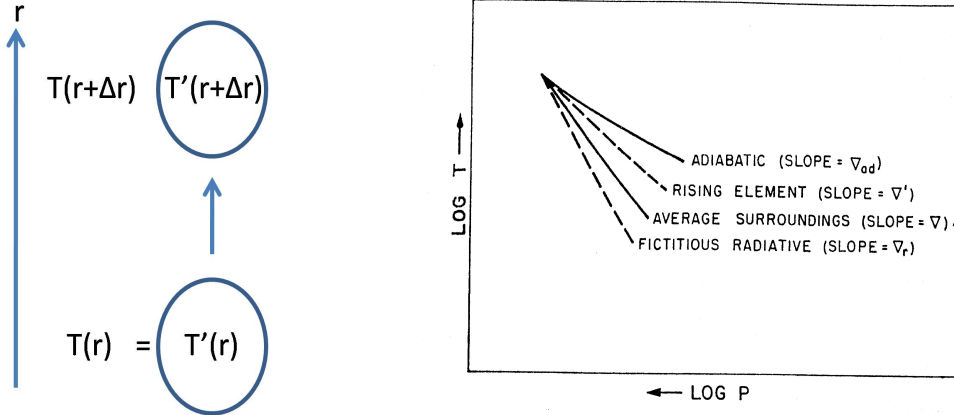
Figure 2.3: Convection in MLT

In general, the equation is

$$\ddot{r} = -g_0 - \frac{1}{\rho_0}\left(\frac{\partial p}{\partial r}\right)_0\left[1 - \frac{\Delta\rho}{\rho_0}\right] = -g_0\frac{\Delta\rho}{\rho_0} \tag{2.11}$$

This says that the clump rises or sinks due to the buoyancy force $f_B = -g\Delta\rho$.

Next, we will notice the work done in moving the clump. We suppose that the clump starts moving with zero velocity at r and is accelerated upward through the distance Δr. We assume that the excess density is virtually zero at r and increases linearly with Δr until it has the value $\Delta\rho(\Delta r)$ at $r + \Delta r$. Neglecting the variation of g over the distance Δr, the work done on unit volume in moving it through the distance Δr is then

$$W(\Delta r) = \int_0^{\Delta r} f_B(\Delta r)'d(\Delta r)' = -g\int_0^{\Delta r}\Delta\rho((\Delta r)')d(\Delta r)' = -\frac{1}{2}g\Delta\rho(\Delta r)\Delta r \tag{2.12}$$

The factor $1/2$ in the last term is added since $\Delta\rho$ increases linearly with $(\Delta r)'$. Note that $W(\Delta r)$ increases quadratically with Δr. We should next average $W(\Delta r)$ over all possible values of Δr. To obtain the consistency with Böhm-Vitense (1958), we should set

$$\overline{W}(\Lambda) = \frac{1}{4}W(\Lambda) = -\frac{1}{8}g\Delta\rho(\Lambda)\Lambda \tag{2.13}$$

The work is transformed into the kinetic energy of the clump. But the clump has to push aside other masses, and thereby imparts some of its kinetic energy to them. Thus we assume that the average of the kinetic energy is equal to that of the work:

$$\overline{\frac{1}{2}\rho(\Delta u)^2} \simeq \frac{1}{2}\rho\overline{(\Delta u)^2} = \frac{1}{2}\overline{W}(\Lambda) = -\frac{1}{16}g\Delta\rho(\Lambda)\Lambda \tag{2.14}$$

22

Hence, we have obtained the excess of velocity as

$$\overline{(\Delta u)^2} = -\frac{1}{8}g\frac{\Delta\rho(\Lambda)}{\rho}\Lambda. \tag{2.15}$$

On the other hand, how is the excess of temperature? As shown in the left panel of Fig.2.3, the clump, at the initial height r, has the same temperature as its surrounding, but gradually comes to have higher temperature than it. When the clump rises length Δr, temperature in the clump T' is described as

$$T'(r + \Delta r) = T(r) + \frac{dT'}{dr}\Delta r \tag{2.16}$$

Hence, the temperature excess becomes

$$\Delta T(r + \Delta r) = T'(r + \Delta r) - T(r + \Delta r) = \left(\frac{dT'}{dr} - \frac{dT}{dr}\right)\Delta r \tag{2.17}$$

Introducing the expressions for temperature gradients

$$\nabla(') \equiv \frac{d\ln T(')}{d\ln p}, \tag{2.18}$$

and replacing Δr with Λ, we have

$$\Delta T(r + \Lambda) = (\nabla - \nabla')\frac{T\Lambda}{H_p} \tag{2.19}$$

where H_p denotes pressure scale height defined as

$$H_p \equiv -\frac{dr}{d\ln p} = \frac{pr^2}{GM_r\rho}. \tag{2.20}$$

The convective flux, which means transferred energy by the clump, is defined as

$$F_C(\Delta r) = \rho c_p \Delta u \Delta T. \tag{2.21}$$

Taking average over all possible Δr, and using Eqs.(2.15) and (2.19), we have

$$L_C = 4\pi r^2 F_C = 4\pi r^2 \rho c_p \overline{\Delta u}\,\overline{\Delta T} \simeq 4\pi r^2 \rho c_p \sqrt{\overline{(\Delta u)^2}}\overline{\Delta T} \tag{2.22}$$

$$= 4\pi r^2 \rho c_p T \left(\frac{\Lambda}{2H_p}\right)^2 \left(\frac{v_T p}{2\rho}\right)^{1/2} (\nabla - \nabla')^{3/2} \tag{2.23}$$

where we have assumed pressure equilibrium while the clump is rising or sinking, and have used the relation

$$\frac{\Delta\rho}{\rho} = -v_T\frac{\Delta T}{T} \quad \text{with} \quad v_T \equiv -\left(\frac{\partial\ln\rho}{\partial\ln T}\right)_p. \tag{2.24}$$

23

By use of ∇_{rad}, we can describe the local total luminosity as

$$L_r = \frac{16\pi ac GM_r T^4}{3p\kappa}\nabla_{\mathrm{rad}}. \tag{2.25}$$

Transforming Eq.(2.3), we get an expression of the radiative luminosity as

$$L_R = \frac{16\pi ac GM_r T^4}{3p\kappa}\nabla. \tag{2.26}$$

Substituting Eq.(2.23), Eq.(2.25) and Eq.(2.26) into Eq.(2.8), we have

$$\nabla_{\mathrm{rad}} = \nabla + \frac{3\kappa\rho^2 c_p\Lambda\overline{\Delta u}}{4acT^3}(\nabla - \nabla') \tag{2.27}$$

Here we introduce a new parameter, efficiency of convection Γ, defined as

$$\Gamma = \frac{\text{``Excess heat content'' just before dissolving}}{\text{Energy radiated during life time}} = \frac{3}{4ac}\frac{c_p\kappa\rho^2\overline{\Delta u}}{T^3}\frac{V_{\mathrm{clump}}}{A_{\mathrm{clump}}}, \tag{2.28}$$

where V_{clump} and A_{clump} are the volume and the surface area of the convective clump. For example, we have $V_{\mathrm{clump}}/A_{\mathrm{clump}} = \Lambda/6$ for a sphere with diameter Λ. Following Böhm-Vitense (1958), we here set $V_{\mathrm{clump}}/A_{\mathrm{clump}} = (2/9)\Lambda$, and we have

$$\Gamma = \frac{c_p}{6ac}\frac{\kappa\rho^2\overline{\Delta u}\Lambda}{T^3} \tag{2.29}$$

Using this, Eq.(2.27) becomes

$$\nabla_{\mathrm{rad}} = \nabla + a_0\Gamma(\nabla - \nabla') \quad \text{with} \ \ a_0 \equiv \frac{9}{4} \tag{2.30}$$

We then require a second expression for Γ. Let us consider the energy lost toward the surrounding while the convective clump is rising or sinking. By considering the diffusion approximation, we can estimate the lost energy as

$$\Delta U_{\mathrm{lost}} = -\frac{4acT^3}{3\kappa\rho}\nabla T \times \tau_C A_{\mathrm{clump}} \sim \frac{4acT^3}{3\kappa\rho}\frac{\overline{\Delta T}}{\Lambda/2}\tau_C A_{\mathrm{clump}}, \tag{2.31}$$

where τ_C denotes the convective timescale, which is the average lifetime of convective clumps. We roughly have $\tau_C = \Lambda/\overline{\Delta u}$. With the ration $V_{\mathrm{clump}}/A_{\mathrm{clump}} = (2/9)\Lambda$, the energy lost by volume unity is

$$\frac{\Delta U_{\mathrm{lost}}}{V_{\mathrm{clump}}} = \frac{4acT^3}{3\kappa\rho}(\nabla - \nabla')\frac{T}{H_p}\frac{9}{2\overline{\Delta u}} \tag{2.32}$$

This loss of energy is made at the expense $\rho\Delta q$ of the internal energy by volume unity, where $\rho\Delta q$ is given by the first law of thermodynamics as

$$\rho\Delta q = \rho c_p\Delta T + \frac{\rho c_p T\nabla_{\mathrm{ad}}}{p}\frac{dp}{dr}\Delta r = \rho c_p T(\nabla' - \nabla_{\mathrm{ad}})\frac{\Delta r}{H_p} \tag{2.33}$$

24

Replace Δr with Λ, and since Eqs.(2.32) and (2.33) equal each other, we have

$$\frac{\nabla - \nabla'}{\nabla' - \nabla_{\mathrm{ad}}} = \frac{c_p}{6ac} \frac{\kappa \rho^2 \overline{\Delta u} \Lambda}{T^3} = \Gamma, \tag{2.34}$$

which is the second expression for Γ. From Eq.(2.15), we can obtain the expression for $\overline{\Delta u}$ as

$$\overline{\Delta u} \simeq \sqrt{\overline{(\Delta u)^2}} = \frac{\Lambda}{2H_p} \left(\frac{v_T p}{2\rho} \right)^{1/2} (\nabla - \nabla')^{1/2}, \tag{2.35}$$

then, Γ also can be described as

$$\Gamma = A(\nabla - \nabla')^{1/2} \quad \text{with} \quad A \equiv \frac{c_p}{6ac} \frac{\kappa \rho^2 \Lambda}{T^3} \frac{\Lambda}{2H_p} \left(\frac{v_T p}{2\rho} \right)^{1/2} \tag{2.36}$$

Now we have three equations for Γ, Eqs.(2.30), (2.34) and (2.36). The first one is derived from the summation of luminosities, $L_r = L_R + L_C$, the second one from the discussion of the heat loss during convection, and the third one from the expression of the average convective velocity $\overline{\Delta u}$. Hereafter, we are going to derive the equation to evaluate ∇ or L_C. First, we eliminate ∇' by combining Eqs.(2.30) and (2.36):

$$\Gamma = A \left(\frac{\nabla_{\mathrm{rad}} - \nabla}{a_0 \Gamma} \right)^{1/2} \tag{2.37}$$

In addition, we also eliminate ∇' by combining Eqs.(2.30) and (2.34):

$$\Gamma = \frac{\nabla_{\mathrm{rad}} - \nabla}{(a_0 \Gamma + 1)\nabla - \nabla_{\mathrm{rad}} - a_0 \Gamma \nabla_{\mathrm{ad}}} \tag{2.38}$$

$$\Rightarrow \quad \nabla = \frac{(\Gamma + 1)\nabla_{\mathrm{rad}} + a_0 \Gamma^2 \nabla_{\mathrm{ad}}}{\Gamma(a_0 \Gamma + 1) + 1} \tag{2.39}$$

By using this, we eliminate ∇ in Eq.(2.37), and after some manipulation we get a cubic equation for Γ,

$$a_0 \Gamma^3 + \Gamma^2 + \Gamma - A^2(\nabla_{\mathrm{rad}} - \nabla_{\mathrm{ad}}) = 0 \tag{2.40}$$

The last term $-A^2(\nabla_{\mathrm{rad}} - \nabla_{\mathrm{ad}})$ is negative in convection zones, and this equation has one positive real solution for Γ. Once getting the value of Γ, we can evaluate ∇, for example, by using Eq.(2.37), and L_C by Eq.(2.23).

2.5 Boundary conditions, atmosphere model and numerical procedures

When we solve structure of a star, we should integrate Eqs.(2.1)–(2.4) between the center and the photosphere. The total mass of the star M and the abundance profiles $X_i(M_r)$ should
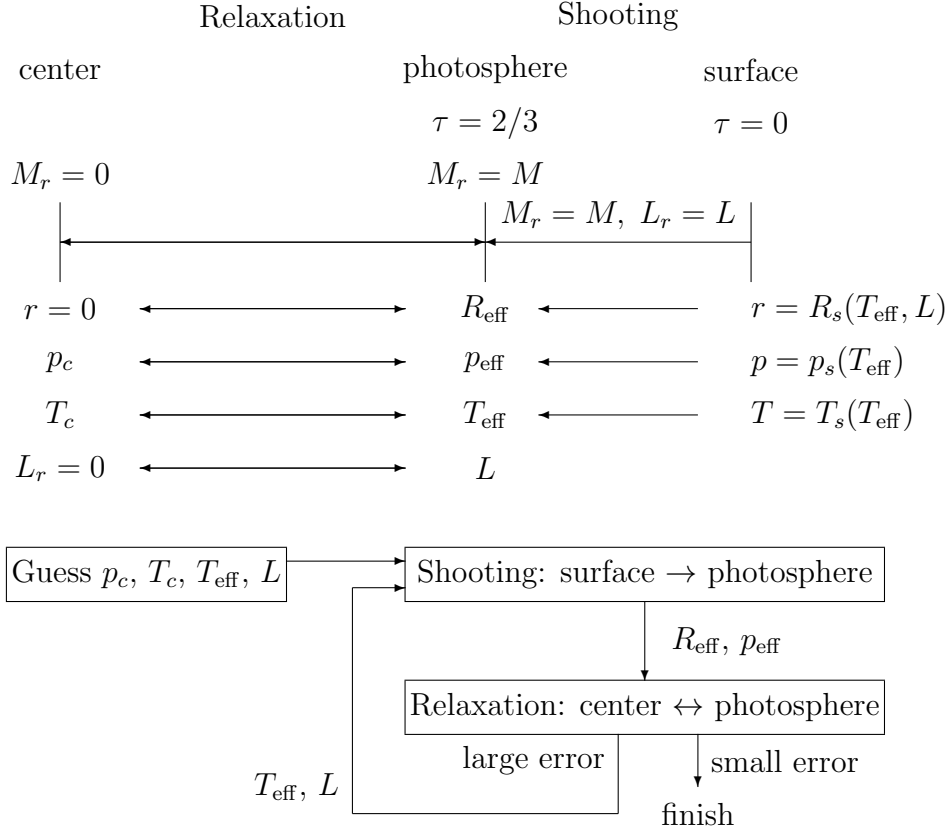
Figure 2.4: Numerical procedure for solving structure of a star

be given, and we should try to obtain the values of the distance from the center r, the local luminosity L_r, the pressure p and the temperature T at each layer by integration. Since the system has the fourth order, we need four boundary conditions. In the usual manner, we set two conditions at each of inner and outer boundaries. At the inner boundary, we set

$$r = 0, \quad L_r = 0 \ \text{ at } \ M_r = 0. \tag{2.41}$$

On the other hand, the outer boundary conditions at the photosphere are obtained with integration from the surface layer over the photosphere. Above the photosphere, the diffusion approximation (2.3) is no longer valid due to the low optical depth, and we have to introduce another treatment.

This study adopts the Eddington approximation to construct atmosphere models (Here we define a region above the photosphere as "atmosphere"). The details for the physics of the atmosphere are discussed in §B. As shown in Fig.2.4, the integration in the atmosphere is carried out by setting M_r and L_r to be homogeneously the total mass M and the total luminosity L, respectively, since the atmosphere occupies negligible amount of the total mass

26

of a star, and has no energy source and no gradient of luminosity. That is, we do not need to integrate the equation of continuity (2.1), and the equation of energy conservation (2.4). Instead, we integrate

$$d\tau = -\kappa\rho dr, \tag{2.42}$$

which is the definition of the optical depth τ. Thus, we have the third order system of the differential equations. The relaxation method is adopted for the integration between the center and the photosphere, while the shooting method from the atmosphere surface to the photosphere. When we start the numerical integrations, we have to guess the values of the pressure p_c and the temperature T_c at the center, and the temperature T_{eff} and the luminosity L at the photosphere. Note that the temperature at the photosphere T_{eff} is called "effective temperature", which is observed in the visible light, but not exactly surface temperature. The values at the atmosphere surface (r_s, p_s and T_s in Fig.2.4) can be evaluated once T_{eff}, L is determined by using

$$(\text{B.10}) : \quad T_s = 2^{-1/4}T_{\text{eff}},$$
$$(\text{B.11}) : \quad R_s = \left(\frac{L}{8\pi\sigma_B T_s^4}\right)^{1/2},$$
$$p_s = p(\rho = 2\times 10^{-11}\text{g cm}^{-3}, T_s, X_i) \tag{2.43}$$

where the pressure is evaluated by the EOS table by assuming the surface density is $\rho_s = 2\times 10^{-11}$ g cm^{-3} in this study. Note that chemical abundances X_i are homogeneous in the whole of the atmosphere. Then, we can integrate the third order differential equations from $\tau = 0$ to $2/3$ to obtain the physical quantities (R_{eff}, p_{eff} in Fig.2.4) at the photosphere.

After that, we go to the two-point boundary value problem between the center and the photosphere with the relaxation method. In the relaxation method, we can evaluate an error of the solution (see §D). If the error is relatively large, we have to repeat the above procedure. In turn, we adopt the values of p_c, T_c, T_{eff} and L obtained with the integration by hoping that they have been improved compared with the initial guess, and again carry out the integration from the atmosphere to the photosphere with the shooting method, and go to the relaxation calculation between the center and the photosphere with the relaxation method. We should continue the repetitive procedure until the error of the solution becomes much small.

<div style="text-align: right; font-size: 4em; color: gray;">**3**</div>

Theory of stellar pulsations with TDC

3.1 Introduction

Stellar pulsations are phenomena that a star expands and contracts periodically or cyclically. The idea that stellar pulsation is responsible to variability of certain types of variable stars dates from Shapley (1914), and was given a firm mathematical foundation by Eddington(1918a, 1918b). Originally, stellar pulsations had been studied by assuming spherical symmetry. We call it "radial pulsation," in which gas on the same spherical surface expands and contracts with the same phase. Dziembowski (1971) then analyzed "nonradial pulsation" for the first time. In nonradial pulsations, pulsation phase depends on the latitude θ or azimuthal angle ϕ. That is, some areas expand while the other contract on the same spherical surface at the same time.

This section introduces the theory of linear nonradial pulsations of stars. We will start from the hydrodynamical equations, and linearize them to obtain description of nonradial pulsations. We will discuss also radial pulsations as a special case.

Most of stars have convection zones, and we cannot avoid treating convection to describe stars. In most cases, the mixing length theory (MLT, Böhm-Vitense, 1958) has been used to describe convection in hydrostatic equilibrium stellar models. But when we deal with convection in pulsations, we should consider its time dependence, which MLT does not take into account. In nonradial pulsations, besides, we should be aware of its dependence on the horizontal directions. So far most of studies have neglected the effect of convection on pulsations because of the difficulty in the treatment.

But this study analyzes pulsations with the time-dependent convection (TDC) theory, which carefully takes into account coupling between convection and pulsation. There are several TDC theories proposed by different authors. We obtain the same equations at equilibrium state, corresponding to MLT, in the different TDC theories. But when we consider perturbed

situations, the different TDC theories give different pictures and equations. Gough (1965, 1977) and Unno (1967) assume phenomenological pictures of convection to derive the TDC formulation. The former is based on Taylor (1915)'s and Prandtl (1925)'s original analogy between turbulence and the kinetic theory of gases. In this description, the convective elements are accelerated by the buoyancy force over a characteristic length (the mixing length) and then exchange their thermal energy with their surroundings. On the other hand, the latter is based on the original ideas of Prandtl (1932). In this description, a turbulent viscosity acts in the opposite direction to the buoyancy force, which leads in the stationary case to convective cells with constant velocities. Although the above two TDC theories are based on the phenomenological pictures, Xiong (1989)'s TDC theory was derived directly from the basic equations of hydrodynamics and turbulence theory with statistical procedures.

The TDC theory this study adopts was originally proposed by Unno (1967) for radial pulsations. Later, Gabriel *et al.* (1974, 1975) arranged and applied it to nonradial pulsations, and it has been improved by the following studies (Gabriel, 1987, 1996, 1998, 2000). Recently, Grigahcène *et al.* (2005) has succeeded in adopting it to the nonadiabatic calculation for nonradial pulsations, and Dupret *et al.* (2005) could explain the suppression of the pulsational instability of δ Scuti stars in the redder side of the classical instability strip.

In the following, we derive the prescription describing the coupling between convection and radial, nonradial pulsations. Specifically, we first decompose the variables into values for the mean flow and for the convective fluctuation. The respective values will be next decomposed into those for the hydrostatic equilibrium and for the pulsational perturbation (Fig.3.1).

3.2   Basic hydrodynamical equations

The basic equations that describe deformations of a star are equations of hydrodynamics. We start from the following four hydrodynamical equations, i.e. the equations of continuity, motion and energy conservations, and the Poisson's equation:

$$\frac{\partial \rho}{\partial t} + \nabla \cdot (\rho \mathbf{u}) = 0, \tag{3.1}$$

$$\rho \left(\frac{\partial}{\partial t} + \mathbf{u} \cdot \nabla \right) \mathbf{u} = -\rho \nabla \Phi - \nabla \mathcal{P}, \tag{3.2}$$

$$\rho \left(\frac{\partial}{\partial t} + \mathbf{u} \cdot \nabla \right) \mathcal{U} + (\mathcal{P}_g + \mathcal{P}_{\mathrm{R}}) \otimes \nabla \mathbf{u} = \rho \varepsilon - \nabla \cdot \mathbf{F}_R, \tag{3.3}$$

$$\nabla^2 \Phi = 4\pi G \rho, \tag{3.4}$$

where ρ is density, $\mathbf{u}$ velocity of fluid, Φ gravitational potential, T temperature, S entropy, $\mathcal{U}$ internal energy, ε nuclear energy production rate per unit mass and time. $\mathcal{P}$ is gaseous and radiative stress tensor, where $\mathcal{P}_g = p_g \mathbf{1} - \beta_g$, $\mathcal{P}_{\mathrm{R}} = p_{\mathrm{R}} \mathbf{1} - \beta_{\mathrm{R}}$. $\mathbf{F}_R$ is radiative flux, which is described with the diffusion approximation,

$$\mathbf{F}_{\mathrm{R}} = -K \nabla T, \tag{3.5}$$
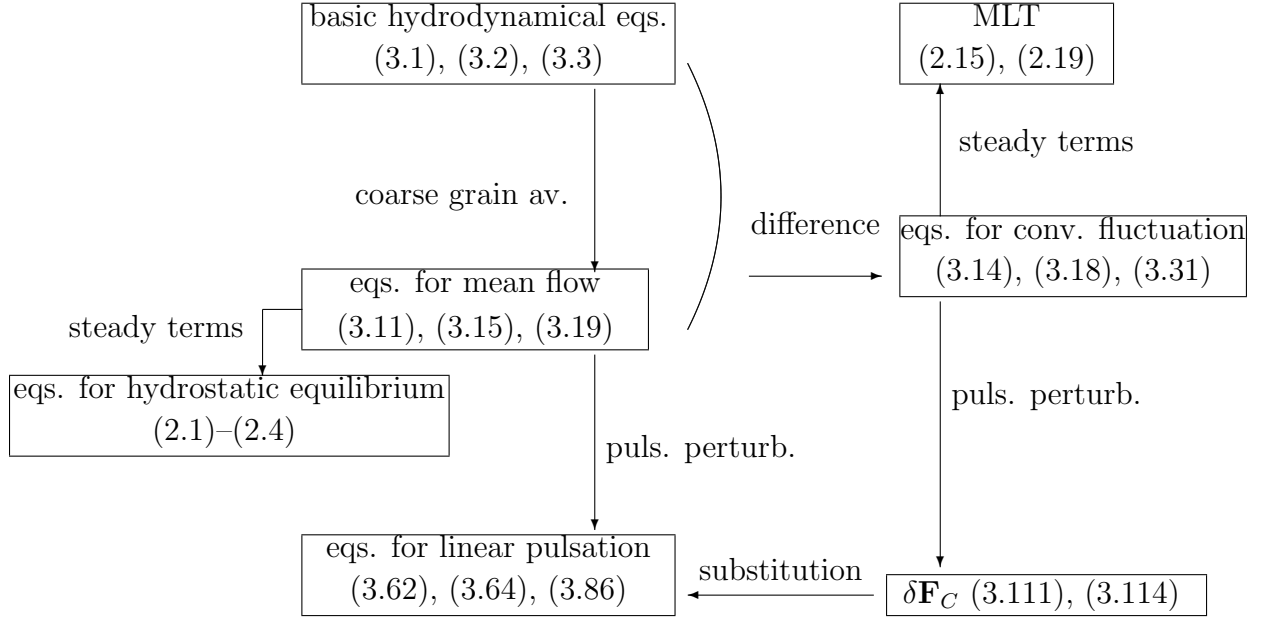
Figure 3.1: Procedure for solving linear pulsation with convection-pulsation coupling

where

$$K \equiv \frac{4ac}{3\kappa\rho}T^3 \tag{3.6}$$

is the radiative conductivity. This represents the radiative energy transfer in regions where movement of photons can be described as diffusion. In stellar interiors, mean free path of photons is very short compared with the scale in which the structure changes. Thus the radiative energy transport can be regarded as diffusive processes.

3.3 Equations for mean flow and convective fluctuation

For exact treatment of convection, we will first consider fluctuation of physical variables due to convection. A physical variable a is decomposed into mean flow and convective fluctuation parts, $\overline{a}$ and Δa respectively, as

$$a = \overline{a} + \Delta a \tag{3.7}$$

The bar means average in a coarse grain, an area having size much larger than convective eddies, but much smaller than pulsational wavelengths or characteristic lengths of spatial variations of physical quantities in stellar structure (Fig.3.2).
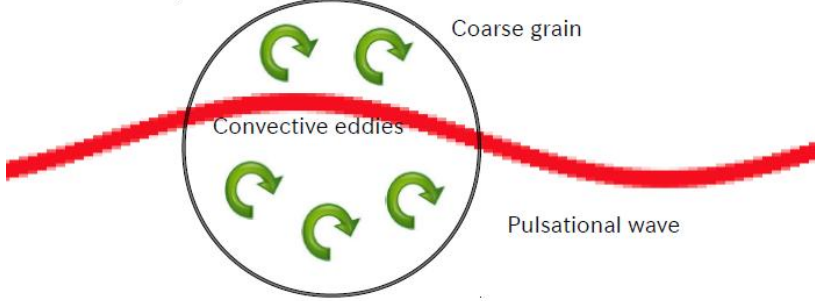
Figure 3.2: Cartoon of a coarse gain. The size of a coarse grain is much larger than convective eddies, but much smaller than pulsational wavelengths or stellar structure.

Below we will take procedures of averaging in a coarse grain by following the Reynolds' rule:

$$\overline{a+b} = \bar{a} + \bar{b}, \quad \overline{\Delta a} = 0, \quad \overline{\bar{a}b} = \bar{a}\bar{b}, \quad \overline{ab} = \bar{a}\bar{b} + \overline{\Delta a \Delta b}, \quad \overline{\frac{\partial a}{\partial x}} = \frac{\partial \bar{a}}{\partial x}. \tag{3.8}$$

But as for velocity $\mathbf{u}$, we adopt

$$\overline{\rho \Delta \mathbf{u}} = \mathbf{0}, \quad \overline{\Delta \mathbf{u}} \neq \mathbf{0}, \tag{3.9}$$

which means that no mass is lost in the considered coarse grain.

Equation of continuity

By following the above procedure, we have the equation of continuity Eq.(3.1) as

$$\frac{\partial(\bar{\rho} + \Delta\rho)}{\partial t} + \nabla \cdot [\rho(\bar{\mathbf{u}} + \Delta\mathbf{u})] = 0 \tag{3.10}$$

Taking coarse gain averages in both sides, we obtain the equation of continuity for mean flow as

$$\frac{\partial \bar{\rho}}{\partial t} + \nabla \cdot (\bar{\rho}\,\bar{\mathbf{u}}) = 0 \tag{3.11}$$

Doing subtraction Eq.(3.10)−(3.11), we get the equation of continuity for convective fluctuation as

$$\bar{\rho}\frac{D}{Dt}\left(\frac{\Delta\rho}{\bar{\rho}}\right) + \nabla \cdot (\Delta\rho\bar{\mathbf{u}}) = 0, \tag{3.12}$$

31

where the Lagrangian time derivative is defined as

$$\frac{D}{Dt} = \frac{\partial}{\partial t} + \overline{\mathbf{u}} \cdot \nabla. \tag{3.13}$$

When we adopt the Boussinesq approximation, which neglects time variation of convective fluctuation of density and assumes homogeneity of density in a coarse grain, this equation becomes

$$\nabla \cdot (\Delta \mathbf{u}) = 0 \tag{3.14}$$

Equation of motion

Taking coarse grain average of both sides of Eq.(3.2), we can derive the equation of motion for mean flow,

$$\frac{\partial \overline{\rho}\, \overline{\mathbf{u}}}{\partial t} + \nabla \cdot (\overline{\rho}\, \overline{\mathbf{u}}\, \overline{\mathbf{u}}) + \nabla \cdot (\overline{\rho \Delta \mathbf{u} \Delta \mathbf{u}}) = -\overline{\rho} \nabla \overline{\Phi} - \nabla \overline{p_{\mathrm{th}}}. \tag{3.15}$$

where $p_{\mathrm{th}} \equiv p_g + p_{\mathrm{R}}$. Taking difference between Eq.(3.2) and Eq.(3.15), and using Eq.(3.11), we get the equation for convective fluctuation,

$$\begin{aligned}
\overline{\rho} \frac{D}{Dt}\left(\frac{\rho \Delta \mathbf{u}}{\overline{\rho}} \right) &= -\rho \Delta \mathbf{u} \cdot \nabla \overline{\mathbf{u}} + \frac{\Delta \rho}{\overline{\rho}} \nabla (\overline{p}_g + \overline{p}_{\mathrm{R}} + \overline{p}_{\mathrm{t}}) - \nabla \Delta (p_g + p_{\mathrm{R}} + p_{\mathrm{t}}) \\
&\quad - \frac{\Delta \rho}{\overline{\rho}} \nabla \cdot (\overline{\beta}_g + \overline{\beta}_{\mathrm{R}} + \overline{\beta}_{\mathrm{t}}) + \nabla \cdot (\Delta \beta_g + \Delta \beta_{\mathrm{R}} + \Delta \beta_{\mathrm{t}})
\end{aligned} \tag{3.16}$$

where convective fluctuations of gravitational potential Φ and pressure p_{th} are neglected. We adopt a scaling approximation as

$$\frac{\Delta \rho}{\overline{\rho}} \nabla \cdot (\overline{\beta}_g + \overline{\beta}_{\mathrm{R}} + \overline{\beta}_{\mathrm{t}}) - \nabla \cdot (\Delta \beta_g + \Delta \beta_{\mathrm{R}} + \Delta \beta_{\mathrm{t}}) = \Lambda_1 \frac{\overline{\rho} \Delta \mathbf{u}}{\tau_C} \tag{3.17}$$

following Unno (1967). Λ_1 is a free parameter, and set to be 8 in this study in order to get consistency with Böhm-Vitense (1958)'s mixing length theory (MLT). Besides, neglecting $\Delta \rho$ in $\frac{D}{Dt}\left(\frac{\rho \Delta \mathbf{u}}{\overline{\rho}} \right)$, we get

$$\overline{\rho} \frac{D \Delta \mathbf{u}}{Dt} = \frac{\Delta \rho}{\overline{\rho}} \nabla \overline{p} - \nabla \Delta p - \overline{\rho} \Delta \mathbf{u} \cdot \nabla \overline{\mathbf{u}} - \Lambda_1 \frac{\overline{\rho} \Delta \mathbf{u}}{\tau_C}. \tag{3.18}$$

Equation of energy conservation

Taking coarse grain average of both sides of Eq.(3.3), we obtain the equation for mean flow,

$$\overline{\rho} \frac{D \overline{\mathcal{U}}}{Dt} + (\overline{p}_g + \overline{p}_{\mathrm{R}}) \nabla \cdot \overline{\mathbf{u}} = -\nabla \cdot (\overline{\mathbf{F}}_{\mathrm{R}} + \mathbf{F}_C) + \overline{\rho \varepsilon} + \overline{\rho \varepsilon_2} + \overline{\Delta \mathbf{u} \cdot \nabla (p_g + p_{\mathrm{R}})} \tag{3.19}$$

where convective flux $\mathbf{F}_C$ is defined as

$$\mathbf{F}_C \equiv \overline{(p_g + p_\mathrm{R} + \rho\mathcal{U})\Delta\mathbf{u}} = \overline{\rho\Delta H\Delta\mathbf{u}} \tag{3.20}$$

where H is enthalpy. The first law of thermodynamics says

$$dH = d\left(\frac{p_\mathrm{th}}{\rho}\right) + d\mathcal{U} = \frac{1}{\rho}dp_\mathrm{th} + TdS, \tag{3.21}$$

Assuming pressure equilibrium between a convective clump and its surrounding, ΔH can be expressed as

$$\Delta H = T\Delta S \tag{3.22}$$

The LHS of Eq.(3.19) is transformed as

$$\overline{\rho}\frac{D\overline{\mathcal{U}}}{Dt} + \overline{p_\mathrm{th}}\nabla\cdot\overline{\mathbf{u}} = \frac{\overline{p_\mathrm{th}}}{\overline{\rho}}\frac{D\overline{\rho}}{Dt} + T\frac{D\overline{S}}{Dt} + \overline{p_\mathrm{th}}\nabla\cdot\overline{\mathbf{u}} = \overline{T}\frac{D\overline{S}}{Dt} \tag{3.23}$$

where Eq.(3.11) is used. Eventually, Eq.(3.19) becomes

$$\overline{\rho}\,\overline{T}\frac{D\overline{S}}{Dt} = -\nabla\cdot(\overline{\mathbf{F}}_\mathrm{R} + \mathbf{F}_C) + \overline{\rho\varepsilon} + \overline{\rho\varepsilon_2} + \overline{\Delta\mathbf{u}\cdot\nabla p_\mathrm{th}} \tag{3.24}$$

where

$$\mathbf{F}_C = \overline{\rho}\,\overline{T}\,\overline{\Delta S\Delta\mathbf{u}} \tag{3.25}$$

Taking difference between Eq.(3.3) and Eq.(3.19), we obtain the equation for convective fluctuation,

$$\overline{\rho}\frac{D}{Dt}\left(\frac{\rho\mathcal{U}}{\overline{\rho}} - \overline{\mathcal{U}}\right) + \nabla\cdot\left(\rho H\Delta\mathbf{u} - \overline{\rho H\Delta u}\right) - \Delta\mathbf{u}\cdot\nabla p_\mathrm{th} + \overline{\Delta\mathbf{u}\cdot\nabla p_\mathrm{th}} + \Delta p_\mathrm{th}\nabla\cdot\mathbf{u}$$
$$-\rho\varepsilon_2 + \overline{\rho\varepsilon_2} = \rho\varepsilon - \overline{\rho\varepsilon} - \nabla\cdot\Delta\mathbf{F}_\mathrm{R} \tag{3.26}$$

We adopt a scaling approximation of Unno (1967) again like Eq.(3.17),

$$\overline{\rho}\,\overline{T}\frac{\Delta S}{\tau_c} = -\overline{\rho}\,\overline{T}\Delta\mathbf{u}\cdot\nabla\overline{S} - \rho\varepsilon_2 + \overline{\rho\varepsilon_2} + (\rho T\nabla S)\cdot\Delta\mathbf{u} - \overline{(\rho T\nabla S)\cdot\Delta\mathbf{u}} \tag{3.27}$$

Then, Eq.(3.26) becomes

$$\frac{\Delta(\rho T)}{\overline{\rho T}}\frac{D\overline{S}}{Dt} + \frac{D\Delta S}{Dt} + \Delta\mathbf{u}\cdot\nabla\overline{S} = \frac{\rho\varepsilon - \overline{\rho\varepsilon} - \nabla\cdot\Delta\mathbf{F}_\mathrm{R}}{\overline{\rho T}} - \frac{\Delta S}{\tau_C} \tag{3.28}$$

Since this study considers convection-pulsation coupling only in outer convective layers, we can set $\varepsilon = 0$. Following the MLT approach (Böhm-Vitense, 1958), we set

$$\nabla\cdot\Delta\mathbf{F}_R = -\omega_R\Delta S\overline{\rho T} \tag{3.29}$$

with

$$\omega_{\mathrm{R}} = \frac{1}{\tau_R} = \frac{4ac}{3} \frac{\overline{T}^3}{c_p \overline{\kappa \rho^2} \mathcal{L}^2}. \tag{3.30}$$

τ_{R} is the cooling timescale of turbulent eddies due to radiative losses, $\mathcal{L}$ is representative surface area of the eddies. It is related to the mixing length Λ by $\mathcal{L}^2 = (2/9)\Lambda^2$ in our equilibrium models. Eventually, we get the equation of energy conservation for convective fluctuation as

$$\frac{\Delta(\rho T)}{\overline{\rho T}} \frac{D\overline{S}}{Dt} + \frac{D\Delta S}{Dt} + \Delta \mathbf{u} \cdot \nabla \overline{S} = -\frac{\omega_R \tau_C + 1}{\tau_C} \Delta S \tag{3.31}$$

As a result, we have gotten the equations for mean flow, Eqs.(3.11), (3.15), (3.19), and the equations for convective fluctuation, Eqs.(3.14), (3.18), (3.31)

3.4 Equilibrium state (zeroth order terms)

To get equations for pulsations, we have to linearize both of the equations for mean flow and convective fluctuation. Before doing so, however, let us make sure of the zeroth order terms, that is, the description for the equilibrium state.

3.4.1 Equations for mean flow

First, we are going to extract the zeroth order terms of the equations for mean flow, and check the consistency with the differential equations appearing in §2.2.

Equation of continuity

We are going to derive the equation of continuity in hydrostatic equilibrium. We start from the mean flow equation,

$$(3.11): \quad \frac{\partial \overline{\rho}}{\partial t} + \nabla \cdot (\overline{\rho}\,\overline{\mathbf{u}}) = 0$$

$$\rightarrow \quad \frac{D\overline{\rho}}{Dt} + \overline{\rho}(\nabla \cdot \overline{\mathbf{u}}) = 0 \tag{3.32}$$

$$\rightarrow \quad \frac{1}{\overline{\rho}^2} \frac{D\overline{\rho}}{Dt} + \frac{\partial}{\partial M_r}\left(4\pi r^2 \frac{Dr}{Dt}\right) = 0 \tag{3.33}$$

where the mass coordinate dM_r is adopted as

$$dM_r \equiv 4\pi r^2 \rho dr. \tag{3.34}$$

Integrating Eq.(3.33) with time t, we have

$$-\frac{1}{\overline{\rho}} + 4\pi r^2 \frac{\partial r}{\partial M_r} = \mathrm{const} = 0, \tag{3.35}$$

which is identical to Eq.(3.34) since r is now independent of t, and the partial differentiation of the second term becomes total differentiation. Namely, the equation of continuity in hydrostatic equilibrium is

$$(2.1): \quad \frac{dr}{dM_r} = \frac{1}{4\pi r^2 \overline{\rho}}$$

We have assumed here that the density $\overline{\rho}$ is steady.

Equation of motion

Secondly, we are going to derive the equation of motion in hydrostatic equilibrium. Like above, we start from the mean flow equation,

$$(3.15): \quad \frac{\partial \overline{\rho}\,\overline{\mathbf{u}}}{\partial t} + \nabla \cdot (\overline{\rho}\,\overline{\mathbf{u}}\,\overline{\mathbf{u}}) + \nabla \cdot (\overline{\rho \Delta \mathbf{u} \Delta \mathbf{u}}) = -\overline{\rho}\nabla\overline{\Phi} - \nabla\overline{p_{\mathrm{th}}}.$$

$$\rightarrow \quad \frac{D\overline{\rho}\overline{\mathbf{u}}}{Dt} + \overline{\rho}\overline{\mathbf{u}} \cdot \nabla\overline{\mathbf{u}} + \nabla \cdot (\overline{\rho \Delta \mathbf{u} \Delta \mathbf{u}}) = -\overline{\rho}\nabla\overline{\Phi} - \nabla\overline{p_{\mathrm{th}}}. \quad (3.36)$$

Now we neglect the acceleration term since we think of hydrostatic equilibrium. The advection term (the second term of the left hand side of Eq.(3.36)) is also neglected since the velocity $\mathbf{u}$ is now much small, and this term has the second order of $\mathbf{u}$. The third term expresses divergence of Reynolds stress tensor. This term is known to be important when a star is located in the cooler side of the HR diagram. But it is beyond the range of this study, and this term is also neglected. That is, we neglect all the terms in the LHS. Assuming spherical symmetry and adopting the mass coordinate, we eventually have the equation of motion in hydrostatic equilibrium,

$$(2.2): \quad \frac{d\overline{p}}{dM_r} = -\frac{GM_r}{4\pi r^4}$$

where the radial gradient of the gravitational potential Φ is described as

$$\frac{d\Phi}{dr} = \frac{GM_r}{r^2}, \quad (3.37)$$

which can be obtained by integrating the Poisson's equation (3.4) with r by assuming spherical symmetry.

Equation of energy conservation

Thirdly, we are going to derive the equation of energy conservation in hydrostatic equilibrium. We start from the mean flow equation,

$$(3.24): \quad \overline{\rho}\overline{T}\frac{D\overline{S}}{Dt} = -\nabla \cdot (\overline{\mathbf{F}}_{\mathrm{R}} + \mathbf{F}_C) + \overline{\rho\varepsilon} + \overline{\rho\varepsilon_2} + \overline{\Delta \mathbf{u} \cdot \nabla p_{\mathrm{th}}}$$

The summation of the last two terms becomes zero in hydrostatic equilibrium (Grigahcène *et al.*, 2005). Assuming spherical symmetry and adopting the mass coordinate, we obtain the equation of energy conservation in hydrostatic equilibrium,

$$(2.4): \quad \frac{dL_r}{dM_r} = \overline{\varepsilon} - \overline{T}\frac{D\overline{S}}{Dt}.$$

3.4.2   Equations for convective fluctuation

Next, we are going to extract the zeroth order terms of equations for convective fluctuation, and check the consistency with the descriptions by MLT (§2.4).

Equation of motion

We start from the equation of motion for convective fluctuation,

$$(3.18): \quad \overline{\rho}\frac{D\Delta \mathbf{u}}{Dt} = \frac{\Delta\rho}{\overline{\rho}}\nabla\overline{p} - \nabla\Delta p - \overline{\rho}\Delta\mathbf{u}\cdot\nabla\overline{\mathbf{u}} - \Lambda_1\frac{\overline{\rho}\Delta\mathbf{u}}{\tau_C}$$

We should neglect the term of the time derivative in the LHS, and the third term in the RHS, having the mean velocity $\overline{\mathbf{u}}$ which is zero in the equilibrium state. In addition, we assume pressure equilibrium between a convective clump and the surrounding following the discussion in §2.4, and neglect the second term. Then, we have

$$\Delta u = \frac{\tau_C}{\Lambda_1\overline{\rho}}\frac{d\overline{p}}{dr}\frac{\Delta\rho}{\overline{\rho}} \tag{3.38}$$

$$= -\frac{1}{\Lambda_1}g\tau_C\frac{\Delta\rho}{\rho} \tag{3.39}$$

Is this consistent with MLT? In §2.4, we have the expression about convective velocity as

$$(2.15): \quad \overline{(\Delta u)^2} = -\frac{1}{8}g\frac{\Delta\rho}{\rho}\Lambda \tag{3.40}$$

We can replace Λ with $\Delta u/\tau_c$, and roughly speaking, we can have

$$\Delta u \sim -\frac{1}{8}g\frac{\Delta\rho}{\rho}\tau_C, \tag{3.41}$$

which is consistent with Eq.(3.39) if the free parameter Λ_1 is set to 8 as mentioned in §3.3.

Equation of energy conservation

Next, we are going to check the consistency between MLT and the equation of energy conservation for convective fluctuation,

$$(3.31): \quad \frac{\Delta(\rho T)}{\overline{\rho T}}\frac{D\overline{S}}{Dt} + \frac{D\Delta S}{Dt} + \Delta\mathbf{u}\cdot\nabla\overline{S} = -\frac{\omega_R\tau_C + 1}{\tau_C}\Delta S$$

In the hydrostatic equilibrium state, the following terms remain:

$$\Delta u \frac{d\overline{S}}{dr} = -\frac{\omega_R \tau_C + 1}{\tau_C} \Delta S \tag{3.42}$$

Noting $\Delta u \sim \Lambda/\tau_C$, $\Gamma = (\omega_R \tau_C)^{-1}$ and $\Delta S = c_p \Delta T/T$ under pressure equilibrium in convective motions, we can transform this equation into

$$\Lambda \frac{d\overline{S}}{dr} = -\left(\frac{1}{\Gamma} + 1\right) c_p \frac{\Delta T}{T} \tag{3.43}$$

The LHS becomes

$$\frac{d\overline{S}}{dr} = -\frac{c_p}{H_p}(\nabla - \nabla_{\mathrm{ad}}) \tag{3.44}$$

$$= -\frac{c_p}{H_p}[(\nabla - \nabla_{\mathrm{rad}}) + (\nabla_{\mathrm{rad}} - \nabla_{\mathrm{ad}})] \tag{3.45}$$

$$= -\frac{c_p}{H_p}\left[\frac{a\Gamma^3}{A^2} - \frac{\Gamma}{A^2}(a\Gamma^2 + \Gamma + 1)\right] \tag{3.46}$$

$$= -\frac{c_p}{H_p}(\nabla - \nabla')\left(1 + \frac{1}{\Gamma}\right), \tag{3.47}$$

where Eq.(2.37) and (2.40) are used from Eq.(3.45) to (3.46), and Eq.(2.36) from Eq.(3.46) to (3.47). Substituting it into Eq.(3.43), we obtain

$$(2.19): \quad \Delta T = (\nabla - \nabla')\frac{T\Lambda}{H_p},$$

which appears in the discussion of MLT in §2.4.

3.5 Equations for pulsations of mean flow

In §3.3, we have derived equations for mean flow and convective fluctuation. Next, we linearize the equations and derive equations to describe behaviors of both the mean flow and the convective fluctuation in pulsations. In this section, we linearize equations for mean flow. Linearization of the equations for convective fluctuation is introduced in §3.6.

Since we have assumed spherically symmetric structure of a star in the equilibrium state, physical quantities in the state depend only on distance from the stellar center, r. When nonradial pulsations take place in the structure, however, the quantities depend also on the altitude θ, the azimuthal angle ϕ and the time t. When taking an Eulerian variation of a scalar physical variable $f_0(r)$, we express in the following form:

$$f(\mathbf{r}, t) = f_0(r) + f'(\mathbf{r})Y_l^m(\theta, \phi)e^{i\sigma t} \tag{3.48}$$
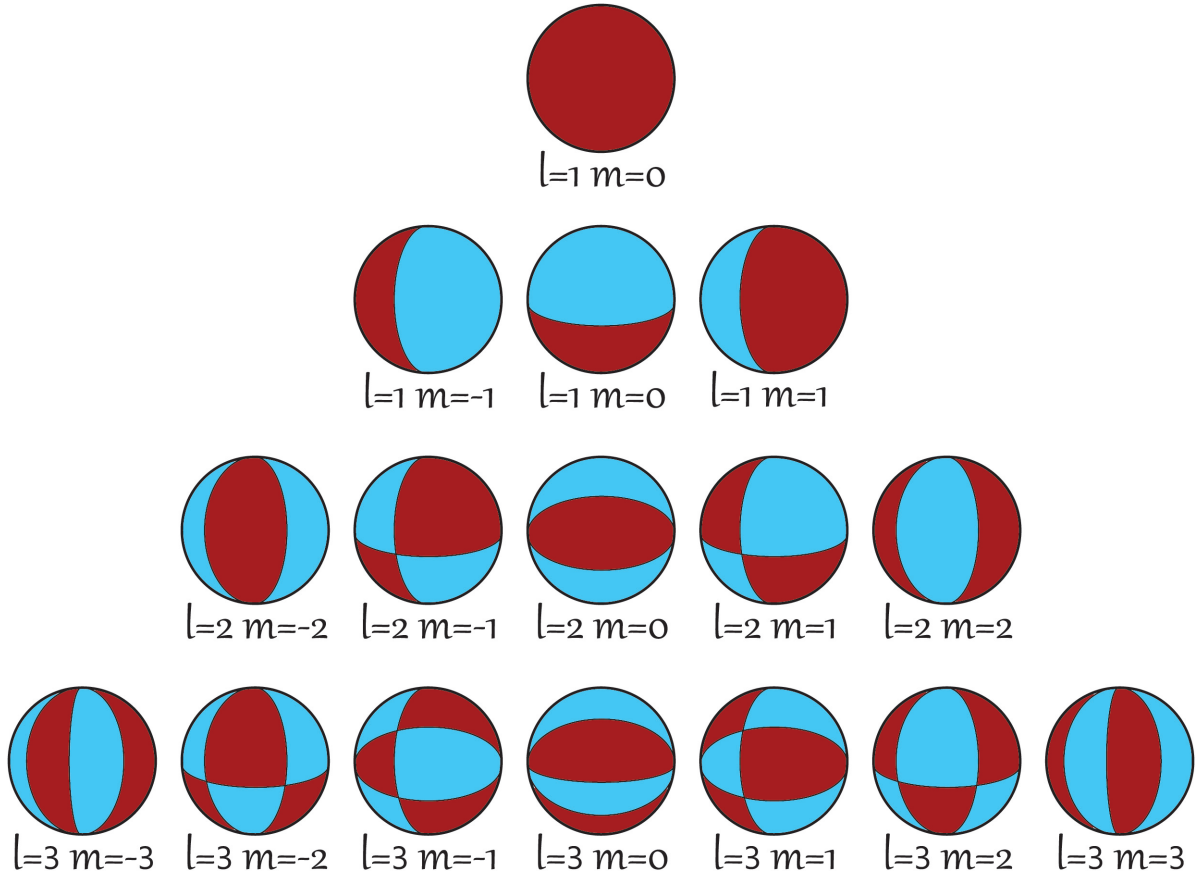
Figure 3.3: Spherical harmonics Y_l^m. The blue and the red parts are opposite in phase. (Godart, 2011)

where Y_l^m is the spherical harmonic function with the spherical degree l and the azimuthal order m,

$$Y_l^m(\theta, \phi) \equiv (-1)^{(m+|m|)/2} \left[\frac{2l+1}{2\pi} \frac{(l-|m|)!}{(l+|m|)!} \right]^{1/2} P_l^{|m|}(\cos\theta) e^{im\phi}. \tag{3.49}$$

l means the number of nodal lines on the spherical surface, while m the number of longitudinal ones (Fig.3.3). The bar expressing the coarse gain average is omitted in this section. For a vector variable $\mathbf{f}(r)$,

$$\mathbf{f}(\mathbf{r}, t) = \mathbf{f}_0(r) + \left[f_r'(r), \ f_h'(r) \frac{\partial}{\partial\theta}, \ f_h'(r) \frac{1}{\sin\theta} \frac{\partial}{\partial\phi} \right] Y_l^m(\theta, \phi) e^{i\sigma t}. \tag{3.50}$$

We assume $\mathbf{u}_0 = 0$, that is,

$$\mathbf{u}(\mathbf{r}, t) = \mathbf{u}'(\mathbf{r}, t). \tag{3.51}$$

Note that the relation between the Eulerian and the Lagrangian perturbations is, for example, given by

$$\delta\rho = \rho' + \boldsymbol{\xi} \cdot \nabla\rho_0 \qquad (3.52)$$

for density and that the Eulerian and the Lagrangian perturbations of $\mathbf{u}$, since $\mathbf{u}_0 = 0$, equal each other,

$$\mathbf{u}' = \delta\mathbf{u} = \frac{D\boldsymbol{\xi}}{Dt} = \frac{\partial\boldsymbol{\xi}}{\partial t}, \qquad (3.53)$$

where D/Dt is the Stokes derivative

$$\frac{D}{Dt} = \frac{\partial}{\partial t} + \mathbf{u}_0 \cdot \nabla. \qquad (3.54)$$

The third equal in Eq.(3.53) is explained by substituting $\mathbf{u}_0 = 0$ into Eq.(3.54).

Equation of continuity

First, we linearize Eq.(3.11). The formula of the first order terms is given by

$$\frac{\partial\rho'}{\partial t} + \mathbf{u}_0 \cdot \nabla\rho' + \mathbf{u}' \cdot \nabla\rho_0 + \rho_0\nabla\mathbf{u}' + \rho'\nabla \cdot \mathbf{u}_0 = 0. \qquad (3.55)$$

Adopting $\mathbf{u}_0 = 0$ and Eq.(3.53), we get

$$\frac{\partial\rho'}{\partial t} + \frac{\partial\boldsymbol{\xi}}{\partial t} \cdot \nabla\rho_0 + \rho_0\nabla \cdot \frac{\partial\boldsymbol{\xi}}{\partial t} = 0. \qquad (3.56)$$

Since all perturbations vary as $e^{i\sigma t}$, we have $\partial/\partial t \to i\sigma$. Therefore, Eq.(3.1) becomes

$$\rho' + \boldsymbol{\xi} \cdot \nabla\rho_0 + \rho_0\nabla \cdot \boldsymbol{\xi} = 0. \qquad (3.57)$$

Using the relation between the Lagrangian and the Eulerian perturbations, we have

$$\frac{\delta\rho}{\rho} + \nabla \cdot \boldsymbol{\xi} = 0, \qquad (3.58)$$

where the subscript "0", meaning the equilibrium state, is omitted, and

$$\boldsymbol{\xi} = (\xi_r, \xi_\theta, \xi_\phi) \qquad (3.59)$$

Following Eq.(3.50), we define ξ_h as

$$(\xi_\theta, \xi_\phi) = \xi_h\left(\frac{\partial}{\partial\theta}, \frac{1}{\sin\theta}\frac{\partial}{\partial\phi}\right)Y_l^m, \qquad (3.60)$$

and the spherical harmonic function $Y_l^m(\theta, \phi)$ satisfies

$$[r^2\nabla_\perp^2 + l(l+1)]Y_l^m = 0. \qquad (3.61)$$

Then, Eq.(3.58) becomes

$$\frac{d}{d\ln r}\frac{\xi_r}{r} = -3\frac{\xi_r}{r} + l(l+1)\frac{\xi_h}{r} - \frac{\delta\rho}{\rho} \qquad (3.62)$$

Equation of motion

Similarly, Eq.(3.15) becomes

$$-\sigma^2 \boldsymbol{\xi} + \frac{1}{\rho}\nabla p' + \nabla \Phi' + \frac{\rho'}{\rho}\nabla \Phi = 0, \tag{3.63}$$

where the term of Reynold's stress is neglected as well as the discussion in §3.4.1, since it is important in the low temperature side on the HR diagram, where is beyond the range of this study. Separate into the radial and horizontal component:

$$-\sigma^2 \xi_r + \frac{1}{\rho}\frac{dp'}{dr} + \frac{d\Phi'}{dr} + \frac{\rho'}{\rho}\frac{d\Phi}{dr} = 0 \tag{3.64}$$

and

$$-\sigma^2 \boldsymbol{\xi}_\perp + \nabla_\perp \left(\frac{p'}{\rho} + \Phi' \right) = 0, \tag{3.65}$$

where

$$\boldsymbol{\xi}_\perp = (0, \xi_\theta, \xi_\phi), \quad \nabla_\perp = \frac{1}{r}\left(0, \frac{\partial}{\partial \theta}, \frac{1}{\sin\theta}\frac{\partial}{\partial \phi} \right). \tag{3.66}$$

By using ξ_h and canceling the terms depending on θ and ϕ, Eq.(3.65) can be written as

$$\xi_h = \frac{1}{\sigma^2 r}\left(\frac{p'}{\rho} + \Phi' \right). \tag{3.67}$$

Equation of energy conservation

Next, we will linearize the equation of energy conservation. Taking Lagrangian perturbation of Eq.(3.19), we have

$$-i\sigma\rho T\delta S = \rho\varepsilon \left(\frac{\delta\rho}{\rho} + \frac{\delta\varepsilon}{\varepsilon} \right) - \delta\left[\nabla \cdot (\mathbf{F}_R + \mathbf{F}_C) \right], \tag{3.68}$$

where the term $\overline{\rho\varepsilon_2 + \Delta\mathbf{u}\cdot\nabla p_{\mathrm{th}}}$ is neglected. Dupret *et al.* (2005) showed that excitation/dumping by this term compensates with that by the turbulent pressure. But we have neglected the Reynold's stress term, including the turbulent pressure, in the equation of motion, and it might be preferable to neglect also this term in terms of the excitation/dumping. Defining $\mathbf{F} \equiv \mathbf{F}_R + \mathbf{F}_C$, the last term becomes

$$\delta(\nabla \cdot \mathbf{F}) = \nabla \cdot \mathbf{F}' + \boldsymbol{\xi}\cdot\nabla(\nabla\cdot\mathbf{F}) \tag{3.69}$$

$$= \nabla\cdot\mathbf{F}' + \boldsymbol{\xi}\cdot\nabla\left(\frac{1}{r^2}\frac{d}{dr}(r^2 F_r) \right) \tag{3.70}$$

$$= \nabla\cdot\mathbf{F}' + \xi_r\frac{d}{dr}\left(\frac{1}{r^2}\frac{d}{dr}(r^2 F_r) \right) \tag{3.71}$$

$$= \frac{1}{r^2}\frac{d}{dr}(r^2 F_r') + \nabla\cdot\mathbf{F}_h' + \xi_r\frac{d}{dr}\left(\frac{1}{r^2}\frac{d}{dr}(r^2 F_r) \right) \tag{3.72}$$

Transforming the first term by use of $\delta L_r = 4\pi r^2 \left(\delta F_r + 2\frac{\xi_r}{r}F_r\right)$, we have

$$\frac{1}{r^2}\frac{d}{dr}(r^2 F_r') = \frac{1}{r^2}\frac{d}{dr}\left(\frac{\delta L_r}{4\pi} - \xi_r \frac{d}{dr}(r^2 F_r)\right) \tag{3.73}$$

$$= \rho\frac{d\delta L_r}{dM_r} - \frac{d}{dr}\left[\xi_r \frac{d}{dr}(r^2 F_r)\right] \tag{3.74}$$

The summation of the second term of Eq.(3.74) and the third term of Eq.(3.72) becomes

$$-\frac{d}{dr}\left[\xi_r\frac{d}{dr}(r^2 F_r)\right] + \xi_r\frac{d}{dr}\left[\frac{1}{r^2}\frac{d}{dr}(r^2 F_r)\right]$$

$$= -\frac{1}{r^2}\frac{d\xi_r}{dr}\frac{d}{dr}(r^2 F_r) - \frac{\xi_r}{r}\frac{d^2}{dr^2}(r^2 F_r) - 2\frac{\xi_r}{r}\frac{\xi_r}{r^3}\frac{d}{dr}(r^2 F_r) \tag{3.75}$$

$$= -\frac{1}{r^2}\frac{d}{dr}(r^2 F_r)\left(2\frac{\xi_r}{r} + \frac{d\xi_r}{dr}\right) \tag{3.76}$$

$$= -\rho\varepsilon\left[l(l+1)\frac{\xi_h}{r} - \frac{\delta\rho}{\rho}\right], \tag{3.77}$$

where we have used the linearized equation of continuity Eq.(3.58) and the horizontal component of the equation of motion Eq.(3.67). The second term of Eq.(3.72) can be decomposed into the radiative and the convective components as $\nabla \cdot \mathbf{F}_h' = \nabla \cdot (\mathbf{F}_{R,h}' + \mathbf{F}_{C,h}')$:

$$\nabla \cdot \mathbf{F}_{R,h}' = -\frac{F_R}{dT/dr}\frac{l(l+1)}{r^2}T' = -\frac{L_R}{4\pi r^3}l(l+1)\left[\frac{\delta T}{r(dT/dr)} - \frac{\xi_r}{r}\right], \tag{3.78}$$

$$\nabla \cdot \mathbf{F}_{C,h}' = \nabla_h \cdot \mathbf{F}_C' = \nabla_h \cdot \delta\mathbf{F}_C - \boldsymbol{\xi}\cdot\nabla_h\mathbf{F}_C \tag{3.79}$$

$$= \frac{1}{r\sin\theta}\frac{\partial}{\partial\theta}\left(\sin\theta\,\delta F_{C,h}\frac{\partial Y_l^m}{\partial\theta}\right) + \frac{1}{r\sin\theta}\frac{\partial}{\partial\phi}\left(\delta F_{C,h}\frac{\partial Y_l^m}{\partial\phi}\right)$$

$$- \left[\frac{1}{r\sin\theta}\frac{\partial}{\partial\theta}\left(\sin\theta\frac{\xi_h F_C}{r}\frac{\partial Y_l^m}{\partial\theta}\right) + \frac{1}{r\sin\theta}\frac{\partial}{\partial\phi}\left(\frac{\xi_h F_C}{r}\frac{1}{\sin\theta}\frac{\partial Y_l^m}{\partial\phi}\right)\right] \tag{3.80}$$

$$= -\frac{l(l+1)}{r}\left(\delta F_{C,h} - F_C\frac{\xi_h}{r}\right)Y_l^m \tag{3.81}$$

Between the first and the second terms of Eq.(3.78), we have used Eq.(3.5). Taking the divergence and the Eulerian perturbation to the horizontal component of Eq.(3.5), we have

$$\nabla_h \cdot \mathbf{F}_{R,h}' = \nabla_h \cdot (-K\nabla_h T') = -K\nabla_h \cdot \nabla_h T' = K\frac{l(l+1)}{r^2}T' = -\frac{F_R}{dT/dr}\frac{l(l+1)}{r^2}T' \tag{3.82}$$

By use of Eqs.(3.74), (3.77) and (3.78), Eq.(3.72) becomes

$$\delta(\nabla\cdot\mathbf{F}) = \rho\frac{d\delta L_r}{dM_r} - \rho\varepsilon\left[l(l+1)\frac{\xi_h}{r} - \frac{\delta\rho}{\rho_0}\right]$$

$$- \frac{L_R}{4\pi r^3}l(l+1)\left[\frac{\delta T}{r(dT/dr)} - \frac{\xi_r}{r}\right] + \frac{l(l+1)}{r}\left(\delta F_{C,h} - F_C\frac{\xi_h}{r}\right) \tag{3.83}$$

41

Substituting it into Eq.(3.68), we obtain

$$
i\omega c_p T \frac{\delta S}{c_p} = -\frac{d(\delta L_R + \delta L_C)}{dM_r} + \left(\frac{\delta \varepsilon}{\varepsilon} + l(l+1)\frac{\xi_h}{r} \right) \varepsilon
$$
$$
+ \frac{l(l+1)}{4\pi r^3 \rho} \left[L_R \left(\frac{\delta T}{r(dT/dr)} - \frac{\xi_r}{r} \right) - L_C \frac{\xi_h}{r} \right] + \frac{l(l+1)}{\rho r} \delta F_{C,h} \tag{3.84}
$$

$$
\rightarrow \quad \frac{L_r}{4\pi r^3 \rho} \frac{d}{d\ln r} \left(\frac{\delta L_r}{L_r} \right) + \varepsilon \frac{\delta L_r}{L_r} = \left(\frac{\delta \varepsilon}{\varepsilon} + l(l+1)\frac{\xi_h}{r} \right) \varepsilon - i\omega c_p T \frac{\delta S}{c_p}
$$
$$
+ \frac{l(l+1)}{4\pi r^3 \rho} \left[L_R \left(\frac{\delta T}{r(dT/dr)} - \frac{\xi_r}{r} \right) - L_C \frac{\xi_h}{r} \right] + \frac{l(l+1)}{\rho r} \delta F_{C,h} \tag{3.85}
$$

$$
\rightarrow \quad \frac{d}{d\ln r} \left(\frac{\delta L_r}{L_r} \right) = \frac{4\pi r^3 \rho \varepsilon}{L_r} \left(-\frac{\delta L_r}{L_r} + \frac{\delta \varepsilon}{\varepsilon} + l(l+1)\frac{\xi_h}{r} \right)
$$
$$
- i\tilde{\omega} \frac{4\pi r^3 \rho c_p T}{L_r} \sqrt{\frac{GM}{R^3}} \frac{\delta S}{c_p} + l(l+1)\frac{L_R}{L_r} \left(\frac{d\ln r}{d\ln T} \frac{\delta T}{T} - \frac{\xi_r}{r} \right) + l(l+1)\frac{L_C}{L_r} \left(-\frac{\xi_h}{r} + \frac{\delta F_{C,h}}{F_{C,r}} \right) \tag{3.86}
$$

Diffusion approximation and Poisson's equation

We have linearized the equations of continuity, motion and energy conservation for mean flow. Besides those, we need to linearize the other two equations. The first one is the equation of the diffusion approximation Eq.(3.5). We have already introduced the linearized form of the horizontal component as Eq.(3.82). Here we linearize its radial component. Taking note of Eq.(3.6) and $L_R = 4\pi r^2 F_{R,r}$, the linearized equation becomes

$$
\frac{\delta L_R}{L_R} = -\frac{\delta \kappa}{\kappa} + 4\frac{\xi_r}{r} - l(l+1)\frac{\xi_h}{r} + 4\frac{\delta T}{T} + \frac{d\left(\frac{\delta T}{T} \right)/d\ln r}{d\ln T/d\ln r}. \tag{3.87}
$$

The second one is Poisson's equation, of which the linearized form is

$$
\frac{1}{r^2} \frac{d}{dr} \left(r^2 \frac{d\Phi'}{dr} \right) - \frac{l(l+1)}{r^2} \Phi' = 4\pi G \rho', \tag{3.88}
$$

where Eq.(3.61) is used for the second term. Thus, we have obtained the equations for pulsations of mean flow, Eqs.(3.62), (3.64), (3.86), (3.87) and (3.88).

3.6 Equations for pulsations of convective fluctuation (TDC theory)

In the previous section, we have linearized the hydrodynamical equations for mean flow, and have obtained the equations for its pulsations. In this section, we introduce the time-dependent convection (TDC) theory by deriving the equations for pulsations of convective fluctuation,

which describes how the excesses of physical variables in convective clumps over those in the surroundings are perturbed by pulsations. Like the previous section, we will linearize the hydrodynamical equations for convective fluctuation, Eqs.(3.14), (3.18), (3.31) following Grigahcène *et al.* (2005).

We can find that these equations include spatial derivatives of variables for convective fluctuation. Such variables vary in the spatial scales of convective eddies, which is much smaller than the pulsational wavelengths or the scale of variation of the surrounding structure. We define $\mathbf{k}$ as the wavenumber of convective eddies, and describe a variable for convective fluctuation as

$$\Delta f = \Delta f_a(\mathbf{r})e^{i\mathbf{k}\cdot\mathbf{r}}e^{i\sigma t}, \tag{3.89}$$

where $e^{i\mathbf{k}\cdot\mathbf{r}}$ expresses the spatial dependence due to the distribution of convective eddies, and that due to the pulsation and the surrounding structure is included by the term $\Delta f_a(\mathbf{r})$. We introduce the parameter A relating to the relation between the components of $\mathbf{k}$,

$$k_\theta^2 + k_\phi^2 = Ak_r^2, \tag{3.90}$$

where $A = 1/2$ corresponds to isotropic turbulence. Then, the equation of continuity for convective fluctuation, Eq.(3.14), becomes

$$\mathbf{k}\cdot\Delta\mathbf{u} = 0 \tag{3.91}$$

Then, taking the Lagrangian perturbation of this equation, besides, Eqs.(3.18) and (3.31), we have

$$(3.91) \rightarrow \mathbf{k}\cdot\delta\Delta\mathbf{u} = 0, \tag{3.92}$$

$$(3.18) \rightarrow i\sigma\overline{\rho}\delta\Delta\mathbf{u} = \delta\left(\frac{\Delta\rho}{\overline{\rho}}\right)\nabla\overline{p} + \frac{\Delta\rho}{\rho}\delta(\nabla\overline{p}) - \delta(\nabla\Delta p)$$

$$-\overline{\rho}\Delta\mathbf{u}\cdot\delta\nabla\mathbf{u} - \frac{\Lambda\overline{\rho}\Delta\mathbf{u}}{\tau_C}\left(\frac{\delta\overline{\rho}}{\overline{\rho}} - \frac{\delta\tau_C}{\tau_C}\right) - \frac{\Lambda\overline{\rho}\delta\Delta\mathbf{u}}{\tau_C} \tag{3.93}$$

$$(3.31) \rightarrow \left(\frac{\Delta\rho}{\overline{\rho}} + \frac{\Delta T}{\overline{T}}\right)i\sigma\delta\overline{S} + i\sigma\delta\Delta S + \delta\Delta\mathbf{u}\cdot\nabla\overline{S} + \Delta\mathbf{u}\cdot\delta(\nabla\overline{S})$$

$$= -\omega_R\delta\Delta S - \delta\omega_R\Delta S - \delta\left(\frac{\Delta S}{\tau_C}\right). \tag{3.94}$$

Below we use the following notations:

$$B = \frac{i\sigma\tau_C + \Lambda_1}{\Lambda_1}, \quad C = \frac{\omega_R\tau_C + 1}{i\sigma\tau_C + \omega_R\tau_C + 1}, \quad D = \frac{1}{i\sigma\tau_C + \omega_R\tau_C + 1}. \tag{3.95}$$

Isolating $(\delta\Delta S/\Delta S)$ in Eq.(3.94), we then have

$$\frac{\delta\Delta S}{\Delta S} = D\left\{-i\sigma\tau_C\frac{v_T+1}{v_T}\frac{\delta\overline{S}}{c_p}\right.$$

$$\left.+(\omega_R\tau_C+1)\left[\frac{\delta\Delta u_r}{\Delta u_r} + \frac{\Delta\mathbf{u}\cdot\nabla(\delta\overline{S})}{\Delta u_r(dS/dr)} - \frac{\Delta\mathbf{u}\cdot\nabla\xi_r}{\Delta u_r}\right] + \left(\frac{\delta\tau_C}{\tau_C} - \omega_R\tau_C\frac{\delta\omega_R}{\omega_R}\right)\right\} \tag{3.96}$$

43

Multiplying by $\Delta u_j/\Delta u_r$ and taking the average gives

$$\overline{\frac{\delta \Delta S \Delta u_j}{\Delta S \Delta u_r}} = D\overline{\frac{\Delta u_r \Delta u_j}{(\Delta u_r)^2}} \left[-i\sigma\tau_C \frac{v_T+1}{v_T} \frac{\delta\overline{S}}{c_p} + \frac{\delta\tau_C}{\tau_C} - \omega_R\tau_C \frac{\delta\omega_R}{\omega_R} \right]$$
$$+ C\left[\left(\frac{\nabla_k \delta\overline{S}}{dS/dr} - \nabla_k \xi_r \right) \overline{\frac{\Delta u_j \Delta u_k}{(\Delta u_r)^2}} + \overline{\frac{\delta \Delta u_j \delta \Delta u_r}{(\Delta u_r)^2}} \right] \tag{3.97}$$

On the other hand, taking the divergence of Eq.(3.93) makes the determination of $\delta\Delta p$ possible. Substituting the values obtained in Eq.(3.93) gives, for a given $\mathbf{k}$,

$$B\frac{\delta\Delta u_j}{\Delta u_r} = \frac{A+1}{A} \frac{\delta\frac{\Delta\rho}{\overline{\rho}}}{\frac{\Delta\rho}{\overline{\rho}}} K_{jr} + \frac{A+1}{A} \left[\frac{dr}{d\overline{p}} \nabla_i \delta\overline{p} - \nabla_i \xi_r \right] K_{ji}$$
$$- \frac{i\sigma\tau_C}{\Lambda} \frac{\Delta u_i}{\Delta u_r} \nabla_i \xi_l K_{lj} - \left(\frac{\delta\overline{\rho}}{\overline{\rho}} - \frac{\delta\tau_C}{\tau_C} \right) \frac{\Delta u_j}{\Delta u_r} \tag{3.98}$$

where

$$K_{ji} = \delta_{ji} - \frac{k_j k_i}{k^2} \quad \text{and} \quad K_{jr} = \frac{A}{A+1} \frac{\Delta u_j}{\Delta u_r} \tag{3.99}$$

Since we can assume the pressure equilibrium between convective clumps and their surroundings, we have

$$\frac{\Delta\rho}{\overline{\rho}} = \frac{1}{v_T} \frac{\Delta S}{c_p} \tag{3.100}$$

Taking the Lagrangian perturbation to this gives

$$\delta\left(\frac{\Delta\rho}{\overline{\rho}} \right) = \frac{\Delta\rho}{\overline{\rho}} \left(\frac{\delta\Delta S}{\Delta S} - \frac{\delta v_T}{v_T} - \frac{\delta c_p}{c_p} \right) \tag{3.101}$$

From this, Eqs.(3.96) and (3.98), we find

$$B\frac{\delta\Delta u_j}{\Delta u_r} = \frac{\Delta u_j}{\Delta u_r} \left\{ -\frac{\delta v_T}{v_T} - \frac{\delta c_p}{c_p} - \frac{\delta\rho}{\rho} + \frac{\delta\tau_C}{\tau_C} \right.$$
$$+ D\left[-i\sigma\tau_C \frac{v_T+1}{v_T} \frac{\delta S}{c_p} + \frac{\delta\tau_C}{\tau_C} - \omega_R\tau_C \frac{\delta\omega_R}{\omega_R} \right.$$
$$\left. + (\omega_R\tau_C + 1)\left(\frac{\delta\Delta u_r}{\Delta u_r} + \frac{\Delta u_k}{\Delta u_r} \left(\frac{\nabla_k \delta S}{dS/dr} - \nabla_k \xi_r \right) \right) \right] \right\}$$
$$+ \frac{A+1}{A} \left[\frac{dr}{dp} \nabla_i \delta p - \nabla_i \xi_r \right] K_{ji} - \frac{i\sigma\tau_C}{\Lambda} \frac{\Delta u_i}{\Delta u_r} \nabla_i \xi_l K_{lj} \tag{3.102}$$

where the values of $\delta\tau_C/\tau_C$ and $\delta\omega_R/\omega_R$ are obtained by

$$\frac{\delta\tau_C}{\tau_C} = \frac{\delta\Lambda}{\Lambda} - \overline{\frac{\delta\Delta u_r}{\Delta u_r}}, \tag{3.103}$$

$$\frac{\delta\omega_R}{\omega_R} = 3\frac{\delta T}{T} - \frac{\delta c_p}{c_p} - \frac{\delta\kappa}{\kappa} - 2\frac{\delta\rho}{\rho} - 2\frac{\delta\Lambda}{\Lambda}, \tag{3.104}$$

44

which can be derived from the definition of $\tau_C \equiv \Lambda/\overline{\Delta u_r}$ and Eq.(3.30). It seems normal to assume that the perturbation of the mixing length Λ is evaluated as

$$\frac{\delta\Lambda}{\Lambda} = \frac{\delta H_p}{H_p} = \frac{\delta p}{p} - \frac{d\delta p}{dp} + \frac{d\xi_r}{dr}, \tag{3.105}$$

which is coherent with the formula $\Lambda = \alpha H_p$. On the other hand, it can be expected that the perturbation of the mixing length becomes negligible when the lifetime of the convective elements is much longer than the period of pulsation. This can be reproduced, for example, by adopting

$$\frac{\delta\Lambda}{\Lambda} = \frac{1}{1 + (\sigma\tau_C)^2}\frac{\delta H_p}{H_p}. \tag{3.106}$$

This study optionally adopts Eq.(3.105) when $\sigma\tau_C \ll 1$, while Eq.(3.106) when $\sigma\tau_C \gg 1$.

On the basis of Eq.(3.102), it is possible to determine explicitly the different perturbed correlation terms. Integrating the particular solutions over all values of k_θ and k_ϕ while satisfying Eq.(3.90), and then taking horizontal averages. Considering the case $j = r$, Eq.(3.102) gives an explicit form for the perturbation of radial convective velocity:

$$\frac{\overline{\delta\Delta u_r}}{\Delta u_r} = \frac{1}{B + (i\sigma\tau_C + 1)D}\left\{-\frac{\delta c_p}{c_p} - \frac{\delta v_T}{v_T} - \frac{\delta\rho}{\rho} + \frac{d\delta p}{dp} - \frac{d\xi_r}{dr}\right.$$
$$-i\sigma\tau_C D\frac{v_T + 1}{v_T}\frac{\delta S}{c_p} + C\left[\frac{d\delta S}{dS} - \frac{d\xi_r}{dr}\right] - \frac{A}{A+1}\frac{i\sigma\tau_c}{\Lambda}\left(\frac{d\xi_r}{dr} + \frac{1}{A}\frac{\xi_r}{r} - \frac{l(l+1)}{2A}\frac{\xi_h}{r}\right)$$
$$\left.-\omega_R\tau_C D\left(3\frac{\delta T}{T} - \frac{\delta c_p}{c_p} - \frac{\delta\kappa}{\kappa} - 2\frac{\delta\rho}{\rho}\right) + (i\sigma\tau_C + 3\omega_R\tau_C + 2)D\frac{\delta\Lambda}{\Lambda}\right\} \tag{3.107}$$

Multiplying Eq.(3.102) (with $j = r$) by Δu_θ and taking the average gives

$$\frac{\overline{\Delta u_\theta \delta\Delta u_r}}{(\Delta u_r)^2} = \frac{\partial Y_l^m/\partial\theta}{B - C}\left\{\frac{1}{2A}\left[\left(\frac{\delta p}{dp/d\ln r} - \frac{\xi_r}{r} + \frac{\xi_h}{r}\right) + C\left(\frac{\delta S}{dS/d\ln r} - \frac{\xi_r}{r} + \frac{\xi_h}{r}\right)\right]\right.$$
$$\left.-\frac{1}{2(A+1)}\frac{i\sigma\tau_C}{\Lambda}\left(\frac{d\xi_h}{dr} + \frac{\xi_r}{r} - \frac{\xi_h}{r}\right)\right\} \tag{3.108}$$

A similar expression can be obtained for $\overline{\Delta u_\phi \delta\Delta u_r/(\Delta u_r)^2}$. Taking the average of Eq.(3.98) with $j = \theta$, on the other hand, gives

$$\frac{\overline{\delta\Delta u_\theta}}{\Delta u_r} = \frac{\partial Y_m^l/\partial\theta}{2B}\left[\frac{C}{A}\left(\frac{\delta S}{dS/d\ln r} - \frac{\xi_r}{r} + \frac{\xi_h}{r}\right) + \frac{A+2}{A}\left(\frac{\delta p}{dp/d\ln r} - \frac{\xi_r}{r} + \frac{\xi_h}{r}\right)\right.$$
$$\left.-\frac{i\sigma\tau_C/\Lambda}{A+1}\left(\frac{\xi_r}{r} - \frac{\xi_h}{r} + (A+2)\frac{d\xi_h}{dr}\right)\right] + \frac{C}{B}\overline{\Delta u_\theta \delta\Delta u_r}(\Delta u_r)^2 \tag{3.109}$$

Then, let us consider the perturbations of convective flux and luminosity, which are required for solving the equation for pulsations of mean flow. Perturbing Eq.(3.25), we have

$$\delta\mathbf{F}_C = \mathbf{F}_C\left(\frac{\delta\rho}{\rho} + \frac{\delta T}{T}\right) + \overline{\rho}\overline{T}\left(\overline{\delta\Delta S\Delta\mathbf{u}} + \overline{\Delta S\delta\Delta\mathbf{u}}\right). \tag{3.110}$$

45

Its radial component becomes

$$\frac{\delta F_{C,r}}{F_{C,r}} = \left(\frac{\delta\rho}{\rho} + \frac{\delta T}{T}\right) + \frac{\overline{\delta\Delta S}}{\Delta S} + \frac{\overline{\delta\Delta u_r}}{\Delta u_r}, \tag{3.111}$$

which can be evaluated by using Eqs.(3.96) and (3.107). When we substitute them, we get

$$\begin{aligned}
\frac{\delta F_{C,r}}{F_{C,r}} &= \frac{\delta\rho}{\rho} + \frac{\delta T}{T} - i\sigma\tau_C D \frac{v_T+1}{v_T}\frac{\delta S}{c_p} + C\left[\frac{d\delta S}{dS} - \frac{d\xi_r}{dr}\right] \\
&\quad -\omega_R\tau_C D\left(3\frac{\delta T}{T} - \frac{\delta c_p}{c_p} - \frac{\delta\kappa}{\kappa} - 2\frac{\delta\rho}{\rho}\right) \\
&\quad +(i\sigma\tau_C + 2\omega_R\tau_C + 1)D\frac{\overline{\delta\Delta u_r}}{\Delta u_r} + (2\omega_R\tau_C + 1)D\frac{\delta\Lambda}{\Lambda}
\end{aligned} \tag{3.112}$$

With this, the perturbation of convective luminosity,

$$\frac{\delta L_C}{L_C} = 2\frac{\xi_r}{r} + \frac{\delta F_{C,r}}{F_{C,r}} \tag{3.113}$$

can be also evaluated.

On the other hand, the θ-component of Eq.(3.110),

$$\frac{\delta F_{C,\theta}}{F_{C,r}} = \frac{\overline{\delta\Delta S\Delta u_\theta}}{\Delta S\Delta u_r} + \frac{\overline{\delta\Delta u_\theta}}{\Delta u_r}, \tag{3.114}$$

can be evaluated with Eq.(3.97) and Eq.(3.109). Taking note of Eq.(3.50), we can get the value of $\delta F_{C,h}$ by canceling the term $\partial Y_m^l/\partial\theta$. Specifically, it becomes

$$\begin{aligned}
\frac{\delta F_{C,h}}{F_{C,r}} &= \frac{C(B+1)}{2A(B-C)}\frac{\delta S}{dS/d\ln r} + \frac{1}{2AB}\left[\frac{C(B+1)}{B-C} + A + 2\right]\frac{\delta p}{dp/d\ln r} \\
&\quad + \left[\frac{C(B+1)(2BA+B+1)}{2BA(A+1)(B-C)} + \frac{B-1}{2B(A+1)} + \frac{A+2}{2AB}\right]\left(\frac{\xi_h}{r} - \frac{\xi_r}{r}\right) \\
&\quad - \frac{B-1}{2B(A+1)}\left[\frac{C(B+1)}{B-C} + A + 2\right]\frac{d\xi_h}{dr}
\end{aligned} \tag{3.115}$$

3.7 Nondimensional expressions for nonradial pulsations

We have obtained the equations of nonradial pulsations for mean flow,

$$(3.62) \quad : \quad \frac{d}{d\ln r}\frac{\xi_r}{r} = -3\frac{\xi_r}{r} + l(l+1)\frac{\xi_h}{r} - \frac{\delta\rho}{\rho},$$

$$(3.64) \quad : \quad -\sigma^2\xi_r + \frac{1}{\rho}\frac{dp'}{dr} + \frac{d\Phi'}{dr} + \frac{\rho'}{\rho}\frac{d\Phi}{dr} = 0,$$

$$(3.86) \quad : \quad \frac{d}{d\ln r}\left(\frac{\delta L_r}{L_r}\right) = \frac{4\pi r^3 \rho \varepsilon}{L_r}\left(-\frac{\delta L_r}{L_r} + \frac{\delta \varepsilon}{\varepsilon} + l(l+1)\frac{\xi_h}{r}\right) - i\omega\frac{4\pi r^3 \rho c_p T}{L_r}\sqrt{\frac{GM}{R^3}}\frac{\delta S}{c_p}$$

$$+ l(l+1)\frac{L_R}{L_r}\left(\frac{d\ln r}{d\ln T}\frac{\delta T}{T} - \frac{\xi_r}{r}\right) + l(l+1)\frac{L_C}{L_r}\left(-\frac{\xi_h}{r} + \frac{\delta F_{C,h}}{F_{C,r}}\right),$$

$$(3.87) \quad : \quad \frac{\delta L_R}{L_R} = -\frac{\delta \kappa}{\kappa} + 4\frac{\xi_r}{r} - l(l+1)\frac{\xi_h}{r} + 4\frac{\delta T}{T} + \frac{d\left(\frac{\delta T}{T}\right)/d\ln r}{d\ln T/d\ln r},$$

$$(3.88) \quad : \quad \frac{1}{r^2}\frac{d}{dr}\left(r^2\frac{d\Phi'}{dr}\right) - \frac{l(l+1)}{r^2}\Phi' = 4\pi G \rho'$$

Since the last one is the second order differential equation with respect to r while the others the first order equations, we have gotten the sixth order differential equation system. Practically, it is convenient to express these equations with nondimensional variables for numerical calculations. We introduce

$$y_1 = \frac{\xi_r}{r}, \quad y_2 = \frac{1}{gr}\left(\frac{p'}{\rho} + \Phi'\right), \quad y_3 = \frac{\Phi'}{gr}, \quad y_4 = \frac{1}{g}\frac{d\Phi'}{dr}, \quad y_5 = \frac{\delta S}{c_p}, \quad y_6 = \frac{\delta L_r}{L_r}, \quad (3.116)$$

and will express the above differential equations with these variables. ξ_h/r can be transformed with Eq.(3.65) as

$$\frac{\xi_h}{r} = \frac{1}{c_1\omega^2}\frac{1}{gr}\left(\frac{p'}{\rho} + \Phi'\right) = \frac{1}{c_1\omega^2}y_2, \tag{3.117}$$

where ω is the nondimensional frequency defined as

$$\omega \equiv \sqrt{\frac{GM}{R^3}}\sigma, \tag{3.118}$$

and

$$c_1 \equiv \frac{(r/R)^3}{M_r/M} \tag{3.119}$$

The other perturbed variables also can be described with y_i's by using the following thermodynamical relations,

$$\frac{\delta p}{p} = \frac{p'}{p} + \frac{d\ln p}{d\ln r}\frac{\xi_r}{r} = V(y_2 - y_1 - y_3), \tag{3.120}$$

$$\frac{\delta T}{T} = \nabla_{ad}\frac{\delta p}{p} + \frac{\delta S}{c_p} = \nabla_{ad}V(y_2 - y_1 - y_3) + y_5, \tag{3.121}$$

$$\frac{\delta \rho}{\rho} = \frac{1}{\Gamma_1}\frac{\delta p}{p} - \nabla_{ad}\frac{\rho T}{p}\delta S = V_g(y_2 - y_1 - y_3) - v_T y_5, \tag{3.122}$$

$$\frac{\rho'}{\rho} = \frac{\delta \rho}{\rho} - \frac{d\ln \rho}{d\ln r}\frac{\xi_r}{r} = A^* y_1 + V_g(y_2 - y_3) - v_T y_5, \tag{3.123}$$

$$\frac{\delta \varepsilon}{\varepsilon} = \varepsilon_{ad}\frac{\delta p}{p} + \varepsilon_S\frac{\delta S}{c_p} = \varepsilon_{ad}V(y_2 - y_1 - y_3) + \varepsilon_S y_5, \tag{3.124}$$

$$\frac{\delta \kappa}{\kappa} = \kappa_{ad}\frac{\delta p}{p} + \kappa_S\frac{\delta S}{c_p} = \kappa_{ad}V(y_2 - y_1 - y_3) + \kappa_S y_5 \tag{3.125}$$

where

$$V \equiv -\frac{d\ln p}{d\ln r} = \frac{GM_r\rho}{rp}, \quad \Gamma_1 \equiv \left(\frac{\partial \ln p}{\partial \ln \rho}\right)_S, \quad V_{\mathrm{g}} \equiv \frac{V}{\Gamma_1}, \quad A^* \equiv -\frac{d\ln \rho}{d\ln r} - V_{\mathrm{g}},$$

$$\varepsilon_{\mathrm{ad}} \equiv \left(\frac{\partial \ln \varepsilon}{\partial \ln p}\right)_S, \quad \varepsilon_S \equiv c_p\left(\frac{\partial \ln \varepsilon}{\partial S}\right)_p, \quad \kappa_{\mathrm{ad}} \equiv \left(\frac{\partial \ln \kappa}{\partial \ln p}\right)_S, \quad \kappa_S \equiv c_p\left(\frac{\partial \ln \kappa}{\partial S}\right)_p,$$

$$(3.126)$$

and the relation among the thermodynamical coefficients,

$$\frac{v_T}{c_p} = \nabla_{\mathrm{ad}}\frac{\rho T}{p} \tag{3.127}$$

is used.

Then, the expression of the differential equations of nonradial pulsations for mean flow becomes

$$\frac{dy_1}{d\ln r} = (V_{\mathrm{g}} - 3)y_1 + \left[\frac{l(l+1)}{c_1\omega^2} - V_{\mathrm{g}}\right]y_2 + V_{\mathrm{g}}y_3 + v_T y_5, \tag{3.128}$$

$$\frac{dy_2}{d\ln r} = (c_1\omega^2 - A^*)y_1 + (A^* - U + 1)y_2 - A^*y_3 + v_T y_5, \tag{3.129}$$

$$\frac{dy_3}{d\ln r} = (1 - U)y_3 + y_4, \tag{3.130}$$

$$\frac{dy_4}{d\ln r} = UA^*y_1 + UV_{\mathrm{g}}y_2 + [l(l+1) - UV_{\mathrm{g}}]y_3 - Uy_4 - Uv_T y_5, \tag{3.131}$$

$$\frac{1}{V}\frac{dy_5}{d\ln r} = [\nabla_{\mathrm{ad}}(U - c_1\omega^2) - 4(\nabla_{\mathrm{ad}} - \nabla) + c_2]y_1$$

$$+ \left[\frac{l(l+1)}{c_1\omega^2}(\nabla_{\mathrm{ad}} - \nabla) - c_2\right]y_2 + c_2 y_3 + \nabla_{\mathrm{ad}}y_4$$

$$+ \nabla(4 - \kappa_S)y_5 - \nabla\frac{1}{f_R}y_6 + \nabla\frac{1 - f_R}{f_R}\frac{\delta L_C}{L_C}(\mathbf{y}, \omega), \tag{3.132}$$

$$\frac{dy_6}{d\ln r} = f_R\left[l(l+1)\frac{\nabla_{\mathrm{ad}} - \nabla}{\nabla} - \varepsilon_{\mathrm{ad}}c_3 V\right]y_1$$

$$+ \left[f_R\left\{\varepsilon_{\mathrm{ad}}c_3 V - l(l+1)\left(\frac{\nabla_{\mathrm{ad}}}{\nabla} - \frac{c_3}{c_1\omega^2}\right)\right\} - (1 - f_R)\frac{l(l+1)}{c_1\omega^2}\right]y_2$$

$$+ f_R\left[l(l+1)\frac{\nabla_{\mathrm{ad}}}{\nabla} - \varepsilon_{\mathrm{ad}}c_3 V\right]y_3 + f_R\left[c_3\varepsilon_S - \frac{l(l+1)}{V\nabla} - i\omega c_4\right]y_5 - f_R c_3 y_6$$

$$+ l(l+1)(1 - f_R)\frac{\delta F_{C,h}}{F_{C,r}}(\mathbf{y}, \omega), \tag{3.133}$$

with

$$f_R \equiv \frac{L_R}{L_r}, \quad U \equiv \frac{d\ln M_r}{d\ln r} = \frac{4\pi r^3\rho}{M_r}, \quad c_2 \equiv (\kappa_{\mathrm{ad}} - 4\nabla_{\mathrm{ad}})V\nabla + \nabla_{\mathrm{ad}}\left(\frac{d\ln \nabla_{\mathrm{ad}}}{d\ln r} + V\right),$$

$$c_3 \equiv \frac{4\pi r^3\rho\varepsilon}{L_{\mathrm{R}}}, \quad c_4 \equiv \frac{4\pi r^3\rho T c_p}{L_{\mathrm{R}}}\sqrt{\frac{GM}{R^3}}. \tag{3.134}$$

The coefficient c_4 is a ratio of local thermal timescale $\tau_{\text{th}} \equiv 4\pi r^3 \rho T c_p / L_R$ to free-fall or dynamical timescale $\tau_{\text{dyn}} \equiv \sqrt{R^3/(GM)}$. $\delta L_C/L_C$ and $\delta F_{C,h}/F_{C,r}$ are perturbations of convective luminosity and of horizontal component of convective flux, respectively. They can be described as the linear combination of y_i's and depends on ω. The evaluation of these quantities are discussed in §3.6.

In most cases, we can adopt the "Cowling approximation", in which the perturbation of the gravitational potential Φ is neglected. It is known that the perturbation of Φ would be important when pulsational amplitude is significantly large in deep interior of a star like the cases of low degree, low order g modes of low mass main sequence stars (e.g. Boury and Noels, 1973; Christensen-Dalsgaard et al., 1974; Shibahashi et al., 1975; Noels et al., 1976; Saio, 1980; Sonoi and Shibahashi, 2011, 2012a,b,c, 2013a,b). In the above expression, we may exclude the Poisson's equation, to which Eqs.(3.130) and (3.131) correspond, and also remove y_3 and y_4 appearing in the other equations. Besides, the definition of y_2 should be changed to $y_2 = \frac{p'}{gr\rho}$.

Then, we have

$$\frac{dy_1}{d\ln r} = (V_{\text{g}} - 3)y_1 + \left[\frac{l(l+1)}{c_1\omega^2} - V_{\text{g}}\right]y_2 + v_T y_5, \tag{3.135}$$

$$\frac{dy_2}{d\ln r} = (c_1\omega^2 - A^*)y_1 + (A^* - U + 1)y_2 + v_T y_5, \tag{3.136}$$

$$\frac{1}{V}\frac{dy_5}{d\ln r} = \left[\nabla_{\text{ad}}(U - c_1\omega^2) - 4(\nabla_{\text{ad}} - \nabla) + c_2\right]y_1 + \left[\frac{l(l+1)}{c_1\omega^2}(\nabla_{\text{ad}} - \nabla) - c_2\right]y_2$$

$$+ \nabla(4 - \kappa_S)y_5 - \nabla\frac{1}{f_R}y_6 + \nabla\frac{1 - f_R}{f_R}\frac{\delta L_C}{L_C}(\mathbf{y}, \omega), \tag{3.137}$$

$$\frac{dy_6}{d\ln r} = f_R\left[l(l+1)\frac{\nabla_{\text{ad}} - \nabla}{\nabla} - \varepsilon_{\text{ad}}c_3 V\right]y_1$$

$$+ \left[f_R\left\{\varepsilon_{\text{ad}}c_3 V - l(l+1)\left(\frac{\nabla_{\text{ad}}}{\nabla} - \frac{c_3}{c_1\omega^2}\right)\right\} - (1 - f_R)\frac{l(l+1)}{c_1\omega^2}\right]y_2$$

$$+ f_R\left[c_3\varepsilon_S - \frac{l(l+1)}{V\nabla} - i\omega c_4\right]y_5 - f_R c_3 y_6$$

$$+ l(l+1)(1 - f_R)\frac{\delta F_{C,h}}{F_{C,r}}(\mathbf{y}, \omega), \tag{3.138}$$

On the other hand, the equations for the adiabatic approximation can be obtained by setting $y_5 = 0$ and excluding y_6. That means the perturbation of entropy is fixed to zero, $\delta S = 0$, and is equivalent with the exclusion of the diffusion approximation Eq.(3.132) and the equation of energy conservation Eq.(3.133). Then, we have

$$\frac{dy_1}{d\ln r} = (V_{\text{g}} - 3)y_1 + \left[\frac{l(l+1)}{c_1\omega^2} - V_{\text{g}}\right]y_2 + V_{\text{g}}y_3, \tag{3.139}$$

$$\frac{dy_2}{d\ln r} = (c_1\omega^2 - A^*)y_1 + (A^* - U + 1)y_2 - A^*y_3, \tag{3.140}$$

$$\frac{dy_3}{d\ln r} = (1 - U)y_3 + y_4, \tag{3.141}$$

$$\frac{dy_4}{d\ln r} = UA^*y_1 + UV_{\mathrm{g}}y_2 + [l(l+1) - UV_{\mathrm{g}}]y_3 - Uy_4, \tag{3.142}$$

In addition, we can reduce by two orders with the Cowling approximation:

$$\frac{dy_1}{d\ln r} = (V_{\mathrm{g}} - 3)y_1 + \left[\frac{l(l+1)}{c_1\omega^2} - V_{\mathrm{g}}\right]y_2, \tag{3.143}$$

$$\frac{dy_2}{d\ln r} = (c_1\omega^2 - A^*)y_1 + (A^* - U + 1)y_2. \tag{3.144}$$

The adiabatic approximation is valid in deep interiors of stars, where the thermal timescale is much longer than dynamical timescale or pulsational periods due to high heat capacity. In this situation, thermal energy hardly transfers during pulsations, and then we can neglect the variation of entropy. In the outer layers, on the other hand, the thermal timescale can be comparable to or shorter than the pulsational periods. The adiabatic approximation is then no longer valid, and we should take into account the perturbation of the entropy.

We have here obtained several types of differential equation systems, having a form like

$$\frac{d}{d\ln r}\begin{bmatrix} y_1 \\ \vdots \\ y_N \end{bmatrix} = \begin{bmatrix} A_{1,1} & \dots & A_{1,N} \\ \vdots & & \vdots \\ A_{N,1} & \dots & A_{N,N} \end{bmatrix}\begin{bmatrix} y_1 \\ \vdots \\ y_N \end{bmatrix}. \tag{3.145}$$

In the systems, ω is the eigenvalue, and y_i's are the eigenfunctions. On the other hand, l is a free integer parameter. Given l, we will find a number of eigenvalues with sets of eigenfunctions in a star. One set of an eigenvalue and eigenfunctions corresponds to one eigenmode of stellar pulsation, and the eigenvalue indicates an eigenfrequency while the eigenfunction expresses distribution of amplitude for each physical variable.

When we practically solve the differential equations, we have to impose the boundary conditions. In the case of the 6th order system having one eigenvalue, Eqs.(3.128)-(3.133), we have to set 6+1 boundary conditions. The details of the derivation and the explanation of the boundary conditions is discussed in §C. Here we just see the equations required for calculations. The first one is the normalization of the eigenfunction. In this study, it is set at the outer boundary, i.e., the surface of a star, as

$$y_1 = 1. \tag{3.146}$$

Then three conditions are set at each of the inner boundary, i.e., the center of the star, and the outer boundary. The inner boundary conditions are

$$c_1\omega^2 y_1 - ly_2 = 0, \tag{3.147}$$

$$ly_3 - y_4 = 0, \tag{3.148}$$

$$y_5 = 0, \tag{3.149}$$

while the outer boundary conditions are

$$\frac{\beta_- - b_{11}}{b_{12}} y_1 - y_2 - \left[\frac{\alpha_1(\beta_- - b_{11})}{b_{12}} - \alpha_2 \right] y_3 = 0, \tag{3.150}$$

$$(l+1)y_3 + y_4 = 0, \tag{3.151}$$

$$(2 - \nabla_{\mathrm{ad}} V)y_1 + 4\nabla_{\mathrm{ad}} V(y_2 - y_3) + 4y_5 - y_6 = 0. \tag{3.152}$$

Eqs.(3.147) and (3.150) are called "mechanical conditions", Eqs.(3.148) and (3.151) "potential conditions", and Eqs.(3.149) and (3.152) "thermal conditions". When we adopt the Cowling or adiabatic approximation, the order of the differential equations reduces and we have to exclude some of the boundary conditions. If adopting the Cowling approximation, we should exclude the potential conditions both at the inner and the outer boundaries, Eqs.(3.148) and (3.151). On the other hand, if adopting the adiabatic approximation, we should exclude the thermal conditions, Eqs.(3.149) and (3.152). As a matter of fact, (3.150) is available when waves are evanescent at the stellar surface. When waves are propagative there, we should adopt the running wave conditions Eq.(C.28) or Eq.(C.31). The detail is discussed in §C.

Note that the systems derived here do not depend on the azimuthal order m. In fact, the solutions with different m's are degenerated without rotation and magnetic field. It means that they have the identical eigenfrequency ω and eigenfunctions $y_i(r)$'s. But the 3-dimensional distribution of amplitude depends on m due to the difference in $Y_l^m(\theta, \phi)$.

3.8 Equations for radial pulsations

How are the equations for radial pulsations? As mentioned in the beginning of §3.5, l indicates the number of nodal lines on the spherical surface. Thus, the case of $l = 0$ corresponds to radial pulsations. In this situation, the equations for pulsations become simpler as

$$(3.62) \quad \rightarrow \quad \frac{d}{d\ln r}\frac{\xi_r}{r} = -3\frac{\xi_r}{r} - \frac{\delta\rho}{\rho}, \tag{3.153}$$

$$(3.64) \quad \rightarrow \quad -\sigma^2 \xi_r + \frac{1}{\rho}\frac{dp'}{dr} + \frac{d\Phi'}{dr} + \frac{\rho'}{\rho}\frac{d\Phi}{dr} = 0, \tag{3.154}$$

$$(3.86) \quad \rightarrow \quad \frac{d}{d\ln r}\left(\frac{\delta L_r}{L_r}\right) = \frac{4\pi r^3 \rho\varepsilon}{L_r}\left(-\frac{\delta L_r}{L_r} + \frac{\delta\varepsilon}{\varepsilon_0}\right) - i\omega\frac{4\pi r^3 \rho c_p T}{L_r}\sqrt{\frac{GM}{R^3}}\frac{\delta S}{c_p}, \tag{3.155}$$

$$(3.87) \quad \rightarrow \quad \frac{\delta L_{\mathrm{R}}}{L_{\mathrm{R}}} = -\frac{\delta\kappa}{\kappa} + 4\frac{\xi_r}{r} + 4\frac{\delta T}{T} + \frac{d\left(\frac{\delta T}{T}\right)/d\ln r}{d\ln T/d\ln r}, \tag{3.156}$$

$$(3.88) \quad \rightarrow \quad \frac{1}{r^2}\frac{d}{dr}\left(r^2\frac{d\Phi'}{dr}\right) = 4\pi G\rho'. \tag{3.157}$$

The last equation (3.157) can be written by using the first equation Eq.(3.153) as

$$\frac{d}{dr}\left(r^2\frac{d\Phi'}{dr}\right) + 4\pi G\left[\rho\frac{d}{dr}(r^2\xi_r) + r^2\xi_r\frac{d\rho}{dr}\right] = 0 \tag{3.158}$$

Integrating this equation under the condition that $d\Phi'/dr$ is non-singular at $r = 0$, we obtain

$$\frac{d\Phi'}{dr} + 4\pi G\rho\xi_r = 0 \tag{3.159}$$

With this, we can eliminate $d\Phi'/dr$ in Eq.(3.154):

$$\frac{1}{\rho}\frac{dp'}{dr} = (\sigma^2 + 4\pi G\rho)\xi_r - \frac{GM_r}{r^2}\frac{\rho'}{\rho} \tag{3.160}$$

In the case of radial pulsations, thus, we have the 4th order differential equation system of Eqs.(3.153), (3.160), (3.155) and (3.156). Introducing the nondimensional variables,

$$Y_1 = \frac{\xi_r}{r}, \quad Y_2 = \frac{\delta p}{p}, \quad Y_3 = \frac{\delta T}{T}, \quad Y_4 = \frac{\delta L_r}{L_r}, \tag{3.161}$$

we obtain the nondimensional expression,

$$\frac{dY_1}{d\ln r} = -3Y_1 - \frac{1}{\chi_\rho}Y_2 + v_T Y_3, \tag{3.162}$$

$$\frac{1}{V}\frac{dY_2}{d\ln r} = (c_1\omega^2 + 4)Y_1 + Y_2, \tag{3.163}$$

$$\frac{1}{V\nabla}\frac{dY_3}{d\ln r} = 4Y_1 + (\nabla_{\rm ad}\kappa_S - \kappa_{\rm ad})Y_2 + (4 - \kappa_S)Y_3 + \frac{1 - f_R}{f_R}\frac{\delta L_C}{L_C}(\mathbf{Y}, \omega), \tag{3.164}$$

$$\frac{1}{f_R}\frac{dY_4}{d\ln r} = [c_3(\varepsilon_{\rm ad} - \nabla_{\rm ad}\varepsilon_S) + i\omega c_4\nabla_{\rm ad}]Y_2 + [c_3\varepsilon_S - i\omega c_4]Y_3 - c_3 Y_4. \tag{3.165}$$

We should set 4+1 boundary conditions in total at the inner and the outer boundaries for the above system. We can adopt the normalization Eqs.(3.146) again as one of them:

$$Y_1 = 1. \tag{3.166}$$

And then we set two conditions at each of the inner and the outer boundaries. For non-singularity of the eigenfunctions, we should impose

$$\frac{d}{d\ln r}\left(\frac{\xi_r}{r}\right) = 0, \quad \text{at } r = 0. \tag{3.167}$$

$$\frac{d}{d\ln r}\left(\frac{\delta L_r}{L_r}\right) = 0 \quad \text{at } r = 0, \tag{3.168}$$

$$\frac{d}{d\ln r}\left(\frac{\delta p}{p}\right) = 0 \quad \text{at } r = R. \tag{3.169}$$

Besides, we should put another condition at the outer boundary, and set the guarantee of outward propagation of the energy flux at the surface

$$\frac{\delta L_r}{L_r} = 2\frac{\xi_r}{r} + 4\frac{\delta T}{T}, \tag{3.170}$$

which is equivalent with Eq.(3.152). For the nonadiabatic case, Eqs.(3.162)-(3.165), then, we have the inner boundary conditions,

$$-3Y_1 - \frac{1}{\chi_\rho}Y_2 + v_T Y_3 = 0,$$
$$[c_3(\varepsilon_{\mathrm{ad}} - \nabla_{\mathrm{ad}}\varepsilon_S) + i\omega c_4 \nabla_{\mathrm{ad}}]Y_2 + [c_3\varepsilon_S - i\omega c_4]Y_3 - c_3 Y_4 = 0 \quad \mathrm{at}\ \ r = 0, \quad (3.171)$$

and the outer boundary conditions,

$$(c_1\omega^2 + 4)Y_1 + Y_2 = 0,$$
$$2Y_1 + 4Y_3 - Y_4 = 0 \quad \mathrm{at}\ \ r = R. \quad (3.172)$$

For the adiabatic approximation, we exclude the equations for diffusion approximation and energy conservation, Eqs.(3.164) and (3.165), respectively, and impose the adiabatic condition, $\delta S = 0$, or

$$\nabla_{\mathrm{ad}}Y_2 = Y_3, \quad (3.173)$$

we obtain

$$\frac{dY_1}{d\ln r} = -3Y_1 - \frac{1}{\Gamma_1}Y_2, \quad (3.174)$$

$$\frac{1}{V}\frac{dY_2}{d\ln r} = (c_1\omega^2 + 4)Y_1 + Y_2. \quad (3.175)$$

We can use Eq.(3.167) and (3.169) as the inner and the outer boundary conditions, respectively. They can be described as

$$-3Y_1 - \frac{1}{\Gamma_1}Y_2 = 0 \quad \mathrm{at}\ \ r = 0, \quad (3.176)$$

$$(c_1\omega^2 + 4)Y_1 + Y_2 = 0 \quad \mathrm{at}\ \ r = R. \quad (3.177)$$

3.9   Numerical examples

Here we see the examples of calculations for radial and nonradial pulsations. Eigen solutions of the differential equation systems introduced above correspond to eigenmodes of pulsations, which are standing waves propagating in interiors of stars. One star has infinite number of eigenmodes.

Fig.3.4 shows a few examples of eigen modes for radial pulsations. The mode labeled as "F" is the fundamental mode, which has the lowest eigenfrequency. The curve of ξ_r/r never intersects the zero line, which means the matter in the whole star moves in the same direction during pulsations of this mode. The mode labeled as "1O" is the first overtone, which has the higher frequency than the fundamental mode and has one cross point of the zero line and the curve of ξ_r/r. The cross point is called as "node". The movement of the matter is opposite inside and outside of the node. As we go to "2O" (second overtone) and "3O" (third overtone), the number of nodes increases one by one, and the frequency becomes higher.
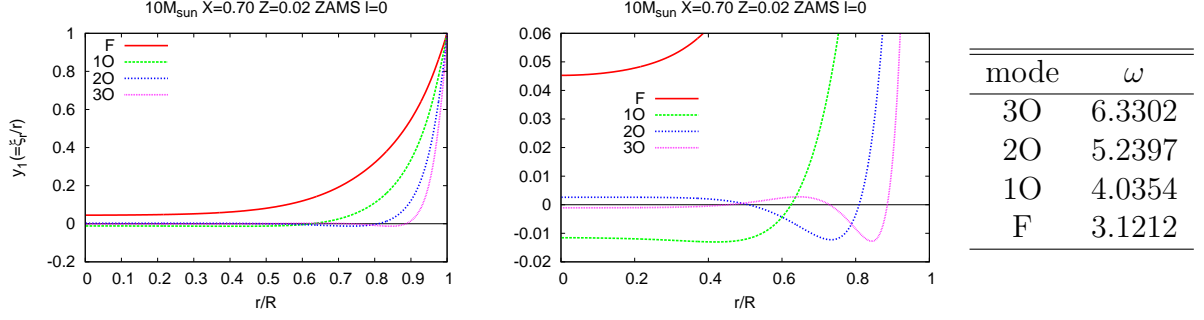
Figure 3.4: Profiles of the displacements ξ_r/r for the radial modes, the fundamental mode (F), the 1st overtone (1O), the 2nd overtone and the 3rd overtone (3O), in a model of a ZAMS star of $10M_\odot$ with $X = 0.70$, $Z = 0.02$, calculated with the differential equation system for the adiabatic approximation, Eqs.(3.174) and (3.175). The values of the displacements are normalized as $\xi_r/r = 1$ at the stellar surface. The middle panel is the enlarged figure of the left panel so as to make sure the nodes. The table shown in the rightmost lists the frequencies for the radial modes shown in the left two panels. The values are normalized by multiplying by the dynamical timescale $\sqrt{R^3/(GM)}$.
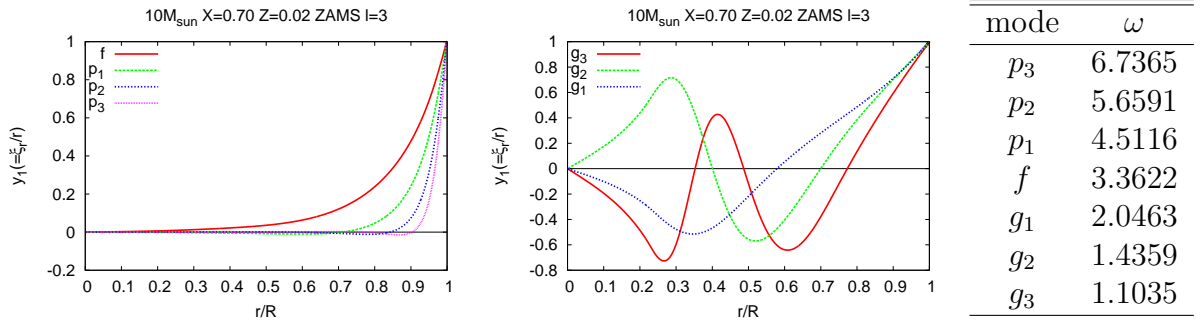
Figure 3.5: Profiles of the displacements ξ_r/r for the nonradial modes with $l = 3$, f and p modes (*Left*) and g modes (*Middle*) in the same stellar model as Fig.3.4, calculated with the differential equation system for the adiabatic Cowling approximation, Eqs.(3.143) and (3.144). The values of the displacements are normalized as $\xi_r/r = 1$ at the stellar surface. The table shown in the rightmost lists the frequencies for the nonradial modes shown in the left two panels. The values are normalized by multiplying by the dynamical timescale $\sqrt{R^3/(GM)}$.

Fig.3.5 shows examples of nonradial modes with $l = 3$, which means there are three nodal lines on the spherical surface. There are three types of nonradial modes, p, f and g modes. p and radial modes are eigenmodes of acoustic waves, f modes are of surface gravity waves, and g modes are of internal gravity waves.

The leftmost panel shows the displacement of p and f modes. The profile is quite similar to that of radial modes, and the pulsational amplitude is concentrated to the surface layer.

54
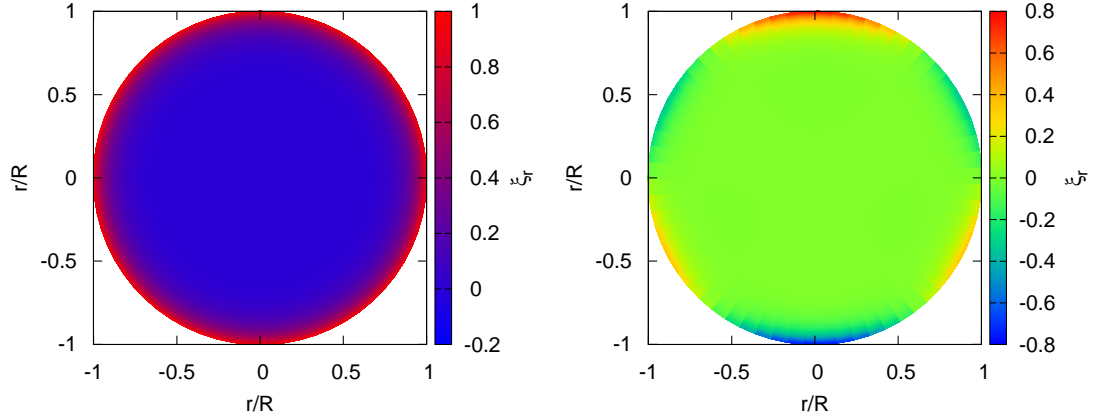
Figure 3.6: Profiles of the displacements ξ_r on a meridional plane for the radial 1O mode (*Left*), and the nonradial p_1 mode ($l = 3$, $m = 0$; *Right*), shown in Figs.3.4 and 3.5, respectively. The top and bottom of the disc correspond to the polars of the stars.

But we find a difference when considering the horizontal directions.[1] Fig.3.6 shows the profile of ξ_r on a meridional plane. The top and the bottom of the discs correspond to polar regions of the stars. From this figure, we can find that a nonradial mode has dependence on the horizontal directions in the right panel, while a radial mode has no dependence as shown in the left panel. The right panel is for a mode with $l = 3$ and $m = 0$. In fact, a mode with $l = 3$ has seven azimuthal orders $m = 0, \pm 1, \pm 2, \pm 3$. m corresponds to the number of longitudinal nodal lines. The sign indicates the way of propagation in the ϕ direction. According to the definition of the spherical harmonics, Eq.(3.49), the positive value of m means that waves propagate in the negative direction of the ϕ coordinate. Here we have $m = 0$, and all the nodal lines at spherical surface are like latitudinal lines.

While the f mode has no node, the p modes has some nodes, and the subscript indicates the number of the nodes along the radial direction.[2] Like the radial modes, the frequency becomes higher as the number of nodes increases.

The middle panel of Fig.3.5, on the other hand, shows the profile of g modes, which have substantial amplitude in deep interior unlike the radial, the p and the f modes. Besides, the frequency becomes lower as the number of nodes increases.

3.10 Local analyses

Here we carry out local analyses, in which we simplify the differential equations for pulsations to understand their physics.

---

[1]Directions on the $\theta - \phi$ plane.
[2]p_1, p_2 and p_3 modes have one, two and three nodes, respectively, along the radial direction.

3.10.1 Radial pulsations

First, we proceed a local analysis for radial pulsation following Saio *et al.* (1998). Combining the differential equations for radial adiabatic pulsations, Eq.(3.174) and (3.175) gives

$$\frac{d^2\mathcal{Y}}{dr^2} + \mathcal{L}\mathcal{Y} = 0 \tag{3.178}$$

with

$$\mathcal{L} = \frac{\sigma^2\rho}{\Gamma_1 p} + \frac{1}{\Gamma_1 pr}\frac{d}{dr}[(3\Gamma_1 - 4)p] - \frac{1}{2\sqrt{\Gamma_1 pr^4}}\frac{d}{dr}\left[\frac{1}{\sqrt{\Gamma_1 pr^4}}\frac{d}{dr}(\Gamma_1 pr^4)\right] \tag{3.179}$$

where $\mathcal{Y} \equiv \sqrt{\Gamma_1 pr^4}\xi_r/r$. We assume the solution to be locally of the form $\mathcal{Y} \propto \exp[ik(r)r]$. Then, Eq.(3.178) becomes $-k^2\mathcal{Y} + \mathcal{L}\mathcal{Y} = 0$. We can immediately find that

- when $\mathcal{L} < 0$, we have $k^2 < 0$ and $\mathcal{Y}$ exponentially and monotonously increases or decreases along r, which means the wave is evanescent.

- when $\mathcal{L} > 0$, we have $k^2 > 0$ and $\mathcal{Y}$ becomes sinusoidal, which means the wave is propagative.

When $\mathcal{L} = 0$, we can derive

$$\sigma_c \simeq \frac{1}{2H_p}, \tag{3.180}$$

if the spatial variation of Γ_1 is small. We have defined σ for which $\mathcal{L} = 0$ as $\sigma_c(r)$. From this, we can find that the waves are propagative when $\sigma > \sigma_c$, while evanescent when $\sigma < \sigma_c$. It means that $\sigma_c(r)$ is the locally lowest frequency or the critical frequency for propagative waves.

Fig.3.7 is a propagation diagram showing a profile of the critical frequency, and meaning the waves are propagative over the curve. As discussed above, the local analysis includes some simplifications, and is indeed rough estimation. Despite the poorness, this analysis suggests that the nodes should appears in the propagative zone, and Fig.3.7 shows that 2O fairly fits into the result of this analysis.

3.10.2 Nonradial pulsations

Next, we proceed into the local analysis of nonradial pulsations. For the analysis, we adopt the differential equation system with the adiabatic Cowling approximation, Eqs.(3.143) and (3.144), and assume that y_1 and y_2 vary much more rapidly in space than the other physical variables appearing in these equations do so that those variables can be considered constant over some limited range of the radial direction. To quantify this, we propose that, like §3.10.1, both y_1 and y_2 vary spatially as $\exp(ik_r r)$, where the wave number k_r is very large compared to r. Substituting this exponential into Eqs.(3.143) and (3.144), we obtain

$$\begin{bmatrix} V_{\mathrm{g}} - 3 - ik_r r & \frac{l(l+1)}{c_1\omega^2} - V_{\mathrm{g}} \\ c_1\omega^2 - A^* & A^* - U + 1 - ik_r r \end{bmatrix} \begin{bmatrix} y_1 \\ y_2 \end{bmatrix} = 0. \tag{3.181}$$
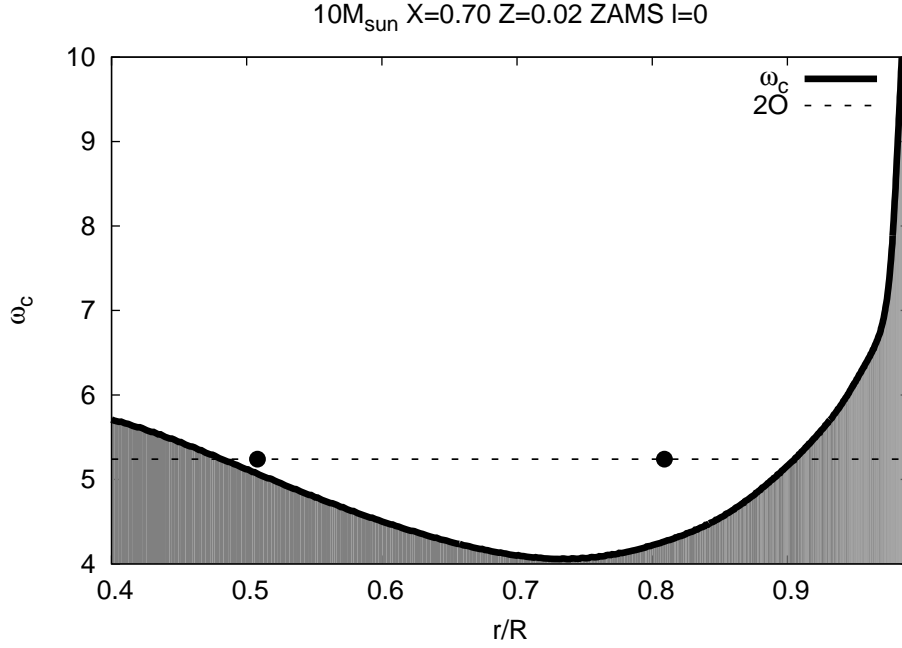
Figure 3.7: Profile of the normalized critical frequency for radial pulsations, $\omega_c = \sigma_c\sqrt{R^3/(GM)}$. The waves are propagative over the curve of ω_c, while evanescent in the gray hatched zone, below the curve. The dashed line means the frequency of 2O shown in Fig.3.4, and the dots on the line indicates the location of the nodes for the displacement ξ_r.

To get nontrivial solutions, the determinant of the coefficient matrix in Eq.(3.181) must be zero. Since the absolute value of $ik_r r$ is much larger than the other terms, we have the dispersion relation as

$$k_r^2 = \frac{1}{c_s^2\sigma^2}(\sigma^2 - S_l^2)(\sigma^2 - N^2) \tag{3.182}$$

where $c_s(\equiv \sqrt{\Gamma_1 P/\rho})$ denotes the acoustic velocity. S_l is "Lamb frequency", defined as

$$S_l^2 \equiv \frac{l(l+1)}{r^2}c_s^2 = k_h^2 c_s^2, \tag{3.183}$$

where $k_h^2(\equiv l(l+1)/r^2)$ is the squared horizontal wave number. The integer l, which is the degree of the spherical harmonics, represents the number of nodal lines on the spherical surface. $l(l+1)$ instead of l^2 is due to the spherical effect. On the other hand, we have

$$N^2 \equiv gr^{-1}A^*, \tag{3.184}$$

which is called "Brunt-Väisälä frequency". From Eq.(3.182), we can say that

- If $\sigma^2 < N^2$, S_l^2 or $\sigma^2 > N^2$, S_l^2, k_r becomes a real number and $\exp(ik_r r)$ reduces to sines. Hence, the solutions implies propagating waves.

57

- If $N^2 < \sigma^2 < S_l^2$ or $S_l^2 < \sigma^2 < N^2$, k_r becomes a purely imaginary number. Hence, the solutions show exponential, or evanescent behavior along r.

Thus N^2 and S_l^2 are critical frequencies for the wave propagation of nonradial pulsations.

Let us think some cases of wave propagation. We define the total wave number $K(\equiv k_r^2 + k_h^2)$. First, if $\sigma^2 \gg N^2,\ S_l^2$, we obtain

$$\sigma^2 \approx K^2 c_s^2 \tag{3.185}$$

from Eq.(3.182). This implies propagation of acoustic waves because only the acoustic velocity enters. Eigenmodes in this frequency range corresponds to p modes, where p means "pressure", because a restoring force of acoustic waves is difference of pressure among gases.

Secondly, if $\sigma^2 \ll N^2,\ S_l^2$, we obtain

$$\sigma^2 \approx \frac{k_h^2}{K^2} N^2. \tag{3.186}$$

This implies propagation of internal gravity waves because of the appearance of the Brunt-Väisälä frequency N, with which the vertically displaced clump oscillates due to the buoyancy. Eigenmodes in this frequency range correspond to g modes, where g means "gravity". Let us discuss the Brunt-Väisälä frequency for more detail. The equation of motion about a convective clump which oscillates due to the buoyancy is

$$\frac{d^2 \Delta r}{dt^2} = -g \frac{\Delta \rho}{\rho} = -N^2 \Delta r \tag{3.187}$$

where Δr denotes the displacement of the clump, $\Delta \rho$ density difference between the clump and its surroundings. The Brunt-Väisälä frequency N is given as frequency of the simple harmonic motion. The expression of $\Delta \rho / \rho$ is given by

$$
\begin{aligned}
\frac{\Delta \rho(r + \Delta r)}{\rho} &\equiv \frac{\rho^*(r + \Delta r) - \rho(r + \Delta r)}{\rho} \\
&= \left[\left(\frac{\partial \ln \rho}{\partial \ln p} \right)_S \frac{d \ln p}{dr} - \frac{d \ln \rho}{dr} \right] \Delta r.
\end{aligned}
\tag{3.188}
$$

Therefore, the Brunt-Väisälä frequency is expressed as

$$N^2 = -\frac{g}{r} \left(\frac{d \ln \rho}{d \ln r} - \frac{1}{\Gamma_1} \frac{d \ln p}{d \ln r} \right), \tag{3.189}$$

which is equivalent with the definition of A^* in Eq.(3.126). The negative N^2 implies convectively unstable, while the positive one convectively stable. According to Eq.(3.186), when $N^2 < 0$, σ becomes purely imaginary, and the perturbation either grows or decays exponentially in time. That is, internal gravity waves cannot propagate in convection zones.

The expression of the Brunt-Väisälä frequency with temperature gradient is given by

$$N^2 = \frac{gV}{r} \left[\frac{4 - 3\beta}{\beta} (\nabla_{\mathrm{ad}} - \nabla) + \nabla_\mu \right]. \tag{3.190}$$
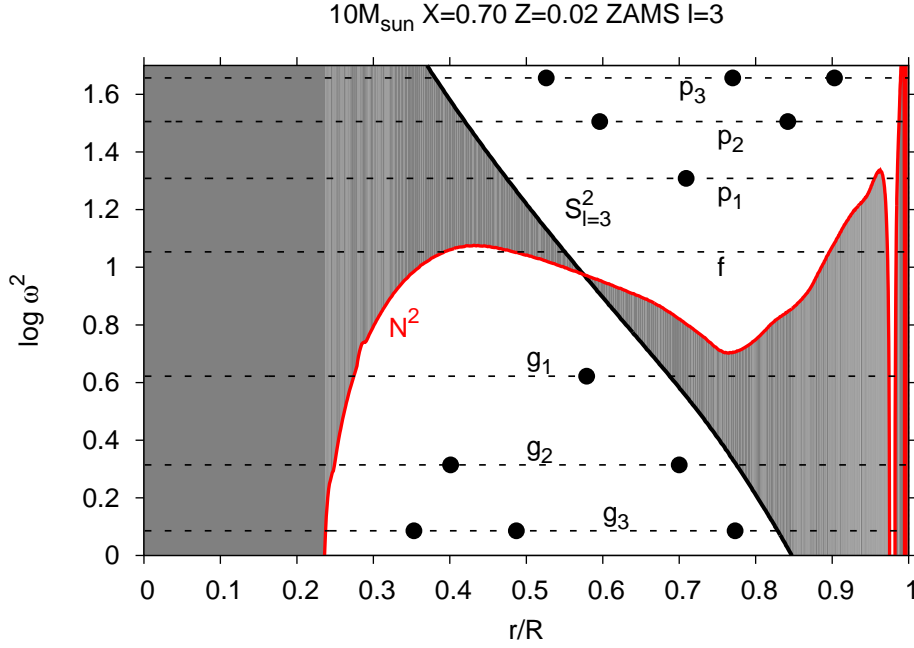
Figure 3.8: Propagation diagram for nonradial, $l = 3$ modes in the ZAMS model of a $10M_\odot$ star. The value of frequency in the vertical axis, and the two critical frequencies, N^2 and $S^2_{l=3}$, are normalized with the dynamical timescale $\sqrt{R^3/(GM)}$. The meanings of the dots and the gray hatched zones are the same as Fig.3.7.

Fig.3.8 shows a propagation diagram for nonradial $l = 3$ modes introduced in Fig.3.5. In the nonradial case, a star has two types of propagation zones. The one appearing in the upper part, corresponding to $\sigma^2 > N^2$, $S^2_{l=3}$, is the propagation zone for acoustic waves, where nodes of p modes show up, while another in the lower part, corresponding to $\sigma^2 < N^2$, $S^2_{l=3}$ is for internal gravity waves, where nodes of g modes do. The acoustic waves propagate from the surface layer to the deep interior, but are reflected at the level where wave's frequency becomes equal to the Lamb frequency. On the other hand, the gravity waves are propagating inside the limit of the Lamb frequency, and reach to the top of the convective core, at $r/R \simeq 0.22$. In convection zones, we have $N^2 < 0$ and the gravity waves cannot be propagating.

3.11   Excitation mechanisms

In the previous section, we have seen that a star has a number of eigenmodes. In practice, however, all eigenmodes do not grow up to have substantial amplitude. Some eigenmodes would be excited by some excitation mechanisms, and grow up during pulsations, while the others would be damped. In this section, we discuss the excitation mechanisms for pulsations.

3.11.1 Work integral

We start with the first law of thermodynamics,

$$TdS = d\mathcal{U} + pd\left(\frac{1}{\rho}\right), \tag{3.191}$$

where $\mathcal{U}$ denotes the internal energy. The LHS means thermal energy which the noted matter receive from its surroundings, and the second term in the RHS work done by the noted matter against its surroundings. For a complete cycle, Eq.(3.191) becomes

$$\oint TdS = \oint d\mathcal{U} + \oint pd\left(\frac{1}{\rho}\right). \tag{3.192}$$

If pulsating matter truly returns to its initial thermodynamic state over one cycle, we have $\oint d\mathcal{U} = 0$ since $\mathcal{U}$ is a state variable. Then we obtain

$$\oint TdS = \oint pd\left(\frac{1}{\rho}\right). \tag{3.193}$$

This means that received thermal energy is converted to mechanical energy by heat engine mechanism. That is, the LHS and the RHS of Eq.(3.193) expresses variations of the thermal energy and the mechanical energy in one cycle, respectively. Particularly, the latter can be regarded as the increment of pulsational energy e_K.

Let us decompose the variables appearing in the RHS into the space and the time depending terms:

$$
\begin{aligned}
\oint de_K &= \oint pd\left(\frac{1}{\rho}\right) = \oint \Re[\delta p(\mathbf{r},t)]\Re[d\delta\rho^{-1}(\mathbf{r},t)] \\
&= \frac{1}{\rho^2}\oint |\delta p(\mathbf{r})|\cos[\sigma_R t + \phi_T(\mathbf{r})]\sigma_R|\delta\rho(\mathbf{r})|\sin[\sigma_R t + \phi_\rho(\mathbf{r})]dt \\
&= \frac{\sigma_R}{2\rho^2}|\delta p||\delta\rho|\oint\{\sin[2\sigma_R t + \phi_p + \phi_\rho] + \sin[\phi_\rho - \phi_p]\}dt \\
&= \frac{\pi}{\rho^2}|\delta p|\,|\delta\rho|\sin[\phi_\rho - \phi_p], \tag{3.194}
\end{aligned}
$$

where ϕ_p and ϕ_ρ are the initial phases of δp and $\delta\rho$, respectively. As we can see, the work is proportional to the amplitudes, $|\delta p|$ and $|\delta\rho|$, and to the sine of the phase lag between δp and $\delta\rho$. While the former values are absolute values, the latter can be either positive or negative, and determine the sign of the work.

Fig.3.9 is a $p - 1/\rho$ plane showing behaviors of pressure and density during one cycle. The red path is for no phase lag between pressure and density, which corresponds to adiabatic process. In this situation, any work is never done. On the other hand, the green and the blue paths, having phase lags, correspond to nonadiabatic processes, and some work is done. The area of the gray-colored zone indicates amount of work done during the cycle. When the values of p and $1/\rho$ changes as orbiting counterclockwise along the path, the work becomes positive,
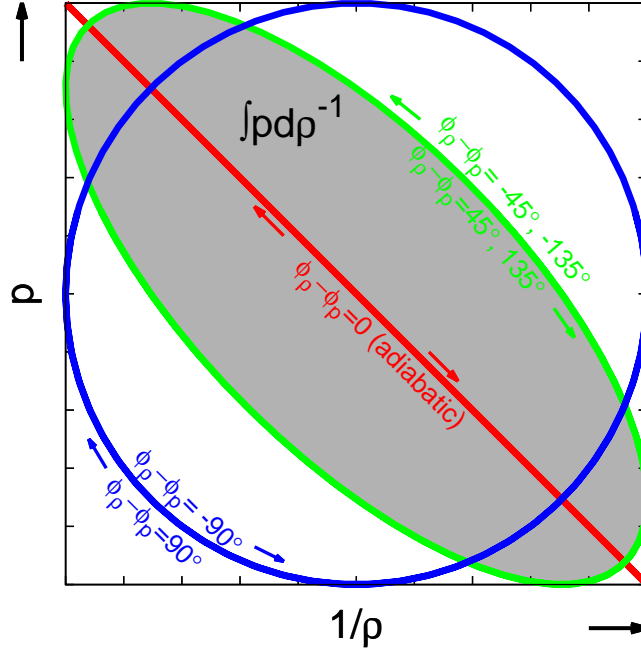
Figure 3.9: $p - 1/\rho$ plane showing behaviors of pressure and density during one cycle. The red, the green and the blue lines are paths for the cases of different phase lags $\phi_\rho - \phi_p$. Particularly, the red line is for no phase lag between pressure and density, which corresponds to adiabatic process. The area of the gray-colored zone indicates amount of work done during the cycle in the case of the green line.

and vice versa. In other words, positive work is done when the density's phase precede the pressure's. Since the amount of work is proportional to $\sin[\phi_\rho - \phi_p]$, it becomes largest when $|\phi_\rho - \phi_p| = 90°$, to which the blue path corresponds, if the amplitudes, $|\delta p|$ and $|\delta \rho^{-1}|$ are fixed.

Next let us transform the LHS of Eq.(3.193). Taking the same procedure as Eq.(3.194) gives

$$
\begin{aligned}
\oint de_K &= \oint T dS = \oint \Re[\delta T(\mathbf{r},t)] \Re[d\delta S(\mathbf{r},t)] \\
&= -\pi |\delta T(\mathbf{r})||\delta S(\mathbf{r})| \sin(\phi_S - \phi_T) = -\pi \Im[\delta T^*(\mathbf{r}) \delta S(\mathbf{r})], \qquad (3.195)
\end{aligned}
$$

where ϕ_T and ϕ_S denotes the initial phases of δT and δS, respectively. Assuming e_K and $E_K(r)$ to be the pulsational energy per unit mass and that inside of the radius r respectively, the increment of $E_K(r)$ per one cycle is given by

$$
\begin{aligned}
W(r) &\equiv \oint dE_K = \int_0^r \int_0^\pi \int_0^{2\pi} \oint de_K(\mathbf{r}) \rho r^2 \sin\theta d\phi d\theta dr \\
&= -4\pi^2 \int_0^r \int_0^\pi \int_0^{2\pi} \Im[\delta T^*(r) Y_l^m(\theta,\phi)^* \delta S(r) Y_l^m(\theta,\phi)] \rho r^2 \sin\theta d\phi d\theta dr
\end{aligned}
$$

61

$$= -4\pi^2 \int_0^r \Im[\delta T^*(r)\delta S(r)]\rho r^2 dr$$

$$= -\pi \int_0^{M_r} \Im[\delta T^*(M_r)\delta S(M_r)]dM_r \tag{3.196}$$

Since the pulsational energy is proportional to the square of the amplitude, we have the relation $dE_K(R)/E_K(R) = \exp(-2\sigma_I t)dt$ and then

$$\frac{W(R)}{E_K(R)} = \oint \exp(-2\sigma_I t)dt = -4\pi\frac{\sigma_I}{\sigma_R}. \tag{3.197}$$

W is called "work integral", which is useful to understand excitation mechanisms for pulsations. The excitation occurs in regions where $dW/dM_r > 0$, while the damping $dW/dM_r < 0$. Though the linear nonadiabatic analysis, solving the system Eq.(3.128)-(3.133), Eq.(3.135)–(3.138) or Eq.(3.162)–(3.165), can evaluate σ_R and σ_I as eigenvalues by itself, the work integral can evaluate the ratio of σ_I to σ_R if $E_K(R)$ is given. E_K can be evaluated as

$$
\begin{aligned}
E_K(r) &= \int_0^r \int_0^\pi \int_0^{2\pi} 2 \times \frac{1}{2}\langle \mathbf{v}^2\rangle(\mathbf{r})\rho r^2 \sin\theta d\phi d\theta dr \\
&= \frac{\sigma_R^2}{2}\int_0^r \int_0^\pi \int_0^{2\pi} \boldsymbol{\xi}^* \cdot \boldsymbol{\xi}\rho r^2 \sin\theta d\phi d\theta dr \\
&= \frac{\sigma_R^2}{2}\int_0^r \rho r^2 dr \left[\xi_r^*\xi_r \int\int Y_l^m(\theta,\phi)^* Y_l^m(\theta,\phi)\sin\theta d\theta d\phi \right. \\
&\quad \left. +\xi_h^*\xi_h \int\int \left(\frac{\partial Y_l^{m*}}{\partial\theta}\frac{\partial Y_l^m}{\partial\theta} + \frac{1}{\sin^2\theta}\frac{\partial Y_l^{m*}}{\partial\phi}\frac{\partial Y_l^m}{\partial\phi} \right)\sin\theta d\theta d\phi \right] \\
&= \frac{\sigma_R^2}{2}\int_0^{M_r} [\xi_r^*\xi_r + l(l+1)\xi_h^*\xi_h]dM_r.
\end{aligned}
\tag{3.198}
$$

where $\langle\ldots\rangle$ means the time average.

By using Eq.(3.68), let us decompose W into W_N and W_F, which are related to the perturbations of the nuclear energy generation rate, and the flux gradient, respectively:

$$W = W_N + W_F \tag{3.199}$$

with

$$W_N = \frac{\pi}{\sigma_R}\int_0^{M_r} \Re\left[\frac{\delta T^*}{T}\delta\varepsilon \right]dM_r, \tag{3.200}$$

$$W_F = \frac{\pi}{\sigma_R}\int_0^{M_r} \Re\left[\frac{\delta T^*}{T}\delta\left(-\frac{1}{\rho}\nabla\cdot\mathbf{F}\right) \right]dM_r. \tag{3.201}$$

where σ is extracted from the parenthesis and converted into σ_R since $\sigma_I/\sigma_R \ll 1$. Moreover, decomposing W_F into $W_{F,h}$ and $W_{F,r}$, which are related to the horizontal and radial components of the perturbation of the flux gradient, we have

$$W_F = W_{F,h} + W_{F,r} \tag{3.202}$$

with

$$W_{F,h} = \frac{\pi}{\sigma_R} \int_0^{M_r} \Re \left[\frac{\delta T^*}{T} \left(-\frac{1}{\rho} \nabla \cdot \mathbf{F}'_h \right) \right] dM_r, \tag{3.203}$$

$$W_{F,r} = \frac{\pi}{\sigma_R} \int_0^{M_r} \Re \left[\frac{\delta T^*}{T} \left(-\frac{d\delta L_r}{dM_r} + l(l+1) \frac{\xi_h}{r} \frac{dL_r}{dM_r} \right) \right] dM_r. \tag{3.204}$$

3.11.2 ε-mechanism

The ε-mechanism is an excitation mechanism in which pulsations grow with nuclear energy. The nuclear energy generation rate increases at shrinking phase in pulsations due to increase in temperature. This makes expansion in the pulsations stronger and the nuclear energy generation more largely drops in the expansion phase. This cyclical behavior makes a star act as a heat engine and the pulsation amplitude will grow.

So far there is no bona fide pulsator excited by the ε-mechanism. But recently a few candidates have been found in observed stars. Shibahashi and Osaki (1976) originally suggested possiblity of excitation of g modes due to the ε-mechanism at the H-burning shell in post-main sequence massive stars. Recently, Moravveji et al. (2012) proposed that excitation of a g mode shown in a B supergiant, Rigel could be explained by this mechanism. Theoretical works have suggested that pre-white dwarfs also have a possibility to exhibit pulsations excited by the ε-mechanism at the He-burning shell (Kawaler et al., 1986; Saio, 1996; Gautschy, 1997). Recently, an observed pre-white dwarf VV47 was found to exhibit unusually short pulsation periods ($\sim 130 - 300$ s). González Pérez et al. (2006) and Córsico et al. (2009) speculated that such pulsations could be excited by the ε-mechanism. On the other hand, Maeda (2014) found the excitation at the H-burning shell in models with relatively thick H envelopes.

In theory, the ε-mechanism instability is also predicted in the other types of stars. The radial fundamental mode had been thought to be excited by this mechanism in massive main-sequence stars with the solar-like composition (Ledoux, 1941; Schwarzschild and Härm, 1959; Stothers and Simon, 1968; Aizenman et al., 1975; Stothers, 1992). However, after the new opacity tables (Rogers and Iglesias, 1992) are released, the fundamental mode was found to be more strongly excited by the κ-mechanism (§3.11.4) at the iron group element opacity bump (Fe bump) rather than by the ε-mechanism. On the other hand, Baraffe et al. (2001) found that the ε-mechanism still mainly acts on the excitation of the fundamental mode in the Population III very massive main-sequence stars because of the lack of the Fe bump.

The ε-mechanism instability has also been considered by association with the solar neutrino problem. Dilke and Gough (1972) suggested that the ε-mechanism by ^{3}He reactions should induce pulsational instability. This instability might induce nonlinear material mixing and reduction of the neutrino flux due to temperature decrease in the nuclear reaction zone. Following this suggestion, pulsational stability analyses demonstrated that low-degree low-order g modes are likely to be destabilized by the ε-mechanism at a certain early evolutionary stage of the Sun and solar-like stars (Boury and Noels, 1973; Christensen-Dalsgaard et al., 1974; Boury et al., 1975; Shibahashi et al., 1975; Noels et al., 1976). However, the presence of a convective envelope, which occupies the outer 20–30 per cent of the stellar radius has

made it hard to reach a definite conclusion on the pulsational stability because of uncertainty in the treatment of the convective envelope. Recently, Sonoi and Shibahashi (2011, 2012a,b,c, 2013a,b) showed that this kind of instability takes place in metal-free, -poor main-sequence stars. Since convection hardly contributes to energy transfer in the envelopes of such stars, their results are free from the uncertainty of the treatment of convection. On the other hand, the g mode instability due to the ε-mechanism is also found in brown dwarf main-sequence models (Rodríguez-López et al., 2012, 2013), and the radial fundamental mode is excited by ^{2}D-burning core in the pre-main sequence stage (Palla and Baraffe, 2005; Rodríguez-López et al., 2012, 2013). In brown dwarfs, convection dominantly contributes to energy transfer and the uncertainty remains in their results. In spite of this, observational efforts are going on (Baran et al., 2011).

W_N expresses the work done exclusively by the ε-mechanism and hence is always positive. $\delta\varepsilon$ is evaluated by Eq.(3.124), where $\varepsilon_{\mathrm{ad}}$ and ε_S appears. By using the temperature and density dependence of the energy generation rate, $\varepsilon_T \equiv (\partial \ln \varepsilon / \partial \ln T)_\rho$ and $\varepsilon_\rho \equiv (\partial \ln \varepsilon / \partial \ln \rho)_T$, these two thermodynamical coefficients can be expressed as

$$\varepsilon_{\mathrm{ad}} = \left(\frac{\partial \ln \varepsilon}{\partial \ln p}\right)_S = \varepsilon_T \nabla_{\mathrm{ad}} + \frac{\varepsilon_\rho}{\Gamma_1} \tag{3.205}$$

$$\varepsilon_S = c_p \left(\frac{\partial \ln \varepsilon}{\partial S}\right)_p = \varepsilon_T - v_T \varepsilon_\rho. \tag{3.206}$$

For a stability analysis relevant to the ε-mechanism, it is important to evaluate ε_T and ε_ρ in the oscillation time scale, which are different from one in the stellar evolution timescale.

In the case of the pp-chain, p(p,$e^+\nu$)^{2}H is the slowest reaction and its nuclear reaction rate dominates that of the whole pp-chain in the time scale of stellar evolution. Therefore, ε_T of the pp-chain is about 4 at $\log T = 7$. However, in the time scale of oscillations, about a few hours, ε_T of pp-chain is dominated by ^{3}He(^{3}He,2p) ^{4}He. In this case, ε_T of the pp-chain becomes about 11 (Dilke and Gough, 1972; Boury and Noels, 1973; Shibahashi et al., 1975; Unno, 1975; Unno et al., 1989).

In the case of CNO-cycle, the timescale of the β-decays [e.g. ^{13}N(e^-,ν)^{13}C, ^{15}O(e^-,ν)^{15}N] is comparable with the oscillation period ($\sim$ 1 hr). This could cause the phase delay that are introduced between creation and destruction of various reactants (Bethe, 1939; Cox, 1954, 1955; Kawaler, 1988).

In the following, the way of the evaluation of ε_ρ and ε_T in the oscillation time scale will be introduced following Unno et al. (1989) for the pp-chain and Kawaler (1988) for the CNO-cycle.

pp-chain

Let N_j, $C_{j,k}$, and $Q_{j,k}$ be the number density of nuclei with the atomic weight j ($j = e$ means electron), the reaction rate of the j- and the k- nuclei, and the energy generated (minus neutrino loss) by a single reaction, respectively. The asterisk will stand for ^{7}Li in order to

distinguish it from ^{7}Be. The ^{8}B- and ^{8}Be-decays are assumed to occur instantaneously. Then, we have

$$\rho\varepsilon = \frac{1}{2}N_1^2 C_{1,1} + N_2 N_1 C_{2,1} Q_{2,1} + N_3\left(\frac{1}{2}N_3 C_{3,3} Q_{3,3} + N_4 C_{3,4} Q_{3,4}\right)$$
$$+ N_7(N_e C_{7,e} Q_{7,e} + N_1 C_{7,1} Q_{7,1}) + N_7^* N_1 C_{7,1}^* Q_{7,1}^* \tag{3.207}$$

$$\frac{\partial N_1}{\partial t} + \nabla\cdot(N_1\mathbf{v}) = -N_1^2 C_{1,1} - N_1 N_2 C_{2,1} + N_3^2 C_{3,3}$$
$$-N_1 N_7^* C_{7,1}^* - N_1 N_7 C_{7,1}, \tag{3.208}$$

$$\frac{\partial N_2}{\partial t} + \nabla\cdot(N_2\mathbf{v}) = \frac{1}{2}N_1^2 C_{1,1} - N_1 N_2 C_{2,1}, \tag{3.209}$$

$$\frac{\partial N_3}{\partial t} + \nabla\cdot(N_3\mathbf{v}) = N_1 N_2 C_{2,1} - N_3(N_3 C_{3,3} + N_4 C_{3,4}), \tag{3.210}$$

$$\frac{\partial N_4}{\partial t} + \nabla\cdot(N_4\mathbf{v}) = \frac{1}{2}N_3^2 - N_3 N_4 C_{3,4} + 2N_1 N_7^* C_{7,1}^*$$
$$+2N_1 N_7 C_{7,1}, \tag{3.211}$$

$$\frac{\partial N_7}{\partial t} + \nabla\cdot(N_7\mathbf{v}) = N_3 N_4 C_{3,4} - N_7(N_e C_{7,e} + N_1 C_{7,1}), \tag{3.212}$$

$$\frac{\partial N_7^*}{\partial t} + \nabla\cdot(N_7^*\mathbf{v}) = N_7 N_e C_{7,e} - N_7^* N_1 C_{7,1}^*. \tag{3.213}$$

where $C_{j,k}$'s are functions of temperature and the values of $Q_{j,k}$ used in this study are summarized in table 3.1. A factor of $1/2$ appears for reactions of identical particles since $N_j^2 C_{j,j}$ counts a single reaction twice; a factor 2 appears in the rate equations (3.208)-(3.213) if two identical particles are integrated or created by a single reaction, and in some terms these two factors cancel each other out.

Let us consider the variation of N_j's in the oscillation. The lifetime of ^{2}D is much shorter than the oscillation period. Then, we have

$$N_2 = \frac{1}{2}N_1\frac{C_{1,1}}{C_{2,1}}. \tag{3.214}$$

Table 3.1: Reactions in the pp-chain and their Q values (the neutrino loss subtracted)

branch	reaction	Q(MeV)
PP-I	p(p,$e^+\nu$)^{2}D	1.179
	^{2}D(p,γ)^{3}He	5.493
	^{3}He(^{3}He,2p)^{4}He	12.859
PP-II	^{3}He(^{4}He,γ)^{7}Be	1.587
	^{7}Be(e^-,ν)^{7}Li	0.049
	^{7}Li(p,γ)2^{4}He	17.347
PP-III	^{7}Be(p,γ)^{8}B	0.137
	^{8}B (,$e^+\nu$)^{8}Be(,^{4}He)^{4}He	1.01

On the other hand, those of other elements are much longer. Then, the contribution of the nuclear reactions to the variation of N_j's is negligible. We have

$$\frac{\delta N_1}{N_1} = \frac{\delta N_3}{N_3} = \frac{\delta N_4}{N_4} = \frac{\delta N_7}{N_7} = \frac{\delta N_7^*}{N_7^*} = \frac{\delta \rho}{\rho}. \tag{3.215}$$

Equilibrium relations are derived if the right hand sides of (3.210), (3.211), (3.212) and (3.213). In addition to (3.214), we get

$$N_{3E}^2 = \frac{b_{\mathrm{I}}}{2} N_1^2 \left(\frac{C_{1,1}}{C_{3,3}} \right)_E, \tag{3.216}$$

$$N_{3E} = \frac{1 - b_{\mathrm{I}}}{2} \frac{N_1^2}{N_4} \left(\frac{C_{1,1}}{C_{3.4}} \right)_E, \tag{3.217}$$

$$N_{7E} = \frac{b_{\mathrm{II}}}{2} \frac{N_1^2}{N_e} \left(\frac{C_{1,1}}{C_{7,e}} \right)_E = \frac{b_{\mathrm{III}}}{2} N_1 \left(\frac{C_{1,1}}{C_{7.1}} \right)_E, \tag{3.218}$$

$$N_{7E}^* = \frac{b_{\mathrm{II}}}{2} N_1 \left(\frac{C_{1,1}}{C_{7,1}^*} \right)_E \tag{3.219}$$

where the branching factors b_{I}, b_{II} and b_{III} defined by

$$\frac{b_{\mathrm{I}}}{1 - b_{\mathrm{I}}} \equiv \frac{N_{3E}^2 C_{3,3E}}{N_{3E} N_4 C_{3,4E}}, \tag{3.220}$$

$$\frac{b_{\mathrm{III}}}{b_{\mathrm{II}}} \equiv \frac{N_{7E} N_1 C_{7,1E}}{N_{7E} N_e C_{7,eE}}, \tag{3.221}$$

$$b_{\mathrm{I}} + b_{\mathrm{II}} + b_{\mathrm{III}} \equiv 1 \tag{3.222}$$

Take the Lagrange variation of (3.207) and use (3.214)-(3.222):

$$\frac{\delta \varepsilon}{\varepsilon} = \frac{\delta \rho}{\rho} + \frac{\sum_{i,j} \nu_{i,j} f_{i,j} Q_{i,j}}{\sum_{i,j} f_{i,j} Q_{i,j}} \frac{\delta T}{T} \tag{3.223}$$

where

$$\nu_{i,j} \equiv \begin{cases} d \ln C_{1,1} / d \ln T & \text{for } (i,j) = (2,1) \\ d \ln C_{i,j} / d \ln T & \text{otherwise} \end{cases} \tag{3.224}$$

and

$$f_{1,1} \equiv 1, \quad f_{2,1} \equiv 1, \quad f_{3,3} \equiv \frac{b_{\mathrm{I}}}{2}, \quad f_{3,4} \equiv 1 - b_{\mathrm{I}}, \quad f_{7,e} \equiv b_{\mathrm{II}}, \quad f_{7,1} \equiv b_{\mathrm{III}}, \quad f_{7,1}^* \equiv b_{\mathrm{II}} \tag{3.225}$$

That is, we obtain $\varepsilon_{\rho,\mathrm{pp}}[\equiv (\partial \ln \varepsilon_{\mathrm{pp}} / \partial \ln \rho)_T] = 1$ and $\varepsilon_{T,\mathrm{pp}}$ is expressed as the coefficient of $\delta T/T$ in Eq.(3.223).

CNO-cycle

The reactions in CN-cycle are introduced in Table 3.2. The reaction of ^{15}N(p,γ)^{16}O can occur instead of the last reaction in the left column of Table 3.2 and this launches the NO-cycle, with which CN-cycle composes CNO-cycle. However, we neglect the NO-cycle since the probability that this reaction will occur is $\sim 10^{-4}$.

i's are defined as the number of species and its decay reaction following Table 3.2. Then, we have

$$N\frac{dy_i}{dt} = -N^2 y_i y_p C_i + N^2 y_{i-1} y_p C_{i-1} \quad (i = 1, 4) \tag{3.226}$$

$$N\frac{dy_i}{dt} = -N y_i \lambda_i + N^2 y_{i-1} y_p C_{i-1} \quad (i = 2, 5) \tag{3.227}$$

$$N\frac{dy_i}{dt} = -N^2 y_i y_p C_i + N y_{i-1} \lambda_{i-1} \quad (i = 3, 6) \tag{3.228}$$

where N denotes the total number density and y_i the number fraction of the element i. C_i denotes the rate of collisional destruction of species i per proton for $i = 1, 3, 4, 6$, and λ_i the rate of decay of species i for $i = 2, 5$. If $i = 1$, $i - 1$ means $i = 6$. p means proton. The reciprocal of the timescale for collisional destruction of species i is

$$K_i \equiv N y_p C_i \tag{3.229}$$

Since the lifetimes of ^{13}N and ^{15}O are comparable with the oscillation period, the phase delay between creation and destruction of species could occur. Then, we have to consider the perturbation of y_i's:

$$\frac{\delta y_i}{y_i} = \alpha_i \frac{\delta\rho}{\rho} + \beta_i \frac{\delta T}{T} \tag{3.230}$$

Since C_i is a function of temperature, we obtain

$$\frac{\delta K_i}{K_i} = \frac{\delta\rho}{\rho} + \nu_i \frac{\delta T}{T} \tag{3.231}$$

Table 3.2: Reactions in CN-cycle and NO-cycle and their Q values (the neutrino loss subtracted)

	CN-cycle		NO-cycle	
i	reaction	Q(MeV)	reaction	Q(MeV)
1	^{12}C(p,γ)^{13}N	1.944	^{15}N(p,γ)^{16}O	12.127
2	^{13}N(e^-,ν)^{13}C	1.511	^{16}O(p,γ)^{17}F	0.600
3	^{13}C(p,γ)^{14}N	7.551	^{17}F(,$e^+\nu$)^{17}O	1.822
4	^{14}N(p,γ)^{15}O	7.297	^{17}O(p,α)^{14}N	1.192
5	^{15}O(e^-,ν)^{15}N	1.761		
6	^{15}N(p,α)^{12}C	4.966		

where $\nu_i \equiv (\partial \ln C_i / \partial \ln T)_{\rho,y}$. The nuclear energy productions are given by

$$\varepsilon_i = \frac{N K_i y_i Q_i}{\rho} \quad (i = 1, 3, 4, 6) \tag{3.232}$$

$$\varepsilon_i = \frac{N \lambda_i y_i Q_i}{\rho} \quad (i = 2, 5) \tag{3.233}$$

Taking the Lagrange variation of $\varepsilon_{\mathrm{CN}} = \sum_i \varepsilon_i$, we have

$$\varepsilon_{\rho,\mathrm{CN}} = \left(\varepsilon_1 + \varepsilon_3 + \varepsilon_4 + \varepsilon_6 + \sum_i \alpha_i \varepsilon_i \right) \Big/ \varepsilon_{\mathrm{CN}} \tag{3.234}$$

$$\varepsilon_{T,\mathrm{CN}} = \left(\nu_1 \varepsilon_1 + \nu_3 \varepsilon_3 + \nu_4 \varepsilon_4 + \nu_6 \varepsilon_6 + \sum_i \beta_i \varepsilon_i \right) \Big/ \varepsilon_{\mathrm{CN}}. \tag{3.235}$$

To evaluate the α_i's and β_i's, taking the Lagrange variation of (3.226)-(3.228):

$$\frac{\delta y_i}{y_i} = \frac{K_i}{i\sigma + K_i} \left[\alpha_{i-1} \frac{\delta\rho}{\rho} + (\beta_{i-1} + \nu_{i-1} - \nu_i) \frac{\delta T}{T} \right] \quad (i = 1, 4) \tag{3.236}$$

$$\frac{\delta y_i}{y_i} = \frac{\lambda_i}{i\sigma + \lambda_i} \left[(\alpha_{i-1} + 1) \frac{\delta\rho}{\rho} + (\beta_{i-1} + \nu_{i-1}) \frac{\delta T}{T} \right] \quad (i = 2, 5) \tag{3.237}$$

$$\frac{\delta y_i}{y_i} = \frac{K_i}{i\sigma + K_i} \left[(\alpha_{i-1} - 1) \frac{\delta\rho}{\rho} + (\beta_{i-1} - \nu_i) \frac{\delta T}{T} \right] \quad (i = 3, 6) \tag{3.238}$$

Then, we obtain the recursive formulae for the α_i's:

$$\alpha_1 = \frac{K_1}{i\sigma + K_1} \alpha_6, \quad \alpha_2 = \frac{\lambda_2}{i\sigma + \lambda_2} (\alpha_1 + 1), \tag{3.239}$$

$$\alpha_3 = \frac{K_3}{i\sigma + K_3} (\alpha_2 - 1), \quad \alpha_4 = \frac{K_4}{i\sigma + K_4} \alpha_3, \tag{3.240}$$

$$\alpha_5 = \frac{\lambda_5}{i\sigma + \lambda_5} (\alpha_4 + 1), \quad \alpha_6 = \frac{K_6}{i\sigma + K_6} (\alpha_5 - 1) \tag{3.241}$$

and for the β_i's:

$$\beta_1 = \frac{K_1}{i\sigma + K_1} (\beta_6 + \nu_6 - \nu_1), \quad \beta_2 = \frac{\lambda_2}{i\sigma + \lambda_2} (\beta_1 + \nu_1), \tag{3.242}$$

$$\beta_3 = \frac{K_3}{i\sigma + K_3} (\beta_2 - \nu_3), \quad \beta_4 = \frac{K_4}{i\sigma + K_4} (\beta_3 + \nu_3 - \nu_4), \tag{3.243}$$

$$\beta_5 = \frac{\lambda_5}{i\sigma + \lambda_5} (\beta_4 + \nu_4), \quad \beta_6 = \frac{K_6}{i\sigma + K_6} (\beta_5 - \nu_6) \tag{3.244}$$

Although Kawaler (1988) showed the analytical solution for the α's and β's derived by assuming $K_i \ll \sigma$, they are evaluated by (3.239)-(3.241) without this assumption in this study since the onset of CNO-cycle occurs at extremely high temperature ($\sim 10^8$K) in the Population III stars and hence K_i's can be comparable with σ. After getting the values of α_i's and β_i's, we can obtain the values of $\varepsilon_{\rho,\mathrm{CN}}$ and $\varepsilon_{T,\mathrm{CN}}$ from (3.234) and (3.235), respectively.

On the Whole Hydrogen Burning

In this study, the temperature and the density dependences of the whole hydrogen burning are given by

$$\varepsilon_T = (\varepsilon_{\mathrm{pp}}\varepsilon_{T,\mathrm{pp}} + \varepsilon_{\mathrm{CN}}\varepsilon_{T,\mathrm{CN}})/\varepsilon \tag{3.245}$$

$$\varepsilon_\rho = (\varepsilon_{\mathrm{pp}}\varepsilon_{\rho,\mathrm{pp}} + \varepsilon_{\mathrm{CN}}\varepsilon_{\rho,\mathrm{CN}})/\varepsilon. \tag{3.246}$$

This study investigates the instability related to the ε-mechanism in the core hydrogen-burning stage of the Population III stars. Actually, central temperature in such stars reaches $\sim 10^8$ K with which the triple alpha reaction can take place. But in a such stage, contribution of this reaction is indeed negligible, and we should only take into account the temperature and the density dependences of pp-chain and CNO-cycle.

3.11.3 Flux absorption and dissipation

W_F denotes the work done by the flux absorption. That is, the flux absorption and hence conversion from received heat to kinetic energy of pulsations occur in the region where $dW_F/dr > 0$, while the conversion from kinetic energy to heat, dissipated to the surrounding, (flux dissipation) in the region where $dW_F/dr < 0$. The flux absorption is one of the excitation mechanisms. Let us modify the expression for W_F given by Eq.(3.201) and change Eq.(3.87) to a form in which all the terms are proportional to $(\delta T/T)^2$ or $[d(\delta T/T)/dr]^2$ following Unno *et al.* (1989). For simplicity, we assume that the adiabatic temperature gradient ∇_{ad} is constant. From the relation between the Eulerian and the Lagrangian perturbation we have

$$\frac{p'}{p} = \frac{\delta p}{p} - \frac{\xi_r}{r}\frac{d\ln p}{d\ln r} \simeq \frac{1}{\nabla_{\mathrm{ad}}}\frac{\delta T}{T} + \frac{\xi_r}{r}V. \tag{3.247}$$

Using the equations for the adiabatic Cowling approximation, Eq.(3.143) and (3.144) with Eq.(3.247), we obtain

$$\frac{\xi_r}{r} \simeq (\nabla_{\mathrm{ad}}\alpha_0)^{-1}\left[\frac{S_l^2}{\Gamma_1\sigma^2} - \frac{\delta T}{T} + H_p\frac{d}{dr}\left(\frac{\delta T}{T}\right)\right], \tag{3.248}$$

where $H_p(\equiv -dr/d\ln p)$ denotes the pressure scale height and

$$\alpha_0 \equiv 4 - U - \frac{l(l+1)}{c_1\omega^2} + c_1\omega^2. \tag{3.249}$$

Substituting Eqs.(3.247) and (3.248) into Eq.(3.87), we obtain

$$\frac{\delta L_R}{L_R} \simeq \alpha_1\frac{\delta T}{T} + \left(\frac{\nabla - \nabla_{\mathrm{ad}}}{\nabla} - \frac{c_1\omega^2 - U}{\alpha_0}\right)\frac{H_p}{\nabla_{\mathrm{ad}}}\frac{d}{dr}\left(\frac{\delta T}{T}\right), \tag{3.250}$$

where

$$\alpha_1 = 4 - \frac{1}{\nabla_{\mathrm{ad}}} - \kappa_T - \frac{\kappa_\rho}{\Gamma_3 - 1} + \left(1 - \frac{S_l^2}{\Gamma_1\sigma^2}\right)\left(\frac{c_1\omega^2 - U}{\alpha_0\nabla_{\mathrm{ad}}}\right) \tag{3.251}$$

and $\kappa_T(\equiv (\partial \ln \kappa / \partial \ln T)_\rho)$ and $\kappa_\rho(\equiv (\partial \ln \kappa / \partial \ln \rho)_T)$ are the temperature and the density dependences of the opacity, which satisfy

$$\kappa_{\mathrm{ad}} = \left(\frac{\partial \ln \kappa}{\partial \ln p} \right)_S = \kappa_T \nabla_{\mathrm{ad}} + \frac{\kappa_\rho}{\Gamma_1}, \tag{3.252}$$

$$\kappa_S = c_p \left(\frac{\partial \ln \kappa}{\partial S} \right)_p = \kappa_T - v_T \kappa_\rho. \tag{3.253}$$

Substituting these equations and disregarding Φ', we obtain, after lengthy manipulations, an approximate expression for W_F:

$$
\begin{aligned}
4\sigma_R W_F \simeq & -\frac{1}{2} \left[\alpha_1 L_R \left(\frac{\delta T}{T} \right)^2 \right]_{r=R} - \frac{1}{2} \int_0^R dr \left(\frac{\delta T}{T} \right)^2 \frac{d}{dr}(\alpha_1 L_R) \\
& + \int_0^R dr L_R \frac{H_p}{\nabla_{\mathrm{ad}}} \left(\frac{\nabla - \nabla_{\mathrm{ad}}}{\nabla} - \frac{c_1 \omega^2 - U}{\alpha_0} \right) \left\{ \left[\frac{d}{dr} \left(\frac{\delta T}{T} \right) \right]^2 + \frac{l(l+1)}{r^2} \left(\frac{\delta T}{T} \right)^2 \right\} \\
& + l(l+1) \int_0^R dr \left(\frac{\delta T}{T} \right)^2 \frac{1}{\nabla_{\mathrm{ad}}} \left[\frac{4-V}{\alpha_0 V} \left(\frac{1}{c_1 \omega^2} \frac{dL_r}{dr} - \frac{L_R}{r} \right) \right. \\
& \left. + \frac{c_1 \omega^2 - U}{c_1 \omega^2 \alpha_0 V} \frac{dL_r}{dr} + \frac{1}{2} \frac{d}{dr} \left(\frac{c_1 \omega^2 L_R - dL_r/d\ln r}{c_1 \omega^2 \alpha_0 V} \right) \right]
\end{aligned} \tag{3.254}
$$

3.11.4 κ-mechanism

The κ-mechanism is the most common excitation mechanism for pulsating stars. It is associated with partial ionization zones. Pulsations of Cepheid, RR Lyrae and δ Scuti are excited at the 2nd He ionization zone, while ones of β Cephei, SPB at the iron group element ionization zone.

The first and the second terms in the RHS of Eq.(3.254) describe the "κ-mechanism", the excitation mechanism by the net positive flux blocking in the pulsation cycle due to the opacity perturbation in phase with the temperature perturbation. In the outer radiative envelope, L_R is constant and the κ-mechanism works if

$$\frac{d}{dr} \left(\kappa_T + \frac{\kappa_\rho}{\Gamma_3 - 1} \right) > 0. \tag{3.255}$$

An example profile of opacity and its derivatives is shown in the top panel of Fig.3.10. The opacity profile takes a form of a bump at an ionization zone. At $\log T \simeq 5.2$, ionizations of iron group elements make an opacity bump, which is called "Fe bump." An bump at $\log T \simeq 4.6 - 4.7$ is called "He bump", which is caused by the 2nd He ionization. At $\log T \simeq 4.1$, H and 1st He ionizations makes so-called "H bump."

The value of κ_T increases around an ionization zone (compare Fig.5.16 and top panel of Fig.5.17). This contributes to make a positive gradient of $\kappa_T + \kappa_\rho/(\Gamma_3 - 1)$ toward the outside. In an ionization zone, an adiabatic exponent $(\Gamma_3 - 1)(> 0)$ is minimum. This spatial variation
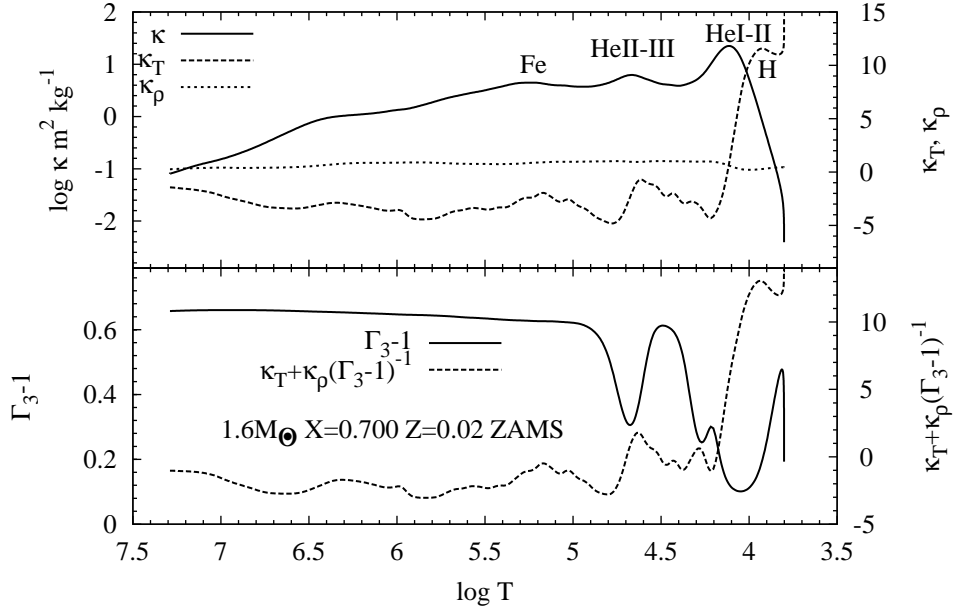
Figure 3.10: Top: Opacity κ and its temperature and density dependences, κ_T and κ_ρ. Bottom: Adiabatic exponent $\Gamma_3 - 1$ and $\kappa_T + \kappa_\rho(\Gamma_3 - 1)^{-1}$, whose spatial differential is the criterion for κ-mechanism (Eq.3.255). The equilibrium model is of a $1.6 M_\odot$ ZAMS star with $X = 0.70$, $Z = 0.02$

of $(\Gamma_3 - 1)$ enhances the effect of the κ-mechanism (bottom panel of Fig.3.10). This effect is sometimes called the "γ-mechanism" (Cox *et al.*, 1966).

As shown in the bottom panel, the value of $\kappa_T + \kappa_\rho/(\Gamma_3 - 1)$ increases outward around each opacity bump, which means the κ-mechanism can take place.

3.11.5 Convective blocking

The "convective blocking" is one of the excitation mechanisms which occurs at bases of convective envelopes. As a matter of fact, this mechanism is not related to convective luminosity perturbations, but to radiative luminosity perturbations. The cause of this mechanism is gradient of radiative luminosity. At a base of a convective envelope, radiative luminosity L_R decreases with increase of convective luminosity L_C as we go to the bulk of the convective envelope. That causes the decrease in $|\delta L_R|$ outward and hence realizes $d|\delta L_R|/dM_r < 0$, which will excite pulsations if $d\delta L_R/dM_r < 0$ is satisfied at the hot phase of the pulsations (Eq.3.204).

This mechanism plays a major role in excitation of γ Doradus pulsations, which is confirmed by analyses both with the frozen-in convection (FC) approximation, under which the perturbation of convective luminosity is neglected (Guzik *et al.*, 2000; Warner *et al.*, 2003),

and TDC (Dupret *et al.*, 2005). On the other hand, Dupret *et al.* (2005) showed the significant difference between results with FC and TDC in δ Scuti stars. In this case, the way of treatment of δL_C can change the behavior of δL_R, and hence the picture of the convective blocking.

3.12 Numerical procedures

In this study, eigenmodes of stellar pulsations are calculated by solving the differential equation systems introduced in §3.7 and 3.8, such as Eqs.(3.128)–(3.133), with the boundary conditions, for example, Eqs.(3.146)–(3.152) for nonadiabatic nonradial pulsations. The differential equations are solved as eigenvalue problems. This study uses the relaxation code developed by the author (Sonoi and Shibahashi, 2012b). The detail of the relaxation method is introduced in §D.

In the relaxation method, we have to give the initial eigenvalue and eigenfunctions, and to make them close to the solution through the iterative procedure. To avoid failing to find the desirable eigenvalues, we have to give the initial value close to the true eigenvalue. Since, moreover, the eigenvalue is complex number, we have to search for the initial value on the complex plane following Shibahashi and Osaki (1981) before truly solving the eigenvalue problem.

For such search, we remove one of the outer boundary conditions except one for the normalization Eq.(3.146). We express the removed condition as $\mathcal{D}(\tilde{\omega}) = 0$, where $\tilde{\omega}$ denotes the true eigenvalue. We solve the differential equations against a given ω. This procedure is a linear algebraic problem since the differential equations in §3.7 and 3.8 are linear. $\mathcal{D}(\omega)$ is used as the discriminant to find the true eigenvalue $\tilde{\omega}$ and assumed to have no singular point in the parameter area considered. Let us consider the mapping from the complex ω-plane to the complex $\mathcal{D}$-plane. A closed loop in the ω plane is mapped into one in the $\mathcal{D}$-plane. If the closed loop in the $\mathcal{D}$-plane winds n times around the origin, there exist n eigenvalues inside the loop of the ω-plane. Fig.3.11 illustrates such a mapping from the ω-plane to the D-plane. The large rectangle ABCD on the ω-plane is mapped to the closed curve A'B'C'D' on the $\mathcal{D}$-plane which winds around the origin once. By dividing the large rectangle into two by a straight line EF, we find that an eigenvalue exists inside the rectangle AEFD but not inside the rectangle EBCF.

This can be understood as follows: If $\mathcal{D}(\omega)$ is a regular function, and there are J eigenvalues $\tilde{\omega}_j$ ($j = 1, 2, \ldots, J$), the discriminant $\mathcal{D}(\omega)$ can be written as

$$\mathcal{D}(\omega) \propto \prod_{j=1}^{J} (\omega - \tilde{\omega}_j). \tag{3.256}$$

That is,

$$\arg[\mathcal{D}(\omega)] = \sum_{j=1}^{J} \arg(\omega - \tilde{\omega}_j) + \text{const.} \tag{3.257}$$
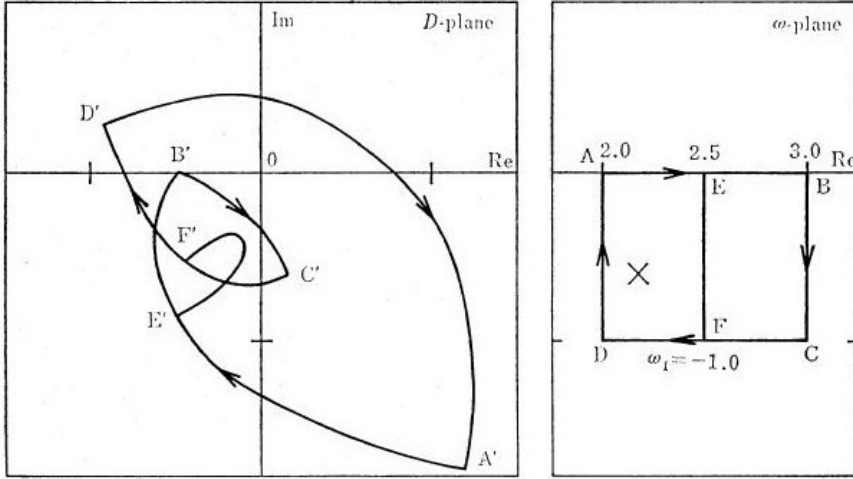
Figure 3.11: Mapping from the ω-plane to the $\mathcal{D}$-plane. The cross in the ω-plane indicates the true eigenfrequency $\tilde{\omega}$ for which $\mathcal{D}(\tilde{\omega}) = 0$ (from Shibahashi and Osaki, 1981)

When ω makes a closed loop C in the ω-plane, we obtain

$$\oint_C d[\arg(\omega - \tilde{\omega}_j)] = \begin{cases} 2\pi & \text{if } \tilde{\omega}_j \text{ is within the loop } C \\ 0 & \text{if } \tilde{\omega}_j \text{ is outside the loop } C \end{cases} \tag{3.258}$$

From Eq.(3.257), we have

$$\frac{1}{2\pi} \oint_C d[\arg(\mathcal{D})] = \text{the number of eigenvalues within the loop } C. \tag{3.259}$$

Thus, what we should do for the search for the eigenvalue is evaluating $\mathcal{D}(\omega)$'s by solving the above algebraic problem against the ω's which make a loop in the ω-plane and determine whether there exist the eigenvalues inside the loop by Eq.(3.259). If some eigenvalues exist there, we should solve the eigenvalue problem with all the boundary conditions by using the initial value of ω which is inside the loop. It should be noted that if the discriminant $\mathcal{D}(\omega)$ has singularities within the loop, it decreases the value of the integral in Eq.(3.259) by -2π.

Part II

Origin and pulsational instability of strange-modes

Stability analysis of radial pulsations

Some parts of this chapter are included in "Analysis of strange-mode instability with time-dependent convection in hot massive stars", in the proceedings, volume 301 of IAU symposium (Sonoi and Shibahashi, in press)

4.1 Introduction

This chapter shows results of pulsational stability analysis of radial pulsations in hot massive stars. In the analysis, eigenmodes of radial pulsations are calculated for different stellar models. Simultaneously, pulsational stability is also investigated by evaluating the growth or damping rate for each eigenmode. Growing eigenmodes are called "unstable modes", while damped ones "stable modes." Unstable modes are expected to be observed as pulsations. In particular, unstable strange-modes have extremely high growth rates and could be influential on stellar evolutions. Unstable strange-modes have been theoretically found in stars with $L/M \gtrsim 10^4 L_\odot/M_\odot$, for instance, hot massive stars (Gautschy, 1992; Glatzel and Kiriakidis, 1993b,a; Kiriakidis *et al.*, 1993; Glatzel and Mehren, 1996; Saio *et al.*, 1998; Saio, 2009, 2011; Saio *et al.*, 2013; Godart *et al.*, 2010, 2011), Wolf-Rayet stars (Glatzel *et al.*, 1993; Kiriakidis *et al.*, 1996), helium stars (Saio and Jeffery, 1988; Saio *et al.*, 1984; Gautschy and Glatzel, 1990; Gautschy, 1995; Saio, 1995), etc.

The evolution of massive stars cannot be described by a classical stellar evolution theory because of a lot of observed peculiar behaviors. Wolf-Rayet (WR) stars are located in the high temperature and luminosity side in the HR diagram. We cannot reproduce a stellar evolution toward such a domain in the HR diagram only by the classical theory. Since WR stars' spectra show a lot of wide emission lines, they are thought to be suffering from strong stellar winds. The mass of WR stars is in the range of 5 to a few tens of solar mass, and they are thought

to be objects into which O type stars evolves while losing substantial their mass. Humphreys and Davidson (1979) found that there is a lack in observed stars in the high luminosity and low temperature side in the HR diagram, and gave the boundary line so-called "Humphreys-Davidson (HD) limit" (the dashed line in Fig.4.1). Luminous blue variables (LBVs) appear near the limit. They irregularly show changes in their visual magnitude in a timescale of hours to hundreds years. During the changes, on the other hand, the luminosity keeps constant. That is, they horizontally move toward the lower effective temperature side in the HR diagram. It might mean that sporadic mass eruptions make a thick envelope around the core, and that a pseudo-photosphere is formed in the envelope. That could explain the apparent decrease in the effective temperature. Stars with $\gtrsim 25 M_\odot$ are expected to be finally WR stars. Ones with $25 - 50 M_\odot$ may first evolve from ZAMS toward the red giant phase. But they would go back to the bluer side of the HR diagram due to stellar winds, and be finally WR stars. On the other hand, ones with $\gtrsim 50 M_\odot$ are not expected to evolve toward the red giant stage because of the existence of the HD limit. Instead, they would experience the LBV phenomenon around the HD limit, lose substantial mass and be WR stars.

However, we have not yet obtained an established mechanism for the sporadic eruptions occurring in LBVs, although many authors have proposed different explanations by effects of radiation pressure in the situation near the Eddington limit, close-binary models, rapid rotations, etc (see Humphreys and Davidson, 1994). The strange-mode instability is also one of the candidates for the mechanism. Glatzel and Kiriakidis (1993a) proposed that the strange-mode becomes unstable around the HD limit.

So far the pulsational stability analyses of the strange-modes have been carried out with the frozen-in convection (FC) approximation, in which perturbation of convective flux is neglected. As a matter of fact, convection does not significantly contribute to energy transfer in envelopes of hot massive stars compared with those of stars in the redder side of the classical instability strip. Besides, theories of convection have still a lot of uncertainties. But most of unstable strange-modes are actually excited in convection zones, and we cannot definitely conclude that convection never affects stability of strange-modes. In particular, Glatzel and Mehren (1996) carried out the stability analysis with the two types of FC approximations, and showed that the extent of the instability sensitively depends on the types of FC. This implies that the instability of strange-modes could be affected by convection.

Recently, Grigahcène et al. (2005) and Dupret et al. (2005) adopted the time-dependent convection (TDC) theory to the pulsational stability analyses of δ Scuti stars, and successfully explained the suppression of the instability in the redder side of the instability strip. The TDC theory adopted by them is originally derived by Unno (1967) for radial pulsations, arranged to deal with nonradial pulsations by Gabriel et al. (1974), and further developed by Gabriel (1987, 1996, 1998, 2000). Here, this TDC theory is adopted to evaluate perturbation of convective luminosity, and substitute it to the differential equation system for nonadiabatic radial pulsations, Eqs.(3.162)–(3.165). Before the result with TDC is shown, however, we discuss the result with FC for comparison. The stability analyses are first carried out with the two types of the FC approximations adopted by Glatzel and Mehren (1996), under which zero Lagrangian and Eulerian perturbations, $\delta L_C = 0$ and $L'_C = 0$, are assumed.
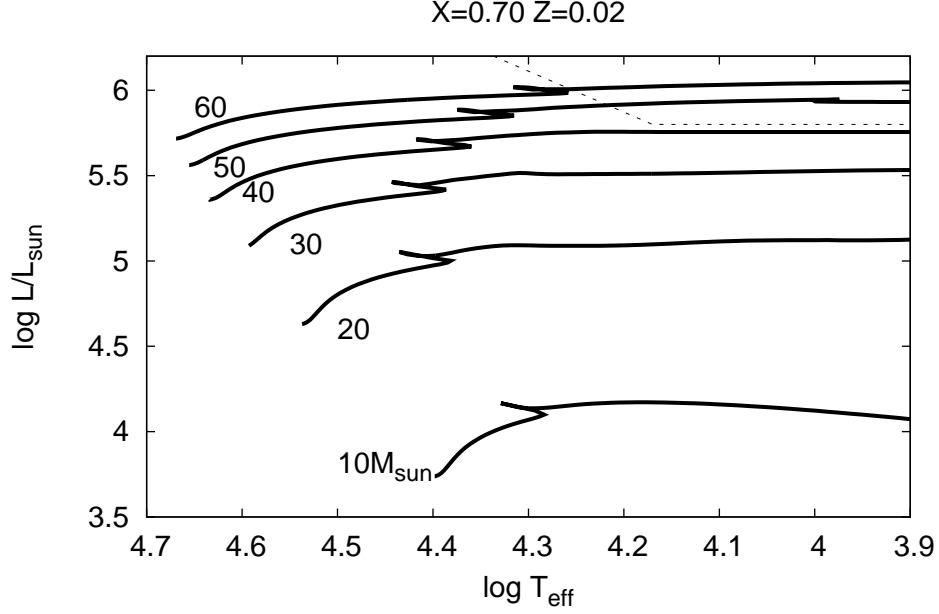
Figure 4.1: Evolutionary tracks of stars with $X = 0.70$, $Z = 0.02$ for which pulsational stability analysis is carried out. The dashed line is the Humphreys-Davidson limit.

4.2 Results with the FC approximation of $\delta L_C = 0$

4.2.1 Change of pulsational characteristics with stellar mass

Here, we discuss results of a pulsational stability analysis for radial modes in hot massive stars with $X = 0.70$, $Z = 0.02$. Fig.4.1 shows evolutionary tracks of the massive stars in the HR diagram. The evolutionary models are constructed with MESA (Paxton *et al.*, 2011). The mixing length parameter is set to $\alpha = 2$. Many of studies about massive stars take into account radiation-driven mass loss during the evolution. But the instability of strange-modes could be another trigger for mass loss in the massive stars, as proposed by studies of nonlinear pulsations (Dorfi and Gautschy, 2000; Chernigovski *et al.*, 2004; Grott *et al.*, 2005). In this study, therefore, the radiation-driven mass loss is neglected to avoid confusing the two triggers. The pulsational stability analysis is carried out with the relaxation code developed by Sonoi and Shibahashi (2012b) in the range of $\log T_{\mathrm{eff}} > 3.9$.

Fig.4.2 show modal diagrams, of which the vertical axis is the pulsational frequency (normalized with the dynamical timescale $\sqrt{R^3/(GM)}$) and the abscissa is some stellar parameter, which is here the effective temperature. Here they show results of nonadiabatic analyses with the frozen-in convection (FC) approximation of $\delta L_C = 0$ for radial pulsations ($l = 0$). This approximation has been so far commonly adopted in the nonadiabatic analyses by previous studies. We may use the differential equations for the eigenfunction, Eqs.(3.162)–(3.165) for

77
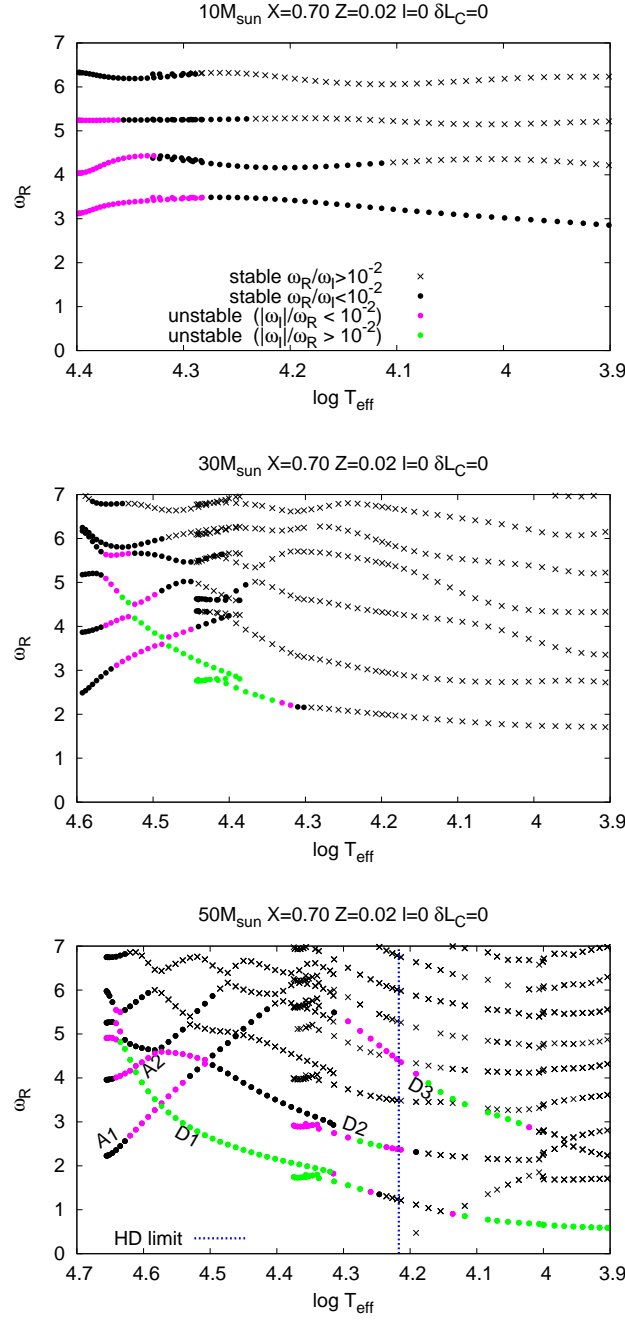
Figure 4.2: Modal diagrams for 10, 30 and $50 M_\odot$ with $X = 0.70$, $Z = 0.02$. The abscissa is the effective temperature (the left part of the figures corresponds to the main sequence, while the right part to the red giant phase), while the vertical axis is the frequency multiplied by the dynamical timescale $\sqrt{R^3/(GM)}$. Each symbol indicates eigenfrequency. The black crosses and dots are stable modes with high and low damping rates, respectively. The magenta and the green dots are unstable modes with low and high growth rates, respectively. The nonadiabatic analysis is carried out with the frozen-in convection (FC) approximation of $\delta L_C = 0$.

the approximation, but remove the last term in Eq.(3.164). Then, the equations become

$$\frac{dY_1}{d\ln r} = -3Y_1 - \frac{1}{\chi_\rho}Y_2 + v_T Y_3, \tag{4.1}$$

$$\frac{1}{V}\frac{dY_2}{d\ln r} = (c_1\omega^2 + 4)Y_1 + Y_2, \tag{4.2}$$

$$\frac{1}{V\nabla}\frac{dY_3}{d\ln r} = 4Y_1 + (\nabla_{\mathrm{ad}}\kappa_S - \kappa_{\mathrm{ad}})Y_2 + (4 - \kappa_S)Y_3, \tag{4.3}$$

$$\frac{1}{f_R}\frac{dY_4}{d\ln r} = [c_3(\varepsilon_{\mathrm{ad}} - \nabla_{\mathrm{ad}}\varepsilon_S) + i\omega c_4\nabla_{\mathrm{ad}}]Y_2 + [c_3\varepsilon_S - i\omega c_4]Y_3 - c_3 Y_4. \tag{4.4}$$

The symbols in Fig.4.2 denote eigenfrequencies at each evolutionary stage corresponding to the effective temperature in the abscissa. The nonadiabatic solutions are plotted while being categorized in terms of the growth rates by use of different types of symbols.

As we can see, the plots compose sequences. The top panel of Fig.4.2 is for $10M_\odot$. The lowest sequence corresponds to the fundamental mode, the second lowest one to the 1st overtone, the third one to the 2nd overtone, ..., etc. The frequencies are almost constant with change in the effective temperature.

As the stellar mass increases, the sequences become waving, which is shown in the middle and the bottom panels of Fig.4.2. Then, there become ascending and descending sequences. In fact, the former and the latter correspond to ordinary modes and strange-modes, respectively. We can see that strong instability, which is expressed as green dots, appears on the descending sequences. In case of $30M_\odot$, the strong instability appears only in the high effective temperature side. In case of $50M_\odot$, however, it appears also in the low temperature side. As a matter of fact, those instabilities in the high and in the low temperature sides are caused by different excitation mechanisms. This issue is discussed in the following section. We can see that two sequences are close to each other at some points for $\gtrsim 30M_\odot$. This phenomenon is called "avoided crossing." In that situation, they never cross each other, but characteristics of pulsational stability move from one to another sequence (Fig.4.3).

4.2.2 Pulsational instability

As mentioned above, pulsational instability appears only in the higher temperature side for $\lesssim 30M_\odot$. It is excited by the classical κ-mechanism, which is one of heat engine mechanisms for excitation of stellar pulsations and works around an opacity bump where absorption of photons is strong due to ionizations. In this case, the κ-mechanism works at the opacity bump of Fe group elements.

Fig.4.4 shows the work integral of the radial fundamental mode for a model in the main sequence stage of a $10M_\odot$ star with $X = 0.70$, $Z = 0.02$. Work integral W is a function of r, and means integrated local work from the center to the radius r. Excitation of pulsations takes place at a location where work integral increases outward. In Fig.4.4, increase in the work integral, that is, excitation appears around $\log T = 5.2 - 5.3$, where the Fe opacity bump is located (notice the green line of this figure).
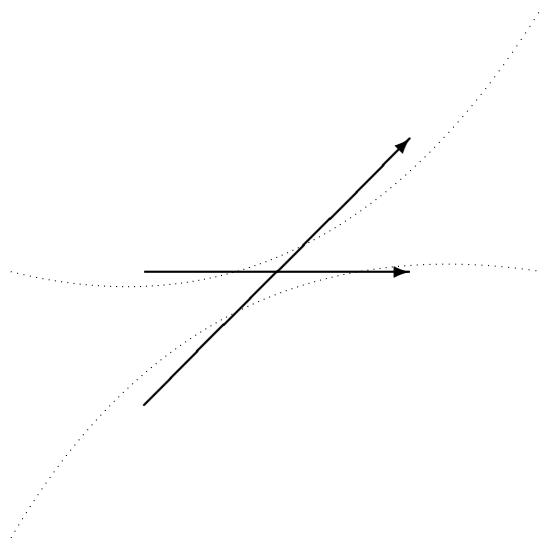
Figure 4.3: Avoided crossing. Two sequences of eigenfrequencies are close to each other, but never crossover (dotted curves). On the other hand, characteristics of pulsational stability move from one to another sequence (solid arrows).

Roughly speaking, the κ-mechanism works in a region satisfying Eq.(3.255), $d[\kappa_T+\kappa_\rho(\Gamma_3-1)^{-1}]/dr > 0$ or

$$\frac{d}{d\log T}\left[\kappa_T + \frac{\kappa_\rho}{\Gamma_3 - 1}\right] < 0. \tag{4.5}$$

In Fig.4.4, we can find that this condition is satisfied in the excitation zone (notice the blue line). By the way, heat engine mechanism works efficiently in case that the thermal timescale is comparable with the pulsational period. If the thermal timescale is much shorter or longer than the period, heat engine mechanism hardly works. The case of long thermal timescale corresponds to adiabatic situation, and heat transfer hardly proceeds in a pulsational cycle. On the other hand, the case of short thermal timescale corresponds to isothermal situation, and heat transfer occurs instantaneously, and it avoids making change of temperature. The black thick horizontal line segment in Fig.4.4 indicates the pulsational period of the fundamental mode, and the cross point of the line segment and the black curve indicates the location where the thermal timescale is identical to the period. We can find that the location matches with the Fe bump. On the other hand, there are other regions with $d[\kappa_T + \kappa_\rho(\Gamma_3 - 1)^{-1}]/d\log T < 0$, but the κ-mechanism does not work in the regions. This is because the thermal timescale does not match with the pulsational period.

As the stellar mass increases, other kinds of instability come to appear on the descending sequences in the modal diagram, which we can see in the panels for 30 and $50M_\odot$ of Fig.4.2. The instability on the ascending sequences has the same characteristics as in cases of lower mass stars, while that on the descending sequences has different characteristics. One of the characteristics is that the growth rates of the unstable modes are much higher than that on
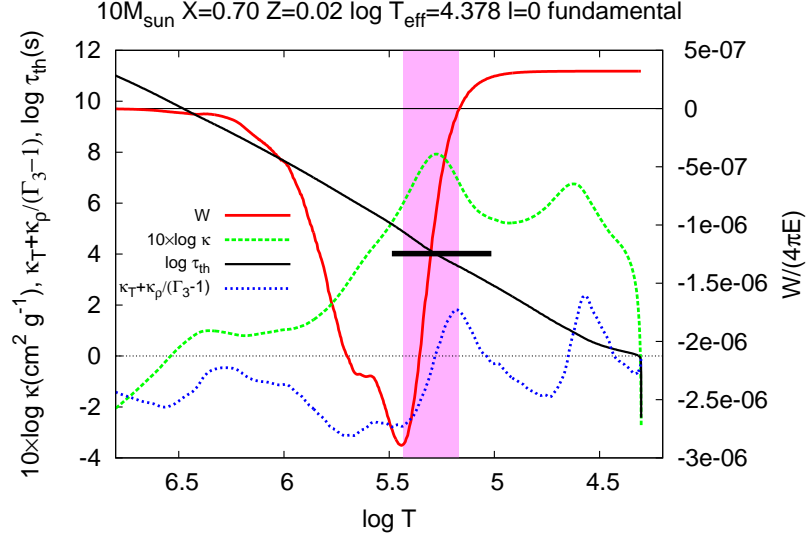
Figure 4.4: Work integral for the radial fundamental mode (*red*), opacity (*green*), the quantity related to the condition for κ-mechanism, $\kappa_T + \kappa_\rho/(\Gamma_3 - 1)$ (*blue*), and thermal timescale (*black*) for a model in the main sequence stage of a $10 M_\odot$ star with $X = 0.70$, $Z = 0.02$. The thick black horizontal line segment indicates the period of the fundamental mode. The magenta colored region denotes the Fe bump excitation zone satisfying the condition for the κ-mechanism, $d[\kappa_T + \kappa_\rho/(\Gamma_3 - 1)]/d\log T < 0$.
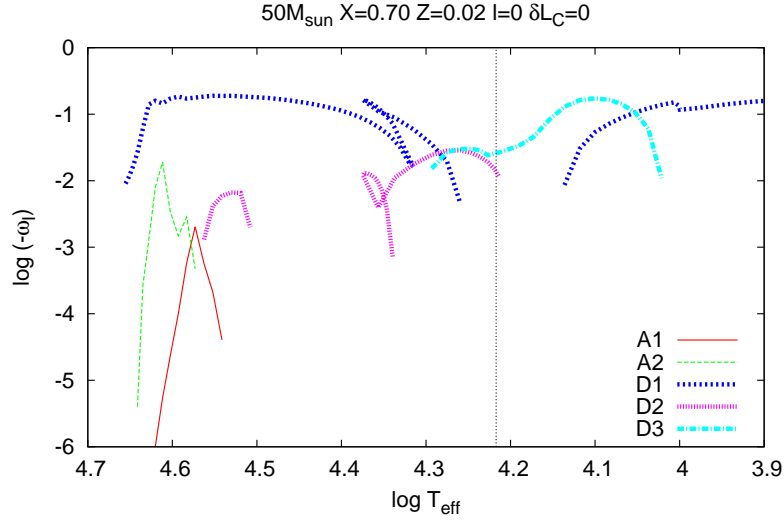
Figure 4.5: Growth rates of unstable modes for $50 M_\odot$ appearing in Fig.4.2. The value is normalized by multiplying by the dynamical timescale $\sqrt{R^3/(GM)}$. The vertical black dashed line corresponds to the evolutionary stage crossing the HD limit in the HR diagram.

81
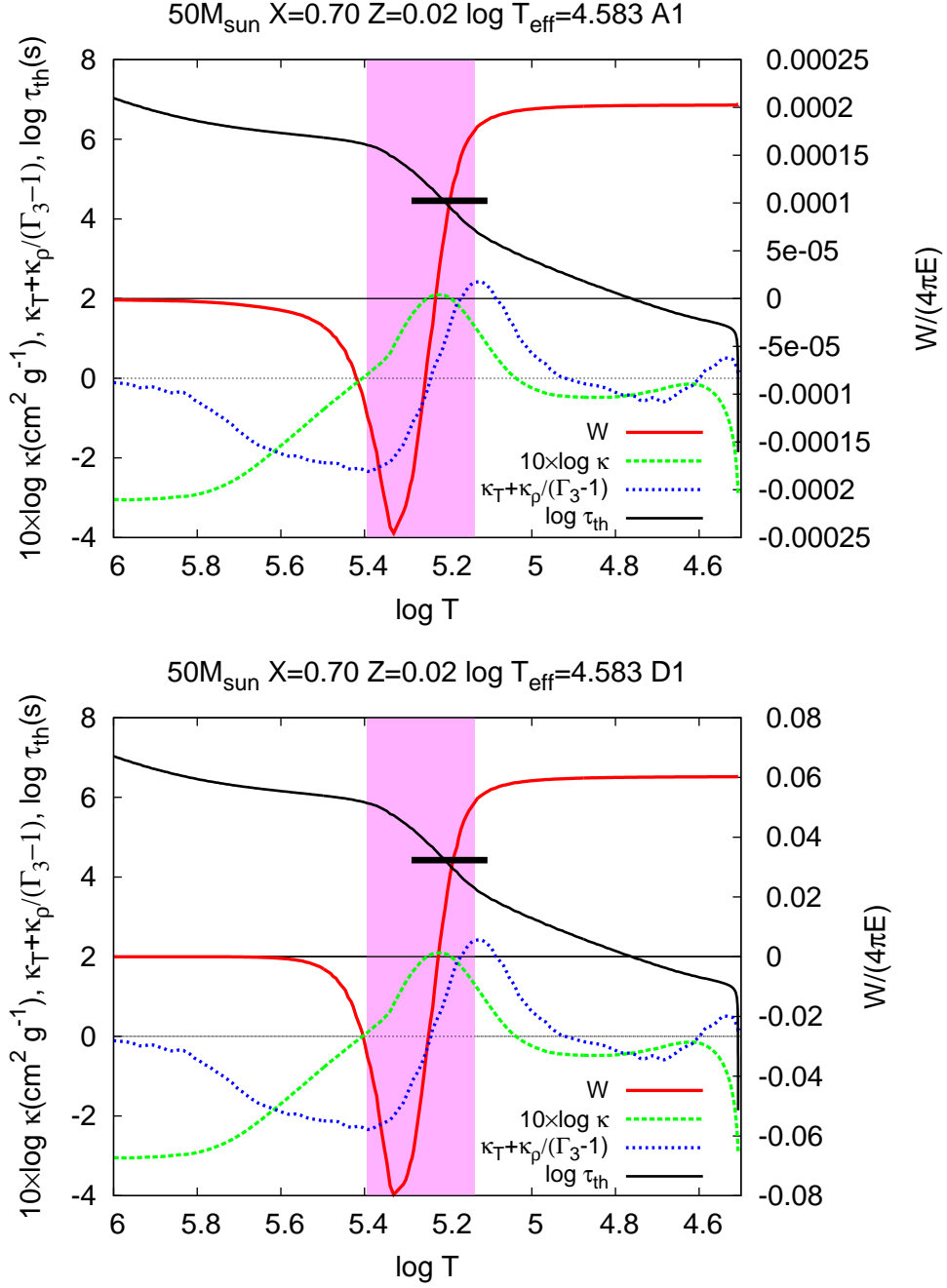
Figure 4.6: Same as Fig.4.4, but for a model in the main sequence stage of a $50M_\odot$ star. The top panel is for the ordinary mode on the ascending sequence A1, while the bottom panel for the strange-mode on the descending sequence D1 shown in Fig.4.2.
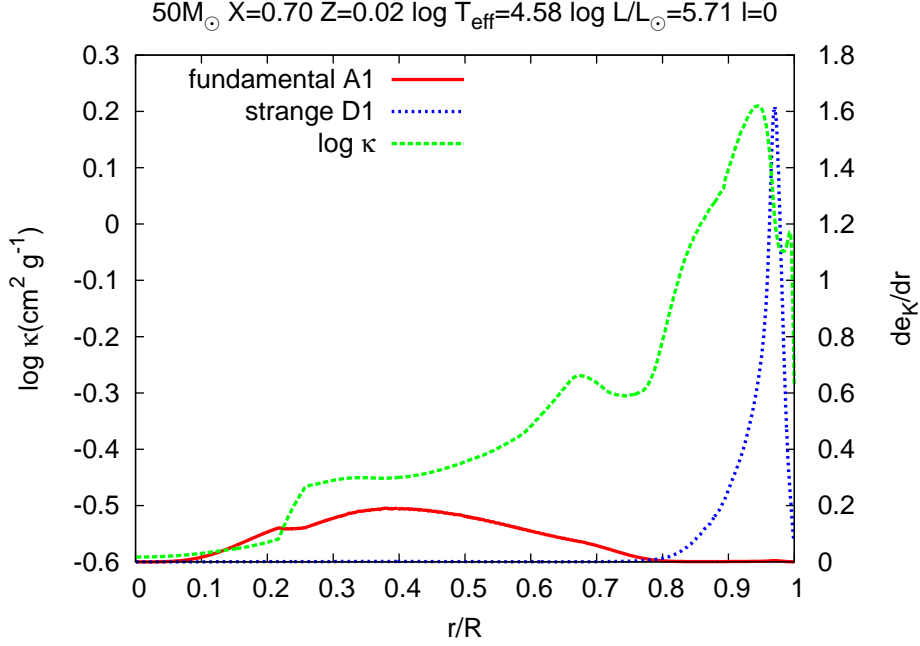
Figure 4.7: Distribution of kinetic energy density de_K/dr for the fundamental mode (A1) and the strange-mode on the descending sequence D1. The values are normalized as $\int_0^R de_K/dr \, dr/R = 1$.

the ascending sequences. We can confirm it in Fig.4.5. In the figure, there are two types of labels, A$*$ and D$*$, which indicate the ascending and the descending sequences, respectively, in the panel for $50M_\odot$ of Fig.4.2.

The top panel of Fig.4.6 shows that the fundamental mode, which is on the ascending sequence A1, is excited at the Fe bump, where $d[\kappa_T + \kappa_\rho(\Gamma_3 - 1)^{-1}]/d\log T < 0$ is satisfied. On the other hand, the bottom panel of Fig.4.6 shows the work integral for the strange-mode on the descending sequence D1. The bottom panel apparently looks identical with the top panel. But the value of $W/(4\pi E)$ and hence the growth rate of amplitude are much higher than those of the fundamental mode. Fig.4.7 shows the distribution of kinetic energy density for the two modes. We can recognize that while the kinetic energy of the fundamental mode distributes evenly in the whole star, that of the strange-mode is confined to the narrow range near the surface. The strange-mode is excited by the κ-mechanism similarly to the fundamental mode, but the excitation is much stronger because of the confinement of the amplitude to the excitation zone. The cause for the confinement of the amplitude will be discussed in §5.2.

In case of $50M_\odot$, by the way, instability of strange-modes appears also in the low temperature side. The excitation mechanism for this instability is different from the κ-mechanism. Fig.4.8 is for the unstable strange-mode on the descending sequence D2 in the panel for $50M_\odot$ of Fig.4.2, and shows that excitation occurs not only in the region with $d[\kappa_T + \kappa_\rho(\Gamma_3 - 1)^{-1}]/d\log T < 0$ around the Fe bump, but also in the outer region, having $d[\kappa_T + \kappa_\rho(\Gamma_3 - $
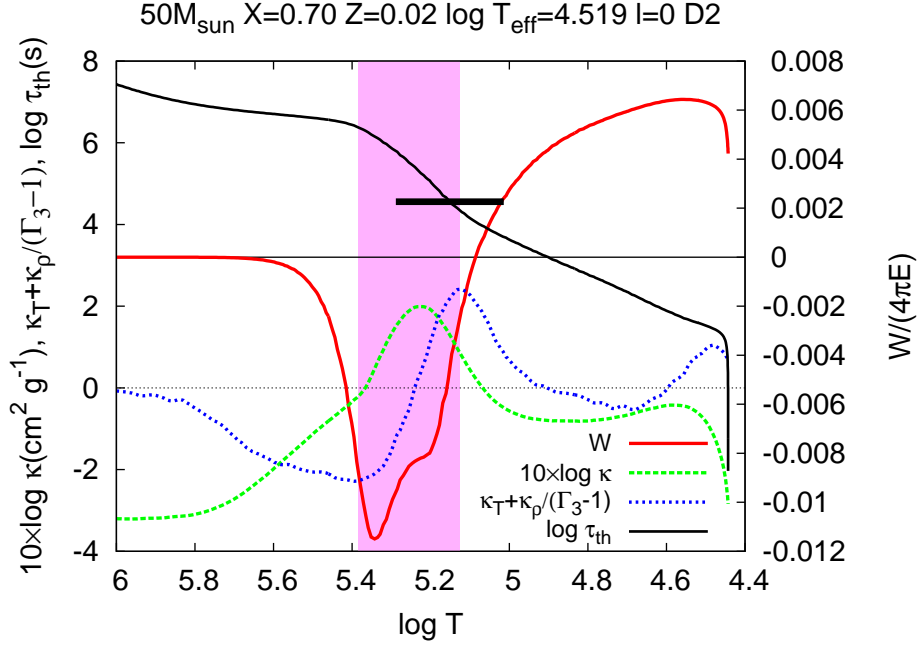
Figure 4.8: Same as Fig.4.6, but for the strange-mode on the descending sequence D2 shown in the panel for $50M_\odot$ of Fig.4.2.

$1)^{-1}]/d \log T > 0$. This implies that the excitation mechanism would be different from the κ-mechanism. The excitation mechanism for this type of instability has been a long-standing problem. Glatzel (1994) and Saio *et al.* (1998) tried to obtain the physical picture by local analyses with the WKB approximation and the two zone model, respectively. According to the two studies, if we assume short thermal timescale and dominance of radiation pressure, a large phase lag between perturbations to pressure and density would take place in pulsations. This then leads to the strong instability. More details are discussed in §5.4.

The extent of the instability for $50M_\odot$ by this study is slightly stronger than the result for $60M_\odot$ by Kiriakidis *et al.* (1993) and Glatzel and Mehren (1996). They adopted evolutionary models with radiation-driven mass loss. Due to the mass loss, increase in the central temperature is suppressed, and the stellar luminosity increases less rapidly during the evolution. The lower luminosity may have resulted in the weaker instability.

4.3   Results with the FC approximation of $L_C' = 0$

The results shown in the previous sections are obtained with the FC approximation of $\delta L_C = 0$. But we do not have convincing reasons for the approximation, which has left uncertainty in results of pulsational stability analyses for many years. We actually have plural ways to neglect effects of convection. Here, we will see results with the approximation of $L_C' = 0$. In this

case, the differential equations for the eigenfunctions become

$$\frac{dY_1}{d\ln r} = -3Y_1 - \frac{1}{\chi_\rho}Y_2 + v_T Y_3, \tag{4.6}$$

$$\frac{1}{V}\frac{dY_2}{d\ln r} = (c_1\omega^2 + 4)Y_1 + Y_2, \tag{4.7}$$

$$\frac{1}{V\nabla}\frac{dY_3}{d\ln r} = \left[4 + c_3 - \frac{d\ln L_R}{d\ln r}\right]Y_1 + (\nabla_{\mathrm{ad}}\kappa_S - \kappa_{\mathrm{ad}})Y_2 + (4 - \kappa_S)Y_3, \tag{4.8}$$

$$\frac{1}{f_R}\frac{dY_4}{d\ln r} = [c_3(\varepsilon_{\mathrm{ad}} - \nabla_{\mathrm{ad}}\varepsilon_S) + i\omega c_4\nabla_{\mathrm{ad}}]Y_2 + [c_3\varepsilon_S - i\omega c_4]Y_3 - c_3 Y_4. \tag{4.9}$$

Fig.4.9 shows modal diagrams for the approximation of $L'_C = 0$. The definitions of symbols and lines are the same as Fig.4.2. First, we can find that the ordinary modes, which appears in the lower mass stars ($\simeq 10M_\odot$) and on the ascending sequences in the higher mass stars ($\gtrsim 30M_\odot$), are stable or less unstable compared with the case of $\delta L_C = 0$. This implies that additional effects caused by the change from $\delta L_C = 0$ to $L'_C = 0$ stabilize the modes. The instability of strange-modes on the D1 and D2 sequences are also weakened or suppressed. But the range and the strength of the instability on the sequence D3 are comparable to in the case of $\delta L_C = 0$. These tendencies are also found by Glatzel and Mehren (1996). For $50M_\odot$, a new sequence labeled as "L" appears at the lower frequency than that of the sequence D1, and has strong instability.

Then, let us discuss why the instability is weaker in whole that in the $\delta L_C = 0$ case. Fig.4.10 shows work integrals of the fundamental mode in the FC approximations of $\delta L_C = 0$ (*top panel*) and of $L'_C = 0$ (*bottom panel*). Particularly, the work integral W are decomposed into W_{L_R} and W_{L_C} as

$$W(M_r) = \frac{\pi}{\sigma_R}\int_0^{M_r}\frac{\delta T^*}{T}\left(-\frac{d\delta L_r}{dM_r}\right)dM_r \tag{4.10}$$

$$= \frac{\pi}{\sigma_R}\int_0^{M_r}\frac{\delta T^*}{T}\left(-\frac{d\delta L_R}{dM_r}\right)dM_r + \frac{\pi}{\sigma_R}\int_0^{M_r}\frac{\delta T^*}{T}\left(-\frac{d\delta L_C}{dM_r}\right)dM_r \tag{4.11}$$

$$= W_{L_R}(M_r) + W_{L_C}(M_r). \tag{4.12}$$

In the case of $\delta L_C = 0$, no work is done in association with convective luminosity perturbation, and the total work integral W is identical to that by the radiative luminosity perturbation W_{L_R}. In the convection zone, the fundamental mode is excited by the κ-mechanism related to the Fe-bump. In the case of $L'_C = 0$, on the other hand, the Lagrangian perturbation of the convective luminosity δL_C is not zero, since we have

$$L'_C = \delta L_C - \xi_r\frac{dL_C}{dr} = 0. \tag{4.13}$$

Then, the work by the convective luminosity perturbation takes place. In this case, the δL_C has the nonzero value in regions with gradient of convective luminosity. The work integrals of the radiative and the convective luminosity perturbations roughly cancel each other out.
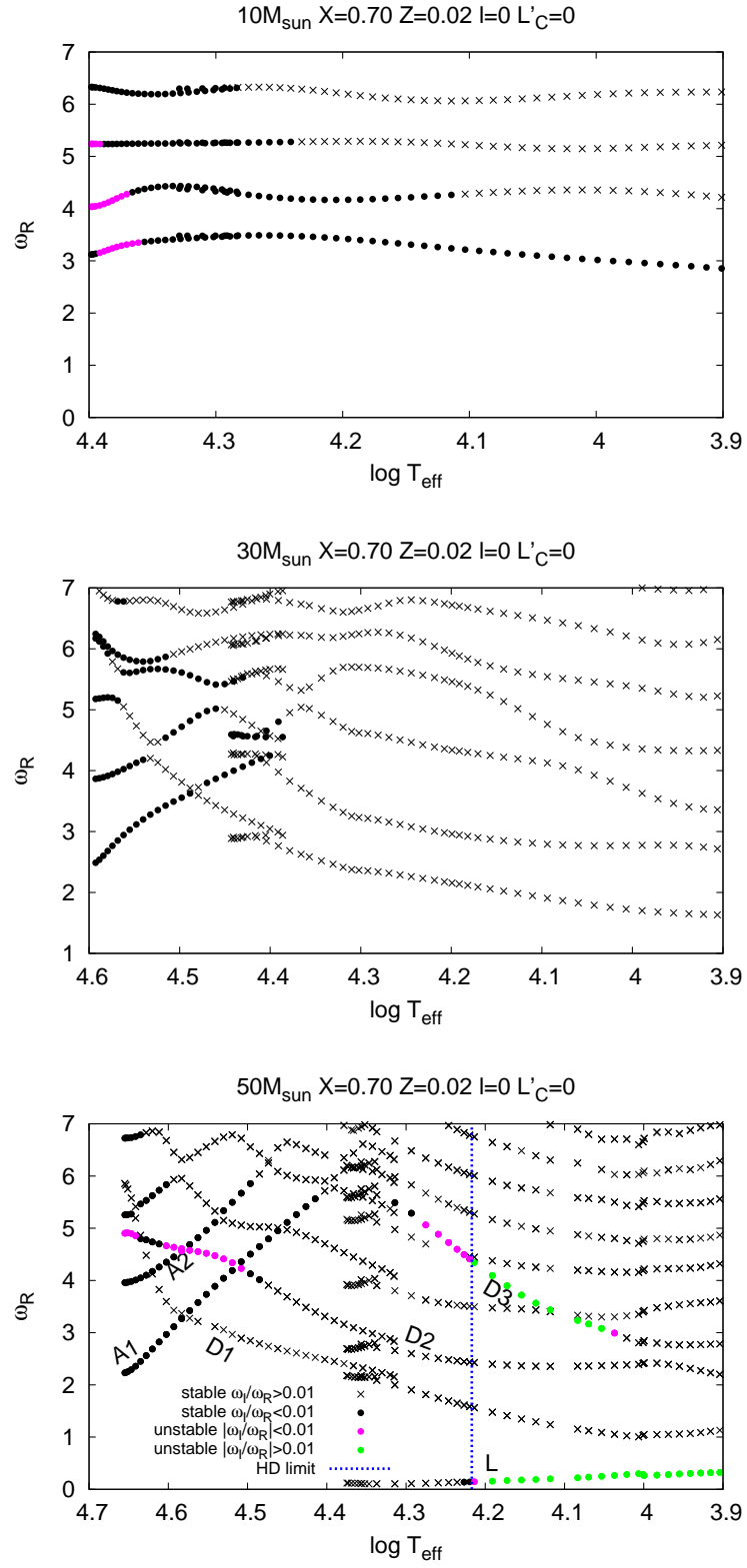
Figure 4.9: Same as Fig.4.2, but for $L'_C = 0$.
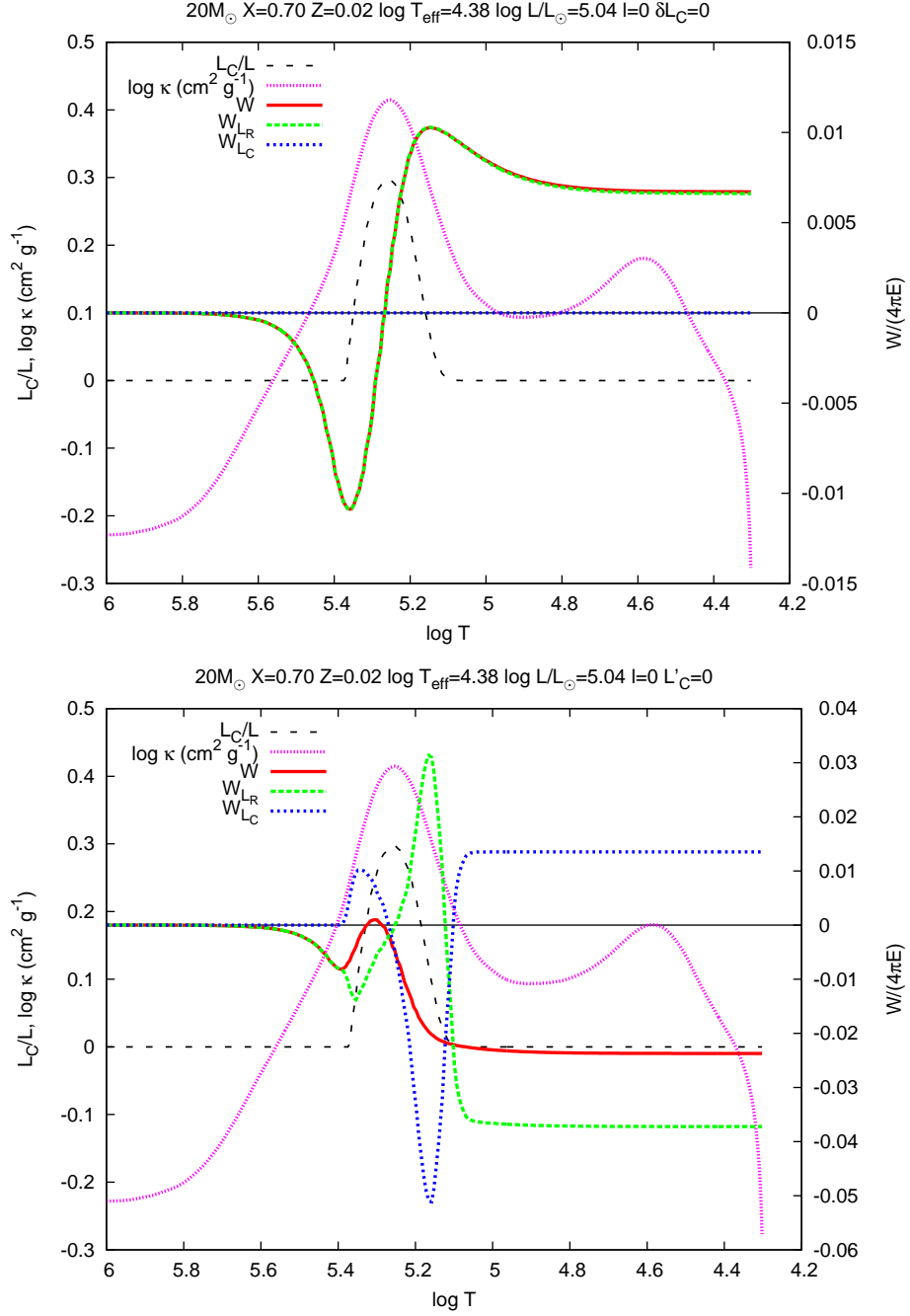
Figure 4.10: Work integrals for the fundamental mode in the FC approximations of $\delta L_C = 0$ (*top panel*) and of $L'_C = 0$ (*bottom panel*). The red line is the total work integral, while the green and the blue lines work integrals related to the radiative and the convective luminosity perturbations, respectively. The black and the magenta lines are the ratio of convective luminosity to the local total luminosity, and the opacity, respectively. The equilibrium model is for the main-sequence stage of $20M_\odot$.
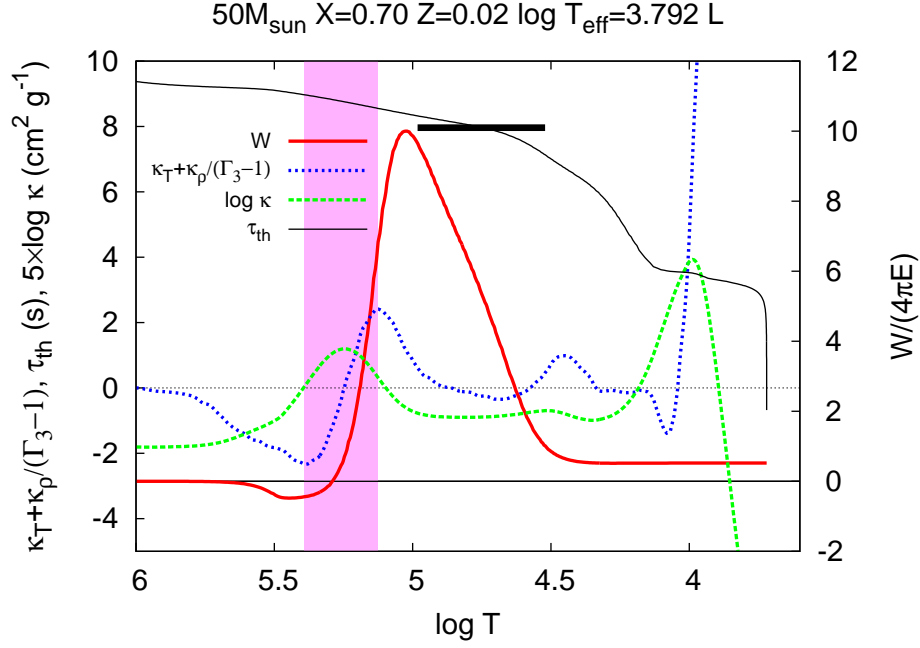
Figure 4.11: Work integral for the mode on the sequence L (*red line*). The green line is $\kappa_T + \kappa_\rho/(\Gamma_3 - 1)$, the blue line is the opacity and the black thin line is the thermal timescale. The black thick line segment indicates the period of the mode.

This implies that when a layer moves along the conflicting gradients of the radiative and the convective luminosities[1] in a pulsation cycle, its radiative luminosity L_R increases (decreases) while its convective luminosity L_R decreases (increases). In fact, the two types of work by the radiative and convective luminosity perturbations, W_{L_R} and W_{L_C}, do not exactly balance each other. That is, one of them slightly dominates over another, and the difference between the two becomes the total work W. In this case, W_{L_C} dominates over W_{L_R} in the whole of the convection zone. W_{L_C} and hence W are positive in the lower part of the convective zone while negative in the upper part. The negative work dominates and leads to the stability of the fundamental mode.

In most cases, the approximation with $L'_C = 0$ show less unstable results than that with $\delta L_C = 0$. But the instability corresponding to D3 does not depend on the types of the approximations. This is because the unstable mode of D3 is excited in a convection zone in which the convective luminosity is negligible to the total luminosity. More details will be discussed in §4.4.

In the bottom panel of Fig.4.9, we can find an additional sequence L, which is never present in the case of $\delta L_C = 0$. Fig.4.11 shows the work integral for a mode on the sequence L. The excitation takes place around the Fe bump. But it works not only in the zone with $d[\kappa_T + \kappa_\rho/(\Gamma_3-1)]/d\log T < 0$, but also in the outer side zone with $d[\kappa_T + \kappa_\rho/(\Gamma_3-1)]/d\log T > 0$.

---

[1] For example, at the bottom of the convection zone, the convective luminosity increases outward and has the positive gradient along r, while the radiative luminosity decreases and has the negative gradient.

We can also see that the location where the thermal timescale is identical to the pulsational period fails to match with the excitation zone. This implies that the excitation may not be classical the κ-mechanism.

4.4   Results with TDC and comparison with FC cases

Next, we discuss the result with TDC. To solve the eigenmodes, the system of differential equations, Eqs.(3.162)–(3.165) is adopted. As a matter of fact, we cannot obtain physically valid results if we directly adopt the TDC theory introduced in §3.6. Although different authors have proposed different TDC theories, the closure problem in the turbulence theories still remains now. That leads to non-physical spatial oscillations of the thermal eigenfunctions with a wavelength much shorter than the mixing length, which is in contradiction with the basic assumptions of the MLT (Baker and Gough, 1979; Gonczi and Osaki, 1980). In this study, the code has been independently developed, and tested in a $1.8 M_\odot$ model near the red edge of the classical instability strip, corresponding to a δ Scuti star. The red curve of Fig.4.12 shows the fictional spatial oscillation in the lower part of the convective envelope.

Let us consider the cause for the phenomenon following Grigahcène *et al.* (2005). First, we describe the linearized equation of energy conservation for radial pulsations in case where most of the energy is transported by convection,

$$i\sigma T \delta S = -\frac{d\delta L_C}{dM_r} \tag{4.14}$$

Isolating the term $d\delta S/dS$ in Eq.(3.112) and considering the case of $\sigma\tau_C \gg 1 \gg \omega_R\tau_C$, we can have

$$\frac{\delta L_C}{L_C} \simeq \left(\frac{\delta L_C}{L_C}\right)_1 + \frac{1}{i\sigma\tau_C}\frac{d\delta S/dr}{dS/dr}. \tag{4.15}$$

Combining Eqs.(4.14), (4.15) and the equilibrium relations of the MLT, we find, after some algebra,

$$\frac{\tau_C}{T}\left[\frac{(\delta L_C)_1}{dM_r} + \frac{2i\pi}{\sigma}\frac{d(\rho r^2 T\overline{(\Delta u_r)^2})}{dM_r}\frac{d\delta S}{dr}\right] - \frac{1}{2}\frac{\Lambda^2}{i\sigma\tau_C}\frac{d^2\delta S}{dr^2} + i\sigma\tau_C\delta S = 0 \tag{4.16}$$

This is the equation of an oscillator whose solutions have a wavelength of $\sqrt{2}\pi\Lambda/(\sigma\tau_C)$. When we deal with convection, we inevitably encounter the closure problem. In the TDC theory this study adopts, we neglect some complex physical phenomena such as turbulent cascade. The simplifications should lead to non-physical results like the spatial oscillations.

Then, Grigahcène *et al.* (2005) proposed a countermeasure against the spatial oscillations. When these oscillations take place, we have $\sigma\tau_C \gg 1$, and the radial derivatives of $\delta\overline{S}$ and $\delta\Delta S$ are in the order of $(\sigma\tau_C/\Lambda)\delta\overline{S}$ and $(\sigma\tau_C/\Lambda)\delta\Delta S$ respectively. In the derivation of the TDC theory in §3.6, by the way, we have adopted the mathematically natural relation,

$$\delta\left(\frac{\Delta S}{\tau_C}\right) = \frac{\Delta S}{\tau_C}\left(\frac{\delta\Delta S}{\Delta S} - \frac{\delta\tau_C}{\tau_C}\right) \tag{4.17}$$
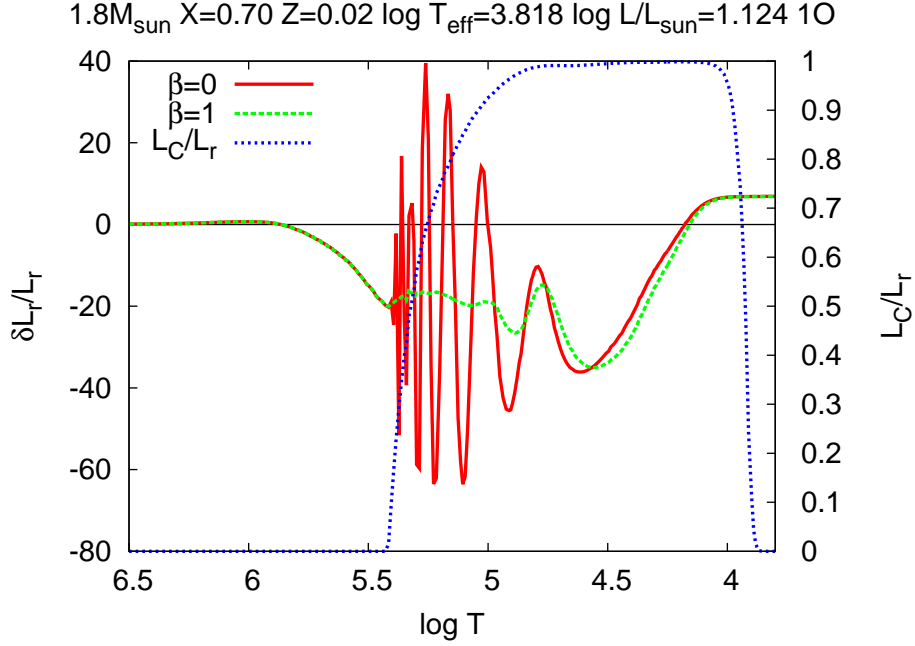
Figure 4.12: Eigenfunction of $\delta L_r/L_r$ for the radial 1O mode in a $1.8M_\odot$ star near the red edge of the classical instability strip. The abscissa is the temperature in the stellar structure. The lower temperature (right) side corresponds to the way to the stellar surface. The figure shows examples for the parameter in the TDC theory $\beta = 0$ and 1. The value of $\delta L_r/L_r$ is given by the normalization of $\xi_r/r = 1$ at the stellar surface.

from Eq.(3.94) to Eq.(3.96). But if we take Eq.(4.17) in case of $\sigma\tau_C \gg 1$, we see that the order of magnitude of the perturbation of the RHS of Eq.(3.27) would be $\sigma\tau_C$ times larger than the LHS. To have the same order in both sides, the perturbation of the LHS should rather be given by

$$\delta\left(\frac{\Delta S}{\tau_C}\right) = \beta\sigma\delta\Delta S - \Delta S\frac{\delta\tau_C}{\tau_C^2} \tag{4.18}$$

where β is a coefficient of the order of unity. In order to get a formula that switch continuously from Eq.(4.17) to (4.18), an expression

$$\delta\left(\frac{\Delta S}{\tau_C}\right) = \frac{\Delta S}{\tau_C}\left[(1 + \beta\sigma\tau_C)\frac{\delta\Delta S}{\Delta S} - \frac{\delta\tau_C}{\tau_C}\right] \tag{4.19}$$

is proposed and adopted. When we adopt this expression, the coefficient $D = (i\sigma\tau_C + \omega_R\tau_C + 1)^{-1}$ in Eq.(3.95) is replaced by $D = ((i + \beta)\sigma\tau_C + \omega_R\tau_C + 1)^{-1}$. Therefore, in the case of $\sigma\tau_C \gg 1$, the coefficient of $d^2\delta\overline{S}/dr^2$ in Eq.(4.16) becomes approximately $-(1/2)\Lambda^2/[(i + \beta)\sigma\tau_C]$ instead of $-(1/2)\Lambda^2/(i\sigma\tau_C)$. Thanks to the real part of β, the non-physical spatial oscillations are no longer present in the eigenfunctions.

By introducing the new parameter β in the order of unity, we indeed get thermal eigenfunctions without the fictional spatial oscillations. Fig.4.12 shows that the spatial oscillation disappears when we adopt $\beta = 1$. As mentioned above, some complex phenomena in turbulence is neglected in the TDC theory. However, phase lags between the pulsations and the way the neglected phenomena adapts to them are allowed to take place by introducing the parameter β.

Fig.4.13 shows modal diagrams for the nonadiabatic analysis with TDC. The parameter is set as $\beta = 1$. Similarly to the FC approximations, the sequences become waving, and finally ascending and descending sequences are formed as the stellar mass increases. Unstable modes on the ascending sequences have moderate growth rates with $|\omega_I|/\omega_R < 0.01$, while some of unstable modes on the descending sequences have high growth rates with $|\omega_I|/\omega_R > 0.01$. The additional sequence in the low frequency found in the $L'_C = 0$ case is not seen in this case.

Figs.4.14–4.16 show the instability range of each sequence for each treatment of convection in the HR diagram. The dots are observed pulsating stars. Roughly speaking, the extent of the instability derived with TDC can be said to be between those with $\delta L_C = 0$ and $L'_C = 0$. As mentioned in §4.3, convection does not make any work with $\delta L_C = 0$, while damping takes place due to convective luminosity gradient appearing at edges of convection zones with $L'_C = 0$. In this TDC case, on the other hand, some phenomena in convection other than the convective luminosity gradient should be included. Most of the modes shown in Figs.4.14–4.16 are excited in convection zones. Fig.4.17 shows the distribution of convection zones in envelopes of the $50 M_\odot$ stars. The convection zone appearing at $\log T \simeq 5 - 5.5$ corresponds to the Fe opacity bump. In stellar envelopes, convection is caused mainly by ionization. It efficiently absorbs the thermal energy flux from the center, which means the opacity κ is significantly large. Then substantially large temperature gradient is required to transfer the energy. It also raises up the radiative temperature gradient,

$$(A.12): \nabla_{\mathrm{rad}} \equiv \left(\frac{d \ln T}{d \ln p} \right)_{\mathrm{rad}} = \frac{3}{16 \pi a c G} \frac{\kappa p}{T^4} \frac{L_r}{M_r},$$

due to the increase of κ. As introduced at the beginning of §2.4, convection occurs when ∇_{rad} exceeds the adiabatic temperature gradient ∇_{ad}. The convection zone appearing around $\log T = 4.5$ corresponds to the opacity bump by the second ionization of helium (so-called "He bump"), and one appearing around the surface does to the opacity bump of the first ionization of hydrogen and helium (so-called "H bump"). The convection zone of the Fe bump has substantial contribution of convective luminosity, while the others have less than 10% contribution of local total luminosity.

In Fig.4.14, the ordinary modes on the sequences A1 and A2 are excited in the cases of $\delta L_C = 0$ and TDC. The instability ranges for $\delta L_C = 0$ keep the almost constant width, while ones for TDC become narrower or disappear with increase in the stellar mass. This is because convection occurring around the Fe bump comes to contribute more and more to energy transport. Then, damping effects of convection depresses the instability of these modes. The green dot indicates an observed β Cephei listed in Sterken and Jerzykiewicz (1993). In terms of the location in the HR diagram, the pulsation of this star can be explained by the A1 mode.

91
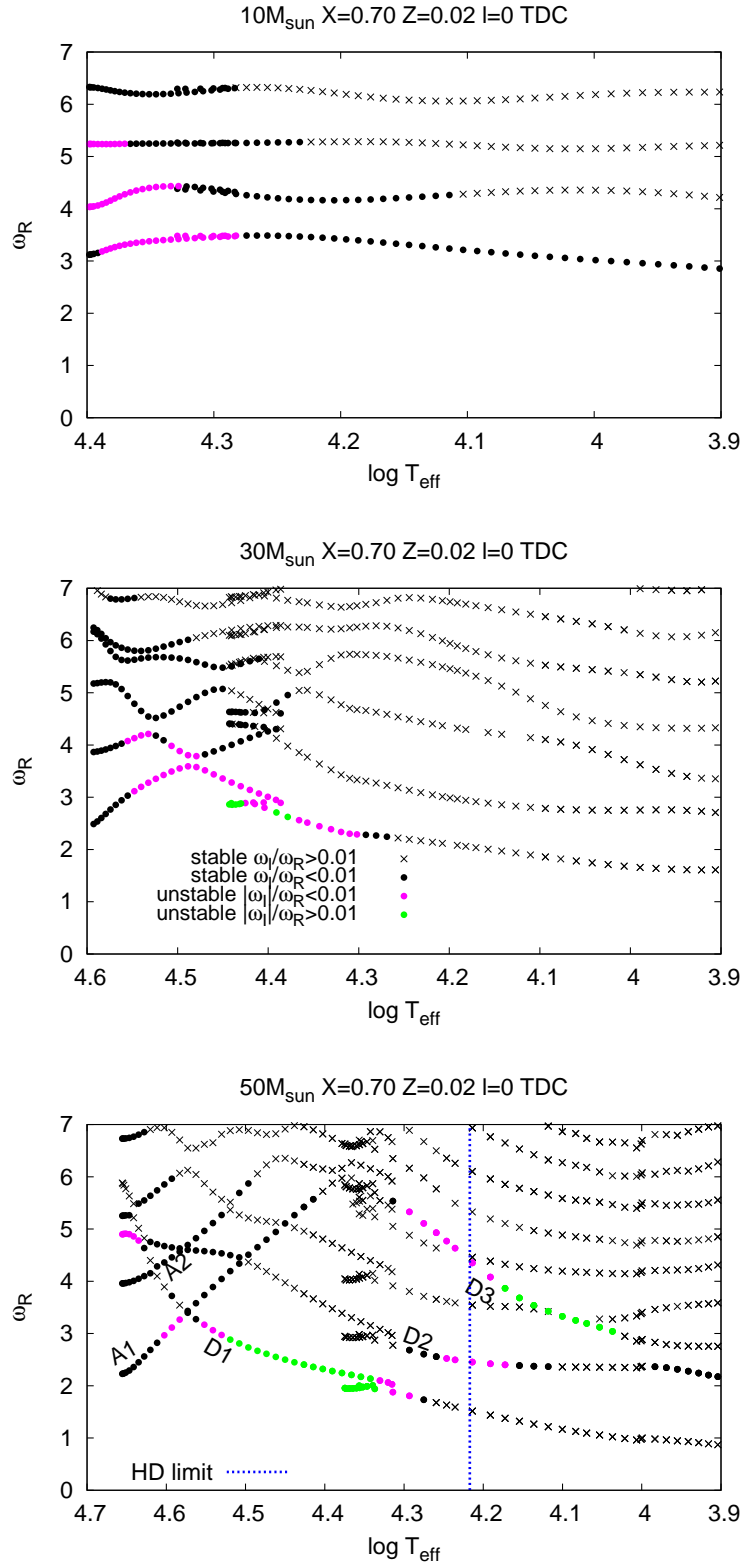
Figure 4.13: Same as Fig.4.2, but for TDC.
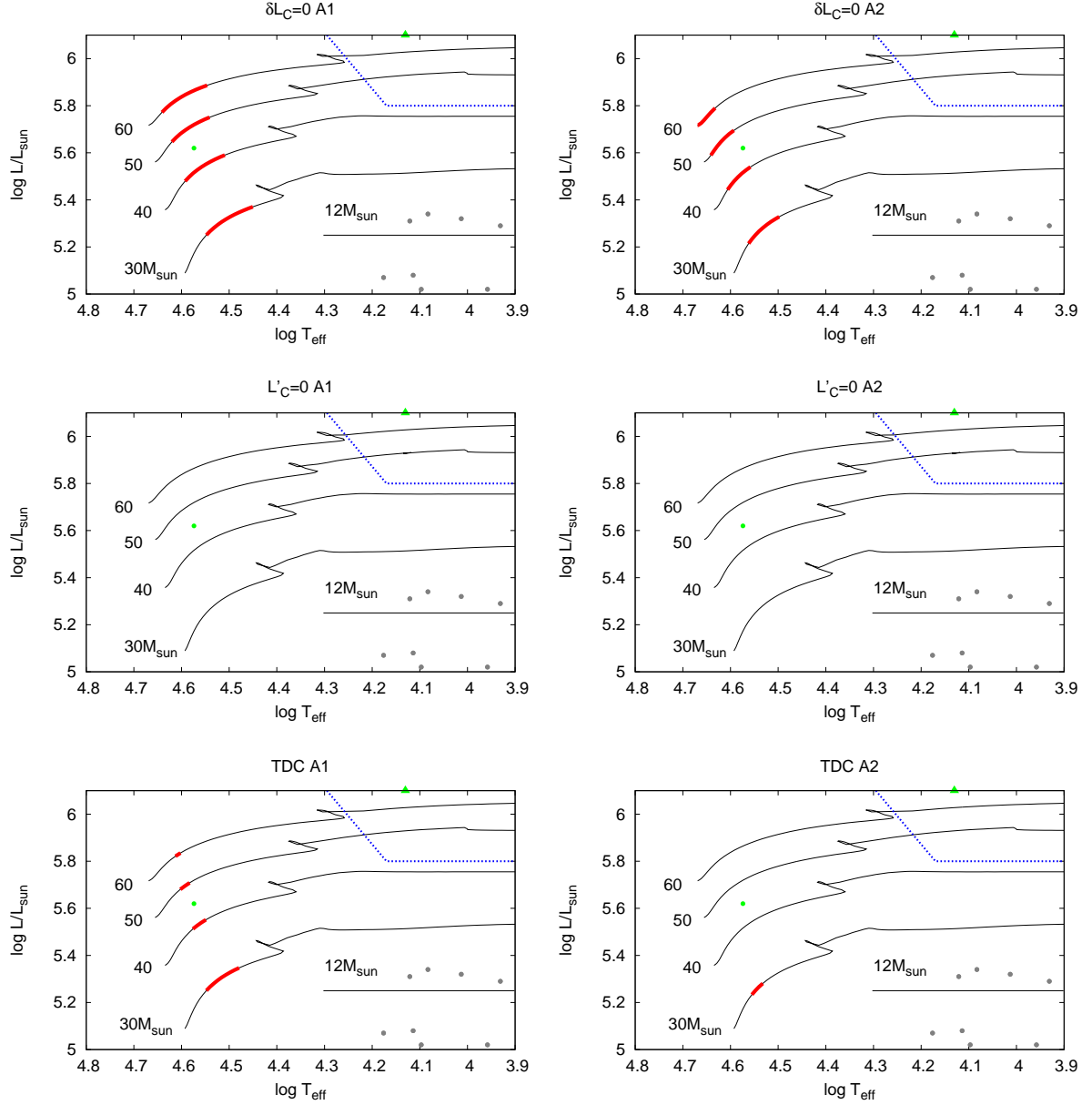
Figure 4.14: The instability domains of the ordinary mode on the sequences A1 (*left*) and A2 (*right*) in the HR diagram for $\delta L_C = 0$ (*top*), $L'_C = 0$ (*middle*) and TDC (*bottom*). The black thin lines are evolutionary tracks, and the red thick parts of them correspond to evolutionary stages with pulsational instability. The green dot are an observed β Cephei star listed in Sterken and Jerzykiewicz (1993), and the grey ones α Cygni variables in the Milky Way listed in Saio *et al.* (2013). The green filled triangle is HD 50064, a candidate for a strange-mode pulsator observed by Aerts *et al.* (2010).
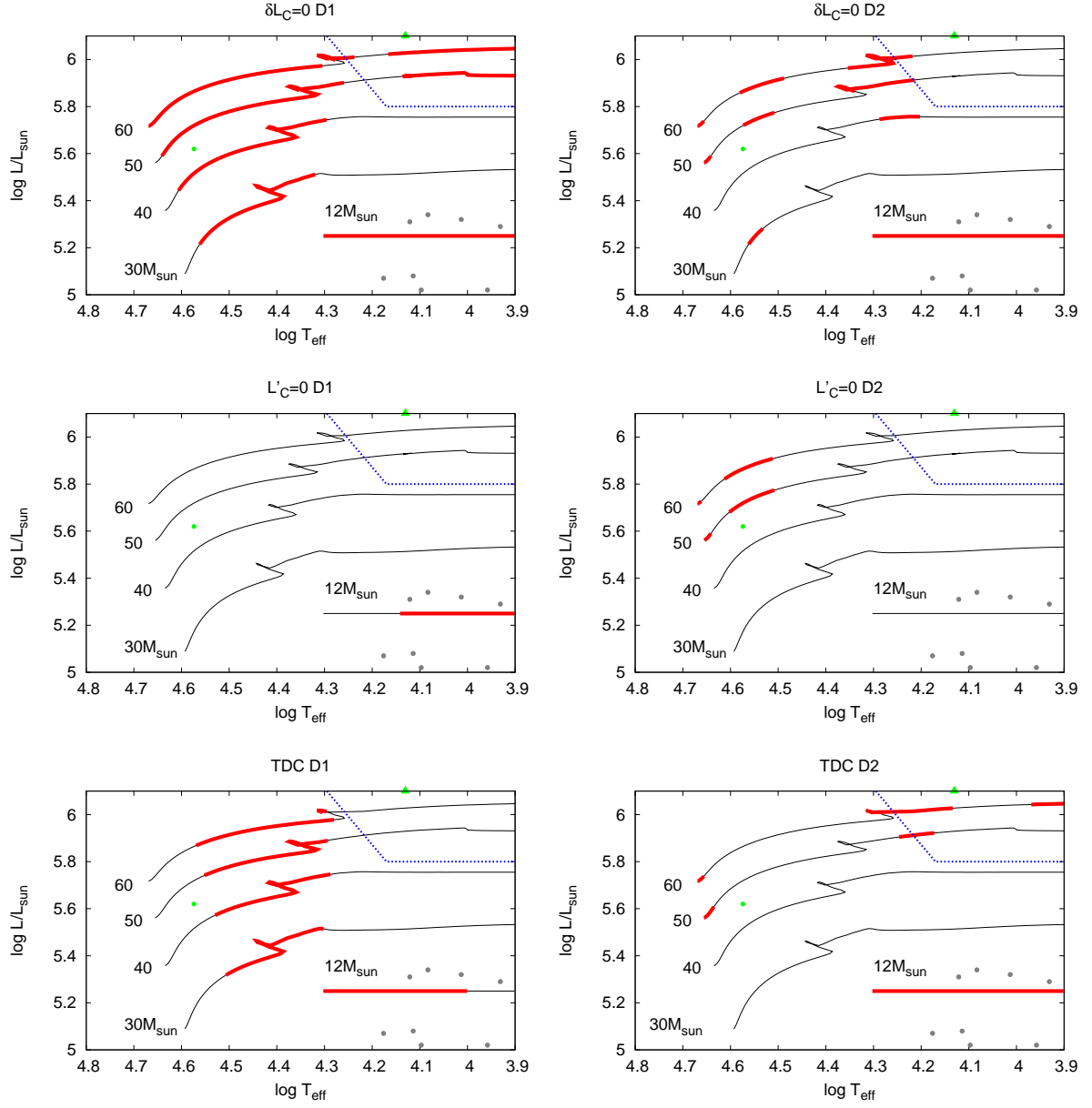
Figure 4.15: The instability domains of the strange-modes on the sequences D1 (*left*) and D2 (*right*) in the HR diagram for $\delta L_C = 0$ (*top*), $L'_C = 0$ (*middle*) and TDC (*bottom*). The definition of the lines and the dots are the same as Fig.4.14.
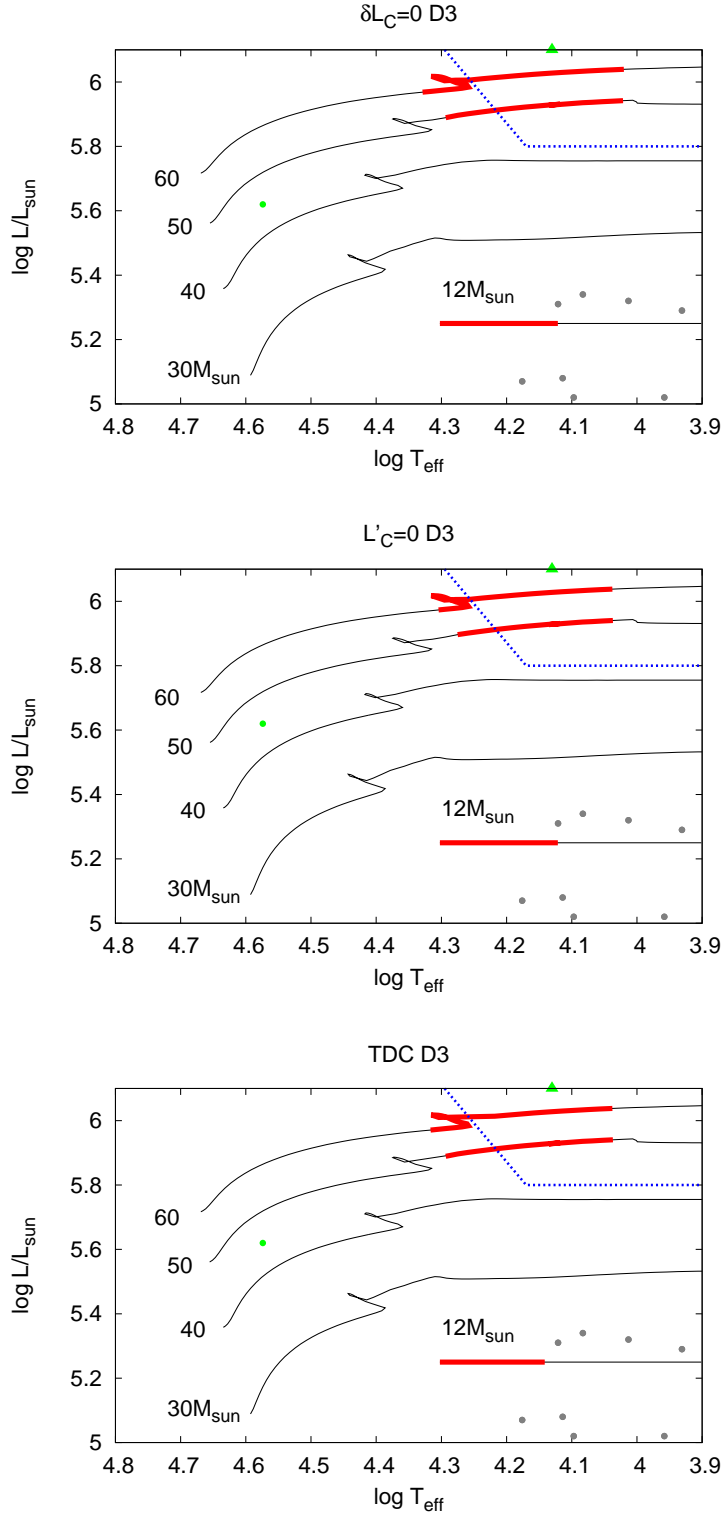
Figure 4.16: The instability domains of the strange-modes on the sequence D3 in the HR diagram for $\delta L_C = 0$ (*top*), $L'_C = 0$ (*middle*) and TDC (*bottom*). The definition of the lines and the dots are the same as Fig.4.14.

95
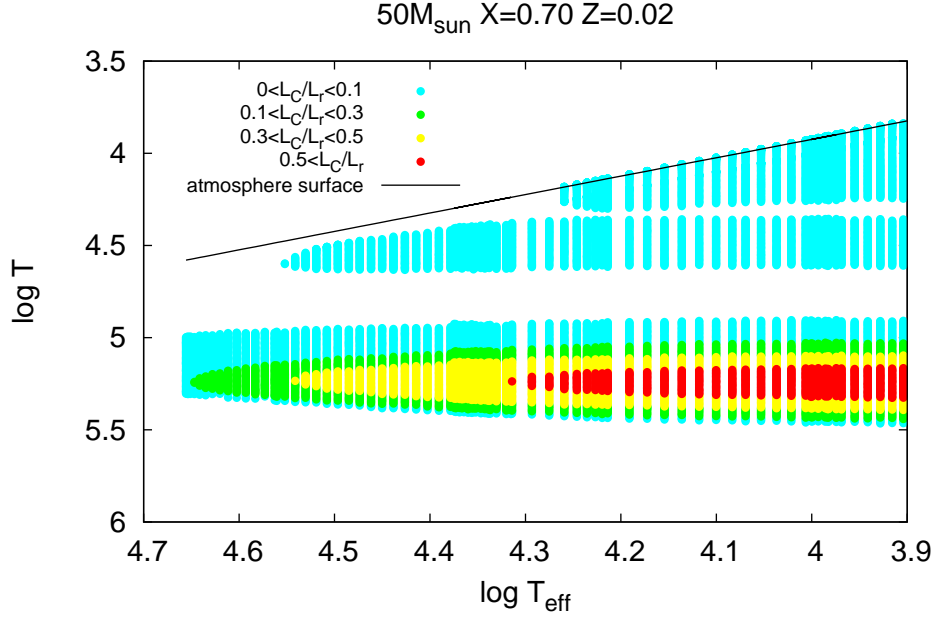
Figure 4.17: Locations of convection zones for $50M_\odot$ with $X = 0.70$, $Z = 0.02$. The color is categorized according to contribution of convective luminosity. The abscissa is the effective temperature, while the vertical axis is temperature in stellar structure, i.e., the direction to higher temperature corresponds to that to the stellar center.

The left panels of Fig.4.15 show that the strange-mode on the sequence D1 has a similar tendency of difference due to treatments of convection to the ordinary A1 and A2 modes. The D1 mode is also excited at the Fe bump, around which convective luminosity substantially contributes to energy transport. The top panel of Fig.4.18 shows the work integral of the D1 mode, and the one for $\delta L_C = 0$ increases in the Fe bump convection zone due to the κ-mechanism. The one for $L'_C = 0$, on the other hand, drastically decrease, since damping due to convective luminosity gradient overcomes the κ-mechanism excitation. In the TDC case, the work integral increases and shows that the damping effects of convection is not so strong as those in the case of $L'_C = 0$. While the FC approximation of $L'_C = 0$ considers convective luminosity perturbation due to displacement in regions having convective luminosity gradient, the TDC theory adds the other phenomena such as effects on convective flux due to change in temperature. From this, the latter effects could be thought to compensate the former one. In the left top panel of Fig.4.15 ($\delta L_C = 0$), the instability appears above the HD limit as well as in the main sequence. As shown by Fig.4.17, the contribution of convective luminosity becomes stronger with decrease in the effective temperature. Then, the D1 mode does not become unstable above the HD limit due to damping by convection in the TDC case.

The right panels of Fig.4.15 shows that instability of D2 around $\log T_{\text{eff}} = 4.3$ appears in the cases of $\delta L_C = 0$ and TDC, but does not exist for $L'_C = 0$ like the above cases of A1, A2 and D1. The middle panel of Fig.4.18 shows the work integrals at an evolutionary stage with

96
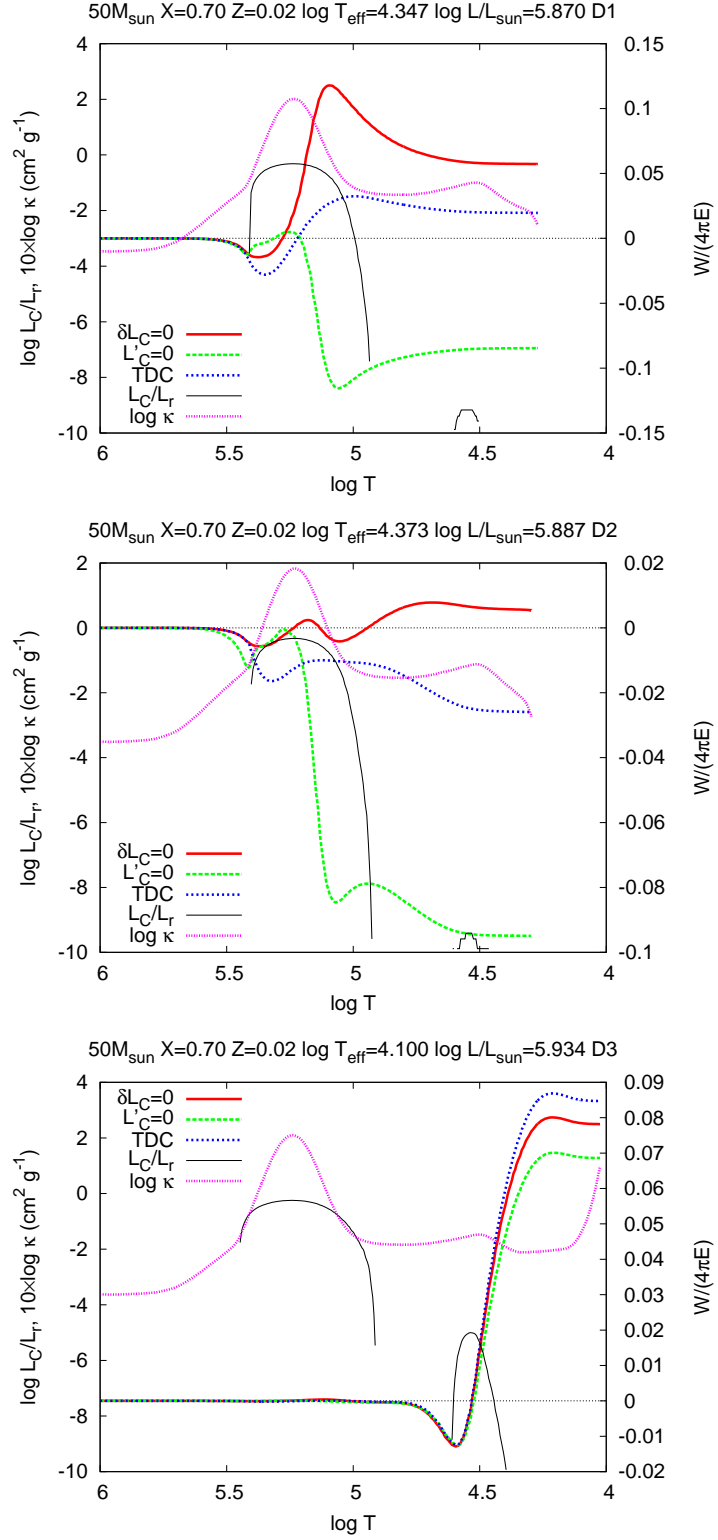
Figure 4.18: Work integrals for modes on the sequences D1, D2 and D3 with $\delta L_C = 0$, $L'_C = 0$ and TDC. These panels also show the profile of the ratio of convective to local total luminosity, and of the opacity.

97

$\log T_{\mathrm{eff}} = 4.373$ having the unstable D2 mode only for $\delta L_C = 0$. The D2 mode is excited in the middle and at the top of the Fe bump convection zone with $\delta L_C = 0$. But the damping dominates over the excitation in cases of $L'_C = 0$ and TDC. The work integral for $L'_C = 0$ also here shows much stronger damping than for the other treatments.

On the other hand, the other D2 instability appearing in the other effective temperature ranges shows different tendencies from the above cases. First, the instability appears around the ZAMS stage with all of the three treatments. In this case, the D2 mode is excited at the He bump, which does not have convection around the ZAMS stage. This is why the instability invariably appears in all the treatments. The instability at $\log T_{\mathrm{eff}} = 4.6-4.5$ appears in the two FC approximations. But the excitation mechanism is not the κ-mechanism, since it occurs not only at the Fe bump κ-mechanism excitation zone satisfying $d[\kappa_T + \kappa_\rho/(\Gamma_3 - 1)]/d\log T < 0$, but also in the upper layers. The corresponding work integral is shown in Fig.4.8. The instability at $\log T_{\mathrm{eff}} = 4 - 3.9$ appears only in the TDC case. It is slightly excited around the Fe bump and mainly around the He bump. Also in this case, the excitation zone does not fit into the κ-mechanism zone. Although the situation is complicated for the D2 mode, the stability is dependent of treatments of convection since the Fe bump having substantial contribution of convective luminosity.

On the other hand, Fig.4.16 shows the instability range of the D3 mode is independent of the treatments. This mode is excited exclusively around the He bump, where convective luminosity is negligible. Then, the work integrals for all the three treatments resemble one another (the bottom panel of Fig.4.18).

Fig.4.19 gives HR diagrams indicating evolutionary stages with at least one unstable radial mode for the two types of FC and TDC. The instability range by TDC is almost the same as the case of $\delta L_C = 0$ for $\lesssim 30 M_\odot$. For the more massive stars, the instability is slightly weakened in the main-sequence stage, and the instability region is separated into several parts. But the instability domain by TDC looks to cover locations of β Cephei. The computed periods are consistent with the observed ones as shown in Fig.4.20, and in the order of a few hours. As the stellar mass increases, the dynamical timescale $\sqrt{R^3/(GM)}$, which is representative timescale of stellar pulsations, and hence the period of β Cephei becomes longer. On the other hand, the treatment of $L'_C = 0$ makes so strong damping that the instability domain is too small to explain the β Cephei.

The α Cygni variables are located in the post–main-sequence region and below the HD limit. They are outside of the instability domain shown by this study. Saio (2011) found unstable nonradial oscillatory convection (g^-) modes having substantial amplitude at the surface of post–main-sequence stars. He also found that the periods of those modes match with those of α Cygni variables. Saio *et al.* (2013) further pursued the explanation for the pulsations of α Cygni variables, and analyzed evolutionary models which experience the blue loop stage. According to them, while strange-modes are not excited in 20 and $25 M_\odot$ stars evolving from the main sequence into red supergiants, blue loop stars, which have experienced the red giant stage and are going back to the higher effective temperature side, have unstable strange-modes. In the red supergiant stage, the stars lose substantial amount of mass. This makes the L/M ratio increase so much that the strange-modes can be excited.

Although Saio *et al.* (2013) adopted the FC approximation, the pulsations at such an
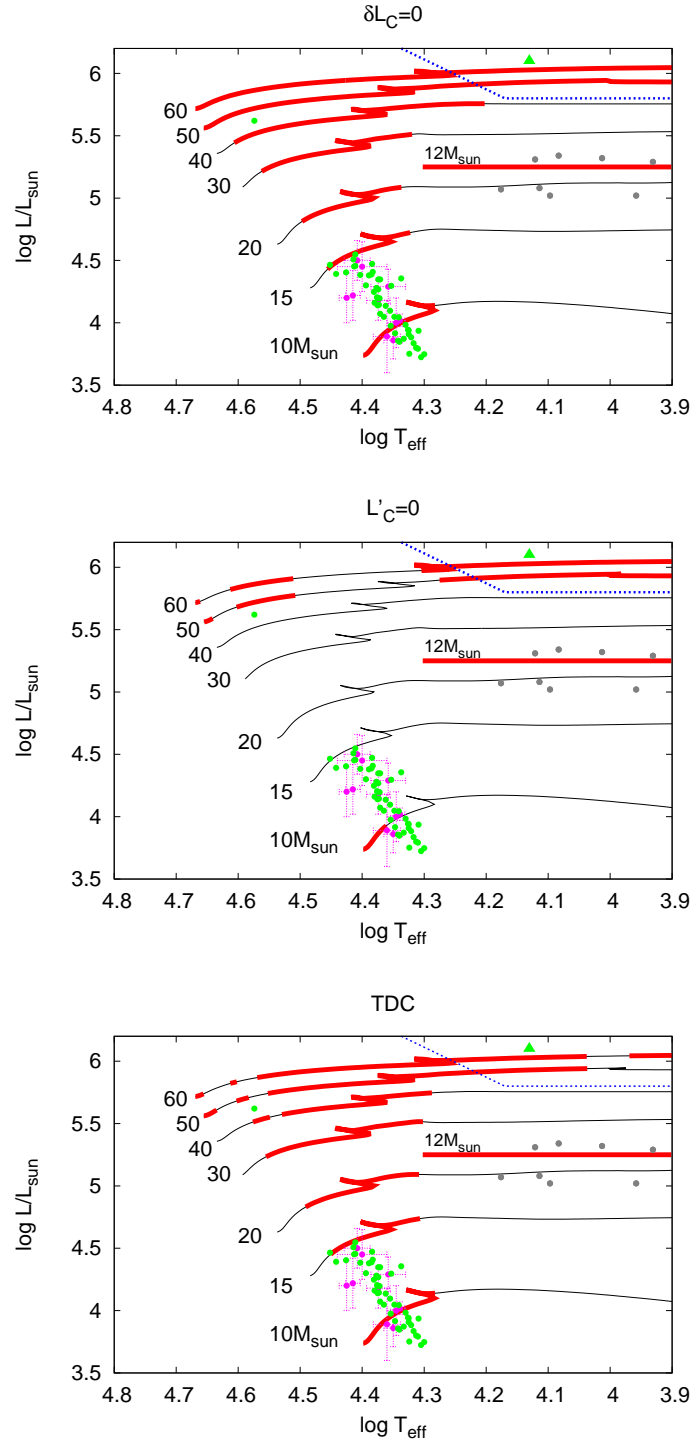
Figure 4.19: Domains having at least one unstable radial mode (*red lines*). The green and the magenta dots are observed β Cephei listed in Sterken and Jerzykiewicz (1993) and Saio *et al.* (2013) respectively, and the grey ones α Cygni variables in the Milky Way listed in Saio *et al.* (2013). The green filled triangle is HD 50064, a candidate for a strange-mode pulsator observed by Aerts *et al.* (2010).
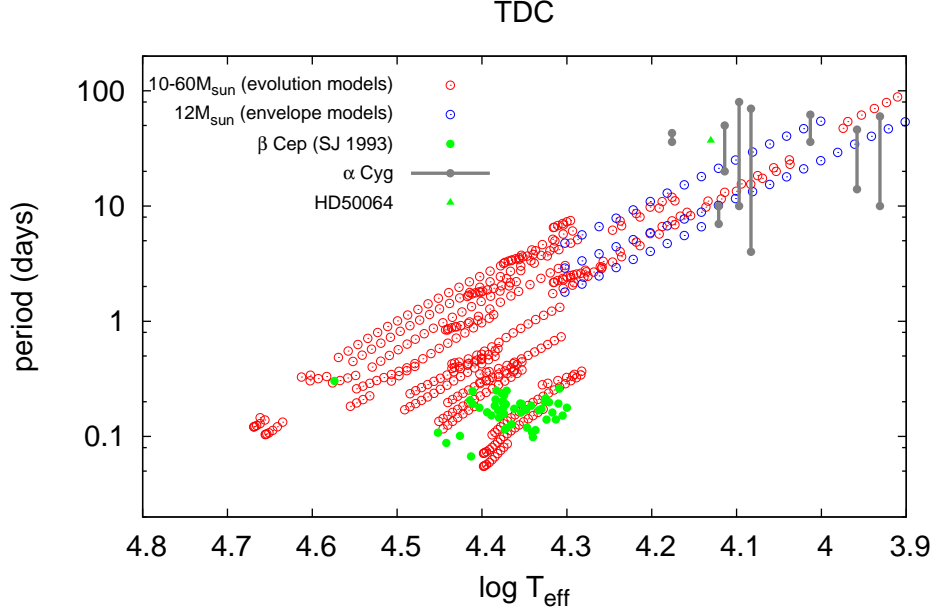
Figure 4.20: Periods of unstable modes computed with TDC and observed pulsations. The open circles correspond to computed unstable modes. The red ones are of evolutionary models with $10 - 60 M_\odot$, while the blue ones are of envelope models with $12 M_\odot$. The filled symbols are observed periods. The green filled circles are β Cephei listed in Sterken and Jerzykiewicz (1993), while the green filled triangle is HD 50064, a candidate for a strange-mode pulsator observed by Aerts *et al.* (2010). The grey line segment with filled circles at the both ends indicate a period range for each α Cygni variable listed in Saio *et al.* (2013).

evolutionary stage are here re-examined with TDC. Saio *et al.* (2013)'s calculations of the stellar evolution with stellar wind mass loss showed that the star with the initial mass of $25 M_\odot$ reduced their own mass to $11.6 M_\odot$ at $\log T \simeq 4.1$ on the blue loop. In this study, therefore, the envelope models with $M = 12 M_\odot$ and $\log L/L_\odot = 5.25$ are constructed in the range of $\log T_{\text{eff}} = 4.3 - 3.9$. Since the amplitude of radial pulsations is confined to the stellar surface at the considered stage, it is allowable to neglect the central part of the stars. The inner boundary conditions $\xi_r = 0$ and $\delta L = 0$ are imposed at the layer with $\log T = 6$, where $r/R = 0.04 - 0.19$. The modal diagram in Fig.4.21 shows that the strange-modes on all of the sequences D1 to D3 are excited. The result for each mode in each treatment is also shown in the HR diagram of Figs.4.15 and 4.16. Also here the instability of the D3 mode invariably appear in all of the treatments, while the result about the D1 and D2 modes depends on the treatments. The periods of the computed unstable modes and the observed α Cygni variations are compared in Fig.4.20. The grey line segment indicates the period range of variations for each α Cygni variable. The blue open circles are the periods of the unstable modes in the envelope model, and overlap the periods in the 50 and $60 M_\odot$ post–main-sequence stars, while
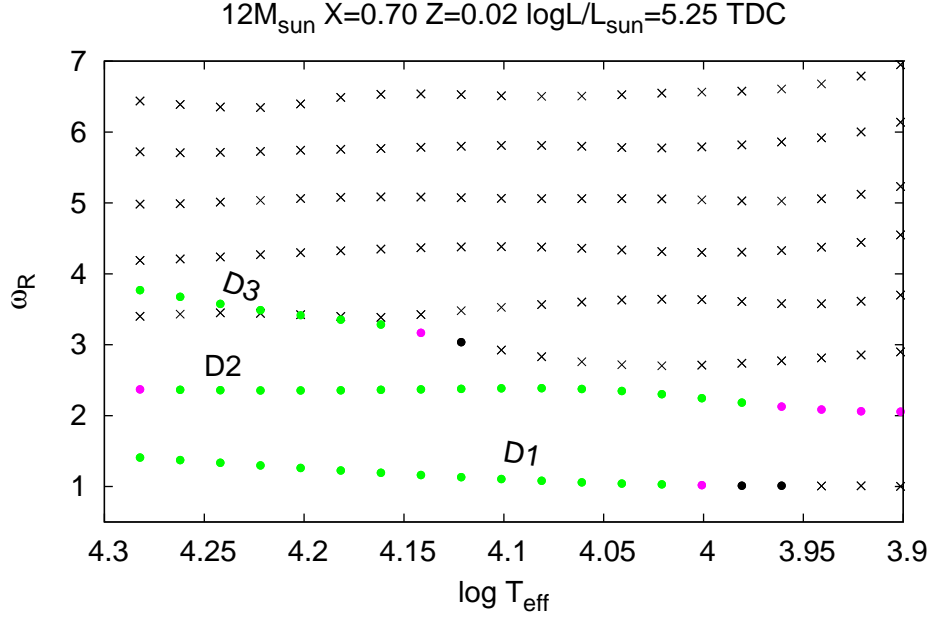
Figure 4.21: Modal diagram of the analysis with TDC for the $12M_\odot$ envelope models. The definition of the symbols are the same as the previous modal diagrams such as Fig.4.2.

the envelope models are located at the substantially lower luminosity than the post–main-sequence stars. Since the stellar mass of the envelope models is much lower, the dynamical timescale $\sqrt{R^3/(GM)}$ is likely to be longer, and to be comparable to that of the more massive post–main-sequence stars. The periods of α Cygni match with that of the envelope models.

From the above results, we can say that convection can affect the pulsational stability of massive stars, and that we have to take into account effects of convection to consider the stability. On the other hand, the instability of the strange-mode on the sequence D3 should definitely exist regardless of the treatments of convection, since its excitation zone has negligible contribution of convective luminosity. The instability of the D3 mode is found around the HD limit, and in the envelope models for α Cygni variables. Although we can expect the responsibility for the HD limit phenomenon and the α Cygni variations, what happens after the growth of the pulsations is beyond this study. It might be possible that the amplitude is saturated at some level (Buchler *et al.*, 1997). On the other hand, there are also attempts to explain the connection of the strange-mode instability to pulsationally driven mass-loss by nonlinear hydrodynamic calculations (Dorfi and Gautschy, 2000; Chernigovski *et al.*, 2004; Grott *et al.*, 2005), although the results seem to remain inconclusive. Aerts *et al.* (2010) observed pulsation of a luminous B star, HD 50064, of which the period is 57 days and may correspond to a strange-mode (Godart *et al.*, 2011). In addition, they found change of mass-loss rate on a timescale of the period of photometric and spectroscopic variation, which suggests a correlation between mass-loss and pulsations. The location of HD 50064 in the HR diagram is shown as the filled green triangle in Figs.4.14-4.16 and 4.19, and looks

in the instability domains of the strange-modes. The period is slightly higher than ones of the computed modes (Fig.4.20), but the dynamical timescales of the evolutionary models and hence the theoretical strange-mode periods could be longer if mass loss takes place by some mechanisms.

4.5   Conclusion

This section has shown results of pulsational stability analysis of radial pulsation in hot massive stars. First, we have discussed change of properties of modal diagrams with increase in stellar mass. In case of stars with $\simeq 10 M_\odot$, normalized frequencies are almost constant with change of effective temperature. As the stellar mass is raised up, the sequences become waving and come to have ascending and descending sequences in the higher effective temperature side. The ascending and descending sequences correspond to ordinary modes and strange-modes, respectively. Pulsational instability is caused by the κ-mechanism on both of the sequences. But growth rates of unstable strange-modes on the descending sequences is much higher than those of unstable ordinary modes on the ascending sequences. When the stellar mass reaches $\sim 50 M_\odot$, instability comes to appear on the descending sequences also in the low effective temperature. But this instability is not excited by the κ-mechanism.

Next, we have compared results with different treatments of perturbation of convective luminosity. This study adopts two types of FC approximations with $\delta L_C = 0$ and $L'_C = 0$, and TDC. First, we have compared the results with the two types of FC, and have found that the result with $L'_C = 0$ shows weaker instability than that with $\delta L_C = 0$. When we have $\delta L_C = 0$, no work is done by convective luminosity perturbation. When $L'_C = 0$, on the other hand, substantial work due to convective luminosity perturbation is done in regions having certain gradient of convective luminosity. Eventually, strong damping occurs in convection zones and the modes are likely to be less unstable. Then, we have discussed the result with TDC. Roughly speaking, the result shows weaker instability than that with $\delta L_C = 0$, and stronger instability than that with $L'_C = 0$. Anyway, we have confirmed that the strange-mode instability certainly exist even if convection is taken into account. Particularly, the instability of the sequence D3 invariably appears in all the treatments. It can mean that the existence of the D3 instability does not depend on the treatment of convection. In the HR diagram, this instability appears around the HD limit, and might be responsible for the lack of observed stars over the limit. Recent observation found a luminous B star, HD 50064, to change mass-loss rate in a timescale of a strange-mode period, and implies connection between the strange-mode and mass loss.

On the other hand, it is confirmed with TDC that periods of unstable strange-modes in envelope models for mass-lost stars in the post main-sequence stage corresponds to those of α Cygni variations. To know the resultant phenomena following the pulsational instability, we need nonlinear analyses. Indeed, some authors are making efforts to determine truth or falsehood of the above suggestions (Dorfi and Gautschy, 2000; Chernigovski *et al.*, 2004; Grott *et al.*, 2005).

5

Existence and excitation of strange-modes

Some parts of this chapter are included in "Vibrational instability of Population III very massive main-sequence stars due to the ε-mechanism", published in Monthly Notices of the Royal Astronomical Society Letters, vol. 421. pp. L34–L38 (Sonoi and Umeda, 2012)

5.1 Introduction

§4 has shown that strange-modes exhibit different behaviors from ordinary modes in modal diagrams. Specifically, while the sequences of ordinary mode frequencies ascend with decrease in effective temperature, those of strange-mode frequency descend. We also have seen that unstable strange-modes are likely to have much higher growth rates than unstable ordinary modes. The above characteristics have been found by previous studies from Wood (1976). In addition, amplitude of strange-modes are known to be confined to thin surface layers. Shibahashi and Osaki (1981) found that strange-modes appear only in very luminous stars with $L/M \gtrsim 10^4 L_\odot/M_\odot$.

Theoretical studies have found strange-modes in hot massive stars, Wolf-Rayet stars, helium stars (references shown in §4.1) and others. Then, the cause for the existence and excitation has been thought to be related to high nonadiabaticity in surface layers of such stars. But we have not yet obtained clear physical pictures of strange-modes in spite of efforts by many authors.

To investigate the origin of the strange-modes, Shibahashi and Osaki (1981) carried out a numerical experiment in which they artificially changed the thermal timescale appearing in the linearized equation of energy conservation. They found that the strange-mode found in the normal stability analysis with the unchanged realistic thermal timescale might become oscillatory convection mode (g⁻ mode) in the limit of infinite thermal timescale, corresponding

to an adiabatic situation. Saio *et al.* (1984) performed a similar experiment, and found a relation to thermal waves.

Gautschy and Glatzel (1990) showed the existence of strange-modes not associated with thermal waves. They carried out a stability analysis with nonadiabatic reversible (NAR) approximation, which is equivalent with setting the thermal timescale to zero in Shibahashi and Osaki's experiment. They demonstrated that strange-modes appear even in the NAR approximation. Although they analyzed stability of hydrogen deficit carbon stars, they found unstable strange-modes both in the normal nonadiabatic analysis and in the NAR approximation. In the latter, particularly, the classical κ-mechanism can no longer work, and hence an alternative physical explanation was needed. To understand the existence and the instability of the above type of strange-mode, Glatzel (1994) exhibited a local analysis with the WKB approximation. He suggested that the derivative of opacity with respect to temperature κ_T is important for the wave propagation of the strange-mode. Besides, dominance of radiation pressure leads to large phase lag between density and pressure perturbations, and to the strange-mode instability.

Since the strange-modes introduced above appear in the environment with short thermal timescale, adiabatic approximation is no longer available for them. But recently, strange-modes were discovered even in the adiabatic approximation in stellar models with newly available opacity tables (Rogers and Iglesias, 1992) by Kiriakidis *et al.* (1993) and Gautschy (1993). Kiriakidis *et al.* (1993) argued that the Fe opacity bump, which appears after the new opacity tables were released, causes a sound speed inversion, and that sound waves are partially reflected. Then, amplitude is extremely confined to surface layers.

Saio *et al.* (1998) contributed considerably to understanding the characteristics of the strange-modes. They proposed that strange-modes are categorized into two types; ones with and without the adiabatic counterpart. The strange-mode with the adiabatic counterpart behaves similarly to the corresponding adiabatic strange-mode in a modal diagram. And the unstable modes are excited by the classical κ-mechanism. On the other hand, solutions of strange-modes without the adiabatic counterparts do not have corresponding adiabatic solutions in a modal diagram. Their instability might not be caused by the κ-mechanism. Instead, it was proposed that the restoring force may be radiation pressure gradient, and that the large phase lag is important like Glatzel (1994).

In this section, the causes for the existence and the excitation of the strange-modes are investigated along massive star models, which is used for the stability analyses in §4. First, we consider the existence of the strange-modes by adopting the WKB approximations. Strange-modes with adiabatic counterparts can be explained with the adiabatic local analysis introduced in §3.10.1. On the other hand, it is difficult to investigate ones without adiabatic counterparts since the equations are complicated compared with the adiabatic case. Their origins are discussed by considering the quasi-isothermal (QIT) and the radiation-pressure dominant (RPD) cases with the Saio *et al.*'s procedure. Secondly, the excitation mechanism of the latter type of strange-modes is investigated by comparing the zero-metallicity case with the solar metallicity case, and by extending the Saio *et al.*'s analysis. In addition, we discuss the phase lags of the computed eigenfunctions.

5.2   Strange-modes with adiabatic counterparts

As shown in §4, the sequences of strange-modes come to appear with increase in stellar mass. What generates strange-modes as eigenmodes? To consider this problem, first, let us compare the results in §4 with solutions by the adiabatic approximation. As introduced in §3.8, we set entropy perturbation to zero in this approximation.

Fig.5.1 is the same as Fig.4.13, but the adiabatic solutions are also plotted. In case of $10M_\odot$, frequencies of nonadiabatic solutions are almost constant with change in the effective temperature, and almost correspond to the adiabatic ones. As the stellar mass increases, however,

a) the nonadiabatic sequences come to deviate from the adiabatic sequences in the low temperature side.

b) both the adiabatic and the nonadiabatic sequences become waving in the high temperature side.

In the following, we discuss the above two properties.

About a)

As the stellar mass increases, nonadiabatic sequences come to deviate from adiabatic sequences especially in the low effective temperature side (, although there are some nonadiabatic sequences which do not have the corresponding adiabatic ones even in the high temperature side). The adiabatic approximation is valid when the thermal timescale is much longer than the dynamical timescale. Fig.5.2 shows the profiles of the ratio of the local thermal timescale to the dynamical timescale. The top panel compares models with $\log T_{\rm eff} = 3.9$ for 10, 30 and $50M_\odot$ stars. It shows that the ratio goes down in the bulk of a star with increase in stellar mass. The cause for this is increase in luminosity. On the other hand, the bottom panel compares $50M_\odot$ models with different effective temperatures. The ratio comes to go down with decrease in the effective temperature. This is because the density becomes lower in the bulk, while it becomes extremely high at the small central region. Those imply that pulsations become out of touch with the adiabatic process with increase in luminosity or with decrease in effective temperature.

About b)

In the high temperature side, most of the nonadiabatic sequences fairly matches with the adiabatic sequences. This implies that properties of nonadiabatic solutions can be discussed in the adiabatic scheme. As mentioned in §4, the ascending and the descending sequences correspond to ordinary modes and strange-modes, respectively. In the panels for 30 and $50M_\odot$ in Fig.5.1, all the ascending sequences correspond to the adiabatic sequences, while not all the descending sequences do so. But it is common in both of the panels that the lowest descending sequence (labeled as D1 in the panel for $50M_\odot$) matches with the adiabatic one.
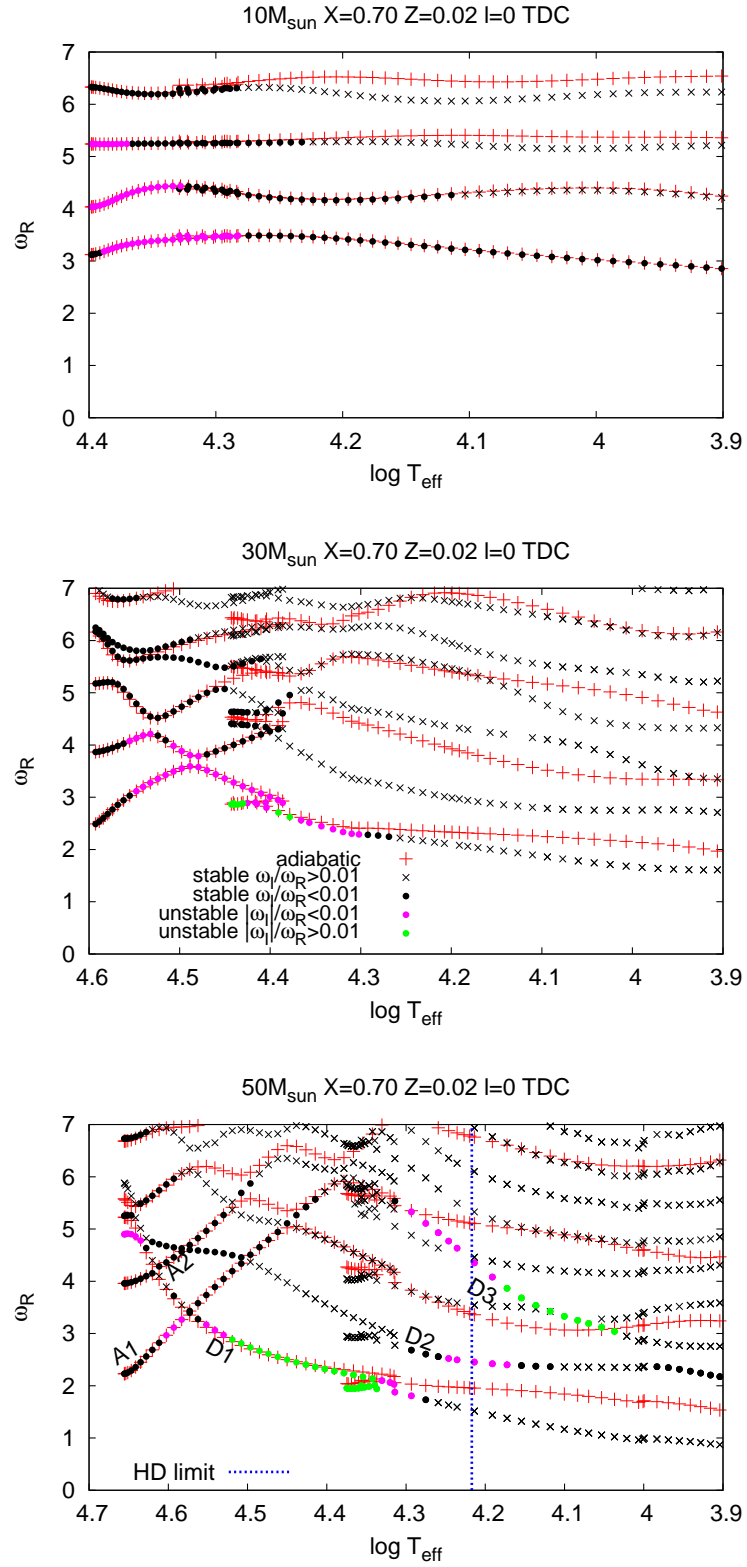
Figure 5.1: Same as Fig.4.13, but solutions by the adiabatic approximation are also plotted as the red crosses.
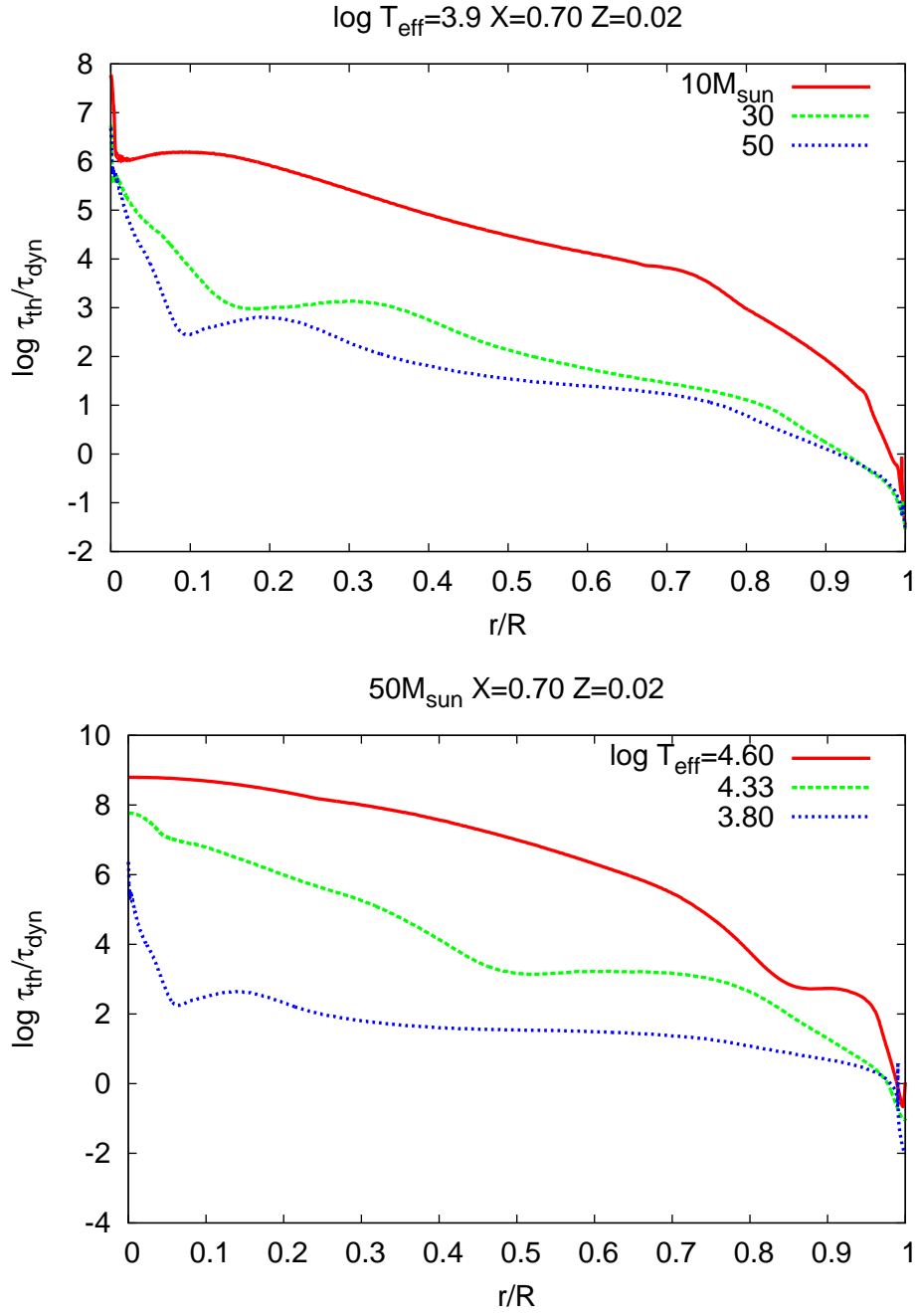
Figure 5.2: Profiles of the ratio of the local thermal timescale $\tau_{\mathrm{th}} \equiv 4\pi r^2 \rho T c_p / L_R$ to the dynamical timescale $\sqrt{R^3/(GM)}$. The top panel is for models with $\log T_{\mathrm{eff}} = 3.9$ for different stellar mass, and the bottom panel is for $50 M_\odot$ models with different effective temperatures.

The unstable strange-modes in the lowest descending sequence has the much higher growth rate than the ordinary unstable modes in the ascending sequences. As discussed in §4.2.2, the excitation mechanism for the unstable strange-modes is the classical κ-mechanism like for the ordinary modes. Since the amplitude is strongly confined to the narrow area near the Fe opacity bump (Fig.4.7), the κ-mechanism works very efficiently.

What causes such confinement of the amplitude? The local analysis is very convenient to discuss this. Here we consider the critical frequency for adiabatic radial pulsations introduced in §3.10.1,

$$(3.180): \quad \sigma_c(r) \simeq \frac{1}{2H_p} = \frac{GM_r\rho}{r^2p},$$

which is the lower limit of frequency for propagating waves. The top panel of Fig.5.3 shows the profile of the critical frequency in ZAMS stars. The profile means that acoustic waves are propagative over the curves of the critical frequency. As the stellar mass increases, a valley of the critical frequency comes to appear at $r/R > 0.9$, and waves become trapped there. This is the reason for the appearance of the strange-modes in the lowest descending sequence. Eq.(3.180) says that the critical frequency is proportional to density ρ. Indeed, the valley of the critical frequency is generated due to the profile of the density. The top part of the bottom panel of Fig.5.3 shows that the density profile becomes flat around the location of the valley with increase in stellar mass. We can particularly find density inversion in the profile for $60M_\odot$. The gradient of density can be described as

$$\frac{d\ln\rho}{dr} = \left(\frac{\partial\ln\rho}{\partial\ln p}\right)_T \frac{d\ln p}{dr} + \left(\frac{\partial\ln\rho}{\partial\ln T}\right)_p \frac{d\ln T}{dr} \tag{5.1}$$

$$= -\frac{GM_r\rho}{r^2p_g}\left[1 - \frac{\kappa L_R}{4\pi cGM_r}\left(1 + \frac{p_g}{4p_R}\right)\right] \tag{5.2}$$

$$\simeq -\frac{GM_r\rho}{r^2p_g}\left[1 - \frac{\kappa L}{4\pi cGM}\right] \tag{5.3}$$

where the equations of hydrostatic equilibrium and the diffusion approximation is used from the first to the second line. From the second to the third line, it is assumed that $L \simeq L_R$, $M_r \simeq M$ and $p_R \gg p_g$, which corresponds to the state of the location near the opacity bump in the massive ZAMS stars' envelopes. The gradient of radiation pressure is written as $dp_R/dr = -\kappa\rho L_R/(4\pi r^2c)$. That is, radiation pressure gradient becomes strong around the opacity bump. In case of $10M_\odot$, the radiation pressure is not so dominant even around the opacity bump. As the stellar mass increases, however, the luminosity goes up and the radiation pressure dominates over the gas pressure. Then, the density gradient can be described as Eq.(5.3), and the condition for the density inversion is

$$\frac{L/L_\odot}{M/M_\odot} \gtrsim \frac{4\pi cG}{\kappa}\frac{M_\odot}{L_\odot} \sim 10^4 \tag{5.4}$$
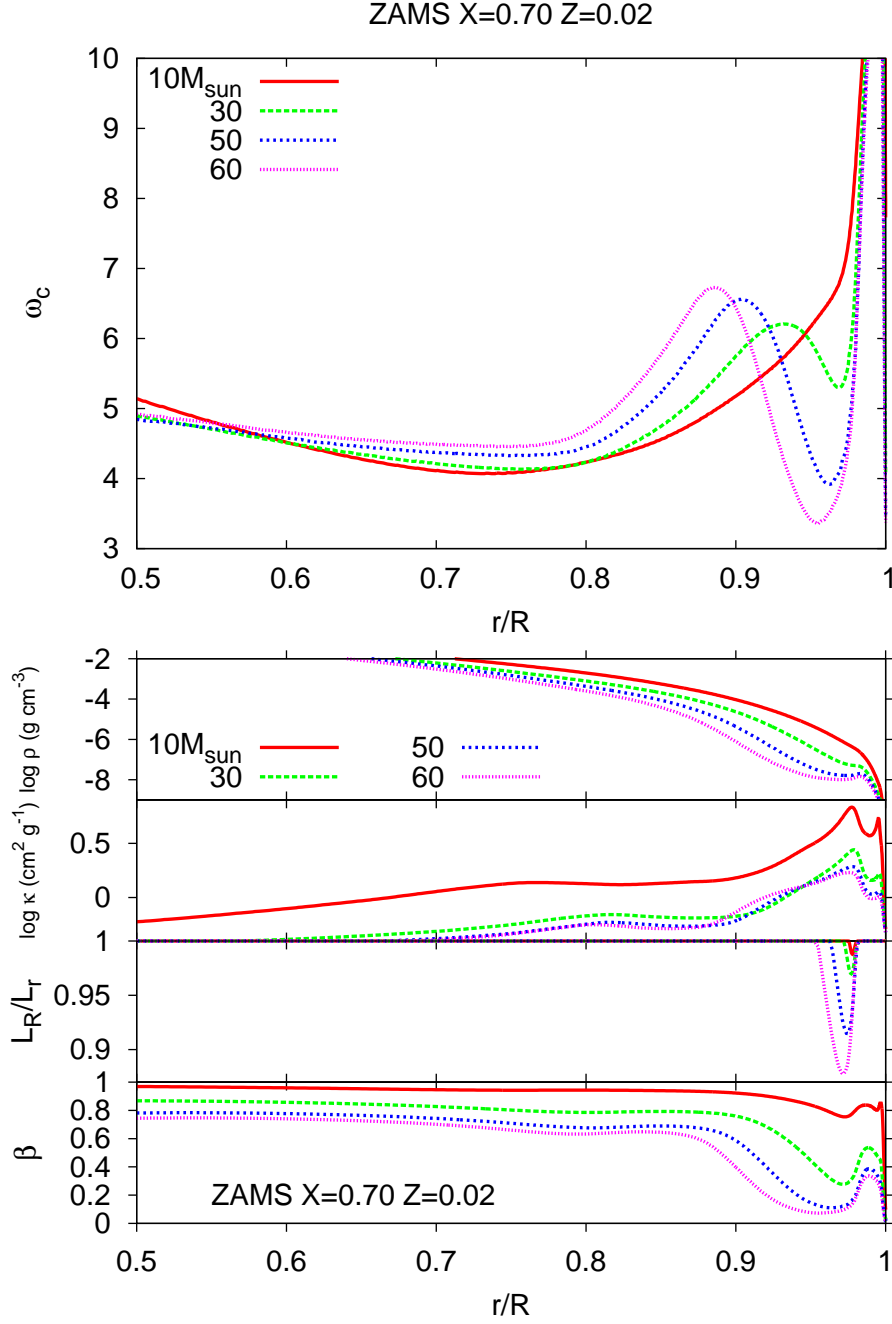
Figure 5.3: Profiles of critical frequency for adiabatic radial pulsations ω_c (*top*), density ρ, opacity κ and the ratio of gas pressure to total pressure β (*bottom*) in ZAMS stars with different stellar mass. The value of the critical frequency is normalized with the dynamical timescale as $\omega_c \equiv \sigma_c \sqrt{R^3/(GM)}$.
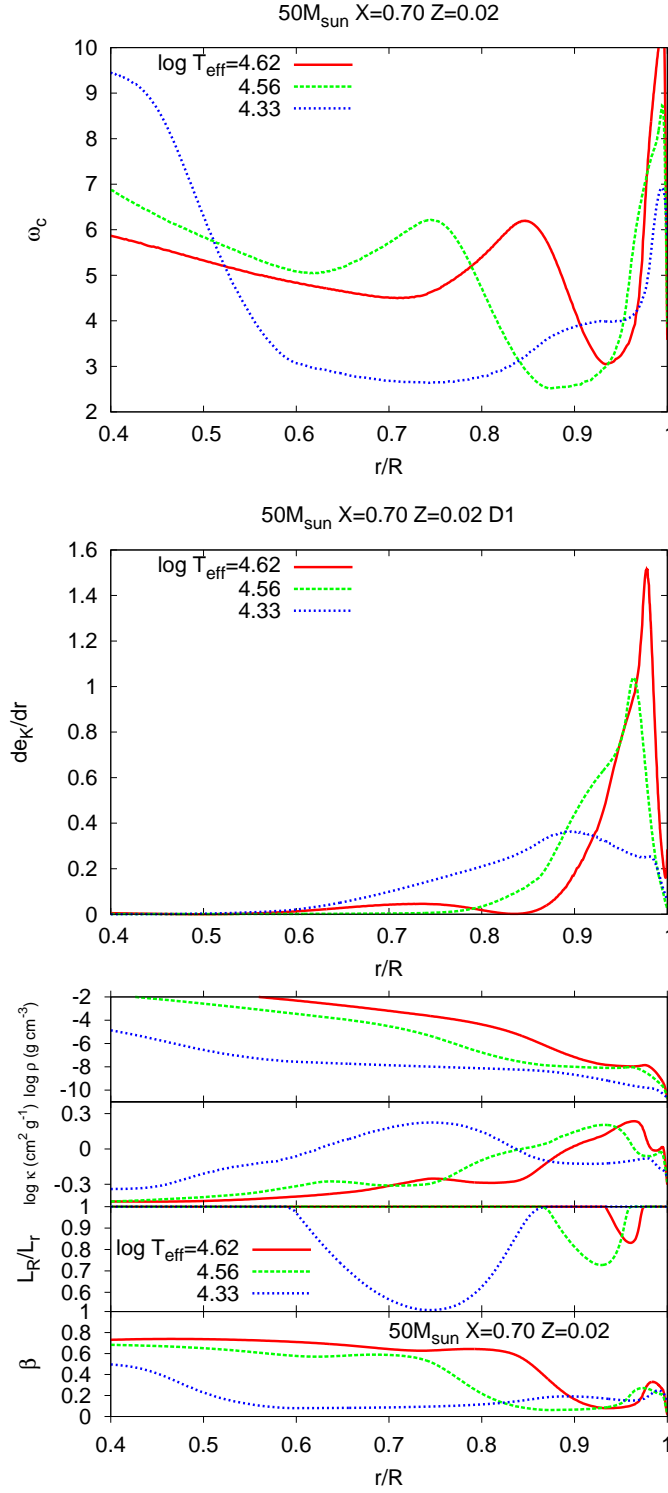
Figure 5.4: Profiles of critical frequency (*top*), kinetic energy density of modes on the sequence D1 (*middle*), and different equilibrium physical variables (density ρ, opacity κ, the ratio of radiative to local total luminosity L_R/L_r and that of gas to local total pressure $\beta \equiv p_g/p$, *bottom*).

where we have assumed $\kappa \sim 1$ cm^2 g^{-1}. Indeed, the ratio $(L/L_\odot)/(M/M_\odot)$ increases with the stellar mass; 5×10^2, 4×10^3, 7×10^3 and 9×10^3 for 10, 30, 50 and $60 M_\odot$. In envelopes of massive stars, thus, the high L/M ratio leads to the flat density profile or density inversion, and then creates the valley of the critical frequency. We should also note that the dominance of radiation pressure leads to increase in radiative temperature gradient. It is favorable for occurrence of convection, and the third top panel shows that the higher the stellar mass is, the more convective luminosity contributes, although the contribution is about 10% of the total luminosity even for $60 M_\odot$. As a matter of fact, the flat profile of density corresponds to the convection.

Let us adopt such discussion also to considering the change with the decrease in effective temperature. The top panel of Fig.5.4 shows profiles of the critical frequency. The valley appears at $r/R \gtrsim 0.9$ around the ZAMS stage. As the star evolves toward the lower effective temperature side, it becomes wider and deeper. That makes lower frequency waves become trapped in the valley. Indeed, the frequency of the sequence D1 decreases with the decrease in effective temperature. The middle panel of Fig.5.4 shows the profiles of kinetic energy density of the D1 modes, and that the distribution of the energy density becomes wider with the valley. The extension of the valley is caused by the change of the density profile as well as the above case of the increase in the mass of a ZAMS star. Also in this case, the density profile becomes flat, while radiation pressure and convection comes to contribute more strongly.

5.3 Existence of strange-modes without adiabatic counterparts

§5.2 introduces the origin of strange-modes having adiabatic counterparts, which appears in the high effective temperature side. On the other hand, the nonadiabatic solutions are likely not to match with the adiabatic ones in the low effective temperature side, since the thermal timescale tends to be as short as the dynamical timescale. In such a situation, the adiabatic approximation is no longer valid, and we should consider the other approaches.

5.3.1 Solutions with NAR approximation

First, let us consider extremely nonadiabatic case, corresponding to the case of zero thermal timescale. In this situation, the ratio of thermal timescale to dynamical timescale becomes zero, $\tau_{\mathrm{th}}/\tau_{\mathrm{dyn}} \to 0$. Then, the linearized equation of energy conservation for radial pulsations (3.155) becomes

$$\frac{d}{d \ln r} \left(\frac{\delta L_r}{L_r} \right) = 0, \tag{5.5}$$

where we have set $\varepsilon = 0$. This means that the perturbation of luminosity $\delta L_r/L_r$ has a constant value in a whole star, and the physically valid solution is

$$\frac{\delta L_r}{L_r} = 0. \tag{5.6}$$
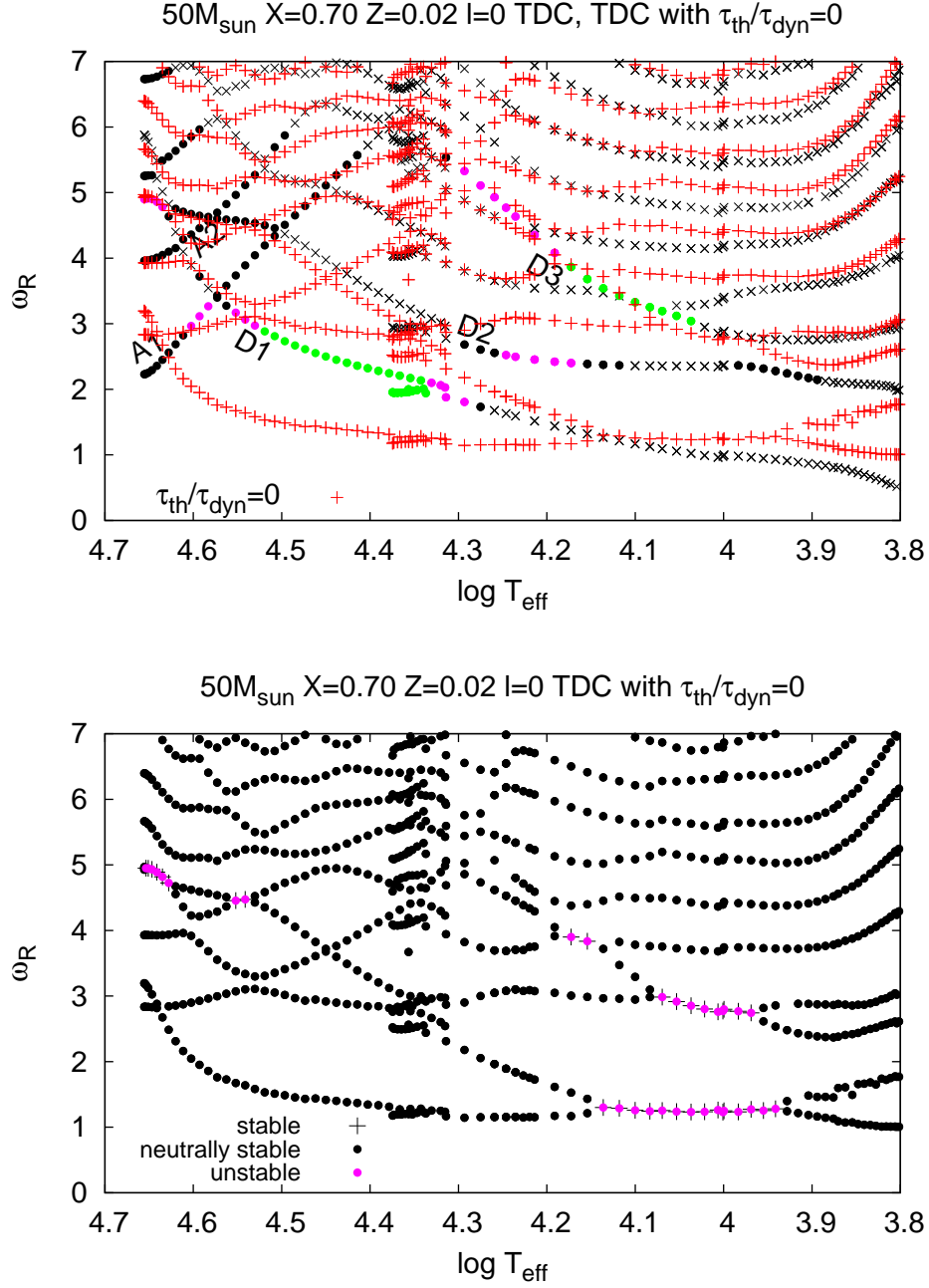
Figure 5.5: Top: Same as the bottom panel of Fig.4.13, but the NAR solutions ($\tau_{th}/\tau_{dyn} = 0$) are also plotted as the red crosses. Bottom: Modal diagram only for the NAR solutions for $50 M_\odot$ with $X = 0.70$, $Z = 0.02$. The solutions are categorized into stable, neutrally stable, and unstable modes as the black crosses, the black dots and the magenta dots, respectively.

112

This procedure is called nonadiabatic reversible (NAR) approximation. The reason for the naming is explained below. In the top panel of Fig.5.5, the solutions with the NAR approximation is plotted with the ordinary nonadiabatic solutions. The figure shows that the NAR solutions fairly fit to the ordinary solutions in the low effective temperature side, and implies that the pulsations come to take on the extremely nonadibatic feature with decrease in effective temperature.

On the other hand, the bottom panel of Fig.5.5 shows only the NAR solutions, for which the symbols are categorized in terms of the stability. In this approximation, the solutions can be real solutions or complex solutions having complex conjugates. Of the coefficients of eigenfunctions y_i or Y_i in the differential equations for pulsations (§3.7), only ω can have a complex value. In the differential equation system of radial pulsations Eqs.(3.162)–(3.165), ω appears in Eqs.(3.163) and (3.165). But now the terms having ω's in Eq.(3.165) vanish since $c_4 = \tau_{\mathrm{th}}/\tau_{\mathrm{dyn}} = 0$. Eq.(3.163) includes ω^2, and if some complex value is the solution of ω, its complex conjugate should also be the solution for which the imaginary parts of the eigenfunctions Y_i should have the opposite sign. That is the reason why this approximation is called "reversible".

5.3.2 WKB approximations

We have made sure that the NAR approximation can explain pulsations in the low effective temperature side. To understand the properties of the strange-modes further, we here carry out the WKB approximations following Saio *et al.* (1998). The differential equations for radial pulsations in the NAR case become

$$\frac{\delta\rho}{\rho} = -\frac{1}{r^2}\frac{d}{dr}(r^2\xi_r) \tag{5.7}$$

$$\left(\sigma^2 + 4\frac{GM_r}{r^3}\right) = \frac{d\delta p}{dr} = \frac{d}{dr}\left(p\chi_\rho\frac{\delta\rho}{\rho} + p\frac{\chi_T}{4}\frac{\delta p_R}{p_R}\right) \tag{5.8}$$

$$\frac{\delta L_r}{L_r} = 4\frac{\xi_r}{r} - \kappa_\rho\frac{\delta\rho}{\rho} - \frac{\kappa_T}{4}\frac{\delta p_R}{p_R} + \frac{1}{dp_R/dr}\frac{d\delta p_R}{dr} = 0 \tag{5.9}$$

where we have neglected the perturbation of convective luminosity as $\delta L_C = 0$ for simplicity. Here the perturbation of temperature are replaced with that of radiation pressure as $4\delta T/T = \delta p_R/p_R$. Below we discuss two cases, quasi-isothermal (QIT) and radiation-pressure–dominant (RPD) situations. In the former case, we assume that $|\kappa_\rho\delta\rho/\rho| \gg |(\kappa_T/4)\delta p_R/p_R|$ and neglect the spatial change of $\chi_T p/p_R$. This approximation is suitable for a case where temperature perturbation is much smaller than density perturbation. In the latter case, on the other hand, we assume that perturbation of radiation pressure is much larger than that of gas pressure. Specifically, we neglect the term $p\chi_\rho\delta\rho/\rho$ in Eq.(5.8). Under the above assumptions, we are going to reduce Eqs.(5.7)–(5.9) to a second-order differential equation.
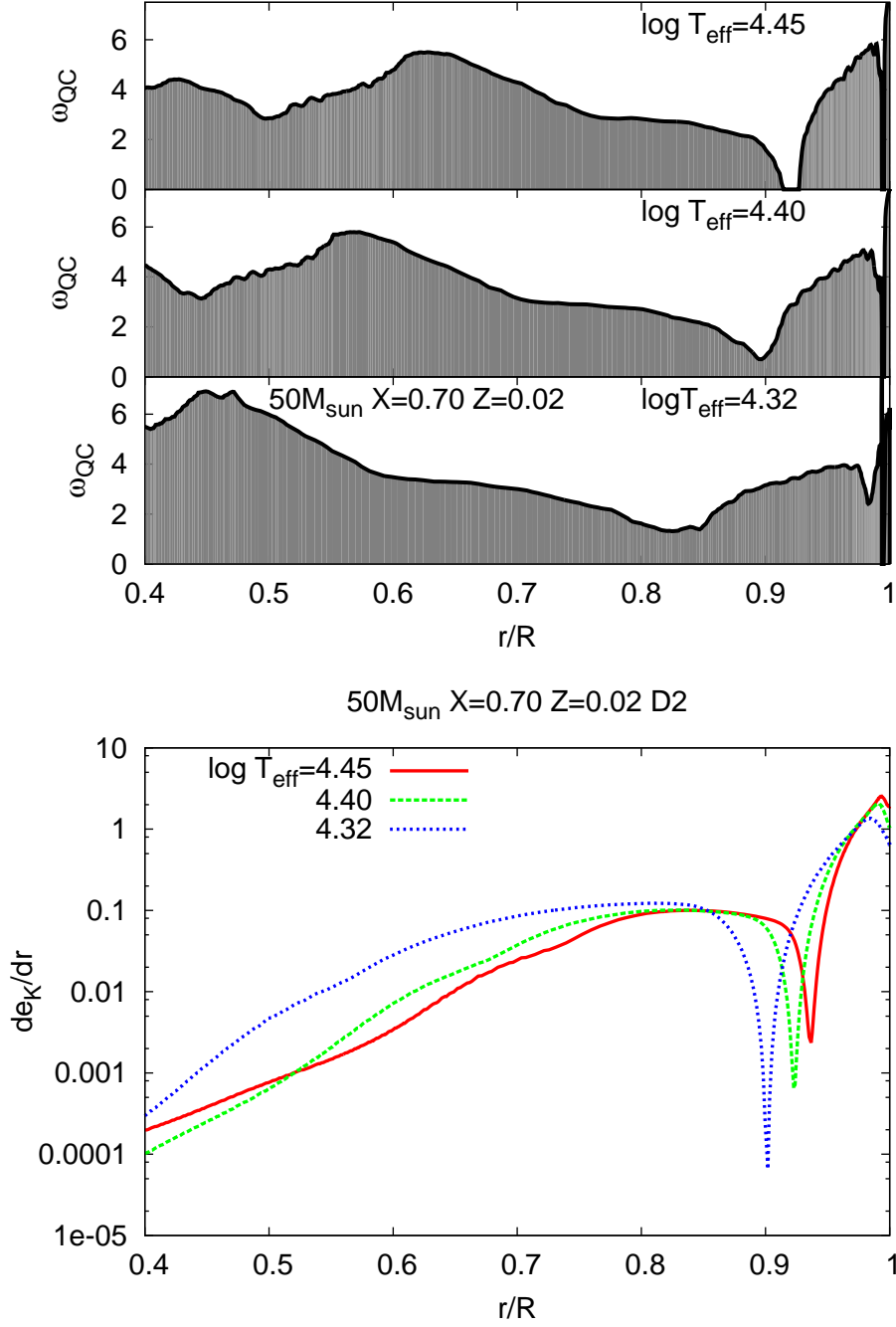
Figure 5.6: Top: Profile of ω_{QC} or propagation diagram for QIT modes in different evolutionary models. The grey zones are evanescent, while the white zones are propagative. Bottom: Distribution of kinetic energy density of modes on the sequence D2 in the corresponding models to the top panel.

Quasi-isothermal (QIT) modes

Neglecting the term $(\kappa_T/4)\delta p_R/p_R$ in Eq.(5.9) and the spatial variation of $\chi_T p/p_R$ in Eq.(5.8), we obtain a second-order differential equation,

$$\frac{d^2\zeta}{dr^2} + \frac{\zeta V}{r^2 \chi_\rho} c_1 (\omega^2 - \omega_{\mathrm{QC}}^2) = 0, \tag{5.10}$$

where

$$\zeta = \xi r \sqrt{p \chi_\rho} \exp\left[\int \frac{\kappa_\rho \chi_T}{8\chi_\rho} \frac{d \ln p_R}{dr} dr\right], \tag{5.11}$$

$$\omega_{\mathrm{QC}}^2 = \frac{1}{c_1}\left[4\chi_T \nabla - 4 + \frac{\chi_\rho}{V}\left(B^2 + \frac{dB}{d \ln r} - B\right)\right] \tag{5.12}$$

$$B = \frac{1}{2}\left[\frac{d \ln(p\chi_\rho)}{d \ln r} - 2 + \frac{\kappa_\rho \chi_T}{4\chi_\rho} \frac{d \ln p_R}{d \ln r}\right] \tag{5.13}$$

We then assume that the dependence of ζ on r is $\exp(ikr)$, and the condition for a propagative solution of ζ becomes

$$\omega^2 > \omega_{\mathrm{QC}}^2. \tag{5.14}$$

The top panel of Fig.5.6 shows the profiles of ω_{QC}. The waves are propagative over the curves of ω_{QC}. The bottom panel of Fig.5.6 shows the distribution of the kinetic energy density for the modes on the sequence D2. This sequence does not have a corresponding adiabatic sequence, and its properties cannot be understood with the adiabatic approximation. The bottom panel shows that the energy density is distributed more deeply in the interior with the decrease in the effective temperature. It means that the waves become propagative more deeply. According to the top panel, a propagative cavity appearing at $0.65 \lesssim r/R \lesssim 0.95$ for $\log T_{\mathrm{eff}} = 4.45$ is broadening with the decrease in effective temperature. That allows waves to propagate in the deeper interior. Besides, lower frequency waves become able to be trapped in the cavity. That may be the reason why the frequency of the sequence D2 goes down with the decrease in effective temperature.

In Eq.(5.10), the wavenumber of QIT modes is

$$k_{\mathrm{QC}} = \frac{1}{r}\sqrt{\frac{c_1 V}{\chi_\rho}(\omega^2 - \omega_{\mathrm{QC}}^2)} \tag{5.15}$$

Then, the condition for standing waves is

$$\int_a^b k_{\mathrm{QC}} dr = \left(n + \frac{1}{2}\right)\pi \tag{5.16}$$

where a and b represent the lower and the upper boundaries of a propagation zone, and n is an integer. The solutions of Eq.(5.16) are plotted as the open circles in Fig.5.7. In the higher temperature side of the contraction phase, which appears as a hook-like shape in an
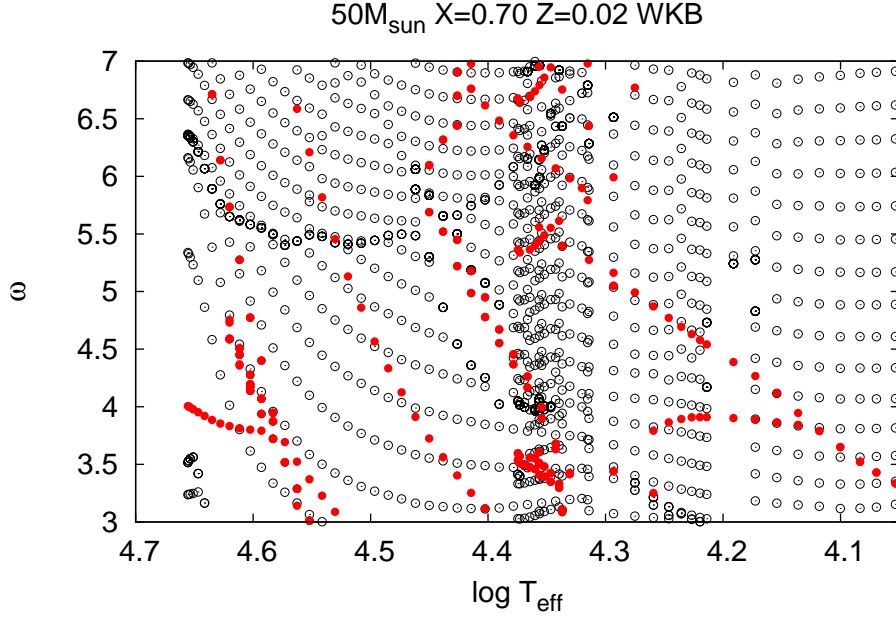
Figure 5.7: Modal diagram for the WKB approximations of QIT (*black open circles*) and RPD modes (*red filled circles*).

evolutionary track on the HR diagram, the frequencies of the sequences are descending with the decrease in effective temperature, while they keep the almost constant value with the change of effective temperature in the lower temperature side. We can recognize this tendency in most of the sequences in the modal diagrams by the normal nonadiabatic and the NAR analyses (See Fig.5.5).

Radiation-pressure–dominant (RPD) modes

Next, we consider radiation-pressure–dominant modes. In this case, we neglect the term $p\chi_\rho\delta\rho/\rho$ in Eq.(5.8). After some manipulations, we obtain a second-order differential equation,

$$\frac{d^2\eta}{dr^2} + \frac{\eta}{r^2}\left[A_0 + A_1\frac{c_1\omega^2}{q} - \left(\frac{c_1\omega^2}{2q}\right)^2\right] = 0 \tag{5.17}$$

where

$$\eta \equiv \xi_r r^{1+h} p^{1/2} \exp\left[-\frac{\omega^2}{2q}\int\frac{c_1(r')}{r'}dr'\right], \tag{5.18}$$

$$A_0 \equiv V\left[\frac{4(4-\kappa_T)}{\chi_T\kappa_\rho} + \frac{U}{2} + \frac{V}{4} + \frac{1}{2}\frac{d\ln\rho}{d\ln r} - 2 - \frac{2}{\kappa_\rho} - \frac{2}{q}\right] - (h+1)(h+2), \tag{5.19}$$

$$A_1 \equiv h + V(4-\kappa_T)\nabla + \frac{U-V}{2}, \tag{5.20}$$

116
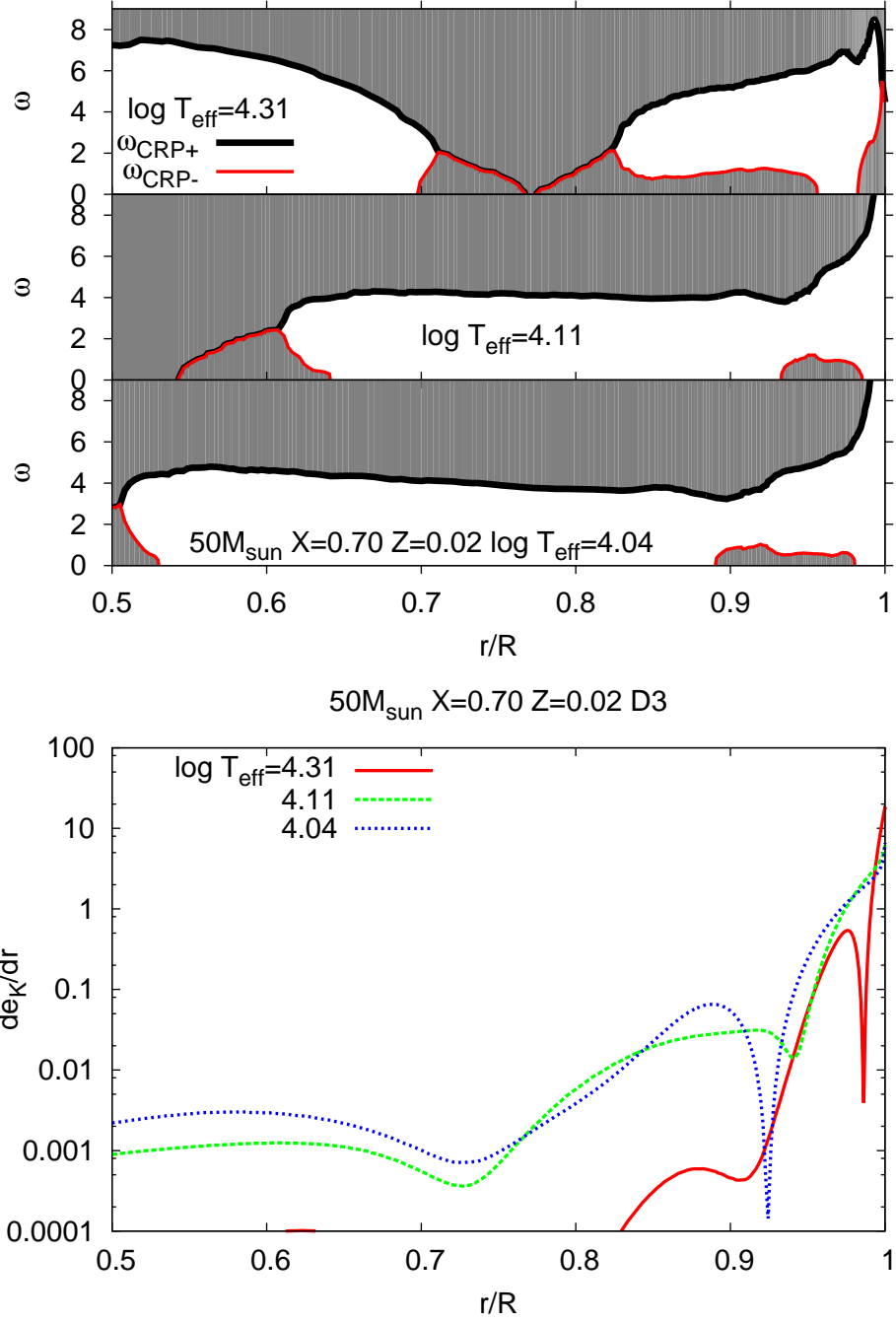
Figure 5.8: Top: Propagation diagram for radiation-pressure–dominant modes in the three evolutionary stages of a $50M_\odot$ star with $\log T_{\rm eff} =4.31$, 4.11 and 4.04. The red and the black lines are the profiles of the critical frequencies. Waves are evanescent in the grey areas, while propagative in the white areas. Bottom: Profiles of kinetic energy density for the modes on the sequence D3 in the evolutionary stages corresponding to the top panel.

$$q \equiv \chi_T \kappa_\rho \nabla, \tag{5.21}$$

$$h \equiv 2(\chi_T \nabla - 1)/q \tag{5.22}$$

Then, the condition for a propagative solution of η is

$$\omega_{\mathrm{CRP}-}^2 < \omega^2 < \omega_{\mathrm{CRP}+}^2, \tag{5.23}$$

where

$$\omega_{\mathrm{CRP}\pm}^2 = \frac{2q}{c_1}\left(A_1 \pm \sqrt{A_1^2 + A_0}\right). \tag{5.24}$$

The top panel of Fig.5.8 shows the runs of the critical frequencies $\omega_{\mathrm{CRP}\pm}$. Waves are propagative when the frequency ω is between the two critical frequencies $\omega_{\mathrm{CRP}\pm}$. In the panel, the white areas are propagation zones, while the grey areas are evanescent zones. It shows the change in the distribution of the propagation zones with the stellar evolution from $\log T_{\mathrm{eff}} = 4.31$ to 4.04. At $\log T_{\mathrm{eff}} = 4.31$, propagation zones appear at $r/R \lesssim 0.71$ and $r/R \gtrsim 0.82$. Then, the latter zone extends to the inner side with the evolution.

Similarly to the above case of the QIT modes, we perform the WKB approximation analysis for the RPD modes. In the second-order differential equation (5.17), we can interpret that the wavenumber is expressed as

$$k_{\mathrm{CRP}} = \frac{1}{r}\sqrt{A_0 + A_1 \frac{c_1 \omega^2}{q} - \left(\frac{c_1 \omega^2}{2q}\right)^2}. \tag{5.25}$$

Then, we should find the value of ω satisfying the standing wave condition,

$$\int_a^b k_{\mathrm{CRP}} dr = \left(n + \frac{1}{2}\right)\pi. \tag{5.26}$$

The solutions for this equation are plotted as the red dots in Fig.5.7. They compose steeper sequences than ones of the QIT modes. This feature is similar to that of the sequence D3. The bottom panel of Fig.5.8 shows the distribution of the kinetic energy density of the D3 mode in the evolutionary stages corresponding to the top panel. The distribution extends to the interior side with the stellar evolution as if to correspond to the extension of the propagation zone for the RPD modes, shown in the top panel of Fig.5.8.

5.4 Excitation mechanism for strange-modes without adiabatic counterparts

As discussed in §4.2.2, the unstable strange-modes having adiabatic counterparts are excited by the classical κ-mechanism. The excitation takes place in regions where the condition $d(\kappa_T + \kappa_\rho/(\Gamma_3 - 1))/dr > 0$ is satisfied. On the other hand, the excitation for the strange-modes having no adiabatic counterparts occurs even in regions where the above condition is not satisfied. It implies that the excitation mechanism should be different from the κ-mechanism. Here we try to clarify the excitation mechanism for this type of strange modes.

5.4.1 Plane-parallel approximation and two-zone model

Criterion for the instability of strange-modes without adiabatic counterparts

While numerical calculation is powerful to pursue and simulate exact physical phenomena, it often has difficulty in letting us grasp the essential physical points because of a lot of complexities. Here, we try to understand the cause for the instability of the strange-mode having no adiabatic counterparts such as the D3 instability by an analytic approach like §5.3.2. First, we follow the procedure by Saio *et al.* (1998) to obtain a criterion for the instability. Since amplitude of the strange-modes is generally confined to thin surface layers, the plane parallel approximation is available to understand the instability. We define r_0 as the distance from the stellar center at the bottom of the considered zone. We introduce the height z from the bottom. Then, we define $r \equiv r_0 + z$. We also use a mass coordinate m defined as

$$dm = \rho dz \tag{5.27}$$

so that $dM_r = 4\pi r_0^2 dm$. Then the equations of motion, continuity and the diffusion approximation are

$$\ddot{z} = -\frac{\partial p}{\partial m} - g, \tag{5.28}$$

$$\frac{\partial z}{\partial m} = \frac{1}{\rho}, \tag{5.29}$$

$$F = -\frac{4ac}{3\kappa}\frac{\partial T}{\partial m} = -\frac{c}{\kappa}\frac{\partial p_R}{\partial m} \tag{5.30}$$

where F denotes radiation flux. Taking the Lagrangian perturbations of the above three equations, and neglecting non-linear terms of the perturbed quantities, we obtain

$$-\sigma^2 \delta z = -\frac{\partial(\delta p_{\mathrm{g}} + \delta p_R)}{\partial m}, \tag{5.31}$$

$$\frac{\partial \delta z}{\partial m} = -\frac{\delta\rho}{\rho^2}, \tag{5.32}$$

$$\frac{\delta F}{F} = -\frac{\kappa_T}{4}\frac{\delta p_R}{p_R} - \kappa_\rho\frac{\delta\rho}{\rho} - \frac{c}{\kappa F}\frac{\partial \delta p_R}{\partial m} = 0 \tag{5.33}$$

where δ indicates the Lagrangian perturbation. The perturbed quantities are proportional to $\exp(i\sigma t)$. Eq.(5.33) represents the extremely nonadiabatic limit. We assume, for simplicity, the gas pressure obeys the ideal gas law,

$$\frac{\delta p_{\mathrm{g}}}{p_{\mathrm{g}}} = \frac{\delta\rho}{\rho} + \frac{1}{4}\frac{\delta p_R}{p_R}. \tag{5.34}$$

Then, we adopt a two-zone model to the above equations (5.31)–(5.33). The lower zone is bounded by z_0 and z_1, and the upper zone by z_1 and z_2. The stellar surface coincides with z_2. Both zones have the same thickness μ in terms of the mass coordinate m. We define p_{g},

p_R and ρ at the middle of each zone. We write these quantities as p_{gi}, p_{Ri} and ρ_i with $i = 1$ and 2 for the lower and upper zones, respectively. Then, Eqs.(5.31) to (5.33) are written as

$$\sigma^2 \delta z_1 = (\delta p_{g2} - \delta p_{g1} + \delta p_{R2} - \delta p_{R1})/\mu, \tag{5.35}$$

$$\sigma^2 \delta z_2 = -2(\delta p_{g2} + \delta p_{R2})/\mu, \tag{5.36}$$

$$\frac{\delta z_1}{\mu} = -\frac{\delta \rho_1}{\rho_1^2}, \tag{5.37}$$

$$\frac{\delta z_2 - \delta z_1}{\mu} = -\frac{\delta \rho_2}{\rho - 2_2}, \tag{5.38}$$

$$\frac{\kappa_{T1}}{8} \frac{\delta p_{R1}}{p_{R1}} + \frac{\kappa_{T2}}{8} \frac{\delta p_{R2}}{p_{R2}} + \frac{\kappa_\rho}{2} \left(\frac{\delta \rho_1}{\rho_1} + \frac{\delta \rho_2}{\rho_2} \right) = 0, \tag{5.39}$$

$$\frac{\kappa_{T2}}{4} \frac{\delta p_{R2}}{p_{R2}} + \kappa_\rho \frac{\delta \rho_2}{\rho_2} - \frac{2c}{\kappa F \mu} \delta p_{R2} = 0 \tag{5.40}$$

where we have used the fact that δp vanishes at the surface, and have neglected the spatial variation of κ and κ_ρ. Applying equations from (5.35) to (5.40) and (5.34) to each zone, we obtain a quadratic equation for σ^2,

$$\sigma^4 \mu^4 - \sigma^2 \mu^2 \Psi + 2\Phi_1 \Phi_2 = 0, \tag{5.41}$$

where

$$\Psi = \Phi_1 + 3\Phi_2 - 2\frac{\rho_2 f_1 Q \kappa_\rho}{s_1 s_2} \tag{5.42}$$

with

$$Q = \frac{\mu F \kappa}{2c} = \frac{p_{R,1} - p_{R,2}}{2}, \tag{5.43}$$

$$\Phi_i = \rho_i \left(p_{gi} + Q \kappa_\rho \frac{f_i}{s_i} \right), \tag{5.44}$$

$$s_i = 1 - \frac{Q \kappa_{Ti}}{4 p_{Ri}}, \tag{5.45}$$

$$f_i = 1 + \frac{p_{gi}}{4 p_{Ri}} \tag{5.46}$$

for $i = 1, 2$. We note that the value of Q roughly represents the value of p_R (see Eq.(5.30)). The determinant for the quadratic equation (5.41) is given by

$$D = \psi^2 - 8\Phi_1 \Phi_2 \tag{5.47}$$

The sign of D gives the property of the solution σ^2. That is, when $D < 0$, σ^2s are complex, while σ^2s are real when $D > 0$. It means that the necessary condition for the instability is $D < 0$. When κ_ρ is zero, the discriminant becomes $D = (\rho_1 p_{g1} - \rho_2 p_{g2})^2 + 8\rho_2 p_{g2} > 0$. Then we need a nonzero value of κ_ρ for the instability.
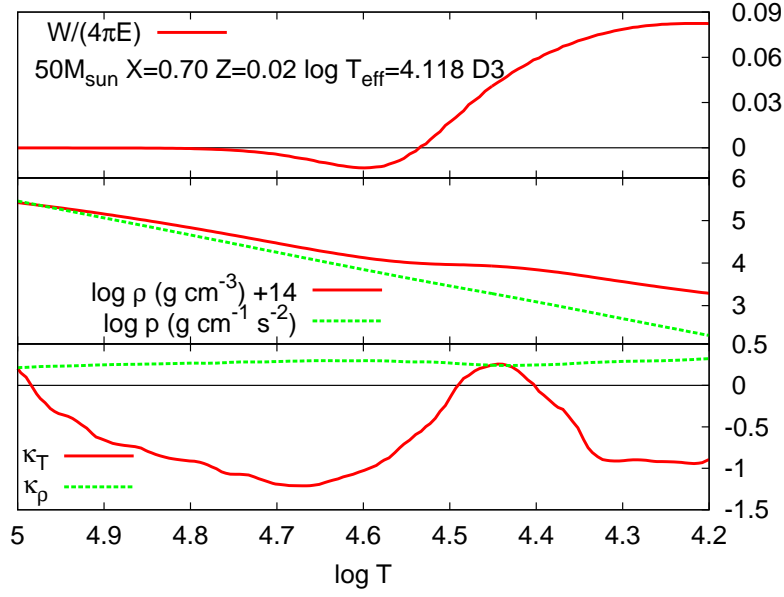
Figure 5.9: Top: work integral of the D3 strange-mode, which does not have the adiabatic counterpart, for the $50 M_\odot$ star model at a stage with $\log T_{\mathrm{eff}} = 4.118$. Middle: the pressure and the density profiles at the same evolutionary stage as the top panel. Bottom: the opacity derivatives with respect to temperature and density, κ_T and κ_ρ, at the same evolutionary stage.

Contribution of radiation pressure to the instability

As we can see in §4, the instability of the strange-modes becomes stronger with increase in the stellar luminosity. As the luminosity increases, radiation pressure contributes more and more. Here, the above discussion is further developed to investigate the contribution of radiation pressure. We introduce $\beta(\equiv p_{\mathrm{g}}/p)$ into the formulation, and assume that β and $\kappa_{T,i}$ are homogeneous through the considered two zones, i.e. $\beta = p_{g1}/p_1 = p_{g2}/p_2$ and $\kappa_T = \kappa_{T,1} = \kappa_{T,2}$. Specifically, we obtain

$$\Phi_1 = \rho_1 p_1 \left\{ \beta + (4 - 3\beta) \frac{\kappa_\rho}{8} \frac{1 - \frac{p_2}{p_1}}{1 - \frac{\kappa_T}{8}\left(1 - \frac{p_2}{p_1}\right)} \right\}, \tag{5.48}$$

$$\Phi_2 = \rho_2 p_2 \left\{ \beta + (4 - 3\beta) \frac{\kappa_\rho}{8} \frac{1 - \frac{p_2}{p_1}}{\frac{p_2}{p_1} - \frac{\kappa_T}{8}\left(1 - \frac{p_2}{p_1}\right)} \right\}, \tag{5.49}$$

$$\frac{\rho_2 f_1 Q \kappa_\rho}{s_1 s_2} = \rho_2 p_2 \frac{(4 - 3\beta)\left(1 - \frac{p_2}{p_1}\right)\kappa_\rho}{\left[1 - \frac{\kappa_T}{8}\left(1 - \frac{p_2}{p_1}\right)\right]\left[\frac{p_2}{p_1} - \frac{\kappa_T}{8}\left(1 - \frac{p_2}{p_1}\right)\right]}. \tag{5.50}$$

With the above formulations, we obtain an expression of $D_1(\equiv D/(p_1\rho_1)^2)$ as a function of β with parameters, p_2/p_1, ρ_2/ρ_1, κ_T and κ_ρ.

Fig.5.9 shows the model with an unstable D3 strange-mode. The top panel shows the work integral. It is increasing in a region from $\log T = 4.6$ to 4.2, which means that the mode
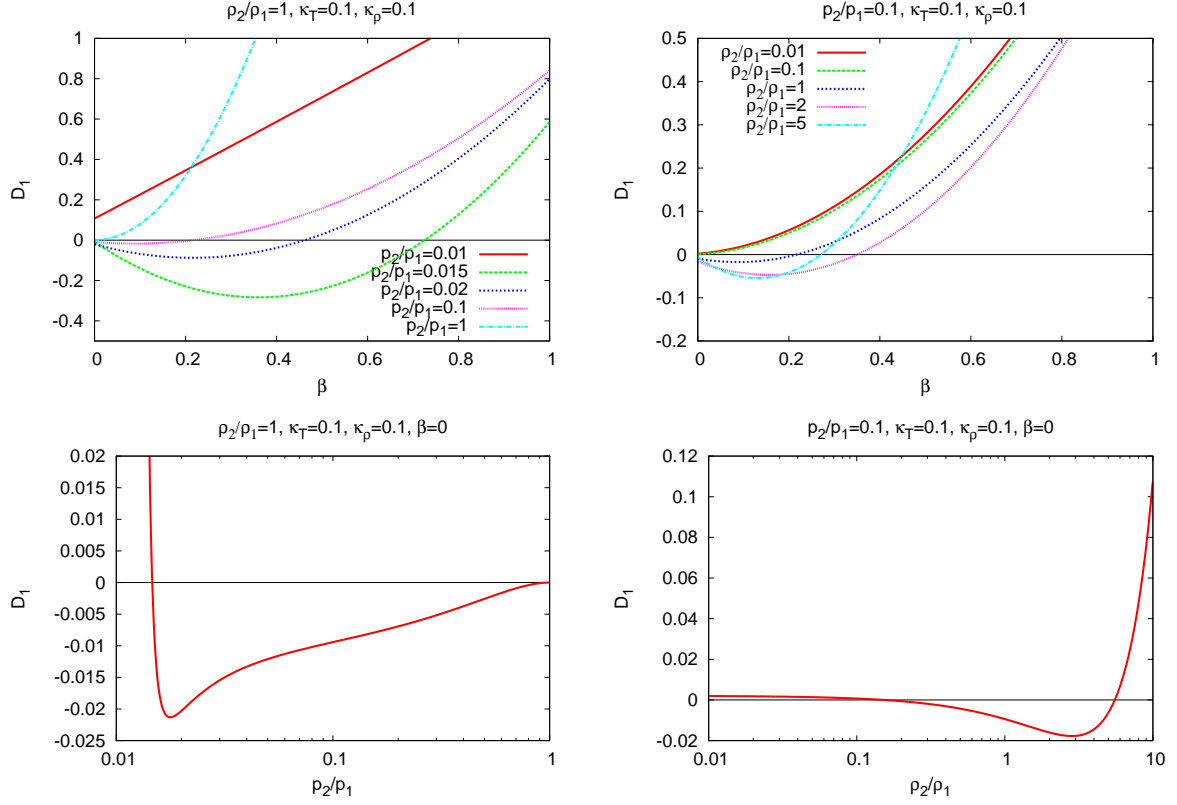
Figure 5.10: Profiles of the determinant D_1. The positive value of D_1 means that the imaginary part of the complex frequency σ is equal to zero, that is, perturbation is neutrally stable. On the other hand, the negative value of D_1 indicates a nonzero value of the imaginary part, which is necessary condition for the pulsational instability. The top two panels show D_1 as a function of β, the ratio of gas to total pressure. The top-left and the top-right panels show D_1 profiles with different values of p_2/p_1 and ρ_2/ρ_1, respectively. The left-bottom and the right-bottom panels show D_1 as a function of p_2/p_1 and ρ_2/ρ_1, respectively, with $\beta = 0$, corresponding to the limit of dominance of radiation pressure. The values of κ_T and κ_ρ are fixed to 0.1 in all the panels. The value of ρ_2/ρ_1 is fixed to 1 in the left panels, while that of p_2/p_1 to 0.1 in the right panels.

is excited there. In this region, the density profile is flat compared with the pressure profile as shown in the middle panel. This flat profile corresponds to convection. In the bottom panel, we can see that κ_ρ has an almost constant value of ~ 0.1. On the other hand, κ_T has a negative value in most of the regions, but a positive value in the middle of the excitation zone. The maximum value is almost the same as the value of κ_ρ.

Fig.5.10 shows profiles of the determinant D_1. In all of the panels, the values of κ_T and κ_ρ are fixed to 0.1. The top panels show D_1 as a function of β. The top-left panel shows D_1 with different values of the ratio p_2/p_1. The value of ρ_2/ρ_1 is fixed to 1, which is based on the flat profiles in the computed evolutionary models such as the one in Fig.5.9. The positive

value of D_1 means that the imaginary part of the complex frequency σ is equal to zero, that is, perturbation is neutrally stable. On the other hand, the negative value means that the imaginary part has nonzero value, and is the necessary condition for the instability. As we can see in the top-left panel, roughly speaking, the value of D_1 is likely to decrease with decrease in β. The negative value tends to appear with the low value of β. This means that dominance of radiation pressure is necessary for the instability. But the situation differs according to the value of p_2/p_1. The negative value of D_1 appears in the limited range of p_2/p_1. The bottom-left panel shows D_1 as a function of p_2/p_1 with $\beta = 0$, and that a negative value of D_1 appears within the range of $10^{-2} \lesssim p_2/p_1 \lesssim 1$.

The similar tendency can be found in the right panels. The top-right panel shows D_1 as functions of β with different values of ρ_2/ρ_1. When the density decreases outward like the cases of ρ_2/ρ_1 =0.1, 0.01, D_1 does not become negative for any value of β. But it can be negative when $\rho_2/\rho_1 \gtrsim 1$. This implies that a flat density profile is required for the instability. But similarly to the ratio of p_2/p_1, there is a finite range of ρ_2/ρ_1 for the negative D_1. The right-bottom panel shows that D_1 becomes negative within the range of $0.1 \lesssim \rho_2/\rho_1 \lesssim 6$ when $\beta = 0$.

Thus, dominance of radiation pressure is favorable for the instability of the strange-modes without adiabatic counterparts, although gradients of pressure and density, to which the ratios p_2/p_1 and ρ_2/ρ_1 correspond, should be within the limited ranges. In particular, a flat density profile is favorable for the instability. In §5.5.2, the effect of radiation pressure on the instability is examined with realistic stellar models.

5.4.2   Large phase lag

Eq.(5.33) represents the extremely nonadiabatic limit. In other words, heat capacity is too small to save thermal energy flowing from the stellar center. This situation would cause isothermal perturbations. Then, we neglect the term $(\kappa_T/4)(\delta p_R/p_R)(= \kappa_T \delta T/T)$. On the other hand, we consider the gradient of temperature perturbation is still substantial, and keep the term $[c/(\kappa F)]\partial \delta p_R/\partial m(= \partial \delta T/\partial T)$. Then, we have

$$\frac{\partial \delta p_R}{\partial m} = -\frac{\kappa_\rho \kappa F}{c}\frac{\delta \rho}{\rho_0}.$$ (5.51)

When the matter shrinks ($\delta \rho > 0$), the opacity increases and it should receive stronger radiation. Then the matter should save thermal energy from the radiation. But we now consider the situation that the radiation is too strong for the matter to save the transferred energy. Then, since the energy must continue to flow instead of being saved, the temperature (or radiation pressure) gradient should take place. When we assume the spatial dependence of the perturbed quantities is $\exp(ikr)$, Eq.(5.51) becomes

$$ik\delta p_R = -\frac{\kappa_\rho \kappa L}{c}\delta \rho.$$ (5.52)

This says that there is a $90°$ phase lag between δp_R and $\delta \rho$. As discussed in §3.11, work during pulsations is product of pulsational amplitude and sine of a phase lag between total
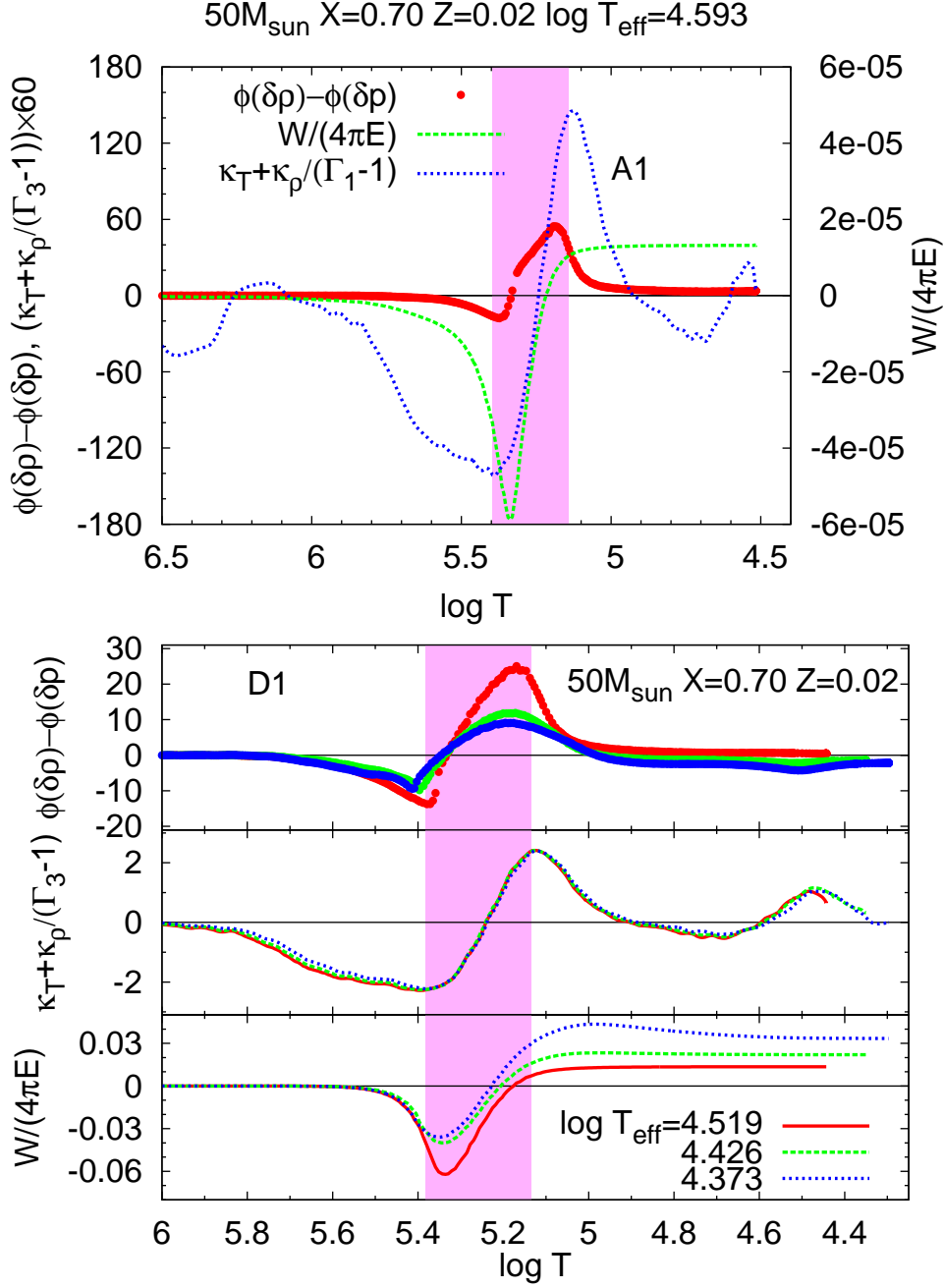
Figure 5.11: Top: Work integral and phase lag between pressure and density for the fundamental mode on the sequence A1, and the run of $\kappa_T + \kappa_\rho/(\Gamma_3 - 1)$ for $50M_\odot$ with $X = 0.70$, $Z = 0.02$. Bottom: phase lag, $\kappa_T + \kappa_\rho/(\Gamma_3 - 1)$ and work integral are shown from top to bottom. These are for the strange-mode with the adiabatic counterpart on the sequence D1 in different evolutionary stages. The magenta colored region indicates the Fe bump excitation region satisfying the condition for the κ-mechanism, $d[\kappa_T + \kappa_\rho/(\Gamma_3 - 1)]/d\log T < 0$.
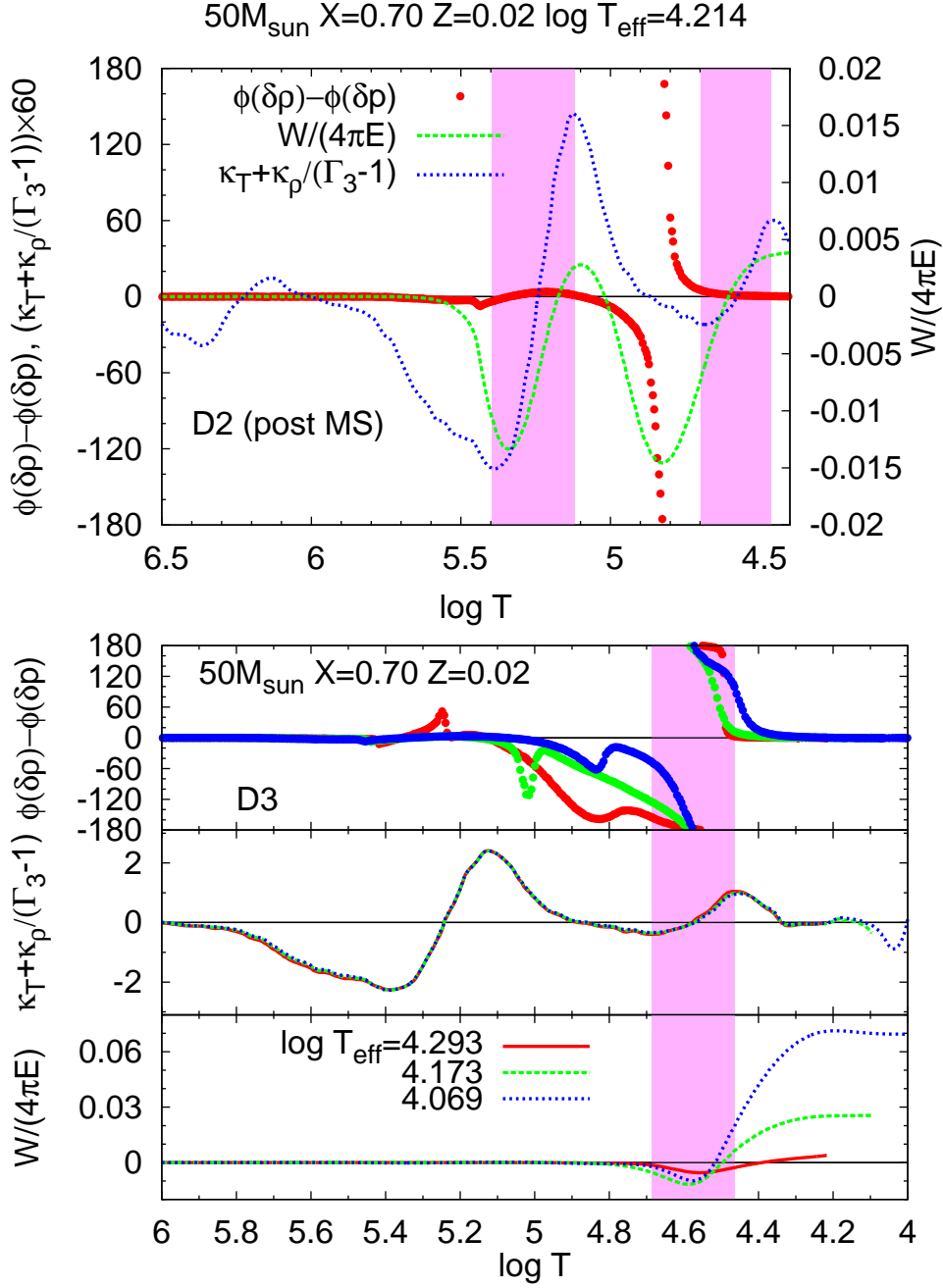
Figure 5.12: Top: Work integral and phase lag between pressure and density for the strange-mode without the adiabatic counterpart on the sequence D2, and the run of $\kappa_T + \kappa_\rho/(\Gamma_3 - 1)$ for $50M_\odot$ with $X = 0.70$, $Z = 0.02$. Bottom: phase lag, $\kappa_T + \kappa_\rho/(\Gamma_3 - 1)$ and work integral are shown from top to bottom. These are for the strange-mode without the adiabatic counterpart on the sequence D3 in different evolutionary stages. The magenta colored regions around $\log T = 5.3$ and 4.6 are the Fe and the He bump excitation zones, respectively, satisfying the condition for the κ-mechanism, $d[\kappa_T + \kappa_\rho/(\Gamma_3 - 1)]/d \log T < 0$.

pressure and density. If we assume that radiation pressure is dominant (that is, total pressure is occupied by radiation pressure), the $90°$ phase lag significantly contributes to excitation or damping. Below, phase lags are compared between ordinary modes and strange-modes in the results of the stability analysis.

First, we check a phase lag in a case of the classical κ-mechanism. The top panel of Fig.5.11 shows the property of the fundamental mode, appearing on the sequence A1. The work integral is increasing in a zone where $d(\kappa_T + \kappa_\rho/(\Gamma_3 - 1))/d\log T < 0$ is satisfied. It means that the mode is excited by the κ-mechanism. Damping takes place just inside the excitation zone, and the value of the phase lag $\phi(\delta\rho) - \phi(\delta p)$ is negative there. At the boundary between the damping and the excitation zones, the phase lag becomes zero, which means the perturbations of pressure and density are in phase. In the excitation zone, the phase lag becomes positive. It has a maximum value in the middle of the excitation zone.

The bottom panel of Fig.5.11 is the profile of the strange-mode on the sequence D1 in different evolutionary stages with $\log T_{\mathrm{eff}} = 4.519,\ 4.426,\ 4.373$. As discussed in §4, the D1 strange-mode has an adiabatic counterpart and is excited by the κ-mechanism in the early evolutionary stage. The excitation takes place within a zone with $d(\kappa_T + \kappa_\rho/(\Gamma_3 - 1))/d\log T < 0$ at least at $\log T_{\mathrm{eff}} = 4.519,\ 4.426$. The phase lag is not so large and zero at the boundary between the damping and the excitation zones similarly to the case of the fundamental mode (A1). As the stellar evolution proceeds and the effective temperature decreases, however, the excitation zone shifts to the outside of that zone. At $\log T_{\mathrm{eff}} = 4.373$, we can see that the excitation occurs also in a zone without $d(\kappa_T + \kappa_\rho/(\Gamma_3 - 1))/d\log T < 0$. This phenomenon should correspond to the fact that the D1 sequence comes to deviate from the adiabatic sequence around $\log T_{\mathrm{eff}} = 4.4 - 4.3$ shown in the modal diagram of the bottom panel in Fig.5.1.

In the case of strange-modes without adiabatic counterparts, on the other hand, profiles of phase lags are significantly different from the above. Fig.5.12 shows the profiles for the strange-modes of the sequences D2 and D3. The D2 mode has two excitation zones. The inner one at $\log T = 5.1 - 5.3$ corresponds to the Fe opacity bump. In this zone, the mode can be said to be excited by the κ-mechanism since the excitation takes place within a zone with $d(\kappa_T + \kappa_\rho/(\Gamma_3 - 1))/d\log T < 0$. On the other hand, most parts of the outer excitation zone has $d(\kappa_T + \kappa_\rho/(\Gamma_3 - 1))/d\log T > 0$ except near the top part of the zone, and the excitation should not be caused by the κ-mechanism. On the other hand, the D3 mode has only one excitation zone around the He opacity bump, and the excitation may not be the κ-mechanism.

This figure also shows that the phase lags of such modes are much larger than the above cases of A1 and D1. Although Eq.(5.52) predicts the phase lag between pressure and density is 90 degree, that of the actual eigenfunctions indeed exceeds 90 degree. At the boundary between the damping and the excitation zones, they reach 180 degree, which means density and pressure are opposite in phase instead of being in phase as seen in the κ-mechanism case.

5.5 Zero-metallicity case

Metallicity is one of important parameters to determine stellar structure and also pulsations. In massive stars, ionizations of Fe group elements substantially contribute to opacity. The ordinary modes like A1 and A2, and some of the strange-modes like D1 and (partially) D2 are excited by the κ-mechanism of the Fe opacity bump. We can expect that such modes should not be excited in case of zero-metallicity. On the other hand, the D3 mode is excited around the He opacity bump, and seems to have nothing to do with the Fe bump.

On the other hand, as an envelope should have smaller opacity, it should receive weaker radiation. This reminds us that radiation should become weaker when the metallicity is reduced. In fact, existence or non-existence of the Fe bump affects strength of radiation pressure around the He bump as shown below. Then, the instability of the D3 mode can be also affected by the metallicity. Besides, zero-metallicity very massive stars can be formed in the early Universe. Since they might significantly contribute to chemical evolution of the early Universe, their stability is worth analyzing.

5.5.1 Overview of Population III very massive stars and the ε-mechanism instability

The first-generation stars born in the early Universe are thought to have no or few heavy elements. They might play an important role in the chemical evolution of the early Universe. The initial mass function for the first-generation stars has not been definitively determined yet. However, a lack of heavy elements leads to a deficiency of the coolants in the star formation stage and hence to an expectation that very massive stars might have been formed (e.g. Bromm *et al.*, 1999; Abel *et al.*, 2002; Omukai and Palla, 2003).

Many authors have proposed and analyzed the ε-mechanism instability in very massive stars. It began to be noticed from Ledoux (1941), who suggested that the influence of high radiation pressure makes the effective ratio of specific heat γ, close to $4/3$. Then the pulsational amplitude in the core becomes comparable with that in the envelope. This situation is favorable for instability due to the ε-mechanism since excitation by this mechanism in the core can exceed flux dissipation in the envelope. Then, the following studies have carried out stability analyses in models of massive stars with solar-like composition, and proposed the critical mass above which the instability occurs (Schwarzschild and Härm, 1959; Stothers and Simon, 1968; Aizenman *et al.*, 1975; Stothers, 1992). Schwarzschild and Härm (1959) proposed that the fundamental mode becomes unstable for $\gtrsim 60 M_\odot$ with pure electron scattering opacity, while Stothers (1992) suggested that the critical mass is $121 M_\odot$ with the recent OPAL opacity table (Rogers and Iglesias, 1992). In the latter case, the fundamental mode is excited mainly by the κ-mechanism of Fe bump rather than the ε-mechanism.

In the zero-metallicity case, however, no or very little metal exists, and Fe bump does not appear. Then, the ε-mechanism is important for the instability in this case. Baraffe *et al.* (2001) analyzed pulsational stability in zero-metallicity very massive stars with $120 - 500 M_\odot$. It was found that the radial fundamental mode becomes unstable due to the ε-mechanism in the main-sequence stage. The ε-mechanism is one of excitation mechanisms for stellar

Table 5.1: Property of zero-metallicity ZAMS models.

M	R	$\log T_{\mathrm{eff}}$	$\log L$	$\log T_{\mathrm{c}}$	M_{cc}
$(M_\odot)$	$(R_\odot)$	(K)	$(L_\odot)$	(K)	$(M_\odot)$
500	10.4	5.04	7.10	8.17	445
1000	14.7	5.06	7.46	8.19	898
3000	25.6	5.07	7.99	8.21	2731

M_{cc} denotes convective core mass.

pulsations. In this mechanism, nuclear energy is the source of thermal energy, and converted into mechanical pulsation energy through heat engine mechanism. In general, nuclear energy increases with temperature. During pulsations, change in amount of nuclear energy is in phase with temperature and density. That is, more nuclear energy is given as the thermal energy source in a shrinking phase. It accelerates pulsation more than the previous cycle, and lets the amplitude grow.

Population III very massive stars might have released a significant amount of heavy elements by supernova explosions and contributed to the chemical evolution of the early Universe. The stars with $\gtrsim 300 M_\odot$ experience a core-collapse supernova explosion at the end of their life, while those with $130 - 300 M_\odot$ experience a pair-instability supernova explosion (Ohkubo *et al.*, 2009). In addition, the former stars leave intermediate-mass black holes, for which several candidates have been found as ultraluminous X-ray sources (Feng and Soria, 2011). Then, the evolution of very massive stars is very important for the above phenomena, and has been investigated by several groups (e.g. Klapp, 1983, 1984; Heger *et al.*, 2003; Bahena and Klapp, 2010).

In this study, therefore, the ε-mechanism instability is investigated in more massive stars with $500 - 3000 M_\odot$. The equilibrium models with 500, 1000 and $3000 M_\odot$ are constructed by stellar evolution code developed by Umeda and Nomoto (2002), Umeda and Nomoto (2005) and Ohkubo *et al.* (2006) during the core hydrogen-burning stage.

For the zero-metallicity stars, the only possible way of stating hydrogen burning is the pp-chain no matter how massive the star is. Hence, the temperature near the stellar center is much higher than in the case of metal-rich stars. During the pre–main-sequence stage, gravitational contraction releases energy so that the energy equilibrium in the whole star can be kept. When the central temperature reaches $\sim 10^7$ K, the pp-chain is activated and releases enough energy to stop the gravitational contraction for stars with $\lesssim 20 M_\odot$. For more massive stars, however, the gravitational contraction cannot be stopped by the pp-chain burning (Marigo *et al.*, 2001). When the central temperature reaches $\sim 10^8$K, the triple alpha reaction produces enough ^{12}C to activate the CNO cycle and then the contraction stops. Thus, the main energy source for core hydrogen-burning of Population III massive stars is the CNO cycle. Table 5.1 shows the properties of the equilibrium models for the zero-age main-sequence (ZAMS) stage, as which we define the time when the gravitational contraction stops. The central temperature is hardly different among the different mass models and corresponds to the occurrence of the triple alpha reaction. Due to the large nuclear energy generation, the convective core is very large and occupies $\simeq 90$ per cent of the stellar mass.
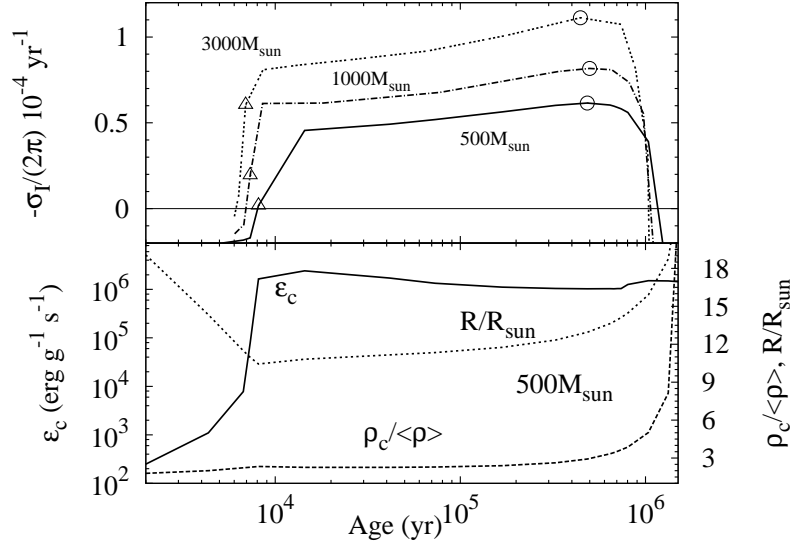
Figure 5.13: Top: variation of the growth rate of the radial fundamental mode for the 500, 1000 and $3000 M_\odot$ stars. The open triangles correspond to the ZAMS models, shown in Table 5.1, while the open circles correspond to the most unstable ones, for which the property of oscillation is shown in Table 5.2. Bottom: variation of the nuclear energy generation rate at the center ε_c, the stellar radius $R/R_\odot$ and the ratio of the central density to the average density in the whole star $\rho_c/\langle\rho\rangle$ for $500 M_\odot$.
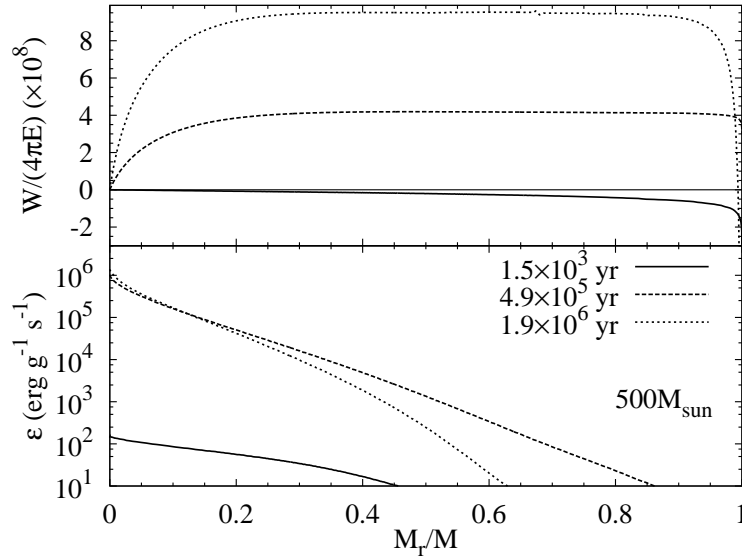
Figure 5.14: Work integral W for the radial fundamental mode (*top*) and nuclear energy generation rate ε (*bottom*) for $500 M_\odot$. The work integral is normalized with the oscillation energy of the mode in the whole star E.

Table 5.2: Property of pulsations for the models marked with open circles in Fig.5.13

Mode	Periods (h)			Growth timescale $\tau_{\rm g}$ (yr)		
	$500M_\odot$	$1000M_\odot$	$3000M_\odot$	$500M_\odot$	$1000M_\odot$	$3000M_\odot$
F	4.31	6.17	10.4	1.63×10^4	1.22×10^4	8.99×10^3
1H	1.70	2.13	2.98	-6.81×10	-2.90×10	-1.97×10
2H	1.24	1.59	2.28	-2.35	-7.12×10^{-1}	-5.45×10^{-1}

As described above, the gravitational contraction continues while only the pp-chain works. When the CNO cycle is activated, the contraction stops since the energy generation of the CNO cycle is much higher than the pp-chain and can maintain energy equilibrium without the contraction.

Such high energy generation induces vibrational instability due to the ε-mechanism. Fig.5.13 shows the variation of the growth rate, $-\sigma_I/(2\pi)$, of the radial fundamental mode for 500, 1000 and $3000M_\odot$ stars and the profiles of the equilibrium models for $500M_\odot$ star with stellar evolution. The positive value of the growth rate means instability. As the nuclear energy generation abruptly increases just before the ZAMS stage due to the onset of the CNO cycle, the growth rate does as well and becomes positive.

Fig.5.14 shows the work integral for the fundamental mode and the nuclear energy generation rate for $500M_\odot$. Before the abrupt increase in the nuclear energy generation rate, the ε-mechanism does not work efficiently in the core. However, after the increase, excitation by the ε-mechanism causes the instability.

Table 5.2 shows the results of the stability analysis of the models marked with the open circles in Fig.5.13. The growth timescale is defined as $\tau_{\rm g} \equiv -2\pi/\sigma_{\rm I}$, i.e. the e-folding time of the amplitude. The positive values of the growth time-scale mean the instability. The radial fundamental mode becomes unstable since the amplitude is relatively large in the core and excitation by the ε-mechanism there exceeds flux dissipation in the envelope. On the other hand, the other radial modes are pulsationally stable since the amplitude is much larger in the envelope.

The instability of the fundamental mode continues during the early stage of core hydrogen burning. The most unstable models, marked with the open circles in Fig.5.13, are at age 5×10^5 yr and the growth time-scale is $\sim 10^4$ yr. As pointed out by Baraffe et $al.$ (2001), the growth time-scale in the case of the ε-mechanism is relatively long. Besides, since the central temperature does not increase efficiently from 500 to $3000M_\odot$, the effect of the nuclear energy generation and the growth rate do not change with stellar mass.

After the activation of the CNO cycle, the stellar radius expands. With this, the density contrast between the inner and outer parts of the star, or the ratio of the central density to the average density in the whole star, $\rho_c/\langle\rho\rangle$, increases. This causes the amplitude in the envelope to be much larger than in the core. Fig.5.14 shows that in such a stage flux dissipation in the envelope exceeds excitation by the ε-mechanism, which works efficiently in the core. The instability disappears at age $\simeq 1 \times 10^6$ yr, or $X_c \simeq 0.4$. According to Baraffe et $al.$ (2001), the duration of the unstable phase becomes longer as the stellar mass increases from 120 to $500M_\odot$. In this mass range, the stellar structure may become more favorable to
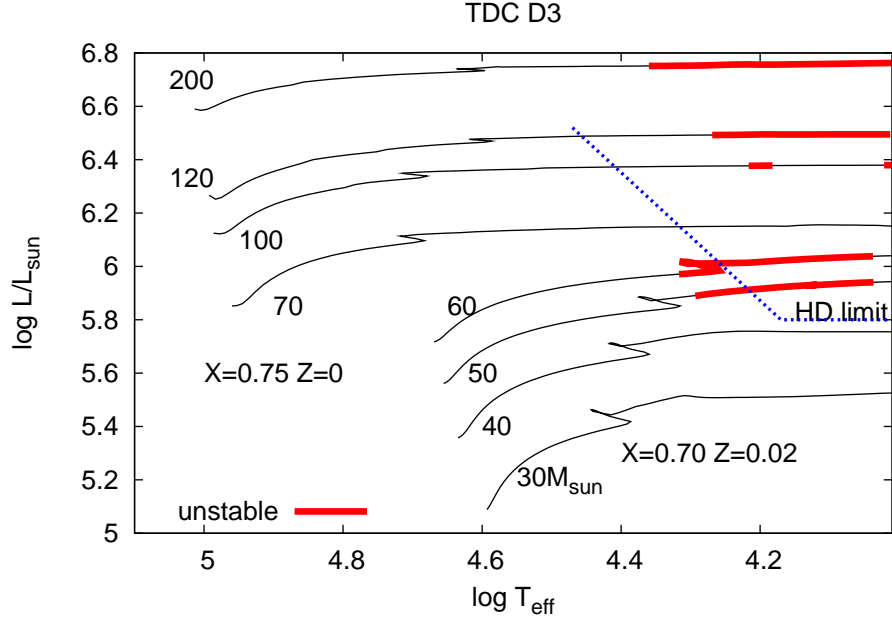
Figure 5.15: The range of D3 instability in the HR diagram for $Z = 0$ case. The $Z = 0.02$ case is also shown for comparison.

the ε-mechanism instability as the stellar mass increases. In the mass range analyzed in this study, on the other hand, the stellar structure and hence the duration of the unstable phase do not change substantially with stellar mass.

Compared with the result of Baraffe *et al.* (2001), the duration of the unstable phase for $500 M_\odot$ is longer, while the maximum value of the growth rate is lower. In their analysis, around the ZAMS stage, the growth rate initially has a positive and extremely high value, and then shows a rapid variation with time due to the adjustment of the stellar structure when the initial CNO is produced (see their fig. 4). In our analysis, on the other hand, the growth rate is initially negative and becomes positive just after the onset of the CNO cycle. This implies a difference in the methods to calculate evolutionary models.

5.5.2 Strange-mode instability in zero-metallicity case and effects of lack in heavy elements

In the main-sequence stage, only the above ε-mechanism instability takes place. Due to the lack of metal, the stars do not have the Fe bump, and the κ-mechanism does not work to excite ordinary modes and strange-modes. In the post–main-sequence stage, on the other hand, the stars have instability of the strange-modes on the sequence D3. Fig.5.15 is the result of the nonadiabatic analysis about D3. In the zero metallicity case, the other sequences, A1, A2, D1 and D2 never possess unstable modes. For this analysis, the evolutionary models are constructed by MESA.
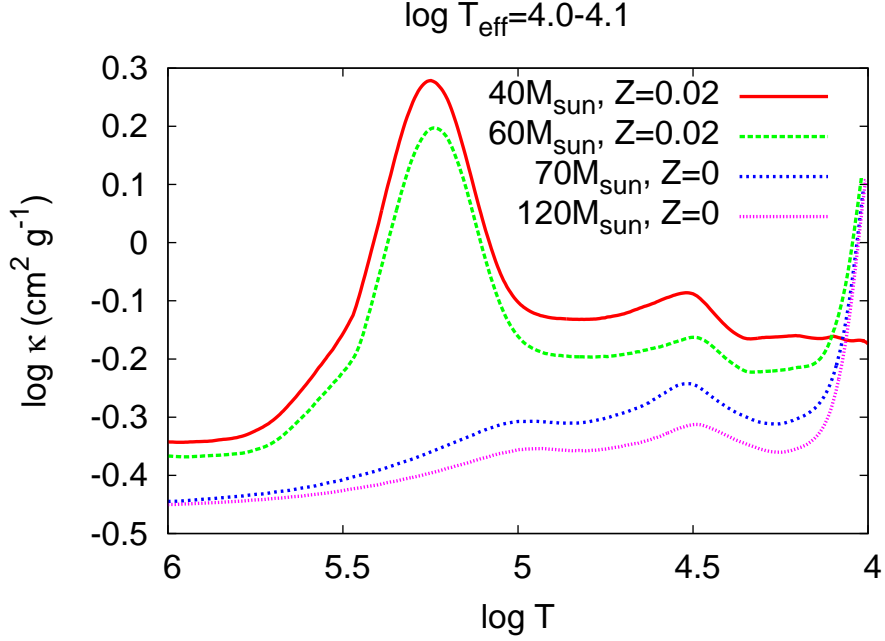
Figure 5.16: Opacity in models at $\log T_{\mathrm{eff}} = 4 - 4.1$ with $Z = 0$ and 0.02, introduced in Table 5.3.

The D3 instability appears in stars having higher luminosity compared with the Population I case. In the discussion of §4.4, we have found that the D3 modes are excited at the He bump (see the bottom panel of Fig.4.18). From this, the D3 instability seems to have nothing to do with existence or non-existence of the Fe bump. Fig.5.16 shows opacity profiles of models having similar effective temperature with $Z = 0$ and $Z = 0.02$. The representative properties of the models are introduced in Table 5.3. The models with $Z = 0.02$ have the Fe bump around $\log T = 5.2 - 5.3$, while those with $Z = 0$ do not. On the other hand, both of models with $Z = 0$ and 0.02 have the He bump. As the stellar mass and hence the luminosity increases, the opacity decreases due to decrease in density. Both in cases of $Z = 0$ and 0.02, on the other hand, the D3 mode becomes unstable as the luminosity increases.

If the opacity were related to the excitation, the derivatives would be responsible. Fig.5.17 shows the profiles of κ_T and κ_ρ in the models of Table 5.3. The top panel is for κ_T. The bump of κ_T appears around $\log T \simeq 4.5$, corresponding to the second helium ionization zone both in

Table 5.3: Stellar models for comparison in different metallicity

$M/M_\odot$	X	Z	$\log T_{\mathrm{eff}}$	$\log L/L_\odot$	D3
40	0.70	0.02	4.01	5.76	stable
60	0.70	0.02	4.09	6.03	unstable
70	0.75	0	4.09	6.15	stable
120	0.75	0	4.08	6.49	unstable
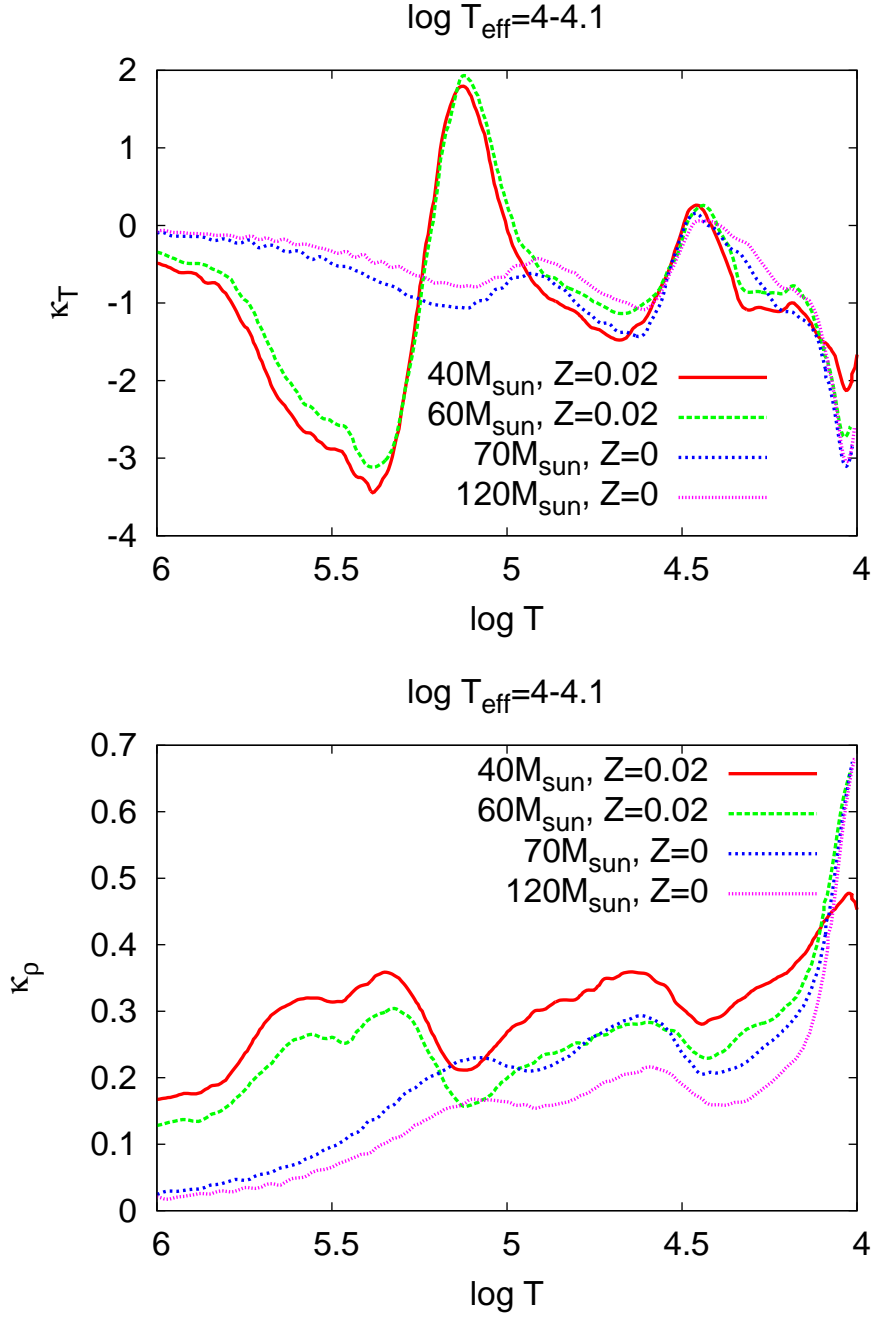
Figure 5.17: First derivatives of opacity, κ_T and κ_ρ in the same models as in Fig.5.16.
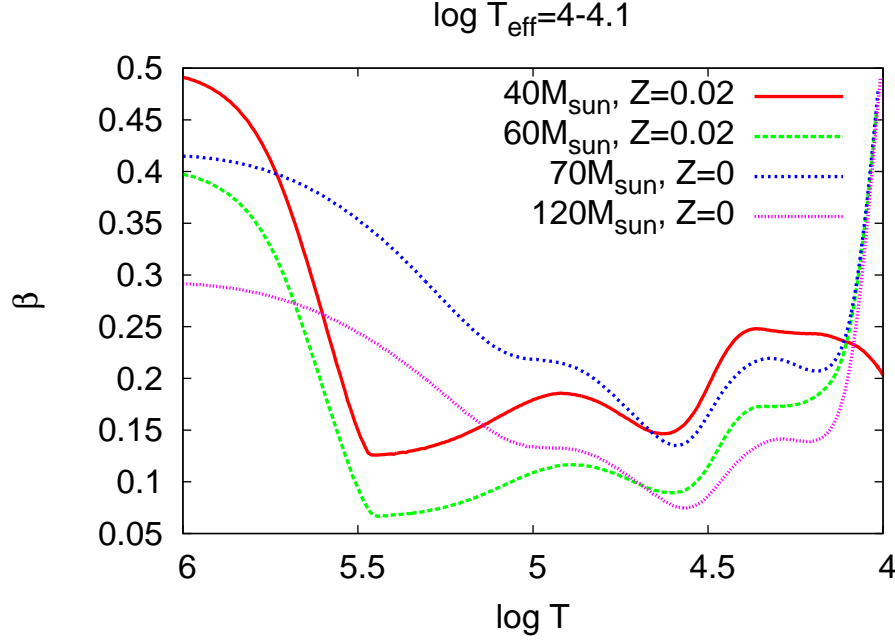
Figure 5.18: Ratio of gas to total pressure, $\beta \equiv p_{\mathrm{g}}/p$ in the same models as in Fig.5.16.

Table 5.4: Property of instability of D3 strange-mode in $Z = 0$ case

$M(M_\odot)$	age (yr)	$\log T_{\mathrm{eff}}$	Periods (h)	Growth timescale τ_{g} (yr)
120	2.8×10^6	4.191	290	1.87
200	2.3×10^6	4.201	378	0.88

the cases of $Z = 0$ and 0.02. For $Z = 0.02$, another bump appears around $\log T = 5.1 - 5.2$, corresponding to the Fe group element ionization zone. As mentioned above, the excitation of the D3 mode takes place around the second helium ionization zone. For $Z = 0.02$, the D3 mode is stable in the $40M_\odot$ model, while unstable in the $60M_\odot$. But there is no substantial difference between the κ_T profiles of the two models. The same is true between the $70M_\odot$ and $120M_\odot$ models with $Z = 0$. The bottom panel shows the profile of κ_ρ. Similarly to the case of κ_T, there is no significant difference between stable and unstable models, though more luminous models are likely to have lower values of κ_ρ.

By the way, existence or non-existence of the Fe bump should causes some differences in envelope properties. As a matter of fact, as an envelope has larger opacity, it becomes subjected to radiation pressure. Fig.5.18 shows the ratio of gas to total pressure, $\beta \equiv p_{\mathrm{g}}/p$. The smaller value of β, the more radiation pressure dominates over gas pressure. The $60M_\odot$, $Z = 0.02$ model and the $70M_\odot$, $Z = 0$ model have the close luminosity in addition to the close effective temperature. But the former model has much stronger dominance of radiation pressure due to the Fe bump. Similarly, when we compare stable and unstable models in the same metallicity, the unstable models have the stronger dominance. This implies that radiation pressure could be the cause for the D3 instability.

The growth rate of the D3 mode is extremely high compared with that of ordinary modes such as the unstable fundamental mode excited by the ε-mechanism (§5.5.1). Then, its instability might be influential on the stellar evolution as discussed at the last of §4.4. The growth timescale of the D3 is ~ 1 yr (Table 5.4), while that of the fundamental mode excited by the ε-mechanism is $\sim 10^4$ yr (Table 5.2). In the Population III case, particularly, stars with the initial mass of $130 - 300 M_\odot$ are thought to experience pair-instability supernova (PISN) explosion, which provides peculiar chemical composition, which is very different from one provided by normal core collapse supernovae. But recent detailed comparisons between the observations of extremely metal poor (EMP) stars (Cayrel *et al.*, 2004) and the nucleosynthesis yields of PISN models (Umeda and Nomoto, 2002; Heger and Woosley, 2002) have shown that the PISN yields are not suitable to reproduce the abundance patterns of EMP stars. The instability of the D3 mode might affect the theoretical scenario of the evolution toward the PISN, and more detailed investigations such as nonlinear analyses are worth doing.

5.6   Conclusion

In this section, we have discussed the cause for the existence and the pulsational instability of strange-modes. There are two types of strange-mode, ones with and without an adiabatic counterpart. First, we discussed one with an adiabatic counterpart. The existence of this type can be explained by the profile of the critical frequency derived from the adiabatic WKB approximation. In the lower mass stars, density monotonically goes down outward. As the stellar mass increases, radiation pressure around the opacity bump comes to dominate over gas pressure, and to push the outer layer more strongly. Then, the density profile becomes flat, since the outer layer needs gravity enough to compete with the radiation pressure. This makes a valley of the critical frequency. Waves are trapped there, and the strange mode appears with large amplitude in this valley. This type of strange-mode is excited by the κ-mechanism as discussed in §4.2.2.

Secondly, we have discussed the strange-modes without adiabatic counterparts. First, we have considered the cause for the existence of the modes. The two types of the WKB approximations are carried out along the model sequence of a massive star evolution for the quasi-isothermal (QIT) and for the radiation-pressure–dominant (RPD) modes. In a modal diagram for the massive star model sequence, the behavior of the QIT modes represents stable strange-modes without adiabatic counterparts, while the RPD modes correspond to unstable ones, that is, the D3 mode. Next, we have investigated the cause for the instability by the local analysis, and found that dominance of radiation pressure is required for the instability. The extremely nonadiabatic situation makes waves having a large phase lag between radiation pressure and density, since flowing radiation flux is too strong for matter to save the flux energy. Profiles of the phase lags are carefully investigated, and it has been found that it changes in the range of from 0 to 180 degree in the excitation zone unlike the κ-mechanism case. The large phase lag substantially contributes to strong excitation, when radiation pressure is dominant.

Finally, we analyzed pulsational instability of the zero-metallicity very massive stars. The ordinary modes and some of strange-modes are excited by the κ-mechanism of the Fe opacity

bump in case of Population I composition. In the zero-metallicity case, the κ-mechanism of the Fe opacity does not work, and these modes become no longer unstable. On the other hand, the D3 mode becomes unstable, but in higher luminosity stars compared with the Population I case. Although the D3 mode is excited around the He bump, its instability is indeed affected by the existence or non-existence of the Fe bump, since the Fe bump leads to dominance of radiation in massive star envelopes in the metal-rich case. In the zero-metallicity case, the D3 mode is unstable for $M \gtrsim 100 M_\odot$. In this mass range, the ε-mechanism instability also appears in the main-sequence stage. But the D3 mode instability has much higher growth rate than the ε-mechanism instability, and might affect the evolutionary scenario toward the pair-instability supernova (PISN). Although PISN has the possibility to provide peculiar chemical abundance to their surroundings, its existence is controversial. The result of this study is in disagreement with the existence of PISN.

<div style="text-align: right; font-size: 3em;">6</div>

Stability analysis of nonradial pulsations

6.1 Introduction

Today, many nonradial pulsators are known as well as radial pulsators. While Cepheids, RR Lyrae stars mainly show radial pulsations, other main sequence stars, red giants and white dwarfs experience nonradial pulsations. Radial pulsations take place by propagation of acoustic waves. On the other hand, nonradial pulsations do by that of internal gravity waves besides acoustic waves. Eigenmodes of acoustic and internal gravity waves are called p and g modes, respectively. Nonradial modes extend our possibility to extract information of stars. Observed nonradial pulsations often show so-called "rotational splitting", which appears in frequency spectra. The width of the splitting indicates rotational frequency. The Sun shows a lot of nonradial p modes. By use of inversion techniques with the modes, the interior profiles of e.g. internal rotation and acoustic velocity has been obtained.

As for hot massive stars, β Cephei variables are classically-known pulsators. They have masses with $M = 8 - 18 M_\odot$. The period is in the range of 2 to 8 hours. The corresponding unstable modes are low-order[1] radial modes, and nonradial p and g modes. The excitation of β Cephei pulsations had been a long-standing problem, since old opacity tables had underestimated the opacity due to the Fe group elements. In the early 1990's, the OPAL and the OP opacity projects provided new opacity tables, in which the opacity of the Fe group elements are enhanced compared with in the old tables. That gave the Fe opacity bump around 200,000 K in the stellar interiors. Especially, it drastically changed models of hot massive stars. Until then, they are believed to have radiative envelopes. But it was found that the Fe bump makes a convection zone having a certain size. Besides, stability analyses demonstrated that the

---

[1]Roughly speaking, it means low number of nodes. With increase in the order, a frequency of p and g modes becomes higher and lower, respectively.

bump leads to the κ-mechanism excitation against the low-order p and g modes, and provides the β Cephei type pulsations.

On the other hand, Waelkens (1991) brought attention to a group of seven young Population I variable mid-B stars, and introduced the term slowly pulsating B (SPB) stars. They show high-order g mode pulsations with the period between 0.5 and 5 days. Their mass is in the range of $2 - 7M_\odot$. Unstable modes of SPB stars are also excited by the κ-mechanism of the Fe opacity bump. Recently, Saio *et al.* (2006) and Godart *et al.* (2009) explained a SPB supergiant (SPBsg) star, HD 163899, in the post main-sequence stage are pulsating with high-order g modes. In such an evolutionary stage, the g modes had been believed to experience strong radiative damping in the core, which has the high density gradient, and never to become unstable, even if they are excited at the Fe bump in the envelope. But if the star has an intermediate convection zone above the hydrogen burning shell, the g mode waves can be reflected by the convection zone, and avoid the damping in the core. This implies the existence of the intermediate convection zone in spite of uncertainties on treatment of convection in stellar models.

In this chapter, we discuss results of stability analysis of nonradial pulsations in hot massive stars. Even though convection zones of the hot massive stars are not so thick as those of the red giants, the Fe opacity bump gives a certain size of convection zone. The pulsations of β Cephei and SPB stars and strange-modes are excited there. Then, the analysis is carried out with the FC approximation and TDC, and effects of convection is discussed. As explained in §3, nonradial pulsations have a number of patterns of node lines on a spherical surface. Then, the dependence of nonradial strange-modes on the spherical degree is also discussed.

6.2   Theoretical unstable nonradial modes

Stability analyses for nonradial pulsations are carried out with the FC approximation and TDC. This study adopts the Cowling approximation, under which the perturbation of gravitational potential is neglected. The corresponding differential equation system is Eqs.(3.135)-(3.138). For the FC approximation, we set $\delta L_C = 0$ and $F'_{C,h} = 0$. Here we discuss the main sequence stage of a $40M_\odot$ star. Fig.6.1 shows modal diagrams of $l = 2$ modes for the $40M_\odot$ main-sequence stage. The abscissa is the effective temperature, and the left and right sides correspond to the ZAMS and the terminal age of main sequence (TAMS) stages. The top panel shows solutions by the adiabatic approximation with the differential equation system Eqs.(3.143)-(3.144). In the middle panel, we can see a descending sequence having green dots, which indicate unstable modes with high growth rates. It corresponds to the strange-mode sequence D1 in the radial pulsation case. As we can see by comparing with the top panel, this sequence has a corresponding adiabatic sequence like the sequence D1 of the radial case. Many ascending sequences cross the descending sequence D1. Around the cross points of the ascending sequence and the sequence D1, modes on the former become unstable. They are excited by the κ-mechanism of the Fe bump, and correspond to the β Cephei type pulsations. The ascending sequences correspond to g modes. In general, g modes have large amplitude in deep interior compared with p modes in the early stage of main-sequence. But they come

to have large amplitude in the outer envelope including the Fe opacity bump with the stellar evolution.

Fig.6.2 shows propagation diagrams at the two evolutionary stages with $\log T_{\text{eff}} =$ 4.634 (ZAMS), 4.488. In these diagrams, the N^2 profile is shown only in the range where the value of N^2 is positive. In the top panel, N^2 is negative in the range of $0 < r/R \lesssim 0.37$, which corresponds to the convective core. On the other hand, the zone with $N^2 < 0$ at $r/R \simeq 0.97$ corresponds to the convective zone around the Fe bump. With the stellar evolution, the convective core shrinks due to decrease in opacity. In the deep interior, the electron scattering opacity is dominant, and expressed as $0.2(1 + X)$ cm^2 g^{-1}. It means that consumption of hydrogen abundance due to nuclear burning reduces the opacity. Then, at the stage with $\log T_{\text{eff}} = 4.488$, the radius of the convective core is less than $r/R = 0.1$. Since the convective core is shrinking with converting hydrogen to helium, a mean molecular weight gradient (μ-gradient) is generated just above the convective core. This gradient makes a large density gradient, and hence raises up the Brunt-Väisälä frequency. Above the μ-gradient zone, an additional convective zone appears at $r/R \simeq 0.15$ due to strong radiation pressure. It makes the μ-gradient propagation zone separated from the above thick propagation zone $(0.18 \lesssim r/R \lesssim 0.7)$.

The blue line segments indicate the frequency and the propagative range of the g_2 mode, indicated as red crosses in Fig.6.1. At the ZAMS stage, the g_2 mode is propagative in the range of $0.4 \lesssim r/R \lesssim 0.8$. As we can see in Fig.6.1, the frequencies of the g modes steeply increase compared with those of the p modes. The increase in the g-mode frequencies is caused by the growth of the μ-gradient just above the convective core. In this situation, some of g modes become propagative in the outer p-mode propagation zone as shown in the bottom panel of Fig.6.2.

The top panel of Fig.6.3 shows work integrals for representative four unstable modes. The top part of the panel shows that the strange-mode is strongly excited at the Fe bump. The situation is similar to the case of the radial D1 mode in §4. The bottom panel of Fig.6.3 shows the distribution of the kinetic energy density de_K/dr. The top part of the bottom panel shows that energy of this mode is mainly distributed in the outer envelope.

The second top part of each panel shows the ordinary g mode having a frequency $\omega =$

Table 6.1: Representative unstable modes ($l = 2$) at the stage with $\log T_{\text{eff}} = 4.488$ for $40 M_\odot$, shown in Fig.6.3 and 6.4.

ω_R	ω_I	Period(hr)	e-folding time (yr)	remarks
3.064	-9.435E-2	1.53778E+01	5.70000E-02	D1 strange-mode by FC
3.147	-1.255E-2	1.49714E+01	4.28470E-01	by TDC
2.133	-2.275E-7	2.20849E+01	2.36353E+04	β Cephei-type by FC
2.133	-6.966E-8	2.20849E+01	7.72026E+04	by TDC
8.885E-1	-3.101E-6	5.30228E+01	1.73495E+03	SPB-type by FC
8.885E-1	-2.801E-6	5.30231E+01	1.91970E+03	by TDC
8.189E-1	-1.284E-2	5.75300E+01	4.19006E-01	strange-mode by FC
7.988E-1	-2.019E-2	5.89782E+01	2.66275E-01	by TDC
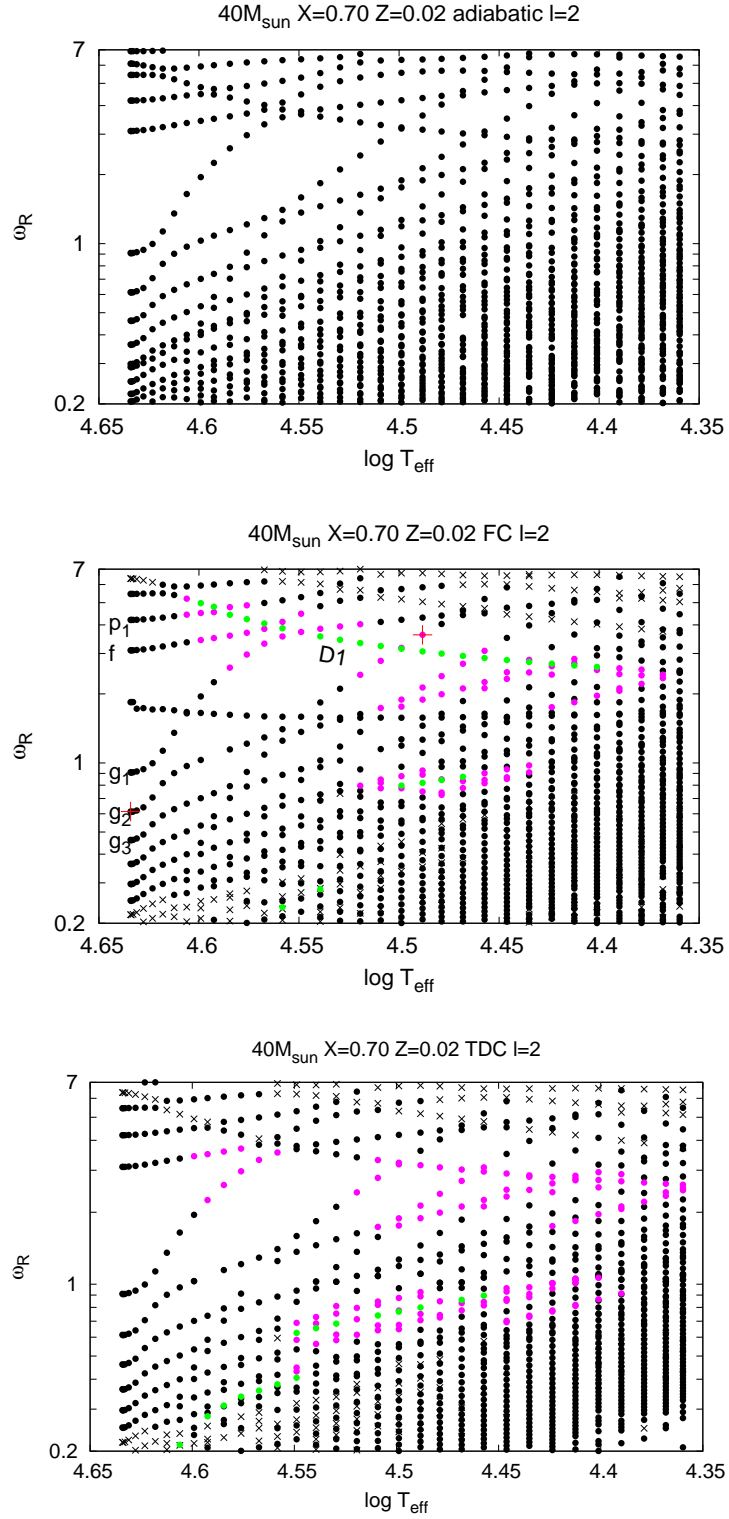
Figure 6.1: Modal diagrams of $l = 2$ modes in the $40 M_\odot$ main-sequence stage by adiabatic (*top*) and FC approximation (*middle*), and TDC (*bottom*). The definition of symbols in the middle and the bottom panels are the same as Fig.4.2.
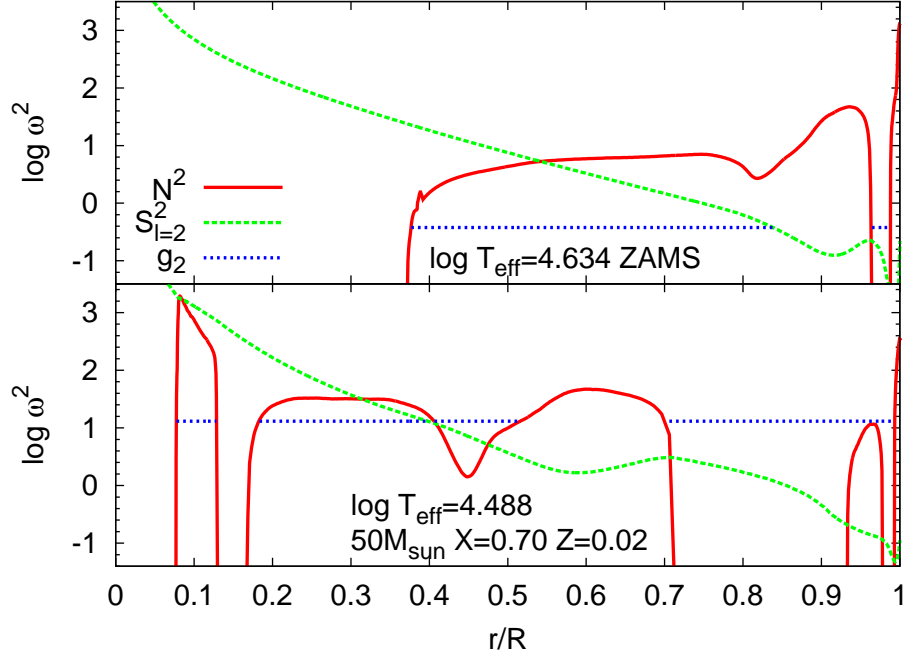
Figure 6.2: Propagation diagrams at the evolutionary stages with $\log T_{\text{eff}} = 4.634(\text{ZAMS})$, 4.488. The abscissa is the distance from the stellar center divided by the stellar radius. The blue line segments indicate the frequency and the range of the propagation for the g_2 mode, indicated as the red cross in Fig.6.1.

2.133, which is close to the frequency of the above strange-mode. This mode experiences the strong damping in the deep interior at $\log T = 7.3 - 7.4$. The energy of this mode is mainly trapped in the μ-gradient zone as shown in the bottom panel. But even though the amplitude in the outer envelope is much small, the excitation at the Fe bump overcomes the radiative damping in the μ-gradient zone. As the reason for this, the outer zone has smaller density, and excitation or damping work more easily. This mode is categorized as a low-order g mode, corresponding to the β Cephei-type pulsations.

In the modal diagrams of Fig.6.1, there is another group of unstable modes with $\omega \simeq 0.7$. They are high-order g modes, and most of them correspond to SPB-type pulsations. The representative mode is shown in the third top part of each panel of Fig.6.3. The mode energy is trapped mainly in the μ-gradient, but the excitation at the Fe bump overcomes the damping in the μ-gradient zone like the above case.

On the other hand, we can see green dots, which indicates unstable modes with high growth rates, in that group of the unstable high-order g modes in Fig.6.1. This mode may be categorized as a strange-mode, since it is strongly excited at the Fe bump, and its kinetic energy is mainly distributed there like the D1 strange-mode as shown in the bottom part of each panel of Fig.6.3. Unstable modes with $\omega_R = 0.2 - 0.4$ appearing in the earlier stages with $\log T_{\text{eff}} \gtrsim 4.55$ are the same type. Fig.6.4 displays the propagative ranges of the four unstable modes shown in Fig.6.3. All of the four modes are propagative both in the inner and
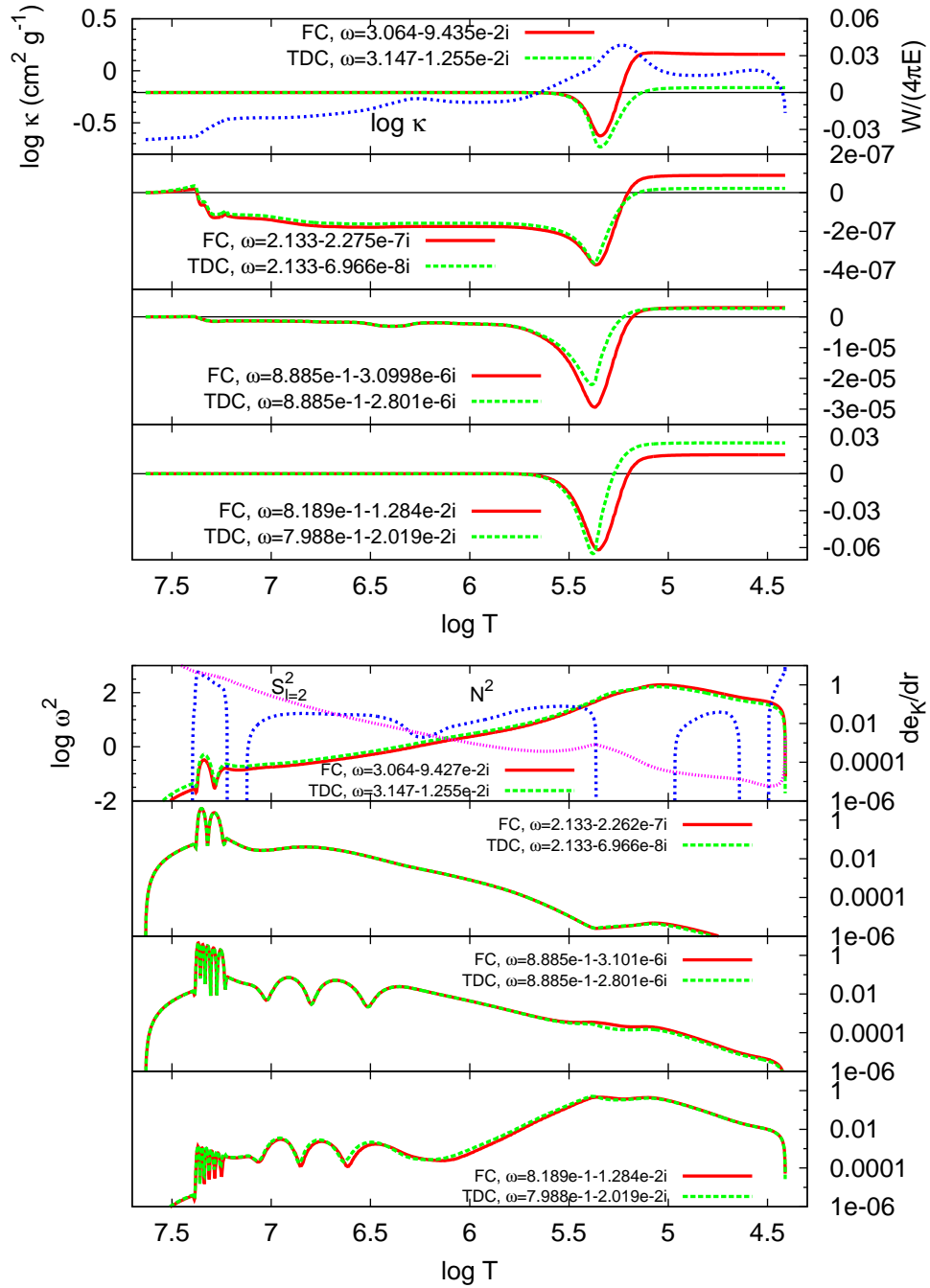
Figure 6.3: Work integrals (*top*) and kinetic energy density distributions (*bottom*). Each panel shows the strange-mode ($\omega \simeq 3.1$), the β Cephei type pulsation ($\omega = 2.133$), the SPB type pulsation ($\omega \simeq 8.885 \times 10^{-1}$), and the high-order g mode with the high growth rate ($\omega \simeq 8 \times 10^{-1}$) from top to bottom. The red and the green lines correspond to FC and TDC, respectively. The top part of the top panel shows the opacity κ profile as the blue line, while that of the bottom panel the Brunt-Väisälä frequency N and the Lamb frequency for $l = 2$, $S_{l=2}$, as the blue and the magenta lines, respectively. The equilibrium model is for the $40 M_\odot$ star at the evolutionary stage with $\log T_{\text{eff}} = 4.488$.
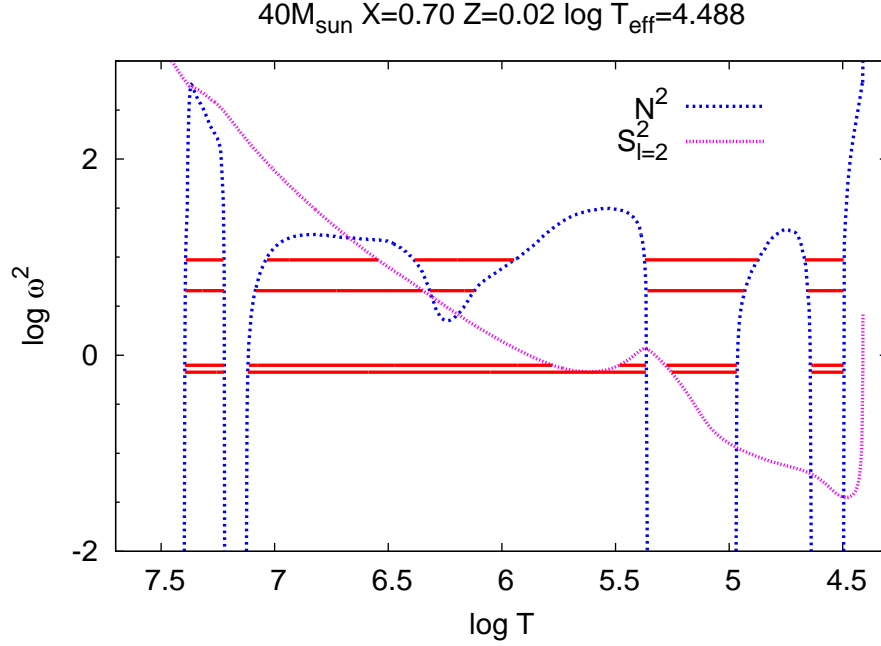
Figure 6.4: Propagation diagrams at the evolutionary stages with $\log T_{\mathrm{eff}} = 4.488$. The abscissa is the temperature. The high and the low temperature sides correspond to the center and the surface, respectively. The red line segments indicate the frequency and the range of the propagation for the four eigenmodes obtained by FC introduced in Fig.6.3 and Table 6.1.

in the outer zones. But there are several evanescent zones in between them, which act as potential barriers. They generate the two types of modes, ones trapped in the deep interior and in the envelope.

Table 6.1 gives the e-folding times of the unstable modes. Those of the strange-modes is in the order of 0.1 yr, and much shorter than those of the ordinary modes, $\sim 10^3 - 10^4$ yr. But since the TAMS age of the $40M_\odot$ is about 4×10^6 yr, the ordinary modes also can grow to finite amplitude.

6.3   Effects of convection

As we can see in Figs.6.1 and 6.3, the D1 strange-mode and the β Cephei-type pulsations are less unstable in the TDC case. Like radial modes, convection stabilizes these types of modes while competing with the excitation by the κ-mechanism. Comparing with the work integrals by FC and TDC, the damping effect by convection is the largest for the D1 mode having the highest frequency. On the other hand, the effect is much smaller for the other lower frequency modes.

Fig.6.5 compares the reciprocal of the convective timescale and the pulsational frequencies. The convective timescale becomes longer, and finally infinity toward the end of the convection
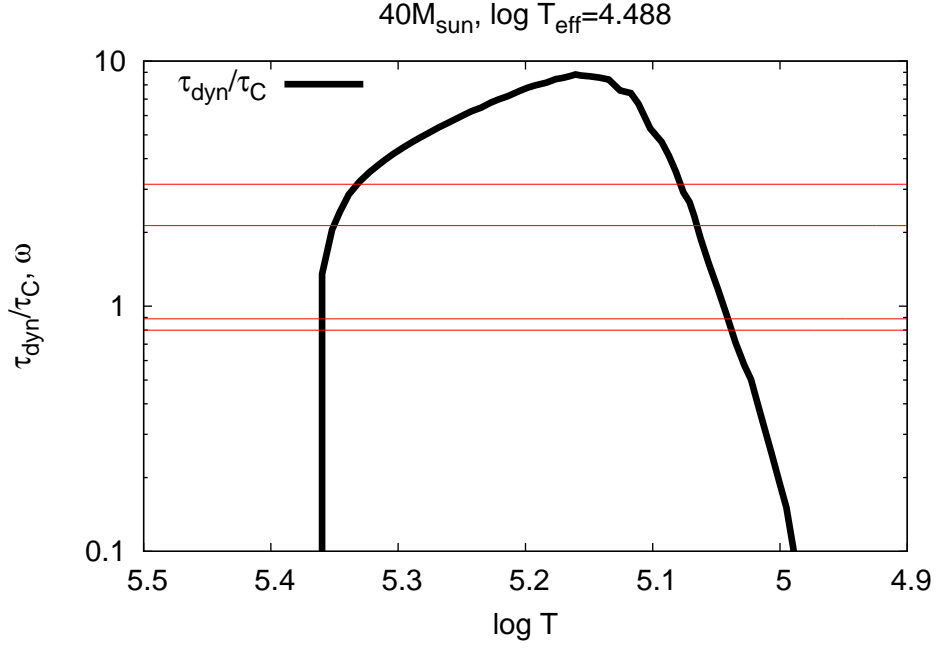
Figure 6.5: This figure compares the reciprocal of convective timescale τ_C with the frequencies of the four unstable modes introduced in Table 6.1 and Fig.6.3. The values are normalized by multiplying the dynamical timescale $\tau_{\rm dyn} = \sqrt{R^3/(GM)}$.

zone, while it becomes shortest in the middle. In the limit of much long convective timescale, convection does not react to pulsational changes. In the opposite limit, it is very sensitive to the changes. We may be able to say that convection is most effective when the convective timescale is comparable to the pulsational period. This discussion has the analogy to that about the effective excitation zone of the κ-mechanism, which works effectively in zones where a pulsational period and thermal timescale are comparable. If the thermal timescale is much longer than the period, the situation is close to an adiabatic process, and thermal flux cannot change effectively enough to enhance the heat engine mechanism. On the other hand, if the thermal timescale is much shorter than the period, the situation becomes very nonadiabatic. That is, thermal energy flows too fast that matter can save the energy, and that the heat engine mechanism can work efficiently. Similarly, convection with extremely long timescale might not be able to produce changes in convective flux like the adiabatic case, while that with extremely short timescale might cause too fast changes in the convective flux to cause the heat engine mechanism.

In this case, we can guess that the convective timescale is, in a whole, comparable to the period of the high frequency modes such as the D1 strange-mode, and that much shorter than that of the high order g modes including SPB-types.

Such a tendency was also found in pulsations of δ Scuti and γ Doradus stars by Dupret et al. (2005). By the FC approximation, p modes of δ Scuti stars are unstable beyond the observed red edge of the classical instability strip. But their TDC computation demonstrates

that the convective damping stabilizes the δ Scuti p modes, and realized the red edge of the theoretical instability domain. While convection hardly affect the stability of high-order g modes corresponding to γ Doradus pulsations. Instead, they are excited mainly by the convective blocking as proposed by Guzik *et al.* (2000).

In Fig.6.1, we can find that high-order g modes have wider instability range in the TDC case than in the FC case. Fig.6.6 compares two high-order g modes obtained by FC and TDC at the evolutionary stage with $\log T_{\text{eff}} = 4.424$. In this stage, unstable high-order g mode exists for TDC, while does not for FC (see Fig.6.1). Although the two modes have almost the same frequencies, $\omega \simeq 3.59$, the one by TDC is pulsationally unstable, while the one by FC is stable. The top panel of Fig.6.6 shows that the kinetic energy distributions resemble each other in a whole, but are different in the outer envelope. But the eigenfunctions of luminosity perturbations are significantly different due to effects of convection (the middle panel of Fig.6.6). Then, even though the convective effects on excitation and damping is weak for the high-order g modes, the distribution of amplitude can be affected by convection, and, as a result, becomes favorable for the κ-mechanism excitation compared with the FC case.

6.4 l-dependence of strange-modes

Nonradial modes have a number of patterns for node lines on a horizontal surface. The spherical degree l represents the number of the node lines (see Fig.3.3)[2]. $l = 0$ corresponds to radial pulsations. When we change l, profiles of eigenfunctions vary not only on a surface, but also along the radial direction. This should cause changes in pulsational stability. Here we discuss l-dependence of the strange-mode on the sequence D1 in the main-sequence stage.

Fig.6.7 shows $l = 2$ modes in the main-sequence stage of the $50M_\odot$ star. Here the modal diagram displays only modes having over 0.2% of their kinetic energy in the p-mode propagation zone in order to pursue the sequence of the strange-modes. This result is obtained by TDC. In this diagram, only the D1 shows instability among the descending sequences. This sequence has the adiabatic counterpart, and the instability is excited by the κ-mechanism. Fig.6.8 shows the growth rates of the D1 modes for $l = 0 - 4$. The radial mode ($l = 0$) is unstable all during the main-sequence stage, and has the highest growth rate, and the e-folding time is in the order of 10^{-1} yr. As the l increases, the growth rate decreases, and finally the mode keeps stable with $l = 4$ all during the main-sequence stage.

Fig.6.9 compares the modes with $l = 0 - 4$ at an evolutionary stage with $\log T_{\text{eff}} = 4.496$, of which properties are summarized in Table 6.2. The top panel shows a propagation diagram. The critical frequency for $l = 0$ shown as a red line is the lower limit frequency for propagative waves. The profile of the critical frequency forms a valley in the outer envelope, and implies that waves having $\log \omega^2 \simeq 1$ is trapped there. As for $l = 1 - 4$, the Brunt-Väisälä frequency N^2 and the Lamb frequency S_l^2 are given as the critical frequencies. As the spherical degree l increases, the Lamb frequency is shifted up. Due to this, the outer p-mode propagation zones

---

[2]Eigenfrequencies and radially dependent parts of eigenfunctions never depends on the azimuthal order m when we do not consider rotation and magnetic field.
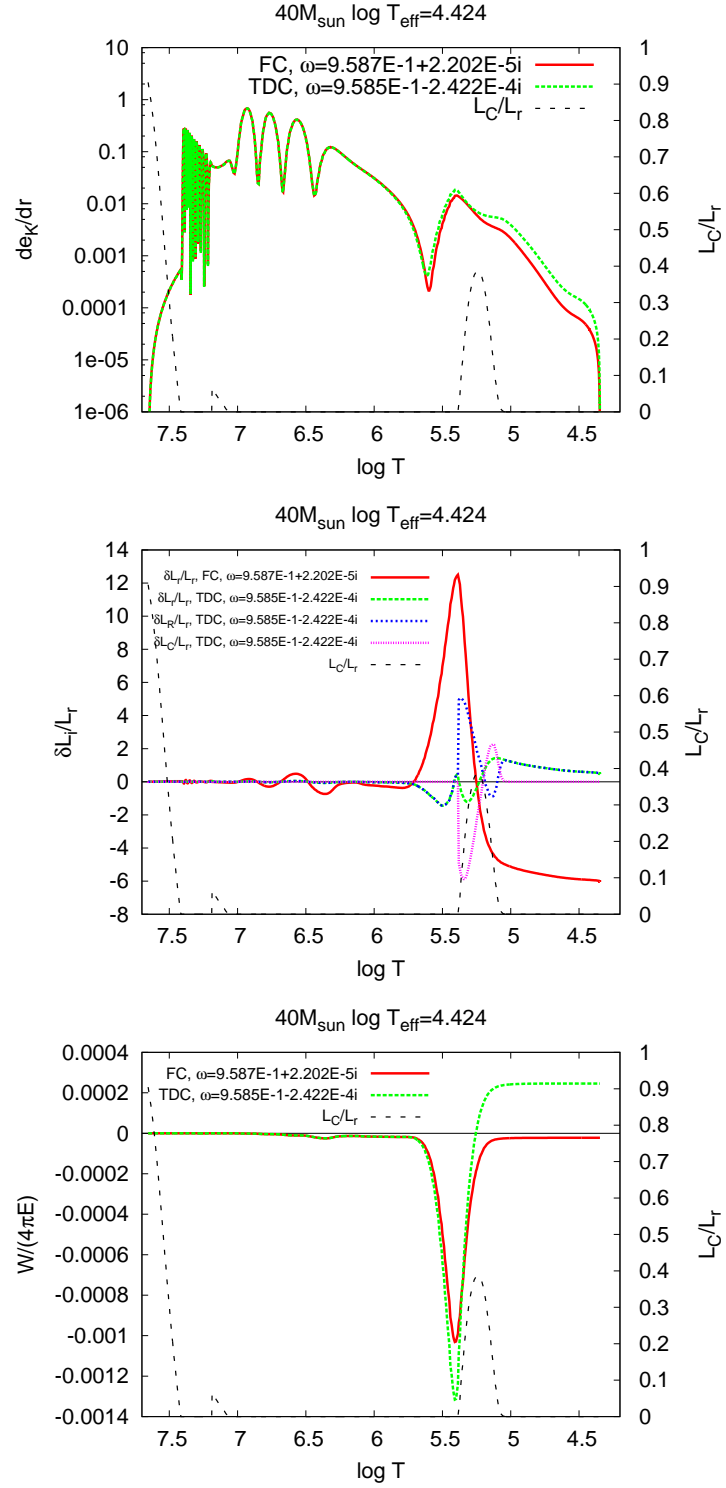
Figure 6.6: Kinetic energy density distribution (*top*), luminosity perturbations (*middle*) and work integrals (*bottom*) for the high-order *g* modes by FC and TDC at the stage with $\log T_{\text{eff}} = 4.424$ for $40M_\odot$. The two modes have close frequency and similar kinetic energy distribution. But the one by FC is stable, while the other by TDC is unstable.

146
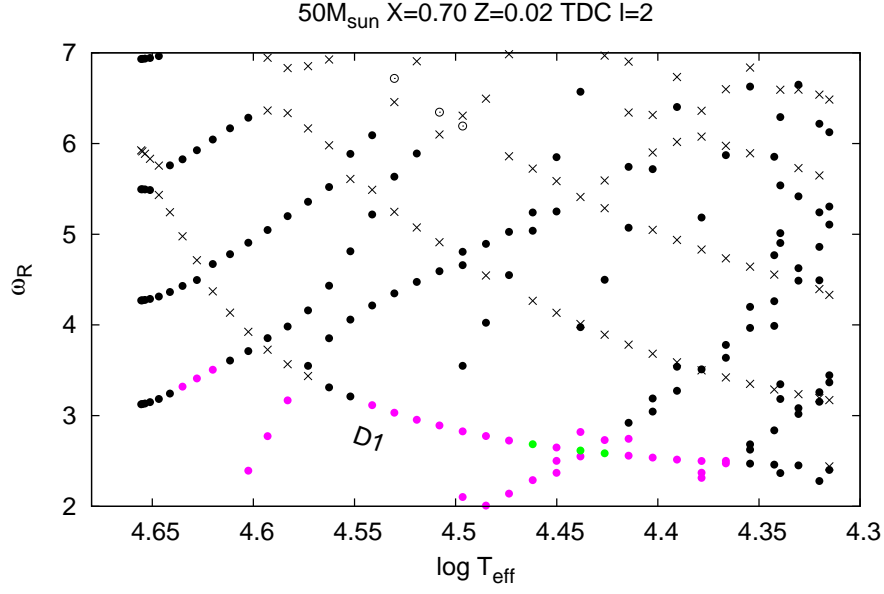
Figure 6.7: Modal diagram of $l = 2$ modes for $50M_\odot$ by TDC. The modes are restricted to ones having over 0.2% of their kinetic energy in the p-mode propagation zone.
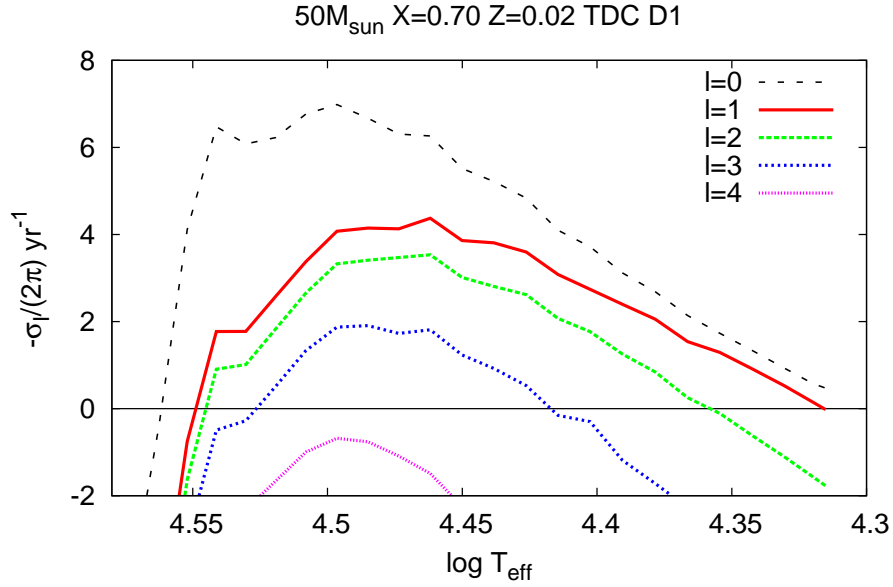
Figure 6.8: Growth rates of the strange-modes on the sequence D1 for $l = 0 - 4$ in the main-sequence stage of $50M_\odot$ by TDC. The positive value of $-\sigma_I/2\pi$ means pulsational instability.
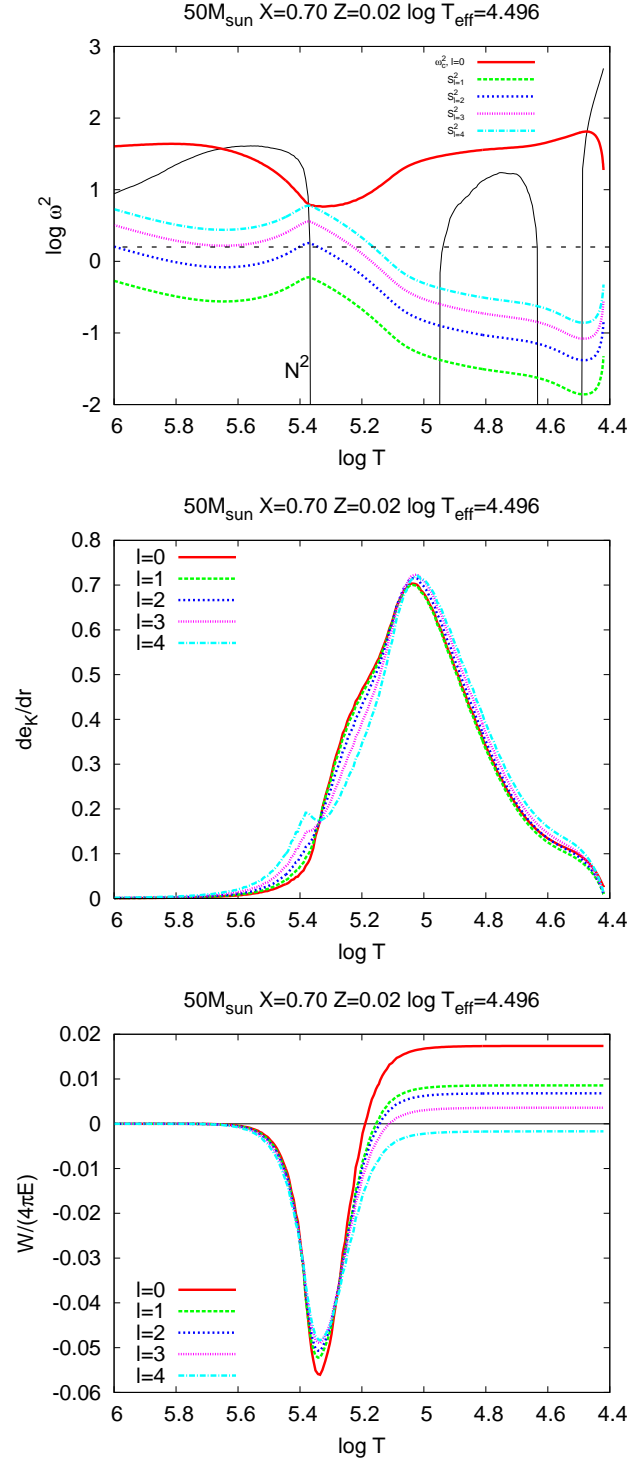
Figure 6.9: Propagation diagram (*top*), kinetic energy density (*middle*) and work integral (*bottom*) of the D1 mode with $l = 0-4$. The equilibrium model is for the evolutionary stage with $\log T_{\text{eff}} = 4.496$ of the $50 M_\odot$ star. The black dashed line in the top panel indicates a pseudo-frequency explaining behaviors of the computed eigenfunctions, although it is lower than the actual computed frequency.

148

Table 6.2: D1 modes with $l = 0 - 4$ at stage with $\log T_{\text{eff}}$=4.496 for $50 M_\odot$.

l	ω_R	ω_I	Period(hr)	e-folding time (yr)^3
0	2.733	-4.271E-02	1.96E+01	1.43E-01
1	2.709	-2.776E-02	2.16E+01	2.41E-01
2	2.827	-2.033E-02	1.90E+01	3.01E-01
3	2.912	-1.145E-02	1.84E+01	5.34E-01
4	3.022	4.152E-03	1.77E+01	-1.47E+00

with $\omega^2 \gg N^2$, S_l^2 becomes narrower, while waves having higher frequencies become able to be propagative in the g-mode propagation zone with $\omega \ll N^2$, S_l^2 and $\log T \gtrsim 5.4$.

Although the frequencies of the D1 modes are in the range of ω =2.7 to 3.0, let us consider a wave with $\log \omega^2 = 0.2$, to which the black horizontal dashed line corresponds in the propagation diagram (the top panel of Fig.6.9). When l =1 and 2, the wave is evanescent in the radiative region with $\log T \gtrsim 5.4$ since $S_l^2 < \omega^2 < N^2$ is satisfied. On the other hand, it is propagative in the two convection zones, the Fe opacity bump convection zone with $\log T \simeq 5.4 - 5$, and the He opacity bump convection zone around $\log T = 4.6$, since $\omega^2 \gg N^2$, S_l^2. When l =3 and 4, it becomes propagative in the radiative region below the Fe bump convection zone since $\omega^2 < N^2$, S_l^2. On the other hand, the propagation zone in the Fe bump convection zone becomes narrower, and the lower part of the convection zone becomes evanescent.

The middle panel of Fig.6.9 shows kinetic energy density distribution. In the lower l case, the energy is confined to the zone above the bottom of the Fe bump convection zone. But as the l increases, the energy becomes reduced in the lower part of the Fe bump convection zone, since waves become evanescent there according to the propagation diagram. Instead, the energy increases in the radiative zone. In other words, the amplitude is confined to the Fe bump excitation zone in the lower l case. With the increasing l, the amplitude comes to leak into the radiative zone with $\log T \gtrsim 5.4$, and the mode comes to suffer from the radiative damping there, and finally to be pulsationally stable. In the main-sequence stage, therefore, the lower l mode is responsible for the instability. The e-folding time is in the order of 10^{-1} as shown in Table 6.2, and much shorter than the evolutionary timescale $\sim 10^6$ yr.

6.5 Conclusion

This chapter has introduced results of pulsational stability analyses for nonradial modes. In the main-sequence stage of massive stars, low-order p and g modes (β Cephei type), high order g modes (SPB type) and strange-modes become unstable. All of them are excited by the κ-mechanism at the Fe bump. Unstable strange-modes are likely to appear near the frequency of the ordinary unstable modes. Especially, the strange-modes appearing in the frequency range of the SPB type are new type, and never found in radial pulsations. They have as high growth rate as the strange-mode on the sequence D1. In the TDC case, higher frequency modes are likely to be less unstable compared with the FC case due to damping by convection.

The l-dependence of the stability of the strange-mode, which appears on the sequence D1 in a modal diagram, is also investigated. As the spherical degree l increases, the amplitude is less confined to the Fe bump κ-mechanism excitation zone, and the mode energy leaks to the radiative zone below the Fe bump convection zone. Then, the instability becomes weaker and finally disappears with $l = 4$. In the main-sequence stage, thus, the radial strange-mode is most responsible for the instability. The e-folding time is in the order of 10^{-1} yr, and much shorter than the evolutionary timescale $\sim 10^6$ yr.

Part III

Conclusions and appendices

7

Conclusions and prospects

7.1 Conclusions

This study examines the properties of the strange-modes. Specifically, their pulsational stability and physical origin are investigated. As for the former, previous studies have carried out pulsational stability analyses with the frozen-in (FC) convection approximation, under which convective effects on pulsations are neglected. This study, however, adopts the time-dependent convection (TDC) theory to the stability analyses of the strange-modes for the first time.

This study focuses on strange-modes in hot massive stars. In the case of $M \simeq 10 M_\odot$, all of eigenmodes are ordinary modes. A normalized frequency which is multiplied by the free-fall or dynamical timescale $\sqrt{R^3/(GM)}$ for each mode keeps constant from the main-sequence to the red giant phase. As the stellar mass increases, however, the ordinary mode frequencies tend to increase with the stellar evolution. Simultaneously, for $M \gtrsim 30 M_\odot$, the strange-modes come to appear while showing that their frequencies going down with the evolution. Some of them are unstable, and have much higher growth rates than the ordinary modes. As the stellar mass increases, unstable strange-modes appear in the lower effective temperature. Especially, some of them are found in evolutionary models around the Humphreys and Davidson (HD,1979) limit.

In this study, the stability analyses are carried out by two types of FC approximation with $\delta L_C = 0$ and $L'_C = 0$, and with TDC. With $\delta L_C = 0$, three strange-modes labeled as D1, D2 and D3 become unstable for $M \gtrsim 50 M_\odot$. When we adopts $L'_C = 0$ and TDC, however, the instability of the D1 and the D2 modes is weaken or suppressed due to convective damping in the Fe bump convection zone, but certainly exists along the evolution of massive stars. On the other hand, the instability of D3 invariably appears in all cases of the two types of FC and TDC, since it is excited around the He bump convection zone having tiny convective luminosity. Then, we can conclude that this instability should definitely appear regardless of

uncertainties on convection. This instability indeed takes place around the HD limit, and could be responsible for the lack of observed stars above the HD limit.

The strange-modes have significantly different properties from the ordinary modes. Unstable strange-modes have extremely high growth rate, and might be influential on stellar evolution. Physical properties of ordinary modes can be explained by the WKB approximation based on the adiabatic approximation. But such a procedure is no longer available for some of the strange-modes. It has been found that the strange-modes appear only in pulsations of very luminous stars with $L/M \gtrsim 10^4 L_\odot/M_\odot$. In envelopes of such stars, the luminosity is too high that matter can save thermal energy flowing from the stellar center. In this very nonadiabatic situation, adiabatic scheme may not be suitable for some of the strange-modes, and then this study carries out local analyses suitable for the situation.

In hot massive stars, there are two types of strange-modes, ones with and without adiabatic counterparts. The type having an adiabatic counterpart appears in the main-sequence stage, while the other type is dominant in the post–main-sequence stage. The former type has the corresponding solutions in the adiabatic approximation. According to the WKB approximation based on the adiabatic approximation, a propagative cavity is formed around the Fe opacity bump due to small density gradient. Then, waves are trapped in the propagative cavity, and the mode amplitude is confined there. This leads to strong excitation of the κ-mechanism at the Fe bump.

On the other hand, the latter type, the strange-modes without adiabatic counterparts, can be explained by the WKB approximations assuming quasi-isothermal (QIT) and radiation-pressure–dominant (RPD) perturbations. In a modal diagram, the latter type seems to correspond to unstable strange-modes without adiabatic counterparts, while the former to most of the other strange-modes.

The unstable modes are not excited by the classical κ-mechanism. Instead, dominance of radiation pressure is important. The excitation of this type of strange-mode is subject to the scheme for the diffusive process of photons. In case that thermal energy flux is extremely strong, matter cannot save the thermal energy efficiently. When some perturbation takes place and one region is compressed, the opacity increases due to the higher density, and the region receive stronger radiation than its surroundings. But since it cannot save the extra received thermal energy generated by the perturbation, temperature (radiation pressure) gradient is produced so that the energy can flow to the other zones. In this process, a large phase lag occurs between the density and the radiation pressure. Indeed, the computed unstable strange-modes without adiabatic counterparts show that the phase lag changes in the range of 0 to 180 degree through the excitation zone unlike the classical κ-mechanism case.

The unstable D3 mode, which does not have an adiabatic counterpart, is excited by the above mechanism around the He bump. Apparently, the instability of this mode seems independent of the metallicity. But this study found that this instability is suppressed by decrease in the metallicity. In the zero-metallicity case, the Fe opacity bump no longer exists. Due to this, radiation pressure is less dominant in the envelope than in the Population I case. Indeed, the opacity profiles around the He bump are almost identical in the Population I and III models having the same effective temperature and luminosity. But we found that the D3 mode becomes unstable for $M \gtrsim 100 M_\odot$ in the Population III case, while for $M \gtrsim 50 M_\odot$

in the Population I case. In the Population III case, cooling process through line emission of heavy elements lacks during the star formation stage. Due to this, core of protostars has high temperature and hence high accretion rate. Then, we can expect that very massive stars were formed in the early Universe. Particularly, the pair-instability supernova (PISN) explosion is proposed in the mass range of $130 - 300 M_\odot$ (Ohkubo *et al.*, 2009). Its existence is controversial since it produces peculiar chemical composition, which is not suitable for observational evidences. The instability of the D3 mode could be inhibitory on the evolutionary scenario toward PISN.

Finally, pulsational stability analysis of nonradial pulsations is carried out in the main-sequence stage of massive stars. As for the ordinary modes, low-order g and p modes, and high-order g modes become unstable and correspond to β Cephei-type and SPB-type pulsations, respectively. Unstable strange-modes appear in the frequency ranges of the both types. In particular, ones with frequencies close to that of the β Cephei type corresponds to the D1 mode of radial pulsation. The instability of low-order ordinary modes and the strange-modes corresponding to D1 is substantially suppressed by the TDC treatment. In addition, the dependence of the D1 mode instability on the spherical degree l is investigated. In the low l cases, the mode amplitude is confined to the envelope including the Fe bump. As the l increases, however, waves become propagative in the radiative zone below the Fe bump convection zone. That is, the amplitude leaks to this zone and the mode suffers from radiative damping. The instability becomes weaker with increasing l, and finally disappears with $l = 4$.

7.2   Future prospects

Finally, we discuss future works following this study.

- This study shows pulsational instability domains in the HR diagram by using TDC, and has found that convection cannot be negligible and influential on pulsational stability. But still now we have a lot of uncertainties on convection theories. In the field of stellar pulsations, several TDC theories have been proposed so far (e.g. Gough, 1965, 1977; Xiong, 1989). Then, it is worth doing that we try to adopt different TDC theories to pulsational stability analyses. Stability analyses with TDC have been mainly carried out for pulsations at the red edge of the classical Cepheid instability strip. In this region, stars have substantially thick convective envelopes due to He and H opacity bumps. On the other hand, convection layers around the Fe bump in hot massive star envelopes is thinner compared with the case of the Cepheid strip. But they have turned out to be influential on pulsational stability by this study. Besides, it is desired to increase the number of observed pulsating massive stars to check the validity of the TDC theories. Recently, solar-like oscillations are detected in massive stars (Belkacem *et al.*, 2009). This type of oscillations is stochastically excited in convection zone. Saio (2011) suggested that unstable oscillatory convection (g^-) modes having substantial amplitude on the stellar surface are excited in the range of $\log T_{\rm eff} \gtrsim 4$ and $\log L/L_\odot \gtrsim 4.5$, and that they could be responsible for variations observed in main-sequence and post–main-sequence massive stars. Godart (in press) demonstrated that the TDC treatment affects the excitation of

154

g^- modes. The above recent results imply that considering convective effects should be indispensable for dealing with pulsations in hot massive stars.

- It is found that the instability of the D3 mode definitely appears around the HD limit regardless of treatments of convection. It could be responsible for the lack of observed stars over the HD limit in the Population I case, and could affect the evolutionary scenario toward PISN in the Population III case. On the other hand, Saio *et al.* (2013) shows variations of α Cygni variables can be explained by unstable strange-modes in stellar models experiencing the blue-loop evolution. This study also confirmed that by TDC with envelope models. To understand phenomena following the pulsational instability, we need to perform nonlinear analyses. As for the Population I (and II) cases, luminous blue variables (LBVs) are observed near the HD limit. They experience sporadic eruption repetitively, and are thought to be Wolf-Rayet (WR) stars after losing substantial mass. Although the results seem to remain inconclusive, several nonlinear analyses for radial strange-modes have been performed (Dorfi and Gautschy, 2000; Chernigovski *et al.*, 2004; Grott *et al.*, 2005) to generate pulsationally-driven mass loss. On the other hand, Aerts *et al.* (2010) found a luminous B star to change its mass loss rate on a timescale of the 57 day period of photometric and spectroscopic variation, and Godart *et al.* (2011) confirmed that the periodicity can be explained by a strange-mode. Recently, there are a number of supernovae which seem to be strongly affected by the interaction with circumstellar media whose densities are too high to be explained by the standard radiation-driven mass loss (Moriya *et al.*, 2013). The mass loss rates of the progenitors before their explosions are estimated to be up to $0.1 M_\odot$ yr^{-1} (e.g. Fox *et al.*, 2011; Kiewe *et al.*, 2012; Taddia *et al.*, 2013), and a mechanism other than radiation-driven mass loss is required.

- In this study, analyses of nonradial pulsations are restricted to the main-sequence stage. In the post main-sequence stage, the density gradient, and hence the Brunt-Väisälä frequency in the deep interiors becomes so high that a number of eigenmodes can exist. Although modes having higher frequency than the reciprocal of the dynamical timescale are p modes which propagate only in the outer envelope in the main-sequence stage, such modes become "mixed modes", which behave like g modes in the deep interior and like p modes in the envelope of post–main-sequence stars. This situation makes it technically difficult to exactly obtain all of desired modes without missing any modes. Then, we need further development of numerical techniques.

- Pulsations can be powerful tools to give constraints on stellar evolution. In particular, massive stars are thought to experience strong mass loss during their evolution. But mass loss theories still includes a lot of uncertainties. Saio *et al.* (2013) constructed evolutionary models by taking into mass loss, and demonstrated the blue-loop evolution. As mentioned above, they explained that the α Cygni variables correspond to blue-loop stars evolving from red supergiants to the WR stars. But the abundance ratios N/C and N/O on the surface of their models seem too high compared with spectroscopic results. Then, further parametric investigations with theoretical models are desired as well as

observational investigations.

A
Radiative transfer

This section introduces description of radiative transfer. We are first going to derive the general expression of radiative flux. Next we will derive the diffusion approximation usually adopted in deep interiors of stars by introducing the Rossland-mean opacity and assuming the isotropy of the intensity.

A.1 Radiative flux

Let us consider photons with frequency ν passing through an area. Energy passing through a solid angle $d\Omega$ around a colatitude angle θ, which denotes angle with the pole perpendicular with the area, per unit area and unit time is expressed as

$$I_\nu(\theta)\cos\theta d\Omega \tag{A.1}$$

where $I_\nu(\theta)$ denotes "intensity" of light passing in direction θ. $\cos\theta$ is multiplied in the RHS of Eq.(A.1) to take into account decrease in the effective area by inclination of direction of the light.

Then, energy flux F_ν, amount of energy passing through a unit area per unit time, is written as

$$F_\nu = \oint_{4\pi} I_\nu(\theta)\cos\theta d\Omega. \tag{A.2}$$

If the intensity I_ν is completely isotropic, $F_\nu = 0$. Although I_ν is in fact almost isotropic in stellar interior, the intensity of outward light is slightly stronger than that of inward light because of the temperature gradient. Therefore, the energy flows outward. The closer to the surface, the stronger the anisotropy of the intensity. At the stellar surface, the intensity of the inward light is zero.

The spatial change of the intensity is caused by emission, absorption and scattering of gas particles is given by

$$\frac{dI_\nu}{ds} = -(\kappa_\nu + \sigma_\nu)\rho I_\nu + \rho\eta_\nu. \tag{A.3}$$

Eq.(A.3) is called "radiative transfer equation". ds denotes a linear element, κ_ν, σ_ν and η_ν the coefficients of the absorption, scattering and emission of the light. For the simplicity, the scattering and emission is hereafter assumed to be isotropic.

Assuming the angle between the pole perpendicular with the area through which the light passing and the direction of ds to be θ and the positive direction of the pole to correspond to the outward of the star, we have

$$ds = dr/\cos\theta. \tag{A.4}$$

Integrating the both sides of Eq.(A.3) after multiplying by $\cos\theta$ and using Eq.(A.4), we obtain

$$F_\nu = -\frac{1}{(\kappa_\nu + \sigma_\nu)\rho}\frac{d}{dr}\oint_{4\pi} I_\nu(\theta;r)\cos^2\theta d\Omega. \tag{A.5}$$

A.2 Diffusion approximation

In deep interiors of stars, photons are repetitively absorbed and re-emitted, and the mean free path is very short compared with scale over which the surrounding structure changes. Thus the radiative energy transport can be described as a diffusive process. Such situation implies the local thermodynamical equilibrium (LTE), and the isotropy of the intensity. In LTE, we can assume the intensity is described as

$$I_\nu(\theta;r) \approx B_\nu(T) \tag{A.6}$$

where B_ν denotes the Planck function, which is the intensity of the black-body radiation,

$$B_\nu = \frac{2h\nu^3}{c^2}\frac{1}{e^{h\nu/kT} - 1} \tag{A.7}$$

where h is the Planck constant and k the Boltzmann constant. By use of this approximation, Eq.(A.5) is transformed into

$$F_\nu = -\frac{4\pi}{3(\kappa_\nu + \sigma_\nu)\rho}\frac{dB_\nu}{dT}\frac{dT}{dr}. \tag{A.8}$$

Although κ_ν depends on the frequency ν, let us introduce the Rossland-mean opacity κ expressed as

$$\frac{1}{\kappa} = \int_0^\infty \frac{1}{\kappa_\nu + \sigma_\nu}\frac{dB_\nu}{dT}d\nu\left(\int_0^\infty \frac{dB_\nu}{dT}d\nu\right)^{-1}. \tag{A.9}$$

Thus we obtain radiative luminosity $L_R(r)$, the energy by the radiative transfer passing through the sphere with the radius r per unit time:

$$L_{\mathrm{R}}(r) = 4\pi r^2 \int_0^\infty F_\nu d\nu = -4\pi r^2 \frac{4ac}{3\kappa\rho}T^3\frac{dT}{dr} \tag{A.10}$$

158

where the following integrated Planck function is used:

$$B(T) = \int_0^\infty B_\nu(T)d\nu = \frac{ca}{4\pi}T^4 \qquad (A.11)$$

Eq.(A.10) is the equation of "diffusion approximation." By transforming Eq.(A.10), we obtain the expression of radiative temperature gradient,

$$\nabla_{\rm rad} \equiv \left(\frac{d\ln T}{d\ln p}\right)_{\rm rad} = \frac{3}{16\pi acG}\frac{\kappa p}{T^4}\frac{L_r}{M_r}, \qquad (A.12)$$

which is required gradient to transport energy by radiation.

B

Atmosphere model

Above the photosphere, the diffusion approximation (A.10) is no longer valid because of the thin opaque. While there are several strategies to overcome such difficulty, this study almost follows Paczyński (1969), adopting the Eddington approximation, to construct atmosphere models. This section introduces the derivation of the differential equations for the atmosphere.

B.1 $T - \tau$ relation in the Eddington approximation

The radiation pressure is described with the intensity as

$$p_R = \frac{2\pi}{c} \int_0^\pi I(\theta) \cos^2 \theta \sin \theta d\theta. \tag{B.1}$$

In the local thermal equilibrium (LTE), the intensity is isotropic, and we have

$$p_R = \frac{4\pi}{3c} I = \frac{4\pi}{3c} B = \frac{1}{3} a T^4, \tag{B.2}$$

where Eqs.(A.6) and (A.11) are used. In the Eddington approximation, the intensity is assumed to be isotropic everywhere, except at $\tau = 0$.

At $\tau = 0$, we assume that $I(\theta)$ is isotropic for all outgoing angles, $0 < \theta < \pi/2$, but set it to be zero for $\pi/2 < \theta < \pi$. It means that no radiation enters the true surface from the outside. Then, the radiation pressure becomes

$$p_R(\tau = 0) = \frac{2\pi}{3c} I(\tau = 0) \tag{B.3}$$

The luminosity L can be described with the intensity as

$$
\begin{aligned}
L &= 4\pi R_s^2 \int_{4\pi} I(\tau = 0) \cos\theta \, d\Omega \\
&= 4\pi R_s^2 2\pi \int_0^{\pi/2} I(\tau = 0) \cos\theta \sin\theta \, d\theta = 4\pi R_s^2 \pi I(\tau = 0)
\end{aligned} \tag{B.4}
$$

where R_s is the stellar radius (distance from the center to the atmosphere surface). Use Eq.(B.4) to eliminate $I(\tau = 0)$ in Eq.(B.3) and find

$$
p_R(\tau = 0) = \frac{2}{3c} \frac{L}{4\pi R_s^2} = \frac{2}{3c} \sigma T_{\text{eff}}^4 \tag{B.5}
$$

Let us derive an expression for the radiation pressure at depth. Recall that we assume LTE except at $\tau = 0$. Then, we can use the diffusion approximation (A.10). By using Eq.(B.2), we can describe the gradient of the radiation pressure as

$$
\frac{dp_R}{dr} = -\frac{\kappa\rho L}{4\pi r^2 c} \tag{B.6}
$$

Integrate it from $\tau = 0$ to some arbitrary depth τ and find

$$
p_R = -\int_{\text{true surface}}^{\text{arbitrary point}} \frac{L}{4\pi r^2 c} \kappa\rho \, dr = \int_0^\tau \frac{L}{4\pi r^2 c} d\tau \tag{B.7}
$$

Since the luminosity L is constant and r is not so different between the photosphere and the atmosphere surface, we can roughly estimate as

$$
p_R(\tau) = \frac{L}{4\pi R_s^2 c}\tau + p_R(\tau = 0) = \frac{\sigma T_{\text{eff}}^4}{c}\tau + p_R(\tau = 0) \tag{B.8}
$$

Substituting Eq.(B.3) into the second term and using Eq.(B.2), we obtain the $T - \tau$ relation in the Eddington approximation,

$$
T^4(\tau) = \frac{1}{2} T_{\text{eff}}^4 \left(1 + \frac{3}{2}\tau\right). \tag{B.9}
$$

In the approximation, thus, the optical depth at the photosphere becomes $\tau = 2/3$, where $T(\tau = 2/3) = T_{\text{eff}}$. Note also that the surface temperature T_s is nonzero, and

$$
T_s = 2^{-1/4} T_{\text{eff}} \tag{B.10}
$$

On the other hand, we can evaluate the stellar radius R_s by using

$$
R_s = \left(\frac{L}{8\pi\sigma_B T_s^4}\right)^{1/2}, \tag{B.11}
$$

which is derived by combining Eqs.(B.3), (B.4), (B.5) and (B.10).

B.2 Differential equations for structure of atmosphere

Here, the procedure to integrate the atmosphere structure will be discussed following Paczyński (1969).

For the integration to construct an atmosphere model, we assume that the mass coordinate M_r is homogeneously equal to the total mass M, and that the local luminosity L_r to the stellar luminosity L. Thus, we abandon the equation of continuity (2.1), and the equation of energy conservation (2.4). Instead, we add the definition of the optical depth

$$(2.42): \ d\tau = -\kappa\rho dr.$$

The equation of motion is unchangedly used:

$$(2.2): \ \frac{\partial p}{\partial M_r} = -\frac{GM_r}{4\pi r^4}$$

The equation for the diffusion approximation Eq.(2.3) is modified to be adopted as follows.

Let us consider matter far from the star. If the coefficient of opacity of that matter were independent on the wavelength of radiation, we would there have the temperature given by

$$T = \left(\frac{L}{8\pi\sigma r^2}\right)^{1/4} \tag{B.12}$$

With no appreciable optical thickness of that matter, there should be a temperature gradient due to the dilution of stellar radiation according to Eq.(B.12). Something similar should be present in the extended stellar atmosphere. Differentiate Eq.(B.12), we have

$$\frac{dT}{dr} = -0.5T_s R_s^{1/2} r^{-3/2} \tag{B.13}$$

By using this, we modify the equation for the diffusion approximation into

$$\frac{dT}{dr} = -\frac{3\kappa\rho L}{64\pi\sigma_B r^2 T^3} - f \times 0.5T_s R_s^{1/2} r^{-3/2} \tag{B.14}$$

where

$$f = \begin{cases} 1 - \frac{3}{2}\tau & \text{for } \tau < \frac{2}{3}, \\ 0 & \text{for } \tau \geq \frac{2}{3} \end{cases} \tag{B.15}$$

To construct atmosphere models in this study, Eqs.(2.42), (2.2) and (B.14) are integrated with the surface boundary conditions Eqs.(B.10), (B.11) and $\rho = 2 \times 10^{-11}$ g cm^{-3}.

C

Boundary conditions for nonradial pulsations

In this section, we derive the boundary conditions for nonradial pulsations. In §3.7, we derived the sixth order system of differential equations, Eqs.(3.128)-(3.133), which has an eigenvalue ω. To solve the system, we require 6+1 boundary conditions in total at the inner and the outer boundaries, which correspond to the center and the surface, respectively, of a star. At the beginning, we give a condition for the normalization of eigenfunctions y_i's,

$$y_1(r = R) = 1 \tag{C.1}$$

at the outer boundary. Then, we will set three conditions each at the center and the surface of a star.

C.1   Inner boundary conditions

First, the boundary conditions at the center are derived. We use the equations Eq.(3.139)-(3.142). Near the center, it is assumed that y_i's are written by the polynomial equations about the radius:

$$y_i = y_{i,0}x^{\beta} + y_{i,2}x^{\beta+2} + \cdots \tag{C.2}$$

where $x \equiv r/R$. Substituting it into Eq.(3.139)-(3.142), we obtain the algebraic equations composed of the coefficients of leading terms:

$$\begin{bmatrix} V_{\mathrm{g}} - 3 - \beta & \frac{l(l+1)}{c_1\omega^2} - V_{\mathrm{g}} & V_{\mathrm{g}} & 0 \\ c_1\omega^2 - A^* & A^* - U + 1 - \beta & -A^* & 0 \\ 0 & 0 & 1 - U - \beta & 1 \\ UA^* & UV_{\mathrm{g}} & l(l+1) - UV_{\mathrm{g}} & U - \beta \end{bmatrix} \begin{bmatrix} y_1 \\ y_2 \\ y_3 \\ y_4 \end{bmatrix} = 0 \tag{C.3}$$

163

Near the center ($r \to 0$),

$$V = \frac{GM_r\rho}{rp} \simeq \frac{4\pi Gr^2\rho_c^2}{3p_c} \to 0 \tag{C.4}$$

$$A^* = \frac{r}{g}N^2 = \frac{3r}{4\pi G\rho_c}N^2 \to 0 \tag{C.5}$$

$$U \to 3 \tag{C.6}$$

Then, we get the values of β as characteristic values:

$$\beta = l - 2,\ -(l + 3) \tag{C.7}$$

The latter is improper since y_i's diverge toward the center. Then, we get the two inner boundary conditions:

$$c_1\omega^2 y_1 - ly_2 = 0 \tag{C.8}$$

and

$$ly_3 - y_4 = 0 \tag{C.9}$$

The first is called "mechanical condition" and the second "potential condition". The last condition is derived from the adiabatic condition, $\delta S = 0$. That is,

$$y_5 = 0, \tag{C.10}$$

which is called as "thermal condition".

C.2   Outer boundary conditions

Next, the boundary conditions at the surface are derived. Also in this case, the mechanical, potential and thermal conditions will be derived and the former two from the differential equations of adiabatic pulsations.

Like the above, the eigenfunctions y_i's are written by the polynomial equations and we get Eq.(C.3). Near the surface ($x \to 1$), we can set as

$$U \to 0 \quad \text{and} \quad c_1 \to 1, \tag{C.11}$$

where the former is explained by that the density is reduced to zero toward the surface. Then, characteristic values of the matrix in Eq.(C.3) are

$$\beta = -l,\ l + 1, \tag{C.12}$$

and

$$\beta_\pm = \frac{1}{2}[(V_g + A^* - 2) \pm \gamma^{1/2}], \tag{C.13}$$

where

$$\gamma = (A^* - V_g + 4)^2 + 4[l(l + 1)/\omega^2 - V_g](\omega^2 - A^*). \tag{C.14}$$

164

The general solution of Eq.(C.3) is then given by

$$
\begin{bmatrix} y_1 \\ y_2 \\ y_3 \\ y_4 \end{bmatrix} = A \begin{bmatrix} \alpha_1 \\ \alpha_2 \\ 1 \\ -(l+1) \end{bmatrix} x^{-l} + B \begin{bmatrix} \beta_1 \\ \beta_2 \\ 1 \\ l \end{bmatrix} x^{l+1}
$$

$$
+ C \begin{bmatrix} 1 \\ (\beta_- - b_{11})/b_{12} \\ 0 \\ 0 \end{bmatrix} x^{\beta_-} + D \begin{bmatrix} 1 \\ (\beta_+ - b_{11})/b_{12} \\ 0 \\ 0 \end{bmatrix} x^{\beta_+}, \quad (C.15)
$$

where

$$
\alpha_1 = \frac{b_{12}b_{23} - b_{13}(b_{22}+l)}{(b_{11}+l)(b_{22}+l) - b_{12}b_{21}}, \quad (C.16)
$$

$$
\alpha_2 = \frac{b_{21}b_{13} - b_{23}(b_{11}+l)}{(b_{11}+l)(b_{22}+l) - b_{12}b_{21}}, \quad (C.17)
$$

$$
\beta_1 = \frac{b_{12}b_{23} - b_{13}(b_{22}-l-1)}{(b_{11}-l-1)(b_{22}-l-1) - b_{12}b_{21}}, \quad (C.18)
$$

$$
\beta_2 = \frac{b_{21}b_{31} - b_{23}(b_{11}-l-1)}{(b_{11}-l-1)(b_{22}-l-1) - b_{12}b_{21}}. \quad (C.19)
$$

Here the coefficient B should be set equal to zero:

$$
B = 0, \quad (C.20)
$$

in order for the potential perturbation y_3 not to increase outward.

The kinetic energy density of oscillations is related to x, y_1 and y_2 as

$$
e_K \equiv \sigma^2 \rho |\boldsymbol{\xi}|^2 \propto x^{-(A^* + V_{\mathrm{g}} - 2)} \left[y_1^2 + \frac{l(l+1)}{\omega^2} y_2^2 \right] \quad (C.21)
$$

For solutions associated with $\beta = \beta_\pm$, the kinetic energy density is then given by

$$
e_K \propto x^{-(A^* + V_{\mathrm{g}} - 2)} x^{2\beta_\pm} = x^{\pm\sqrt{\gamma}} \quad (C.22)
$$

and oscillations near the surface are evanescent waves or propagating waves depending on whether $\gamma > 0$ or $\gamma < 0$. The roots of $\gamma = 0$ give two critical frequencies ω_{c_1} and ω_{c_2} ($\omega_{c_1} < \omega_{c_2}$):

$$
\gamma = -\frac{4V_{\mathrm{g}}}{\omega^2}(\omega^2 - \omega_{c_1}^2)(\omega^2 - \omega_{c_2}^2) \quad (C.23)
$$

In the case of $\omega_{c_1} < \omega < \omega_{c_2}$, the quantity γ is positive and the oscillations associated with $\beta = \beta_\pm$ are evanescent. In the case of $\omega < \omega_{c_1}$ or $\omega > \omega_{c_2}$, on the other hand, the quantity γ is negative, and solutions associated with $\beta = \beta_\pm$ represent progressive waves. The latter case means that the oscillation energy leaks to the outside of a star and hence that the global

oscillation cannot grow to a finite amplitude. These critical frequencies ω_{c_1} and ω_{c_2} are similar to N and S_l of the local analysis in §3.10. Thus ω_{c_1} and ω_{c_2} represent the critical frequencies for propagating gravity waves and for propagating acoustic waves near the surface, respectively.

Let us consider the case that the eigenfrequency ω is between these critical frequencies ($\gamma > 0$). The kinetic energy density of the β_+-solution monotonically increases outward while that of the β_--solution monotonically decreases. Therefore, the β_+-solution should be rejected, and

$$D = 0 \tag{C.24}$$

Eliminating x^{l+1} and x^{β_+} from Eq.(C.15) with $B = D = 0$, we finally obtain two homogeneous relations among y_1, y_2, y_3 and y_4, as follows:

$$(l + 1)y_3 + y_4 = 0 \tag{C.25}$$

and

$$\frac{\beta_- - b_{11}}{b_{12}}y_1 - y_2 - \left[\frac{\alpha_1(\beta_- - b_{11})}{b_{12}} - \alpha_2\right]y_3 = 0 \tag{C.26}$$

These are the two boundary conditions at the surface. Eq.(C.25) and (C.26) are the potential and mechanical boundary conditions, respectively.

We have to be careful for the mechanical condition in case of $\gamma < 0$, which means that waves are propagative at the surface. Such situation takes place when $\omega < \omega_{c_1}$ or $\omega > \omega_{c_2}$. The former corresponds to gravity running waves, while the latter to acoustic running waves. Pulsational energy for both the waves leaks to the outside of a star.

When $\omega > \omega_{c_2}$, the solution associated with β_+ is improper, so that

$$D_1 = 0 \tag{C.27}$$

and the mechanical condition becomes

$$\frac{\beta_- - b_{11}}{b_{12}}y_1 - y_2 - \left[\frac{\alpha_1(\lambda_- - b_{11})}{b_{12}} - \alpha_2\right]y_3 = 0 \tag{C.28}$$

with

$$\beta_- = \frac{1}{2}[(V_g + A^* - 2) - i|\gamma|^{1/2}] \tag{C.29}$$

When $\omega < \omega_{c_1}$, on the other hand, the solution associated with β_- should be rejected so that

$$C_1 = 0. \tag{C.30}$$

Then, the mechanical condition becomes

$$\frac{\beta_+ - b_{11}}{b_{12}}y_1 - y_2 - \left[\frac{\alpha_1(\lambda_- - b_{11})}{b_{12}} - \alpha_2\right]y_3 = 0 \tag{C.31}$$

with

$$\beta_+ = \frac{1}{2}[(V_g + A^* - 2) + i|\gamma|^{1/2}]. \tag{C.32}$$

As introduced above, in the case of the running waves, $\beta_\pm$ is complex number and the eigenvalue and the eigenfunctions can be also complex even under the adiabatic approximation.

The thermal outer boundary condition is derived from the assumption that there is no inward radiative flux at the surface:

$$F_R = f_E J = f_E \frac{\sigma_{\mathrm{rad}}}{\pi} T^4 \tag{C.33}$$

where J is the mean intensity and f_E the Eddington factor, which is reduced to 2π in the Eddington approximation. Perturbing Eq.(C.33) gives

$$\frac{\delta F_R}{F_R} = \frac{\delta f_E}{f_E} + 4\frac{\delta T}{T}. \tag{C.34}$$

However, it is very difficult to obtain the perturbation of the Eddington factor δf_E since it is necessary to solve nonlocal radiative transfer incorporating perturbations due to nonradial oscillations (Christensen-Dalsgaard and Frandsen, 1983). Therefore, this term is not taken into account for simplicity in this study. The expression of Eq.(C.34) with y_i's is given by

$$(2 - 4\nabla_{\mathrm{ad}}V)y_1 + 4\nabla_{\mathrm{ad}}V(y_2 - y_3) + 4y_5 - y_6 = 0. \tag{C.35}$$

D
Relaxation method

This section introduces the relaxation method, which is used for calculations for stellar structure and pulsations in this study. In particular, differential equation systems for stellar pulsations are eigenvalue problems. We then introduce the relaxation method which can simultaneously determine eigenfunctions $\mathbf{y}$ and eigenvalues $\boldsymbol{\omega}$. On the other hand, the system for stellar structure does not include any eigenvalues, which makes the method easier.

In the relaxation method, we have to give the initial eigenvalue and eigenfunctions and make them close to the solution by the iterative procedure. As described in §3.12, to avoid failing to find the desirable eigenvalues, we have to find the initial eigenvalue close to the true eigenvalue by evaluating discriminant $\mathcal{D}(\overline{\omega})$ [1] before solving the eigenvalue problem. The evaluation of $\mathcal{D}(\overline{\omega})$ is a linear algebraic problem since the equation systems, e.g. Eq.(3.128)–(3.133), are linear differential equations, and can be done by using a part of the relaxation method. Below, we first introduce the method for an eigenvalue problem, and then the procedure of evaluating $\mathcal{D}(\overline{\omega})$ at the end.

D.1 Difference equations

Let us consider solving an eigenvalue problem of N first-order differential equations and L eigenvalues. The differential equations can be described as

$$\frac{d\mathbf{y}}{dx} = \mathbf{f}(x, \mathbf{y}, \boldsymbol{\omega}). \tag{D.1}$$

where $\mathbf{y}$ denotes an N-dimensional eigenvector and $\boldsymbol{\omega}$ is an N_ω-dimensional vector containing all the eigenvalues. Let us dividing the considered range of x into M meshes. Then, the

---

[1]In §3.12, the true eigenvalue is expressed with tilde as $\tilde{\omega}$. But it is here written as ω. The bar means the guess value.

168

eigenvector at the mesh k and the vector of the eigenvalues are expressed as

$$
\mathbf{y}^k = \begin{bmatrix} y_1^k \\ \vdots \\ y_i^k \\ \vdots \\ y_N^k \end{bmatrix} , \ \boldsymbol{\omega} = \begin{bmatrix} \omega_1 \\ \vdots \\ \omega_l \\ \vdots \\ \omega_{N_\omega} \end{bmatrix}
\tag{D.2}
$$

The i-th differential equation of Eq.(D.1) becomes

$$
\frac{y_i^k - y_i^{k-1}}{\Delta x_k} = (1 - \theta_i) f_i(x_k, y_j^k, \boldsymbol{\omega}) + \theta_i \mathbf{f}(x_{k-1}, y_j^{k-1}, \boldsymbol{\omega})
\tag{D.3}
$$

for $k = 2, \ldots, M$ and $j = 1, \ldots, N$ and where $\Delta x_k \equiv x_k - x_{k-1}$. θ_i should be set to 0.5 for the central difference scheme. In nonadiabatic analyses, however, we should encounter a numerical instability, which may be caused by c_4 appearing in the equation of energy conservation. We can avoid this by adopting the forward and the backward difference schemes to the difference equations for the linearized equations of energy conservation and of the diffusion approximation. For example, we should set $(\theta_5, \theta_6) = (0, 1)$ or $(1, 0)$ for the system of Eq.(3.128)–(3.133). Eq.(D.3) becomes the following $N \times (M - 1)$ difference equations:

$$
E_i^k(x_{k-1}, x_k, \mathbf{y}^{k-1}, \mathbf{y}^k, \boldsymbol{\omega}) \equiv y_i^k - y_i^{k-1} - \Delta x_k[(1 - \theta_i) f_i(x_k, y_i^k, \boldsymbol{\omega}) + \theta_i f_i(x_{k-1}, y_i^{k-1}, \boldsymbol{\omega})] = 0
\tag{D.4}
$$

for $i = 1, \ldots, N$ and $k = 2, \ldots, M$. Let us describe the inner boundary conditions as an n_{ib}-dimensional vector

$$
\mathbf{B}^{\mathrm{in}}(x_1, \mathbf{y}^1 \boldsymbol{\omega},) = 0
\tag{D.5}
$$

and the outer boundary conditions as an n_{ob}-dimensional vector

$$
\mathbf{B}^{\mathrm{out}}(x_M, \mathbf{y}^M, \boldsymbol{\omega}) = 0.
\tag{D.6}
$$

The number of the boundary conditions have to be equal to the sum of the dimension of the eigenvector $\mathbf{y}_k$ and of the vector of eigenvalues $\boldsymbol{\omega}$:

$$
n_{\mathrm{ib}} + n_{\mathrm{ob}} = N + N_\omega
\tag{D.7}
$$

Thus, we have to calculate $N \times M + N_\omega$ equations simultaneously.

D.2   Linearization

Let us linearize the difference equations and boundary conditions. We define $\overline{\mathbf{y}}$ and $\overline{\boldsymbol{\omega}}$ as the guess values for the true solutions $\mathbf{y}$ and $\boldsymbol{\omega}$, and $\delta \mathbf{y}$ and $\delta \boldsymbol{\omega}$ as the difference between them, respectively:

$$
\begin{aligned}
\mathbf{y}_k &= \overline{\mathbf{y}}_k + \delta \mathbf{y}_k \quad \text{for } k = 1, 2, \ldots, M \tag{D.8} \\
\boldsymbol{\omega} &= \overline{\boldsymbol{\omega}} + \delta \boldsymbol{\omega} \tag{D.9}
\end{aligned}
$$

Then, the expansion of the inner boundary condition Eq.(D.5) to the first order becomes

$$0 = B_i^{\text{in}}(x_1, \overline{\mathbf{y}}^1, \boldsymbol{\omega}) \simeq \overline{B}_i^{\text{in}} + \frac{\partial B_i^{\text{in}}}{\partial y_j^1} \delta y_j^1 + \frac{\partial B_i^{\text{in}}}{\partial \omega_l} \delta \omega_l \tag{D.10}$$

for $i = 1, \ldots, n_{\text{ib}}$, where $\overline{B}_i^{\text{in}} \equiv B_i^{\text{in}}(x_1, \overline{\mathbf{y}}^1)$ and the second and third terms of the RHS are the sums for $j = 1, \ldots, N$ and $l = 1, \ldots, N_\omega$, respectively. The expansion of the difference equations Eq.(D.4) becomes

$$0 = E_i^k(x_{k-1}, x_k, \mathbf{y}^{k-1}, \mathbf{y}^k) \simeq \overline{E}_i^k + \frac{\partial E_i^k}{\partial y_j^{k-1}} \delta y_j^{k-1} + \frac{\partial E_i^k}{\partial y_j^k} \delta y_j^k + \frac{\partial E_i^k}{\partial \omega_l} \delta \omega_l \tag{D.11}$$

for $k = 2, \ldots, N$ where $\overline{E}_i^k \equiv E_i^k(x_{k-1}, x_k, \overline{\mathbf{y}}_{k-1}, \overline{\mathbf{y}}_k)$ and

$$\frac{\partial E_i^k}{\partial y^{k-1}} \delta y^{k-1} = \left[-\delta_{i,j} - \theta_i \Delta x_k \frac{\partial f_i(x_{k-1}, \mathbf{y}^{k-1}, \boldsymbol{\omega})}{\partial y_j^{k-1}} \right] \delta y_j^{k-1} \tag{D.12}$$

$$\frac{\partial E_i^k}{\partial y^k} \delta y^{k-1} = \left[\delta_{i,j} - (1 - \theta_i) \Delta x_k \frac{\partial f_i(x_{k-1}, \mathbf{y}^k, \boldsymbol{\omega})}{\partial y_j^k} \right] \delta y_j^k \tag{D.13}$$

$$\frac{\partial E_i^k}{\partial \omega_l} \delta \omega_l = \left[-\theta_i \Delta x_k \frac{\partial f_i(x_{k-1}, \mathbf{y}^{k-1}, \boldsymbol{\omega})}{\partial \omega_l} - (1 - \theta_i) \Delta x_k \frac{\partial f_i(x_{k-1}, \mathbf{y}^k, \boldsymbol{\omega})}{\partial \omega_l} \right] \delta \omega_l \tag{D.14}$$

where $\delta_{i,j}$ is Kronecker delta and becomes 1 when $i = j$ or otherwise 0. Lastly, the expansion of outer boundary condition Eq.(D.6) to the first order becomes

$$0 = B_i^{\text{out}}(x_1, \overline{\mathbf{y}}^M) \simeq \overline{B}_i^{\text{out}} + \frac{\partial B_i^{\text{out}}}{\partial y_j^M} \delta y_j^M + \frac{\partial B_i^{\text{out}}}{\partial \omega_l} \delta \omega_l \tag{D.15}$$

for $i = 1, \ldots, n_{\text{ob}}$, where $\overline{B}_i^{\text{out}} \equiv B_i^{\text{out}}(x_M, \overline{\mathbf{y}}^M)$. Thus, we obtain the following $N \times M + N_\omega$ equations:

$$\frac{\partial B_i^{\text{in}}}{\partial y_j^1} \delta y_j^1 + \frac{\partial B_i^{\text{in}}}{\partial \omega_l} \delta \omega_l = -\overline{B}_i^{\text{in}} \quad \text{for } i = 1, \ldots, n_{\text{ib}} \tag{D.16}$$

$$\frac{\partial E_i^k}{\partial y_j^{k-1}} \delta y_j^{k-1} + \frac{\partial E_i^k}{\partial y_j^k} \delta y_j^k + \frac{\partial E_i^k}{\partial \omega_l} \delta \omega_l = -\overline{E}_i^k \quad \text{for } i = 1, \ldots, N \text{ and } k = 2, \ldots, M \tag{D.17}$$

$$\frac{\partial B_i^{\text{out}}}{\partial y_j^M} \delta y_j^M + \frac{\partial B_i^{\text{out}}}{\partial \omega_l} \delta \omega_l = -\overline{B}_i^{\text{out}} \quad \text{for } i = 1, \ldots, n_{\text{ob}} \tag{D.18}$$

The matrix expression of these equations is

$$
\begin{bmatrix}
\frac{\partial \mathbf{B}^{\text{in}}}{\partial \mathbf{y}^1} & 0 & 0 & \dots & 0 & 0 & 0 & \frac{\partial \mathbf{B}^{\text{in}}}{\partial \boldsymbol{\omega}} \\
\frac{\partial \mathbf{E}^2}{\partial \mathbf{y}^1} & \frac{\partial \mathbf{E}^2}{\partial \mathbf{y}^2} & 0 & \dots & 0 & 0 & 0 & \frac{\partial \mathbf{E}^2}{\partial \boldsymbol{\omega}} \\
0 & \frac{\partial \mathbf{E}^3}{\partial \mathbf{y}^2} & \frac{\partial \mathbf{E}^3}{\partial \mathbf{y}^3} & \dots & 0 & 0 & 0 & \frac{\partial \mathbf{E}^3}{\partial \boldsymbol{\omega}} \\
\vdots & & \ddots & \ddots & \vdots & \vdots & \vdots & \vdots \\
\vdots & \vdots & \vdots & \ddots & \ddots & & \vdots & \vdots \\
0 & 0 & 0 & \dots & \frac{\partial \mathbf{E}^{M-1}}{\partial \mathbf{y}^{M-2}} & \frac{\partial \mathbf{E}^{M-1}}{\partial \mathbf{y}^{M-1}} & 0 & \frac{\partial \mathbf{E}^{M-1}}{\partial \boldsymbol{\omega}} \\
0 & 0 & 0 & \dots & 0 & \frac{\partial \mathbf{E}^M}{\partial \mathbf{y}^{M-1}} & \frac{\partial \mathbf{E}^M}{\partial \mathbf{y}^M} & \frac{\partial \mathbf{E}^M}{\partial \boldsymbol{\omega}} \\
0 & 0 & 0 & \dots & 0 & 0 & \frac{\partial \mathbf{B}^{\text{out}}}{\partial \mathbf{y}^M} & \frac{\partial \mathbf{B}^{\text{out}}}{\partial \boldsymbol{\omega}}
\end{bmatrix}
\begin{bmatrix}
\delta \mathbf{y}^1 \\ \delta \mathbf{y}^2 \\ \delta \mathbf{y}^3 \\ \vdots \\ \vdots \\ \delta \mathbf{y}^{M-1} \\ \delta \mathbf{y}^M \\ \delta \boldsymbol{\omega}
\end{bmatrix}
= -
\begin{bmatrix}
\overline{\mathbf{B}}^{\text{in}} \\ \overline{\mathbf{E}}^2 \\ \overline{\mathbf{E}}^3 \\ \vdots \\ \vdots \\ \overline{\mathbf{E}}^{M-1} \\ \overline{\mathbf{E}}^M \\ \overline{\mathbf{B}}^{\text{out}}
\end{bmatrix}.
$$
(D.19)

We have gotten $N \times M + N_\omega$ algebraic equations for the same number of unknown values, N components of the errors for the eigenfunctions, $\delta \mathbf{y}^k$'s at M meshes, and N_ω components of the errors for the eigenvalue vector, $\delta \boldsymbol{\omega}$.

D.3 Repartition of Matrix

Let us repartition the above matrix. Parting by N lines from above, we obtain

$$
\begin{pmatrix} \frac{\partial \mathbf{B}^{\text{in}}}{\partial \mathbf{y}^1} \\ \mathcal{U}\frac{\partial \mathbf{E}^2}{\partial \mathbf{y}^1} \end{pmatrix} \delta \mathbf{y}^1 + \begin{pmatrix} 0 \\ \mathcal{U}\frac{\partial \mathbf{E}^2}{\partial \mathbf{y}^2} \end{pmatrix} \delta \mathbf{y}^2 + \begin{pmatrix} \frac{\partial \mathbf{B}^{\text{in}}}{\partial \boldsymbol{\omega}} \\ \mathcal{U}\frac{\partial \mathbf{E}^2}{\partial \boldsymbol{\omega}} \end{pmatrix} \delta \boldsymbol{\omega} = - \begin{pmatrix} \overline{\mathbf{B}}^{\text{in}} \\ \mathcal{U}\overline{\mathbf{E}}^2 \end{pmatrix}
$$
(D.20)

as the first band. $\mathcal{U}$ means the upper $(N - n_{\text{ib}})$ lines. For example, if $\mathbf{v}$ is a N-dimensional vector,

$$
\mathcal{U}\mathbf{v} = \begin{bmatrix} v_1 \\ \vdots \\ v_{N-n_{\text{ib}}} \end{bmatrix}.
$$
(D.21)

Similarly, we introduce $\mathcal{L}$ meaning the lower n_{ib} lines. For example,

$$
\mathcal{L}\mathbf{v} = \begin{bmatrix} v_{N-n_{\text{ib}}+1} \\ \vdots \\ v_N \end{bmatrix}.
$$
(D.22)

Next, the second band is expressed as

$$
\begin{pmatrix} \mathcal{L}\frac{\partial \mathbf{E}^2}{\partial \mathbf{y}^1} \\ 0 \end{pmatrix} \delta \mathbf{y}^1 + \begin{pmatrix} \mathcal{L}\frac{\partial \mathbf{E}^2}{\partial \mathbf{y}^2} \\ \mathcal{U}\frac{\partial \mathbf{E}^3}{\partial \mathbf{y}^2} \end{pmatrix} \delta \mathbf{y}^2 + \begin{pmatrix} 0 \\ \mathcal{U}\frac{\partial \mathbf{E}^3}{\partial \mathbf{y}^3} \end{pmatrix} \delta \mathbf{y}^3 + \begin{pmatrix} \mathcal{L}\frac{\partial \mathbf{E}^2}{\partial \boldsymbol{\omega}} \\ \mathcal{U}\frac{\partial \mathbf{E}^3}{\partial \boldsymbol{\omega}} \end{pmatrix} \delta \boldsymbol{\omega} = - \begin{pmatrix} \mathcal{L}\overline{\mathbf{E}}^2 \\ \mathcal{U}\overline{\mathbf{E}}^3 \end{pmatrix}.
$$
(D.23)

Then, the second and the following bands are generally expressed as

$$
\left(\begin{array}{c} \mathcal{L}\frac{\partial \mathbf{E}^k}{\partial \mathbf{y}^{k-1}} \\ \mathbf{0} \end{array} \right) \delta\mathbf{y}^{k-1} + \left(\begin{array}{c} \mathcal{L}\frac{\partial \mathbf{E}^k}{\partial \mathbf{y}^k} \\ \mathcal{U}\frac{\partial \mathbf{E}^{k+1}}{\partial \mathbf{y}^k} \end{array} \right) \delta\mathbf{y}^k + \left(\begin{array}{c} \mathbf{0} \\ \mathcal{U}\frac{\partial \mathbf{E}^{k+1}}{\partial \mathbf{y}^{k+1}} \end{array} \right) \delta\mathbf{y}^{k+1}
$$

$$
+ \left(\begin{array}{c} \mathcal{L}\frac{\partial \mathbf{E}^k}{\partial \boldsymbol{\omega}} \\ \mathcal{U}\frac{\partial \mathbf{E}^{k+1}}{\partial \boldsymbol{\omega}} \end{array} \right) \delta\boldsymbol{\omega} = - \left(\begin{array}{c} \mathcal{L}\overline{\mathbf{E}}^k \\ \mathcal{U}\overline{\mathbf{E}}^{k+1} \end{array} \right) \tag{D.24}
$$

for $k = 2, \ldots, M-1$. The last band consists of the $(N + N_\omega)$ lines:

$$
\left(\begin{array}{c} \mathcal{L}\frac{\partial \mathbf{E}^M}{\partial \mathbf{y}^{M-1}} \\ \mathbf{0} \end{array} \right) \delta\mathbf{y}^{M-1} + \left(\begin{array}{c} \mathcal{L}\frac{\partial \mathbf{E}^M}{\partial \mathbf{y}^M} \\ \frac{\partial \mathbf{B}^{\mathrm{out}}}{\partial \mathbf{y}^M} \end{array} \right) \delta\mathbf{y}^M + \left(\begin{array}{c} \mathcal{L}\frac{\partial \mathbf{E}^M}{\partial \boldsymbol{\omega}} \\ \frac{\partial \mathbf{B}^{\mathrm{out}}}{\partial \boldsymbol{\omega}} \end{array} \right) \delta\boldsymbol{\omega} = - \left(\begin{array}{c} \mathcal{L}\overline{\mathbf{E}}^M \\ \overline{\mathbf{B}}^{\mathrm{out}} \end{array} \right) \tag{D.25}
$$

Let us rewrite Eq.(D.20) as

$$
D^1\delta\mathbf{y}^1 + U^1\delta\mathbf{y}^2 + Q^1\delta\boldsymbol{\omega} = -\mathbf{R}^1 \tag{D.26}
$$

where D^1 and U^1 are $N \times N$ matrices, Q^1 an $N \times N_\omega$ matrix and $\overline{R}^1$ an N-dimensional vector:

$$
D^1 \equiv \left(\begin{array}{c} \frac{\partial \mathbf{B}^{\mathrm{in}}}{\partial \mathbf{y}^1} \\ \mathcal{U}\frac{\partial \mathbf{E}^2}{\partial \mathbf{y}^1} \end{array} \right), \ U^1 \equiv \left(\begin{array}{c} \mathbf{0} \\ \mathcal{U}\frac{\partial \mathbf{E}^2}{\partial \mathbf{y}^1} \end{array} \right), \ Q^1 \equiv \left(\begin{array}{c} \frac{\partial \mathbf{B}^{\mathrm{in}}}{\partial \boldsymbol{\omega}} \\ \mathcal{U}\frac{\partial \mathbf{E}^2}{\partial \boldsymbol{\omega}} \end{array} \right) \text{ and } \mathbf{R}^1 \equiv \left(\begin{array}{c} \overline{\mathbf{B}}^{\mathrm{in}} \\ \mathcal{U}\overline{\mathbf{E}}^2 \end{array} \right) \tag{D.27}
$$

Similarly, Eq.(D.24) becomes

$$
L^k\delta\mathbf{y}^{k-1} + D^k\delta\mathbf{y}^k + U^k\delta\mathbf{y}^{k+1} + Q^k\delta\boldsymbol{\omega} = -\mathbf{R}^k \tag{D.28}
$$

for $k = 2, \ldots, M-1$ with

$$
L^k \equiv \left(\begin{array}{c} \mathcal{L}\frac{\partial \mathbf{E}^k}{\partial \mathbf{y}^{k-1}} \\ \mathbf{0} \end{array} \right), \ D^k \equiv \left(\begin{array}{c} \mathcal{L}\frac{\partial \mathbf{E}^k}{\partial \mathbf{y}^k} \\ \mathcal{U}\frac{\partial \mathbf{E}^{k+1}}{\partial \mathbf{y}^k} \end{array} \right), \ U^k \equiv \left(\begin{array}{c} \mathbf{0} \\ \mathcal{U}\frac{\partial \mathbf{E}^{k+1}}{\partial \mathbf{y}^{k+1}} \end{array} \right), \tag{D.29}
$$

$$
Q^k \equiv \left(\begin{array}{c} \mathcal{L}\frac{\partial \mathbf{E}^k}{\partial \boldsymbol{\omega}} \\ \mathcal{U}\frac{\partial \mathbf{E}^{k+1}}{\partial \boldsymbol{\omega}} \end{array} \right) \text{ and } \mathbf{R}^k \equiv \left(\begin{array}{c} \mathcal{L}\frac{\partial \mathbf{E}^k}{\partial \boldsymbol{\omega}} \\ \mathcal{U}\frac{\partial \mathbf{E}^{k+1}}{\partial \boldsymbol{\omega}} \end{array} \right). \tag{D.30}
$$

Finally, Eq.(D.25) becomes

$$
L^M\delta\mathbf{y}^{M-1} + D^M\delta\mathbf{y}^M + Q^M\delta\boldsymbol{\omega} = -\mathbf{R}^M, \tag{D.31}
$$

where L^M and D^M are $(N + N_\omega) \times N$ matrices, Q^M an $(N + N_\omega) \times N_\omega$ matrix and $\mathbf{R}^M$ an $(N + N_\omega)$-dimensional vector:

$$
L^M \equiv \left(\begin{array}{c} \mathcal{L}\frac{\partial \mathbf{E}^M}{\partial \mathbf{y}^{M-1}} \\ \mathbf{0} \end{array} \right), \ D^M \equiv \left(\begin{array}{c} \mathcal{L}\frac{\partial \mathbf{E}^M}{\partial \mathbf{y}^M} \\ \frac{\partial \mathbf{B}^{\mathrm{out}}}{\partial \mathbf{y}^M} \end{array} \right), \ Q^M \equiv \left(\begin{array}{c} \mathcal{L}\frac{\partial \mathbf{E}^M}{\partial \boldsymbol{\omega}} \\ \frac{\partial \mathbf{B}^{\mathrm{out}}}{\partial \boldsymbol{\omega}} \end{array} \right) \text{ and } \mathbf{R}^M \equiv \left(\begin{array}{c} \mathcal{L}\overline{\mathbf{E}}^M \\ \overline{\mathbf{B}}^{\mathrm{out}} \end{array} \right)
$$

$$
\tag{D.32}
$$

Thus, Eq.(D.19) becomes

$$
\begin{bmatrix}
D^1 & U^1 & 0 & 0 & \dots & 0 & 0 & 0 & Q^1 \\
L^2 & D^2 & U^2 & 0 & \dots & 0 & 0 & 0 & Q^2 \\
0 & L^3 & D^3 & U^3 & \dots & 0 & 0 & 0 & Q^3 \\
\vdots & & \ddots & \ddots & \ddots & \vdots & \vdots & \vdots & \vdots \\
\vdots & \vdots & \vdots & \ddots & \ddots & \ddots & & \vdots & \vdots \\
0 & 0 & 0 & \dots & L^{M-2} & D^{M-2} & U^{M-2} & 0 & Q^{M-2} \\
0 & 0 & 0 & \dots & 0 & L^{M-1} & D^{M-1} & U^{M-1} & Q^{M-1} \\
0 & 0 & 0 & \dots & 0 & 0 & L^M & D^M & Q^M
\end{bmatrix}
\begin{bmatrix}
\delta\mathbf{y}^1 \\ \delta\mathbf{y}^2 \\ \delta\mathbf{y}^3 \\ \vdots \\ \vdots \\ \delta\mathbf{y}^{M-1} \\ \delta\mathbf{y}^M \\ \delta\boldsymbol{\omega}
\end{bmatrix}
= -
\begin{bmatrix}
\mathbf{R}^1 \\ \mathbf{R}^2 \\ \mathbf{R}^3 \\ \vdots \\ \vdots \\ \mathbf{R}^{M-2} \\ \mathbf{R}^{M-1} \\ \mathbf{R}^M
\end{bmatrix}.
$$

$$(D.33)$$

D.4 Recurrence Formulae

Transforming Eq.(D.26), we have

$$\delta\mathbf{y}^1 = a^1 \delta\mathbf{y}^2 + \mathbf{b}^1 + c^1 \delta\boldsymbol{\omega} \tag{D.34}$$

with

$$a^1 \equiv -(D^1)^{-1} U^1, \ \ \mathbf{b}^1 \equiv -(D^1)^{-1}\mathbf{R}^1 \ \text{ and } \ c^1 \equiv -(D^1)^{-1}Q^1. \tag{D.35}$$

Substituting Eq.(D.34) into Eq.(D.28) for $k = 2$, we obtain

$$(L^2 a^1 + D^2)\delta\mathbf{y}^2 + U^2\delta\mathbf{y}^3 + (L^2 c^1 + Q^2)\delta\boldsymbol{\omega} = -(L^2\mathbf{b}^1 + \mathbf{R}^2). \tag{D.36}$$

This can be expressed as

$$\delta\mathbf{y}^2 = a^2 \delta\mathbf{y}^3 + \mathbf{b}^2 + c^2 \delta\boldsymbol{\omega} \tag{D.37}$$

with

$$
\begin{aligned}
a^2 &\equiv -(L^2 a^1 + D^2)^{-1} U^2, \ \ \mathbf{b}^2 \equiv -(L^2 a^1 + D^2)^{-1}(L^2\mathbf{b}^1 + \mathbf{R}^2) \\
&\text{and } \ c^2 \equiv -(L^2 a^1 + D^2)^{-1}(L^2 c^1 + Q^2).
\end{aligned} \tag{D.38}
$$

In general, for $k = 2, \dots, M - 1$, we have

$$\delta\mathbf{y}^k = a^k \delta\mathbf{y}^{k+1} + \mathbf{b}^k + c^k \delta\boldsymbol{\omega} \tag{D.39}$$

with

$$
\begin{aligned}
a^k &\equiv -(L^k a^{k-1} + D^k)^{-1} U^k, \ \ \mathbf{b}^k \equiv -(L^k a^{k-1} + D^k)^{-1}(L^k\mathbf{b}^{k-1} + \mathbf{R}^k) \\
&\text{and } \ c^k \equiv -(L^k a^{k-1} + D^k)^{-1}(L^k c^{k-1} + Q^k).
\end{aligned} \tag{D.40}
$$

Thus, we can obtain $\delta\mathbf{y}^k$ by using Eq.(D.34) and (D.39), if $\delta\mathbf{y}^{k+1}$ is evaluated. It means that we can get $\mathbf{y}_k$ for all the meshes once $\delta\mathbf{y}^M$ is evaluated. The evaluation of $\mathbf{y}_M$ is realized by eliminating $\delta\mathbf{y}^{M-1}$ in Eq.(D.31) with Eq.(D.39) for $k = M - 1$:

$$(L^M a^{M-1} + D^M)\delta\mathbf{y}^M + (L^M c^{M-1} + Q^M)\delta\boldsymbol{\omega} = -(L^M\mathbf{b}^{M-1} + \mathbf{R}^M) \tag{D.41}$$

Defining an $(N + N_\omega) \times (N + N_\omega)$ matrix Z as

$$
Z_{ij} \equiv \begin{cases} \left[L^M a^{M-1} + D^M \right]_{ij} & \text{for } j = 1, \dots, N \\ \left[L^M c^{M-1} + Q^M \right]_{i(j-N)} & \text{for } j = N+1, \dots, N+N_\omega \end{cases},
$$
(D.42)

we have

$$
\begin{bmatrix} \delta y_1^M \\ \vdots \\ \delta_N^M \\ \delta\omega_1 \\ \vdots \\ \delta\omega_{N_\omega} \end{bmatrix} = -(Z)^{-1}(L^M \mathbf{b}^{M-1} + R^M).
$$
(D.43)

To solve the eigenvalue problem, we should first guess the values of $\mathbf{y}^k$ for all k and $\boldsymbol{\omega}$, and set them to $\overline{\mathbf{y}}^k$ and $\overline{\boldsymbol{\omega}}$, respectively. Then we should iterate evaluating $\mathbf{y}^k$ and $\boldsymbol{\omega}$ until, for example, $\sum_k \left| \delta\mathbf{y}^k \right|$ or $|\delta\boldsymbol{\omega}|$ becomes small enough.

Alternative Evaluation of $\delta\mathbf{y}^M$ and $\delta\boldsymbol{\omega}$

In the nonadiabatic analysis of this study, Q^k's and hence c^k's are vectors since $N_\omega = 1$[2]. Moreover, one of the outer boundary conditions is the normalization, $y_1^M = 1$, which is independent of $\overline{\mathbf{y}}$, $\overline{\boldsymbol{\omega}}$ and the used equilibrium models. Let us consider the method in which the normalization is not included in the above matrices. That is, L^M and D^M are set to be $N \times N$ matrices, and $\mathbf{Q}^M$ to be an N-dimensional vector. Then, Eq.(D.41) becomes

$$
\delta\mathbf{y}^M = \mathbf{b}^M + \mathbf{c}^M \delta\omega
$$
(D.44)

with

$$
\mathbf{b}^M \equiv -(L^M a^{M-1} + D^M)^{-1}(L^M \mathbf{b}^{M-1} + \mathbf{R}^M),
$$
(D.45)

$$
\mathbf{c}^M \equiv -(L^M a^{M-1} + D^M)^{-1}(L^M \mathbf{c}^{M-1} + \mathbf{Q}^M).
$$
(D.46)

Substituting $\delta y_1^M = 1 - \overline{y}_1^M$, we have

$$
\delta\omega = (1 - \overline{y}_1^M - b_1^M)/c_1^M.
$$
(D.47)

Then, δy_i^M for $i = 2, \dots, N$ can be obtained from Eq.(D.44).

---

[2]In the nonadiabatic code of this study, $\mathbf{y}$ and $\boldsymbol{\omega}$ are calculated as complex variables, and are set to be N dimensional vector and scalar, respectively.

D.5 Evaluation of Discriminant

To search the region where there exist the eigenvalues in the complex plane, one of the outer boundary conditions, except for the normalization $y_1^1 = 1$, should be excluded and set to be the discriminant $\mathcal{D}(\omega) = 0$. Note that the notations about ω are different from in §3.12. Here the true eigenvalue is expressed as ω, while the temporal eigenvalue for the search as $\overline{\omega}$. Excluding $\delta\omega$ in the above discussion, Eq.(D.19) becomes

$$
\begin{bmatrix}
\frac{\partial \mathbf{B}^{\mathrm{in}}}{\partial \mathbf{y}^1} & 0 & 0 & \dots & 0 & 0 & 0 \\
\frac{\partial \mathbf{E}^2}{\partial \mathbf{y}^1} & \frac{\partial \mathbf{E}^2}{\partial \mathbf{y}^2} & 0 & \dots & 0 & 0 & 0 \\
0 & \frac{\partial \mathbf{E}^3}{\partial \mathbf{y}^2} & \frac{\partial \mathbf{E}^3}{\partial \mathbf{y}^3} & \dots & 0 & 0 & 0 \\
\vdots & \ddots & \ddots & & \vdots & \vdots & \vdots \\
\vdots & \vdots & \vdots & \ddots & \ddots & & \vdots \\
0 & 0 & 0 & \dots & \frac{\partial \mathbf{E}^{M-1}}{\partial \mathbf{y}^{M-2}} & \frac{\partial \mathbf{E}^{M-1}}{\partial \mathbf{y}^{M-1}} & 0 \\
0 & 0 & 0 & \dots & 0 & \frac{\partial \mathbf{E}^M}{\partial \mathbf{y}^{M-1}} & \frac{\partial \mathbf{E}^M}{\partial \mathbf{y}^M} \\
0 & 0 & 0 & \dots & 0 & 0 & \frac{\partial \mathbf{B}^{\mathrm{out}}}{\partial \mathbf{y}^M}
\end{bmatrix}
\begin{bmatrix}
\delta\mathbf{y}^1 \\
\delta\mathbf{y}^2 \\
\delta\mathbf{y}^3 \\
\vdots \\
\vdots \\
\delta\mathbf{y}^{M-1} \\
\delta\mathbf{y}^M
\end{bmatrix}
= -
\begin{bmatrix}
\overline{\mathbf{B}}^{\mathrm{in}} \\
\overline{\mathbf{E}}^2 \\
\overline{\mathbf{E}}^3 \\
\vdots \\
\vdots \\
\overline{\mathbf{E}}^{M-1} \\
\overline{\mathbf{E}}^M \\
\overline{\mathbf{B}}^{\mathrm{out}}
\end{bmatrix} .
\tag{D.48}
$$

And then the repartitioned matrix corresponding to Eq.(D.33) becomes

$$
\begin{bmatrix}
D^1 & U^1 & 0 & 0 & \dots & 0 & 0 & 0 \\
L^2 & D^2 & U^2 & 0 & \dots & 0 & 0 & 0 \\
0 & L^3 & D^3 & U^3 & \dots & 0 & 0 & 0 \\
\vdots & \ddots & \ddots & \ddots & & \vdots & \vdots & \vdots \\
\vdots & \vdots & \vdots & \ddots & \ddots & \ddots & & \vdots \\
0 & 0 & 0 & \dots & L^{M-2} & D^{M-2} & U^{M-2} & 0 \\
0 & 0 & 0 & \dots & 0 & L^{M-1} & D^{M-1} & U^{M-1} \\
0 & 0 & 0 & \dots & 0 & 0 & L^M & D^M
\end{bmatrix}
\begin{bmatrix}
\delta\mathbf{y}^1 \\
\delta\mathbf{y}^2 \\
\delta\mathbf{y}^3 \\
\vdots \\
\vdots \\
\delta\mathbf{y}^{M-1} \\
\delta\mathbf{y}^M
\end{bmatrix}
= -
\begin{bmatrix}
\mathbf{R}^1 \\
\mathbf{R}^2 \\
\mathbf{R}^3 \\
\vdots \\
\vdots \\
\mathbf{R}^{M-2} \\
\mathbf{R}^{M-1} \\
\mathbf{R}^M
\end{bmatrix}
\tag{D.49}
$$

Since $n_{\mathrm{ib}} + n_{\mathrm{ob}} = N$ here, L^k, D^k and U^k are $N \times N$ matrices and $\mathbf{R}^k$ is an N-dimensional vector for all k. To evaluate $\mathcal{D}(\overline{\omega})$, we need only $\delta\mathbf{y}^M$, which can be obtained from

$$
\delta\mathbf{y}^M = \mathbf{b}^M
\tag{D.50}
$$

where $\mathbf{b}$ is defined by Eq.(D.45). Here the normalization $\mathbf{y}^M = 1$ is included in the matrices. Thus, what we should do to evaluate $\mathcal{D}(\overline{\omega})$ is to calculate a^k and $\mathbf{b}^k$ from $k = 1$ to $M - 1$ with Eq.(D.35) and Eq.(D.40) in order to obtain $\mathbf{b}^M$ and then calculate $\delta\mathbf{y}^M$ with Eq.(D.50). Unlike the case of solving the eigenvalue problem, we do not have an iterative process when Eq.(D.1) are linear differential equations since this is a linear algebraic problem.

D.6 About calculation of stellar structure

We can adopt Eq.(D.49) to calculate stellar structure. But the differential equations for the stellar structure, Eq.(2.1)–(2.4), are nonlinear, and we require some iterations to get
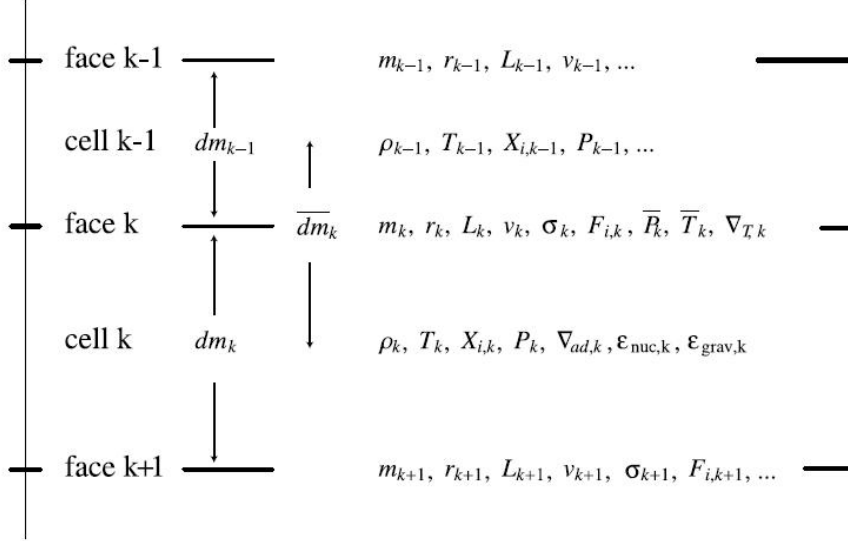
Figure D.1: Schematic of some cell and face variables in MESA (from Paxton *et al.*, 2011).

convergence. This study adopts MESA (Paxton *et al.*, 2011) to construct stellar models. While some stellar evolution codes use the method introduced above, MESA adopts the scheme of staggered cells developed by Sugimoto *et al.* (1981). This scheme has two types of variables as shown in Fig.D.1: the first type is the cell mass-averaged variables, which are density ρ, temperature T and mass fraction of chemical elements X_i. The second one is the variables defined at the boundaries of the cells, which are mass interior to the face m, radius r, luminosity L and velocity v. In addition to these basic variables, the other different variables are calculated for every cell and face, such as ε, κ. Refer to Sugimoto *et al.* (1981) and Paxton *et al.* (2011) for the detail of the scheme and the way to apply it to the relaxation method.

Bibliography

Abel, T., Bryan, G. L., and Norman, M. L. (2002). The Formation of the First Star in the Universe. *Science*, **295**, 93–98.

Aerts, C., Lefever, K., Baglin, A., Degroote, P., Oreiro, R., Vučković, M., Smolders, K., Acke, B., Verhoelst, T., Desmet, M., Godart, M., Noels, A., Dupret, M.-A., Auvergne, M., Baudin, F., Catala, C., Michel, E., and Samadi, R. (2010). Periodic mass-loss episodes due to an oscillation mode with variable amplitude in the hot supergiant HD 50064. *Astronomy and Astrophysics*, **513**, L11.

Aizenman, M. L., Hansen, C. J., and Ross, R. R. (1975). Pulsation Properties of Upper-Main Stars. *The Astrophysical Journal*, **201**, 387–391.

Ando, H. (1982). Active picture of rotation. *Astronomy and Astrophysics*, **108**, 7–13.

Ando, H. (1986). Wave-rotation interaction and episodic mass-loss in Be stars. *Astronomy and Astrophysics*, **163**, 97–104.

Angulo, C., Arnould, M., Rayet, M., Descouvemont, P., Baye, D., Leclercq-Willain, C., Coc, A., Barhoumi, S., Aguer, P., Rolfs, C., Kunz, R., Hammer, J. W., Mayer, A., Paradellis, T., Kossionides, S., Chronidou, C., Spyrou, K., degl'Innocenti, S., Fiorentini, G., Ricci, B., Zavatarelli, S., Providencia, C., Wolters, H., Soares, J., Grama, C., Rahighi, J., Shotter, A., and Lamehi Rachti, M. (1999). A compilation of charged-particle induced thermonuclear reaction rates. *Nuclear Physics A*, **656**, 3–183.

Appenzeller, I. (1970a). Mass Loss Rates for Vibrationally Unstable Very Massive Main-sequence Stars. *Astronomy and Astrophysics*, **9**, 216.

Appenzeller, I. (1970b). The evolution of a vibrationally unstable main-sequence star of 130 M sun. *Astronomy and Astrophysics*, **5**, 355–371.

Bahena, D. and Klapp, J. (2010). First stars. I. Evolution without mass loss. *Astrophysics and Space Science*, **327**, 219–232.

Baker, N. H. and Gough, D. O. (1979). Pulsations of model RR Lyrae stars. *The Astrophysical Journal*, **234**, 232–244.

Baraffe, I., Heger, A., and Woosley, S. E. (2001). On the Stability of Very Massive Primordial Stars. *The Astrophysical Journal*, **550**, 890–896.

Baran, A. S., Fox-Machado, L., Lykke, J., Nielsen, M., and Telting, J. H. (2011). Mt. Suhora Survey - Searching for Pulsating M Dwarfs in Kepler Public Dataset. *Acta Astronomica*, **61**, 325–343.

Belkacem, K., Samadi, R., Goupil, M.-J., Lefèvre, L., Baudin, F., Deheuvels, S., Dupret, M.-A., Appourchaux, T., Scuflaire, R., Auvergne, M., Catala, C., Michel, E., Miglio, A., Montalban, J., Thoul, A., Talon, S., Baglin, A., and Noels, A. (2009). Solar-Like Oscillations in a Massive Star. *Science*, **324**, 1540–.

Bethe, H. A. (1939). Energy Production in Stars. *Physical Review*, **55**, 434–456.

Böhm-Vitense, E. (1958). Über die Wasserstoffkonvektionszone in Sternen verschiedener Effektivtemperaturen und Leuchtkräfte. Mit 5 Textabbildungen. *Zeischrift für Astrophysik*, **46**, 108.

Boury, A. and Noels, A. (1973). Pulsational Instability of a Star of 0.5 M0 during Core Hydrogen Burning. *Astronomy and Astrophysics*, **24**, 255.

Boury, A., Gabriel, M., Noels, A., Scuflaire, R., and Ledoux, P. (1975). Vibrational instability of a 1 solar mass star towards non-radial oscillations. *Astronomy and Astrophysics*, **41**, 279–285.

Bromm, V., Coppi, P. S., and Larson, R. B. (1999). Forming the First Stars in the Universe: The Fragmentation of Primordial Gas. *The Astrophysical Journal Letters*, **527**, L5–L8.

Buchler, J. R., Yecko, P. A., and Kollath, Z. (1997). The nature of strange modes in classical variable stars. *Astronomy and Astrophysics*, **326**, 669–681.

Caughlan, G. R. and Fowler, W. A. (1988). Thermonuclear Reaction Rates V. *Atomic Data and Nuclear Data Tables*, **40**, 283.

Cayrel, R., Depagne, E., Spite, M., Hill, V., Spite, F., François, P., Plez, B., Beers, T., Primas, F., Andersen, J., Barbuy, B., Bonifacio, P., Molaro, P., and Nordström, B. (2004). First stars V - Abundance patterns from C to Zn and supernova yields in the early Galaxy. *Astronomy and Astrophysics*, **416**, 1117–1138.

Charbonnel, C. and Talon, S. (2005). Influence of Gravity Waves on the Internal Rotation and Li Abundance of Solar-Type Stars. *Science*, **309**, 2189–2191.

Chernigovski, S., Grott, M., and Glatzel, W. (2004). A grid reconstruction procedure for the simulation of instabilities in luminous blue variables. *Monthly Notices of the Royal Astronomical Society*, **348**, 192–200.

Christensen-Dalsgaard, J. and Frandsen, S. (1983). Radiative transfer and solar oscillations /Invited review/. *Solar Physics*, **82**, 165–204.

Christensen-Dalsgaard, J., Dilke, F. W. W., and Gough, D. O. (1974). The stability of a solar model to non-radial oscillations. *Monthly Notices of the Royal Astronomical Society*, **169**, 429–445.

Córsico, A. H., Althaus, L. G., Miller Bertolami, M. M., González Pérez, J. M., and Kepler, S. O. (2009). On the Possible Existence of Short-Period g-Mode Instabilities Powered by Nuclear-Burning Shells in Post-Asymptotic Giant Branch H-Deficient (PG1159-Type) Stars. *The Astrophysical Journal*, **701**, 1008–1014.

Cox, A. N. (1954). A study of the galactic cluster NGC 2287. *Publications of the Goethe Link Observatory*, **12**, 107–115.

Cox, J. P. (1955). The Pulsational Stability of Models for Red Giant Stars. *The Astrophysical Journal*, **122**, 286.

Cox, J. P., Cox, A. N., Olsen, K. H., King, D. S., and Eilers, D. D. (1966). Self-Excited Radial Oscillations in Thin Stellar Envelopes. I. *The Astrophysical Journal*, **144**, 1038.

Cox, J. P., Wheeler, J. C., Hansen, C. J., King, D. S., Cox, A. N., and Hodson, S. W. (1980). Pulsations of the R Coronae Borealis stars. *Space Science Reviews*, **27**, 529–534.

Dilke, F. W. W. and Gough, D. O. (1972). The Solar Spoon. *Nature*, **240**, 262–294.

Dorfi, E. A. and Gautschy, A. (2000). Where Are the Regularly Pulsating Massive Stars? *The Astrophysical Journal*, **545**, 982–991.

Dupret, M.-A., Grigahcène, A., Garrido, R., Gabriel, M., and Scuflaire, R. (2005). Convection-pulsation coupling. II. Excitation and stabilization mechanisms in δ Sct and γ Dor stars. *Astronomy and Astrophysics*, **435**, 927–939.

Dziembowski, W. A. (1971). Nonradial Oscillations of Evolved Stars. I. Quasiadiabatic Approximation. *Acta Astronomica*, **21**, 289–306.

Eddington, A. S. (1918a). Stars, Gaseous, On the pulsations of a gaseous star. *Monthly Notices of the Royal Astronomical Society*, **79**, 2–22.

Eddington, A. S. (1918b). The problem of the Cepheid variables. *Monthly Notices of the Royal Astronomical Society*, **79**, 2.

Feng, H. and Soria, R. (2011). Ultraluminous X-ray sources in the Chandra and XMM-Newton era. *New Astronomy Reviews*, **55**, 166–183.

Fox, O. D., Chevalier, R. A., Skrutskie, M. F., Soderberg, A. M., Filippenko, A. V., Ganeshalingam, M., Silverman, J. M., Smith, N., and Steele, T. N. (2011). A Spitzer Survey for Dust in Type IIn Supernovae. *The Astrophysical Journal*, **741**, 7.

Gabriel, M. (1987). Influence of the perturbation of the Reynold tensor on the stability of the solar 5-minute oscillations. *Astronomy and Astrophysics*, **175**, 125–135.

Gabriel, M. (1996). Solar oscillations : theory. *Bulletin of the Astronomical Society of India*, **24**, 233.

Gabriel, M. (1998). Mode Excitation and Damping. In S. Korzennik, editor, *Structure and Dynamics of the Interior of the Sun and Sun-like Stars*, volume 418 of *ESA Special Publication*, page 863.

Gabriel, M. (2000). Linear interaction between pulsations and convection, scattering and line profiles of solar p-modes. *Astronomy and Astrophysics*, **353**, 399–408.

Gabriel, M., Scuflaire, R., Noels, A., and Boury, A. (1974). Influence de la Convection sur la Stabilité des Oscillations Nonradiales des Etoiles. *Bulletin de l'Academie Royale de Belgique*, **60**, 866–887.

Gabriel, M., Scuflaire, R., Noels, A., and Boury, A. (1975). Influence of convection on the vibrational stability of stars towards non-radial oscillations. *Astronomy and Astrophysics*, **40**, 33–39.

Gautschy, A. (1992). Nonradial, nonadiabatic pulsations of evolving massive stars. *Astronomy and Astrophysics*, **260**, 175–182.

Gautschy, A. (1993). Pulsating Post-Asymptotic Giant Branch Stars. *Monthly Notices of the Royal Astronomical Society*, **265**, 340.

Gautschy, A. (1995). Wolf-Rayet-type central stars of planetary nebulae: Are there pulsations involved? *Astronomy and Astrophysics*, **302**, 401.

Gautschy, A. (1997). A further look into the pulsating PG 1159 stars. *Astronomy and Astrophysics*, **320**, 811–822.

Gautschy, A. and Glatzel, W. (1990). On Highly Non-Adiabatic Stellar Pulsations and the Origin of Strange Modes. *Monthly Notices of the Royal Astronomical Society*, **245**, 597.

Glatzel, W. (1994). On the origin of strange modes and the mechanism of related instabilities. *Monthly Notices of the Royal Astronomical Society*, **271**, 66.

Glatzel, W. and Kiriakidis, M. (1993a). Stability of Massive Stars and the Humphreys / Davidson Limit. *Monthly Notices of the Royal Astronomical Society*, **263**, 375.

Glatzel, W. and Kiriakidis, M. (1993b). The stability of massive main-sequence stars. *Monthly Notices of the Royal Astronomical Society*, **262**, 85–92.

Glatzel, W. and Mehren, S. (1996). Non-radial pulsations and stability of massive stars. *Monthly Notices of the Royal Astronomical Society*, **282**, 1470–1482.

Glatzel, W., Kiriakidis, M., and Fricke, K. J. (1993). On the stability and pulsations of Wolf-Rayet stars. *Monthly Notices of the Royal Astronomical Society*, **262**, L7–L11.

Godart, M. (2011). *Unveiling the internal structure and evolution of massive stars through their pulsation modes*. Ph.D. thesis, Université de Liége.

Godart, M. (in press). Pulsations in hot supergiants. In *IAU Symposium*, volume 301 of *IAU Symposium*.

Godart, M., Noels, A., Dupret, M.-A., and Lebreton, Y. (2009). Can mass loss and overshooting prevent the excitation of g-modes in blue supergiants? *Monthly Notices of the Royal Astronomical Society*, **396**, 1833–1841.

Godart, M., Dupret, M.-A., Noels, A., Aerts, C., Simón-Díaz, S., Lefever, K., Puls, J., and Ventura, P. (2010). Strange mode pulsations i massive stars. In *Proceedings of 4th HELAS International Conference: Seismological challenges for stellar structure*, volume 272 of *Astronomical Notes*, page 331.

Godart, M., Dupret, M.-A., Noels, A., Aerts, C., Simón-Díaz, S., Lefever, K., Puls, J., Montalban, J., and Ventura, P. (2011). Pulsations in massive stars: effect of the atmosphere on the strange mode pulsations. In C. Neiner, G. Wade, G. Meynet, and G. Peters, editors, *IAU Symposium*, volume 272 of *IAU Symposium*, pages 503–504.

Gonczi, G. and Osaki, Y. (1980). On local theories of time-dependent convection in the stellar pulsation problem. *Astronomy and Astrophysics*, **84**, 304–310.

González Pérez, J. M., Solheim, J.-E., and Kamben, R. (2006). A search for photometric variability of hydrogen-deficient planetary-nebula nuclei. *Astronomy and Astrophysics*, **454**, 527–536.

Gough, D. O. (1965). *in Geophys. Fluid Dynamics, Wood Hole Oceanographic Institutions*, **2**, 49.

Gough, D. O. (1977). Mixing-length theory for pulsating stars. *The Astrophysical Journal*, **214**, 196–213.

Grigahcène, A., Dupret, M.-A., Gabriel, M., Garrido, R., and Scuflaire, R. (2005). Convection-pulsation coupling. I. A mixing-length perturbative theory. *Astronomy and Astrophysics*, **434**, 1055–1062.

Grott, M., Chernigovski, S., and Glatzel, W. (2005). The simulation of non-linear stellar pulsations. *Monthly Notices of the Royal Astronomical Society*, **360**, 1532–1544.

Guzik, J. A., Kaye, A. B., Bradley, P. A., Cox, A. N., and Neuforge, C. (2000). Driving the Gravity-Mode Pulsations in γ Doradus Variables. *The Astrophysical Journal Letters*, **542**, L57–L60.

Heger, A. and Woosley, S. E. (2002). The Nucleosynthetic Signature of Population III. *The Astrophysical Journal*, **567**, 532–543.

Heger, A., Fryer, C. L., Woosley, S. E., Langer, N., and Hartmann, D. H. (2003). How Massive Single Stars End Their Life. *The Astrophysical Journal*, **591**, 288–300.

Humphreys, R. M. and Davidson, K. (1979). Studies of luminous stars in nearby galaxies. III - Comments on the evolution of the most massive stars in the Milky Way and the Large Magellanic Cloud. *The Astrophysical Journal*, **232**, 409–420.

Humphreys, R. M. and Davidson, K. (1994). The luminous blue variables: Astrophysical geysers. *Publications of the Astronomical Society of the Pacific*, **106**, 1025–1051.

Iglesias, C. A. and Rogers, F. J. (1993). Radiative opacities for carbon- and oxygen-rich mixtures. *The Astrophysical Journal*, **412**, 752–760.

Iglesias, C. A. and Rogers, F. J. (1996). Updated Opal Opacities. *The Astrophysical Journal*, **464**, 943.

Kawaler, S. D. (1988). The hydrogen shell game - Pulsational instabilities in hydrogen shell-burning planetary nebula nuclei. *The Astrophysical Journal*, **334**, 220–228.

Kawaler, S. D., Winget, D. E., Hansen, C. J., and Iben, Jr., I. (1986). The helium shell game - Nonradial g-mode instabilities in hydrogen-deficient planetary nebula nuclei. *The Astrophysical Journal Letters*, **306**, L41–L44.

Kiewe, M., Gal-Yam, A., Arcavi, I., Leonard, D. C., Emilio Enriquez, J., Cenko, S. B., Fox, D. B., Moon, D.-S., Sand, D. J., Soderberg, A. M., and CCCP, T. (2012). Caltech Core-Collapse Project (CCCP) Observations of Type IIn Supernovae: Typical Properties and Implications for Their Progenitor Stars. *The Astrophysical Journal*, **744**, 10.

Kiriakidis, M., Fricke, K. J., and Glatzel, W. (1993). The Stability of Massive Stars and its Dependence on Metallicity and Opacity. *Monthly Notices of the Royal Astronomical Society*, **264**, 50.

Kiriakidis, M., Glatzel, W., and Fricke, K. J. (1996). The stability of Wolf-Rayet stars. *Monthly Notices of the Royal Astronomical Society*, **281**, 406–424.

Klapp, J. (1983). Very massive stars - Evolution with mass loss. I - The hydrogen and helium burning phase. *Astrophysics and Space Science*, **93**, 313–345.

Klapp, J. (1984). Very massive stars - Evolution with mass loss. *Astrophysics and Space Science*, **106**, 215–229.

Leavitt, H. S. and Pickering, E. C. (1912). Periods of 25 Variable Stars in the Small Magellanic Cloud. *Harvard College Observatory Circular*, **173**, 1–3.

Ledoux, P. (1941). On the Vibrational Stability of Gaseous Stars. *The Astrophysical Journal*, **94**, 537.

Ledoux, P. and Walraven, T. (1958). Variable Stars. *Handbuch der Physik*, **51**, 353–604.

Lee, U. (1993). Angular Momentum Transfer by Tidally Forced Oscillations in Massive Main-Sequence Stars. *The Astrophysical Journal*, **417**, 697.

Maeda, K. (2014). *Asteroseismology of Pre-White Dwarfs: Pulsations and Envelope Thickness of Pre-White Dwarfs*. Master's thesis, The University of Tokyo.

Marigo, P., Girardi, L., Chiosi, C., and Wood, P. R. (2001). Zero-metallicity stars. I. Evolution at constant mass. *Astronomy and Astrophysics*, **371**, 152–173.

Moravveji, E., Moya, A., and Guinan, E. F. (2012). Asteroseismology of the nearby SN II Progenitor Rigel. II. epsilon-mechanism Triggering Gravity-mode Pulsations? *The Astrophysical Journal*, **749**, 74.

Moriya, T. J., Maeda, K., Taddia, F., Sollerman, J., Blinnikov, S. I., and Sorokina, E. I. (2013). An analytic bolometric light curve model of interaction-powered supernovae and its application to Type IIn supernovae. *Monthly Notices of the Royal Astronomical Society*, **435**, 1520–1535.

Noels, A., Boury, A., Gabriel, M., and Scuflaire, R. (1976). Vibrational Stability towards Non-radial Oscillations during Central Hydrogen Burning. *Astronomy and Astrophysics*, **49**, 103.

Nomura, T., Naito, J., and Shibahashi, H. (2012). Numerical Simulations of Line-Profile Variation beyond a Single-Surface Approximation for Oscillations in roAp Stars. *Publications of the Astronomical Society of Japan*, **64**, 9.

Ohkubo, T., Umeda, H., Maeda, K., Nomoto, K., Suzuki, T., Tsuruta, S., and Rees, M. J. (2006). Core-Collapse Very Massive Stars: Evolution, Explosion, and Nucleosynthesis of Population III 500-1000 M_{solar} Stars. *The Astrophysical Journal*, **645**, 1352–1372.

Ohkubo, T., Nomoto, K., Umeda, H., Yoshida, N., and Tsuruta, S. (2009). Evolution of Very Massive Population III Stars with Mass Accretion from Pre-main Sequence to Collapse. *The Astrophysical Journal*, **706**, 1184–1193.

Omukai, K. and Palla, F. (2003). Formation of the First Stars by Accretion. *The Astrophysical Journal*, **589**, 677–687.

Paczyński, B. (1969). Envelopes of Red Supergiants. *Acta Astronomica*, **19**, 1.

Palla, F. and Baraffe, I. (2005). Pulsating young brown dwarfs. *Astronomy and Astrophysics*, **432**, L57–L60.

Papaloizou, J. C. B. (1973a). Non-linear pulsations of upper main sequence stars-I.A perturbation approach. *Monthly Notices of the Royal Astronomical Society*, **162**, 143.

Papaloizou, J. C. B. (1973b). Non-linear pulsations of upper main sequence stars-II.Direct numerical integrations. *Monthly Notices of the Royal Astronomical Society*, **162**, 169.

Paxton, B., Bildsten, L., Dotter, A., Herwig, F., Lesaffre, P., and Timmes, F. (2011). Modules for Experiments in Stellar Astrophysics (MESA). *The Astrophysical Journal Supplement*, **192**, 3.

Prandtl, L. (1925). . *Zs. f. angew. Math. Mech.*, **5**, 136.

Prandtl, L. (1932). . *Beitr. z. Phys. d. freien Atm.*, **19**, 188.

Rodríguez-López, C., MacDonald, J., and Moya, A. (2012). Pulsations in M dwarf stars. *Monthly Notices of the Royal Astronomical Society*, **419**, L44–L48.

Rodríguez-López, C., MacDonald, J., Amado, P. J., Moya, A., and Mullan, D. (2013). The theoretical instability strip of M dwarf stars. *Monthly Notices of the Royal Astronomical Society*.

Rogers, F. J. and Iglesias, C. A. (1992). Radiative atomic Rosseland mean opacity tables. *The Astrophysical Journal Supplement*, **79**, 507–568.

Rogers, F. J. and Nayfonov, A. (2002). Updated and Expanded OPAL Equation-of-State Tables: Implications for Helioseismology. *The Astrophysical Journal*, **576**, 1064–1074.

Saio, H. (1980). Stability of nonradial g/+/-mode pulsations in 1 solar mass models. *The Astrophysical Journal*, **240**, 685–692.

Saio, H. (1995). A linear analysis of the radial pulsations of H-deficient stars. *Monthly Notices of the Royal Astronomical Society*, **277**, 1393–1398.

Saio, H. (1996). Linear models for hydrogen-deficient star pulsations. In C. S. Jeffery and U. Heber, editors, *Hydrogen Deficient Stars*, volume 96 of *Astronomical Society of the Pacific Conference Series*, page 361.

Saio, H. (2009). Strange modes. *Communications in Asteroseismology*, **158**, 245.

Saio, H. (2011). Linear analyses for the stability of radial and non-radial oscillations of massive stars. *Monthly Notices of the Royal Astronomical Society*, **412**, 1814–1822.

Saio, H. and Jeffery, C. S. (1988). Radial pulsation in luminous hot helium stars. *The Astrophysical Journal*, **328**, 714–725.

Saio, H., Wheeler, J. C., and Cox, J. P. (1984). Very nonadiabatic radial pulsations in luminous helium stars. *The Astrophysical Journal*, **281**, 318–336.

Saio, H., Baker, N. H., and Gautschy, A. (1998). On the properties of strange modes. *Monthly Notices of the Royal Astronomical Society*, **294**, 622.

Saio, H., Kuschnig, R., Gautschy, A., Cameron, C., Walker, G. A. H., Matthews, J. M., Guenther, D. B., Moffat, A. F. J., Rucinski, S. M., Sasselov, D., and Weiss, W. W. (2006). MOST Detects g- and p-Modes in the B Supergiant HD 163899 (B2 Ib/II). *The Astrophysical Journal*, **650**, 1111–1118.

Saio, H., Georgy, C., and Meynet, G. (2013). Evolution of blue supergiants and α Cygni variables: puzzling CNO surface abundances. *Monthly Notices of the Royal Astronomical Society*, **433**, 1246–1257.

Schwarzschild, M. and Härm, R. (1959). On the Maximum Mass of Stable Stars. *The Astrophysical Journal*, **129**, 637.

Shapley, H. (1914). On the Nature and Cause of Cepheid Variation. *The Astrophysical Journal*, **40**, 448.

Shibahashi, H. and Ishimatsu, H. (2013). Traditional Approximation for Low-Frequency Modes in Rotating Stars and A Working Hypothesis About Episodic Mass Loss in Be Stars. In J. C. Suárez, R. Garrido, L. A. Balona, and J. Christensen-Dalsgaard, editors, *Stellar Pulsations: Impact of New Instrumentation and New Insights*, volume 31 of *Advances in Solid State Physics*, page 49.

Shibahashi, H. and Osaki, Y. (1976). Vibrational stability of gravity modes in massive stars during the shell-hydrogen-burning stage. *Publications of the Astronomical Society of Japan*, **28**, 533–542.

Shibahashi, H. and Osaki, Y. (1981). Nonradial Oscillations for Stars on the Left-Hand Side of the Cepheid Instability Strip. *Publications of the Astronomical Society of Japan*, **33**, 427.

Shibahashi, H., Osaki, Y., and Unno, W. (1975). Nonradial g-mode oscillations and the stability of the sun. *Publications of the Astronomical Society of Japan*, **27**, 401–410.

Sonoi, T. and Shibahashi, H. (2011). Vibrational Instability of Population III Low-Mass Stars due to the ϵ-Mechanism. *Publications of the Astronomical Society of Japan*, **63**, 95–104.

Sonoi, T. and Shibahashi, H. (2012a). Dipole low-order g-mode instability of metal-poor low-mass main-sequence stars due to the ε-mechanism. *Monthly Notices of the Royal Astronomical Society*, **422**, 2642–2647.

Sonoi, T. and Shibahashi, H. (2012b). Fully Nonadiabatic Analysis of Vibrational Instability of Population III Stars due to the ε-Mechanism. *Publications of the Astronomical Society of Japan*, **64**, 2.

Sonoi, T. and Shibahashi, H. (2012c). Vibrational Instability of Metal Poor Stars due to ε-Mechanism. In H. Shibahashi, M. Takata, and A. E. Lynas-Gray, editors, *Progress in Solar/Stellar Physics with Helio- and Asteroseismology*, volume 462 of *Astronomical Society of the Pacific Conference Series*, page 32.

Sonoi, T. and Shibahashi, H. (2013a). Dipole Low-Order g-Mode Instability of Metal-Free and Metal-Poor Main-Sequence Stars due to the ε-Mechanism. In H. Shibahashi and A. E. Lynas-Gray, editors, *Progress in Physics of the Sun and Stars*, volume 469 of *Astronomical Society of the Pacific Conference Series*, page 55.

Sonoi, T. and Shibahashi, H. (2013b). Vibrational Instability of Metal-Poor Low-Mass Main-Sequence Stars. In J. C. Suárez, R. Garrido, L. A. Balona, and J. Christensen-Dalsgaard, editors, *Stellar Pulsations: Impact of New Instrumentation and New Insights*, volume 31 of *Advances in Solid State Physics*, page 17.

Sonoi, T. and Shibahashi, H. (in press). Analysis of strange-mode instability with time-dependent convection in hot massive stars. In *IAU Symposium*, volume 301 of *IAU Symposium*.

Sonoi, T. and Umeda, H. (2012). Vibrational instability of Population III very massive main-sequence stars due to the ε-mechanism. *Monthly Notices of the Royal Astronomical Society*, **421**, L34–L38.

Sterken, C. and Jerzykiewicz, M. (1993). Beta Cephei stars from a photometric point of view. *Space Science Reviews*, **62**, 95–171.

Stothers, R. and Simon, N. R. (1968). On the Pulsational Stability of Blue Supergiants. *The Astrophysical Journal*, **152**, 233.

Stothers, R. B. (1992). Upper limit to the mass of pulsationally stable stars with uniform chemical composition. *The Astrophysical Journal*, **392**, 706–709.

Sugimoto, D., Nomoto, K., and Eriguchi, Y. (1981). Stable Numerical Method in Computation of Stellar Evolution. *Progress of Theoretical Physics Supplement*, **70**, 115–131.

Taddia, F., Stritzinger, M. D., Sollerman, J., Phillips, M. M., Anderson, J. P., Boldt, L., Campillay, A., Castellón, S., Contreras, C., Folatelli, G., Hamuy, M., Heinrich-Josties, E., Krzeminski, W., Morrell, N., Burns, C. R., Freedman, W. L., Madore, B. F., Persson, S. E., and Suntzeff, N. B. (2013). Carnegie Supernova Project: Observations of Type IIn supernovae. *Astronomy and Astrophysics*, **555**, A10.

Talbot, Jr., R. J. (1971a). Nonlinear Pulsations of Unstable Massive Main-Sequence Stars. I. - Amplitude Tests of an Approximation Technique. *The Astrophysical Journal*, **163**, 17.

Talbot, Jr., R. J. (1971b). Nonlinear Pulsations of Unstable Massive Main-Sequence Stars. II. Finite-Amplitude Stability. *The Astrophysical Journal*, **165**, 121.

Taylor, G. I. (1915). Eddy Motion in the Atmosphere. *Royal Society of London Philosophical Transactions Series A*, **215**, 1–26.

Umeda, H. and Nomoto, K. (2002). Nucleosynthesis of Zinc and Iron Peak Elements in Population III Type II Supernovae: Comparison with Abundances of Very Metal Poor Halo Stars. *The Astrophysical Journal*, **565**, 385–404.

Umeda, H. and Nomoto, K. (2005). Variations in the Abundance Pattern of Extremely Metal-Poor Stars and Nucleosynthesis in Population III Supernovae. *The Astrophysical Journal*, **619**, 427–445.

Unno, W. (1967). Stellar Radial Pulsation Coupled with the Convection. *Publications of the Astronomical Society of Japan*, **19**, 140.

Unno, W. (1975). On the stability of the solar core. *Publications of the Astronomical Society of Japan*, **27**, 81–99.

Unno, W., Osaki, Y., Ando, H., Saio, H., and Shibahashi, H. (1989). *Nonradial oscillations of stars*.

van Genderen, A. M. (2001). S Doradus variables in the Galaxy and the Magellanic Clouds. *Astronomy and Astrophysics*, **366**, 508–531.

Waelkens, C. (1991). Slowly pulsating B stars. *Astronomy and Astrophysics*, **246**, 453–468.

Warner, P. B., Kaye, A. B., and Guzik, J. A. (2003). A Theoretical γ Doradus Instability Strip. *The Astrophysical Journal*, **593**, 1049–1055.

Wood, P. R. (1976). Pulsation of high luminosity helium stars. *Monthly Notices of the Royal Astronomical Society*, **174**, 531–539.

Xiong, D.-R. (1989). Radiation-hydrodynamic equations for stellar oscillations. *Astronomy and Astrophysics*, **209**, 126–134.

Acknowledgments

First of all, I would like to thank my supervisor, Hiromoto Shibahashi. He has been my supervisor since I was an undergraduate student. When I go to ask him, he always welcomes and kindly advises me in spite of his crowded schedule. I am always impressed by a lot of his knowledge about different things besides about researches. He also has given me precious opportunities to see foreign researches. In particular, Hakone meeting he held was the first one I have attended in my life, and encouraged me to research harder. I also would like to thank his wife, Minako Shibahashi, for talking in conferences and for always cooking amazing foods for us in house parties.

Shibahashi group members enormously support my research and life in my graduate school. Masao Takata always helps me when I encounter difficulties in my research. His advises accurately point out my problems, and let my works proceed. I am very grateful to Takashi Sekii for advising and encouraging me about my careers after my graduation, and for discussing together in Shibahashi group seminars in spite of his tight schedule. Mélanie Godart helped me a lot with this thesis. I am very pleased to share her deep knowledge about massive stars, and would like to thank her for encouraging and giving me a figure in her thesis. Othman Benomar helped me a lot with office procedures and accommodation for my stay in France after my graduation, and told me his experiences in France. Kazuhiro Maeda is willing to manage our group, and supports my research life. I am very grateful to him for often inviting me to lunch and dinner.

I was very pleased that Hideyuki Saio asked me about my research for the first time when I was a master student. Although I have asked a lot of questions to him so far, he always replies and explains very kindly. I am also very pleased to have discussions with Umin Lee in Sendai, and I would like to thank him and Saio-sensei for driving us for sightseeing in Mt. Zaoh-san. I appreciate Kévin Belcacem inviting me to France and helping me with office procedures to visit there.

I was very lucky to be invited to "Rotating star seminar." I really enjoyed discussions with Hideyuki Umeda, Takashi Hosokawa, Takashi Yoshida, Shingo Hirano, Gen Chiaki and Koh Takahashi.

I am very glad that I have seen and talked with a lot of people in conferences. I am grateful to my friends for mentally supporting me, Soh Ikarashi, Ryo Ohsawa, Mei Sasaki, Yasuhiro Takahashi, Kimihiko Nakajima, Kohei Hattori, Takayuki Hayashi and Takashi Moriya.

I thank the jury members, Masanori Iye, Wako Aoki, Hirohisa Hara, Toshitaka Kajino and Umin Lee for spending a lot of time to read this thesis.

I was very grateful to Masanori Iye for giving me a chance to talk with him when I was a

high school student. That experience strongly encouraged me to go into astronomy.

Finally, I appreciate Kenichi Sonoi and Naoko Sonoi. They always encourage and support me. Especially, I am extremely thankful for letting me study astronomy for a long time.